DEVELOPMENT OF COMPLETELY SULFONATED SODIUM POLYSTYRENE SULFONATE AND ITS DYNAMICS IN LOW-SALT SOLUTIONS

A Dissertation
Presented to
The Academic Faculty

by

Paul L. Balding

In Partial Fulfillment
of the Requirements for the Degree
Doctorate of Philosophy in the
School of Chemistry and Biochemistry

Georgia Institute of Technology
August 2020

COPYRIGHT © 2020 BY PAUL L. BALDING

DEVELOPMENT OF COMPLETELY SULFONATED SODIUM POLYSTYRENE SULFONATE AND ITS DYNAMICS IN LOW-SALT SOLUTIONS

Approved by:

Dr. Paul S. Russo Advisor
School of Materials Science and Engineering
Georgia Institute of Technology

Dr. Jesse McDaniel
School of Chemistry and Biochemistry
Georgia Institute of Technology

Dr. Blair Brettmann
School of Chemical and Biomolecular Engineering
Georgia Institute of Technology

Dr. John Reynolds
School of Chemistry and Biochemistry
Georgia Institute of Technology

Dr. Will Gutekunst
School of Chemistry and Biochemistry
Georgia Institute of Technology

Date Approved: July 21, 2020

ACKNOWLEDGEMENTS

I would like to first and foremost express my eternal gratitude and love to my family, for without them I would not have been able to accomplish any part of this dissertation. I am forever indebted to my parents for their unwavering support, love and guidance. Thank you Dan and Antonia Balding for teaching me the importance of education, of pursuing your passion, of hard work and independence, to discover right from wrong and how to love myself and others equally. They taught me to value what you can only acquire through life experience, through pushing your boundaries, through cherishing every opportunity to learn and grow and be better and make mistakes and to value these things over what can simply be handed to you or purchased. To Phil and James, the three bald dogs for life, I wanted to thank you both for everything. Even though I am the eldest alpha dog I have learnt more from you both than you have from me. Forever be hanging down Minnos on the river and surfing at mystics with you both.

I would also like to thank my extended family. Firstly on the Palazzotto side. Thank you Nonno and Nonna for immigrating to Australia with nothing in your pockets and starting something very special in Campsie. Thank you to all my zia and zio, Lena and David, Filipa, Vita and Frank, and Guisepina and Silvio for loving me and raising me and spoiling me. A massive thank you to all the cousins for all the fun we have had over the years - thanks Lisa, Cathy, Frank, Giorgio and Samantha, Anthony, Sarah and Tanya. Now over to the Balding side. I would like to honor my grandfather Brian Balding who I never had the chance to meet and especially thank my Nanna, the strongest woman I have ever met, who taught me to be humble, respectful and selfless. I would like to thank all my aunts

and uncles and great aunts and great uncles who have cared for me and put up with me from a young age. Thank you Pauline, Steve and Kerry, Ben and Linda, Mary, Ruth, Jill, Bill and Cathy, David and Zach, Denise and Dennis, Greg and Jillian. Thanks to the long list of cousins who made summer holidays a great time – Noni and Malcolm, Anissa, Majda, Kinza, Emma, Jeremy, Sophie, Brian, Aaron, Cassandra, Clare, Lucy, Royce, Grace, Tilly, Rory, Noah, Tom and Jessie, and thanks to the even longer list of extended cousins and their kids.

I have been incredibly fortunate with the friends I have made during my time in Australia. To all my Kiama/Minnamurra mates growing up. Biggest shout out to Jonno, my best mate and brother growing up and the whole Moorhead family for including me as a son and brother. Thanks Penny, Steve, Matt and Liz. Thank you to all my neighbors in the Oxley Ave community, to all my friends at Minnamurra public school, the fellas I played with for the Kiama Cavaliers cricket club, the lads at Kiama Power juniors and to their families who often drive me from one sporting event or surf spot to another. Thanks to the amazing people I met and made lifelong friends with along the way at Smiths Hill. Those were the best years. Thank you Allira, Bob, Crabbot, Chergs, Chumsmash, ClareBear, Dana, Delish, DeSnooze, Gaz, God, Holly, Hummer, Iris, Jacqui, Jack, Joey, Kate, Kev, Linda, Lenny, Lozzo, Lucy, Miki, Nicko, Roachbag, Robbo, Rupak Snakpak, SatyaBowl, Simmo, Smithdog, Squimpdog, Teddy, Tilly, Tunedog, Xander, Wolski, Wuestner, Yono and their families for 5 star teenage hospitality. Foye ave, trips to the farm, surfing for sport, downhill, ski trip, 18ths, never forget. Full credit to the teachers for dealing with us, I owe it to them for somehow inspiring a pretty reckless young kid to strive for something greater. Much love to everyone at the mighty Wollongong Lions footy club.

Thanks to all the U18s and seniors guys, especially Aido, Cookie, Choc Chip Jr, Wellsy, A-train, Thommo, J-Train, Jez, Daly and Mitch Simmo. I would also like to thank the IGA crew. An enormous amount of gratitude goes to my fellow students, researchers and professors during my time at the University of Wollongong. Thanks to Anita, Alana, Sian, Chris, Renae, Beth, Elise, Emily, Sam, Tish, Izzy, Ifrah, Jess, Nick, Darren, Courtney, Neck, Corbs, Big Red, Cezwan, Georgia, Holly, Rhys, Bowley, the Sweetman, Shannon, Damien Danika, Lloyd, Leighton, Tom, Leo and all the folks who convened at the Coniston Manor to partake in retro nights. A very special thank you to my undergraduate advisor Dr. Marc in het Panhuis, keep up the pursuit of that Slater style, and the Soft Materials Lab along with Dr. Geoff Spinks, Dr. Gordon Wallace, Dr. Adam Trevitt, Dr. Robert Gorkin, Dr. Paul Carr and the international science program.

I have also been lucky to meet many incredible people in my home away from home out here in the US. I have been welcomed with open arms and have many to thank for this great experience. I would like to thank all my friends at CU Boulder – Hannah, Ron, Celli, Matty, Court, Voldy, Josh, Klarka, Katie, the College Inn, C4C, the house on the hill, the Bodenhamer family and the Kadar Family.

I would like to thank everybody I have had the pleasure of befriending during my graduate studies at Georgia Tech. To start I would like to thank everyone in the greater Atlanta community for showing me a great time during my stay in the A. Thank you to the Clemson tailgate crew, the Clemson Atlanta alums, the respectable men of Lambda Chi Alpha, the mirror house, Steve's House, the Atlanta Kookaburras USAFL gents, Herb mayoHouse, the Corepower yoga community, Goodfellas and all the great spots around Atlanta and the people who rode some of the way. A special thank you to the almighty

Midnight Ramblers. Dr. Brett, Future Dr. Joe, Master Ben, Master Will and Master DK. You guys taught me it all and were my family on this side of the globe. Another special thank you to Mark and Becs, Ginni Reaves, Lindsey, Kevin and Elyse, tennis coach Brenny and Mattie, spiritual leader Duke, Aman and Ayla, Maddie, Taylor, Gorman, Brandon, Schmatz, Elyse, Luc, Prateek, Harry and Jess, Dylan, Ron, Nomi, Zach, Cameron, Alex, Anthony, Federico, Gio, Nasreen, Manali, Krysten, Brian, Bailey and Scott, Gus, Bonner, Murph, Tyler, Marlow, Hailey, SB, Kristen, Sandy, Dylan, Conlon, Zack and Kylie, Rachel and a shout out to Koopa Cow and Holden doodle. I would also like to thank the Hester family, Kaplan family, Chamlee family, Bracewell and Askey family for everything you have done to care for me and support me. My mother is eternally grateful for including me over holidays and important occasions. Finally I would like to extend an enormous show of thanks and love to Cassidy Bracewell for her support and encouragement during a challenging yet equally rewarding time in my life. She has brought me so much happiness and I cannot wait to begin our next chapter.

This work would not have been possible without the help of the Georgia Tech staff and administration in the Chemistry and MSE departments. Thank you Kenyetta Johnson, Cameron Tyson, the helpful staff at OIE, Richard Bedell, Kevin Green, Hope Payne, Jasmin Frett-Hodge, Mechelle Kitchings, Frank Moss, Nadia Williamson, the student run teams over at the MILL and Invention Studio, the helpful staff at the Montgomery Machine Hall including Frank and Nathan, members of OPALL, the STAMI team of Sharon Lawrence, Dr. Anna Osterholm, Dr .Timothy Parker and Dr. Jung Ok Park. I want to extend a great amount of appreciation for all those who were previously and are currently involved with the SPN at Georgia Tech and STAMI for fostering an environment of polymer

research. I would also like to thank all of those involved with my TA experiences, a huge thank you to Dr. Robert Braga and Dr. Amanda Stephens for making teaching fun and to the students who challenged me every day.

Finally, I would like to thank those who directly contributed their time, intellect and expertise to this work, specifically Dr. Paul Russo for his guidance and support throughout my graduate studies. I thank all Russo Lab members past and present. A special thanks to my office pals Dr. Alyssa Blake and Dr. Graham Parkinson, and to Dr. Drew Gorman, Dr. Bailey Risteen, Dr. Xujun Zhang, Dr. Cornelia Rosu and Dr. Jinxin Fu. I thank the amazing Rachel Borrelli and Ron Volkovinsky for their enormous amount of research assistance. I would like to thank research collaborators, namely, Dr. Rafael Cueto, Dr. Qinlin Wu, Dr. Will Gutekunst and Dr. Meichun Li, and also thank my thesis committee - Dr. Blair Brettmann, Dr. Jesse McDaniel, Dr. Will Gutekunst and Dr. John Reynolds.

TABLE OF CONTENTS

LIST OF TABLES

LIST OF FIGURES

LIST OF SYMBOLS AND ABBREVIATIONS

A	Ratio of Bleach to Read Beam Intensity
AOM	Acousto-Optic Modulator
d_A	Abbe diffraction limit
g_1	First-Order Autocorrelation Function
g_2	Second-Order Autocorrelation Function
APD	Avalanche Photodiode
Λ	Average Separation Between Polymer Chains in Solution
N_A	Avogadro's Number
ATR	Attenuated Total Reflectance
ATRP	Atom Transfer Radical Polymerization
AUC	Analytical Ultracentrifugation
bpy	2,2'-bipyridine
l_B	Bjerrum Length
k_b	Boltzmann constant
Q	Charge Polymer Chain
ω	Circular Frequency
C	Concentration
C_p	Concentration of Polymer
C_s	Concentration of Salt/Electrolyte
C_κ	Concentration Upper Limit Dilute Regime
C_e	Entanglement Concentration
C^*	Overlap Concentration

C^{**}	Concentrated Regime
C^{***}	Hydrated Melt Regime
C_{matrix}	Concentration of Matrix Polymer
C-NaPSS	Commercially sourced NaPSS
ξ	Correlation Length
ξ_{LR}	Correlation Length from Langevin-Rondelez Equation
r_0	Cylinder Radius of Rod-like Polymer
DAQ	Data Acquisition Card
ξ_D	Debye Length
Γ	Decay Rate
α	Degree of Ionization
DP	Degree of Polymerization
ρ	Solution Density
ρ_0	Solvent Density
DNA	Deoxyribonucleic Acid
ϵ	Dielectric Constant of a Medium
ϵ_0	Dielectric Permittivity in Vacuum
DOSY	Diffusion Ordered Spectroscopy
D	Diffusion Coefficient
D_m	Mutual Diffusion Coefficient
D_f	Diffusion Coefficient Fast Mode
D_s	Diffusion Coefficient Slow Mode
D_{self}	Self-Diffusion Coefficient
D_0	Probe Diffusion Absent of Matrix

D_{SE}	Diffusion Coefficient from Stokes-Einstein Law
β	Diffusion-Relation Molecular Weight Scaling Exponent
dRI	Differential Refractive Index
DMF	N'N-Dimethyl Formamide
DSC	Direct Scanning Calorimetry
$Đ$	Dispersity
l_p	Distance Between Polymer Charge Groups
DLS	Dynamic Light Scattering
Δ	Effective Interation
v_{eff}	Effective Size Polyelectrolyte
$\boldsymbol{E}$	Electric Field
U_{ij}	Electrostatic Interaction Energy
e	Electronic charge
μ	Electrophoretic Mobility
ξ_e	Electrostatic Blob Size
R	End-to-End Distance Polymer Chain
ν	Flory Exponent
χ	Flory-Huggins Parameter
FCS	Fluorescence Correlation Spectroscopy
FITC	Fluorescein Isothiocyanate
FPR	Fluorescence Photobleaching Recovery
K	FPR Spatial Frequency
K_{depth}	FPR Bleach Depth
J	Flux in Steady State

FTIR	Fourier-Transform Infrared Spectroscopy
τ_D	FPR Diffusion Recovery Time
f	Friction Coefficient
T_g	Glass Transition Temperature
X	Halogen Atom
HMTETA	1,1,4,7,10,10-Hexamethyltriethylenetetramine
$[I]$	Initiator Concentration
$I_{scattered}$	Intensity of Scattered Light
κ	Inverse Debye Screening Length
$z_i e$	Ionic Charge
z_p	Ionizable Groups per Segment
kDa	Kilodalton
N	Kuhn Segment Number
l	Kuhn Segment Length
L_n	Coordinating Ligand
a	Mark-Houwink Exponent
MALS	Multi-Angle static Light Scattering
MeOH	Methanol
Me_6TREN	CuBr/tris(2-methylaminoethyl)amine
M	Molar Mass
M_n	Number Average Molecular Weight
M_w	Weight Average Molecular Weight
M_z	Z Average Molecular Weight
MWCO	Molecular Weight Cut-Off

$[M]$	Monomer Concentration
NaPSS	Sodium Poly(styrene sulfonate)
NaP4SS	NaPSS obtained by polymerization of 4-styrene sulfonate monomer
NMP	Nitroxide Mediated Polymerization
NMR	Nuclear Magnetic Resonance
NA	Numerical Aperture
H_{p}	NMR Polymer Peak Proton
H_{m}	NMR Monomer Peak Proton
H_{b}	NMR Polymer Backbone Proton
D1	NMR Pulse Delay
n_0	Number Concentration
g	Number Segments in Electrostatic Blob
Π	Osmotic Pressure
K^*	Optical Constant
$\tilde{v}$	Partial Specific Volume
$P(\theta)$	Particle Form Factor
φ	Phase difference between converging laser beams
PAA	Poly(acrylic acid)
PAH	Poly(allylamine hydrochloride)
PAM	Polyacrylamide
PAMPS	Poly(2-acrylamido-2-methyl-1-propanesulfonic acid)
PDADMAC	Poly(diallyldimethylammonium chloride)
PLL	Poly-L-lysine
P_0	Power Laser Beam
PMT	Photomultiplier Tube

k_p	Propagation Constant
k_{deact}	Deactivation Constant
k_{disp}	Disproportionation Constant
k_t	Termination Constant
$R^{\cdot}$	Propagating Radical
PS	Polystyrene
QELS	Quasi-Elastic Light Scattering
q_e	Quantum Efficiency
w	Radial Laser Beam Resolution
RF	Radio Frequency
R_G	Radius of Gyration
R_H	Hydrodynamic Radius
R_p	Rate Polymerization
$R(\theta)$	Rayleigh Ratio
n	Refractive Index of Medium
dn/dc or $\delta n/\delta c$	Specific Refractive Index Increment
τ	Relaxation Time
RAFT	Reversible Addition-Fragmentation chain-Transfer
RDRP	Reversible-Deactivation Radical Polymerization
RITC	Rhodamine Isothiocyanate
q	Scattering Wave Vector
k_m	Scattering Wave Vector of Polyelectrolyte Peak
s	seconds
SARA-ATRP	Supplemental Activator and Reducing Agent Atom Transfer Radical Polymerization

SEC	Size-Exclusion Chromatography
SET-LRP	Single-Electron Transfer Living Radical Polymerization
SFRP	Stable Free Radical mediated Polymerization
T	Temperature in Kelvin
TEM	Transverse Electromagnetic
TERP	Tellurium mediated Radical Polymerization
TGA	Thermogravimetric Analysis
T_d	Thermal Decomposition Temperature
Mt^m	Transition Metal Compound
TPMA	Tris(2-pyridylmethyl)amine
UV-Vis	Ultraviolet-Visible
v_p	Velocity Polymer Chain
A_2	Second Virial Coefficient
η_0	Solvent Viscosity
η	Solution Viscosity
$[\eta]$	Intrinsic Viscosity
V	Volume Containing Polymer Chains
λ	Wavelength of Radiation in Medium
λ_0	Wavelength of Radiation in Vacuum
w	Weight Fraction

SUMMARY

In the four decades since Lin, Lee and Schurr's famous dynamic light scattering (DLS) experiments on low-salt solutions of poly(L-lysine) and subsequent discovery of the experimentally observed phenomenon termed the "ordinary-extraordinary" transition,[1] no aspect in the field of polyelectrolyte physics has proven to be more confusing and controversial to understand.[2-4] The term refers to the simultaneous observation of an ordinary or fast diffusive mode and extraordinary or slow diffusive mode in low ionic strength solutions of single-sized charged macromolecules and colloids.

The ordinary diffusive behavior, represented by a comparatively faster mode of dynamics, displays a measured diffusion coefficient D_f value from DLS that increases above the expected D_{SE} value from the Stokes-Einstein law for dilute polyelectrolyte solutions, and is independent of molecular weight M_w and polymer concentration C_p over several orders of magnitude of each variable. Essentially, $D_f \approx \left(C_p M_w\right)^0$ which is unlike neutral polymer solutions where D_f depends on M_w and C_p.[5-6] The slow diffusion coefficient of the extraordinary mode D_s is orders several orders of magnitude smaller than both D_{SE} and D_f, and unlike the fast mode D_s depends on on M_w and C_p, showing a strong decrease as either variable is increased.[7] Such small D_s values suggests the presence of very large aggregates, which is strange for like charged, and hence electrostatically repulsive, polyelectrolytes. Since termed temporary aggregates, due to the reasoning that the role of counterions at low ionic strength causes the formation of quadrupoles between and along polymer chains, which has the effect of bringing like-charged chains together in

a temporary fashion.[8] The simultaneous existence of the ordinary fast diffusive mode and extraordinary slow diffusive mode clearly relies on the presence and concentration of low molecular weight salt in the polyelectrolyte solution. Drifford and Dalbiez[9-10] proposed that the emergence of the ordinary-extraordinary transition occurs at a particular threshold value of the ratio of polymer concentration C_p to salt concentration C_s, which varies depending on the polymer and salt combination.

Sodium Poly(styrene sulfonate) (NaPSS) is a synthetic polyanion that in aqueous solution bears a fully charged sulfonate repeat unit balanced by a sodium counterion. NaPSS has a variety of applications such as multilayer polyelectrolyte membranes for controlled drug delivery,[11] medicines to treat abnormally high potassium or lithium levels in blood (hyperkalemia),[12] ion-exchange resins for metal ion selectivity and separation,[13-14] flocculants,[15] concrete additives,[16] cosmetics,[17] proton exchange membranes for fuel cells,[18-19] and dopants for conducting polymers.[20-21] NaPSS is widely regarded as a model polyelectrolyte, and it occupies a focal role in the fundamental and applied sciences of polyelectrolytes, being used for fundamental experimental studies for several decades.[10] Parameters investigated have included osmotic pressure and viscosity,[22] chain conformation and counterion condensation,[23] multilayer swelling and uptake of free ions,[24] and dynamics in solution, in particular the investigation of the ordinary-extraordinary transition.

Evidence for the ordinary-extraordinary transition as observed by DLS is plentiful, but completely lacking when measured using other techniques that probe dynamics. Fluorescence photobleaching recovery (FPR) describes a three-part experiment used to obtain a self-diffusion coefficient of inherently fluorescent or fluorescently labelled entities

in a medium. First, the fluorescence of a small, select region of the sample is measured using a dim beam that does not cause rapid degradation of the signal. Next, some of the fluorescent moieties are destroyed within a selected region of the sample using a bright pulse of light. Finally, the return of fluorescence to that same region, due to the exchange by diffusion of bleached molecules with unbleached molecules that originally lay outside the selected volume, is monitored photometrically. System kinetics are manifested by a recovery profile, changing the otherwise static pre-bleach signal into an exponentially varying one that produces a characteristic relaxation time for a species based on the rate of its diffusion. FPR is advantageous in its ability to track fluorescent entities in heterogeneous media where a multitude of sized structures can influence the motion of the object of interest without contaminating the measured signal.[25-27]

The research projects described herein were conducted to improve a model polyelectrolyte system via a controlled and repeatable synthesis to obtain completely sulfonated NaPSS, reveal discrepancies in the physical properties of NaPSS depending on the method of its production, gain insight into temporary aggregates and mixed NaPSS diffusion in solutions of low salt via FPR measurements on binary NaPSS mixtures, and finally create and develop a holographic FPR instrument to probe NaPSS at spatial frequencies comparable to that of the DLS technique that routinely observes the ordinary-extraordinary transition. These findings aim to aid in further understanding and explaining the most challenging problem encountered in the field of polyelectrolyte physics.

The establishment of a convenient and robust synthetic method to produce completely sulfonated NaPSS on gram scales is warranted for the purposes of diffusive measurements to probe the ordinary-extraordinary transition. The vast majority of

researchers who investigate this diffusive transition do so with commercially obtained NaPSS which is not 100% sulfonated and thus contains hydrophobic patches that could give rise to aggregation.[28-29] When studying a model polyelectrolyte system an emphasis must be placed on the material being without impurities or defects which will ultimately corrupt the results. Reversible-deactivation radical polymerization (RDRP) techniques, in particular atom transfer radical polymerization (ATRP), have grown substantial interest owing to their ability to produce polymers in a controlled synthetic fashion. Conducting ATRP in polar media is a major limitation of the technique and the ability to produce well defined functional materials in aqueous media is highly desirable.[30] Synthesizing NaPSS over a range of molecular weights via aqueous ATRP in a controllable fashion is of interest to the RDRP community in that it adds to the scope of polymerizable water soluble monomers and ability of the technique to succeed in an environmentally friendly solvent.[31] Once successful reaction parameters are determined ATRP is a relatively straightforward technique that any researcher could replicate to produce NaPSS in gram scales. This research project was designed to determine the reaction parameters required to conduct a controlled polymerization and to expand the typical range of molecular weights that are achievable with an RDRP approach. A key contribution to the field of polymer synthesis was producing high molecular weight NaPSS and doing so using a parametric approach rather than conventional variation in the monomer:initiator ratio.

Applications of producing a better NaPSS material extend far beyond fundamental polyelectrolyte studies. While a better understanding of ordinary-extraordinary behavior will aid in future processing of polyelectrolytes into advanced material devices, a NaPSS material with specific and completely charged repeat units will be beneficial for researchers

investigate topics that vary from charge carrying properties of solid polymer electrolytes to coacervate formation of oppositely charged polyelectrolyte complexes. A project that focused on the changes in the physical properties of NaPSS synthesized via ATRP compared to NaPSS that is commonly used and commercially sourced was therefore required. Determination of discrepencies in the solution and bulk properties between samples has major implications for the countless studies conducted with what was claimed to be NaPSS and were actually been done on a NaPSS-polystyrene copolymer. NaPSS has applications in ion exchange resins,[13-14] cosmetics,[32] flocculants,[15] concrete additives,[16] medicine to treat hyperkalemia,[33] polyelectrolyte multilayers and complexes,[34-35] flexible organic solar cells,[36] polymer electrolytic capacitors,[18-19] and organic light-emitting diodes,[37] and dopants for conducting polymers.[20-21] It was expected that a higher degree of sulfonation for the NaPSS materials we synthesized would alter known viscosity, conductivity and ion uptake values, which are important for other researchers using polyelectrolytes such as NaPSS in applications where material performance is critical. This project intended to characterize any structural and chemical differences between NaPSS we synthesized compared to several samples purchased from a variety of vendors and determine if a select number of solution and bulk properties were substantially different. Significant re-evaluation of many fundamental polyelectrolyte properties may need to be addressed with this improved NaPSS material.

The use of FPR to compliment DLS as another diffusion measurement technique to observe ordinary-extraordinary behaviour is needed. Previous analysis of NaPSS solutions at low salt revealed that the FPR instrument, which operates on long time and distance scales, was unable to capture the same bimodal diffusive behavior observed by

DLS.[38] This is owed to the temporary nature of the aggregates that account for the slow diffusive mode. But FPR is able to measure the average diffusion of both events, polymers entrained in these large slow moving aggregates or those free of them and moving around more quickly as single chains. Diffusion as a function of the C_p/C_s ratio through the critical transition would reveal a greater decrease if the formation of larger structures were contributing to the dynamics. In addition, FPR is advantageous in its ability to solely track fluorescent moities in a non-fluorescent background. Mixing fluorescently labeled NaPSS probes in with unlabeled NaPSS matrices is a unique method to investigate potential temporal aggreagate behavior. Variation in the concentrations and molecular weights of the probe and matrix component permit several questions to be asked of temporary aggregate behavior. Is probe diffusion independent of rising matrix concentration, indicative of being entrained in an aggregate? At what matrix concentration and/or molecular weight do probes being to enter temporary aggregates? And can the temporary aggregate concentration be saturated by rising matrix concentration or molecualer weight? Regardless of what can be learned about temporary aggregates the diffusion of mixed molecular weight polyelectrolytes at low salt is important for reasons ranging from polydispersity to biological function as charged macromolecules are often found with others.[39] Treatment of the data with scaling theories on neutral polymer systems of probes diffusing through matrices guide our results and warrant the need of new theory to incorporate electrostatic interactions along with the present topological and hydrodynamic forces. The observations we made that reveal deviation of probe diffusion from Stokes-Einstein behavior and the relationship between probe diffusion and matrix correlation length are important contributions to the field of polyelectrolyte physics.

Knowing that current FPR technology is limited the final research project addressed the imperfect comparison between FPR and DLS by reducing the distance scale of the FPR measurement. The spatial frequency of the FPR is defined by the grating periodicity that is photobleached on a sample, typically done by placing a Ronchi ruling mask in the rear image plane. A crossed-beam holographic FPR instrument was developed to produce finer grating periods and thus higher spatial frequencies. This theoretically permits observation of much faster events such as the exchange of charged polymers into and out of temporary aggregates.[40] Variation of the holographic FPR beam crossing angle changed the grating periodicity allows access to a broad range of spatial frequencies, reaching spatial frequencies equivalent to previous FPR technology extending to values over an order of magnitude greater and nearly equivalent to that DLS accesses to observe the slow diffusive mode. The focus of this project is the design, construction and implementation of a holographic FPR instrument with image-based analysis method to observe the decaying interference pattern of fluorescent NaPSS in solutions of low salt. The aim is to measure the diffusion coefficient for NaPSS and seek out any multi exponential character to the decaying contrast signal to establish that temporary aggregates can be measured by this technique. Validation of DLS data is critical to understand the nature and longevity of temporary aggregates and conclude the near 50 year debate on the meaning of the ordinary-extraordinary transition. Expanding the scope of what is measurable by the FPR technique is a feat in itself but the crossed beam instrument has a significant advantage over DLS for probing the dynamics of the slow mode because DLS does not probe relatively long distance scales. Diffusion measurements as a function of spatial frequency may show a transition point between where temporary aggregates are and are not observed. The time

scale at this point produces a value for the residence time of a single NaPSS chain as it exchanges in and out of the aggregate. A greater understanding of the slow diffusive mode is integral in explaining the ordinary-extraordinary transition and is also vital for potential applications where the processing of polyelectrolytes in salt-free or low salt solutions is required.

CHAPTER 1. INTRODUCTION

1.1 Polyelectrolyte materials and their classes

1.1.1 Polymer

A polymer is defined as a macromolecule composed of many repeat units called monomers. Polymers compared to molecules are bulky in nature due to their large molecular weights and are considered to be neutral entities which exist as random coils in suitable nonpolar organic solvents.

General forms of polymer classification are based on their origin, topological structure, chemical heterogeneity, functionality, method of polymerization, and intermolecular forces that hold them together.

Polymers can be classed as natural; such as wool, proteins, cellulose and rubber, or synthetic; such as polyethylene, nylon, polystyrene (PS) and polycarbonate. Topologies such as linear, branched, star, comb, crosslinked or network, or dendritic are ways to classify polymers. So too is the composition of chemical identity along the polymer structure, classed as homopolymer, block, periodic, random and gradient copolymer, along with graft copolymer. Polymers can have side functional groups, end functionalities, site specific functionality, be telechelic and multifunctional. There are two main classes of polymerization reaction mechanisms; chain-growth, which is the addition of monomer to a growing chain, or step-growth, the addition of two molecules of any length to form a longer polymer. Polymers can also be classed as elastomers, thermoplastics, thermosets and fibers depending on the forces holding them together (Figure 1).

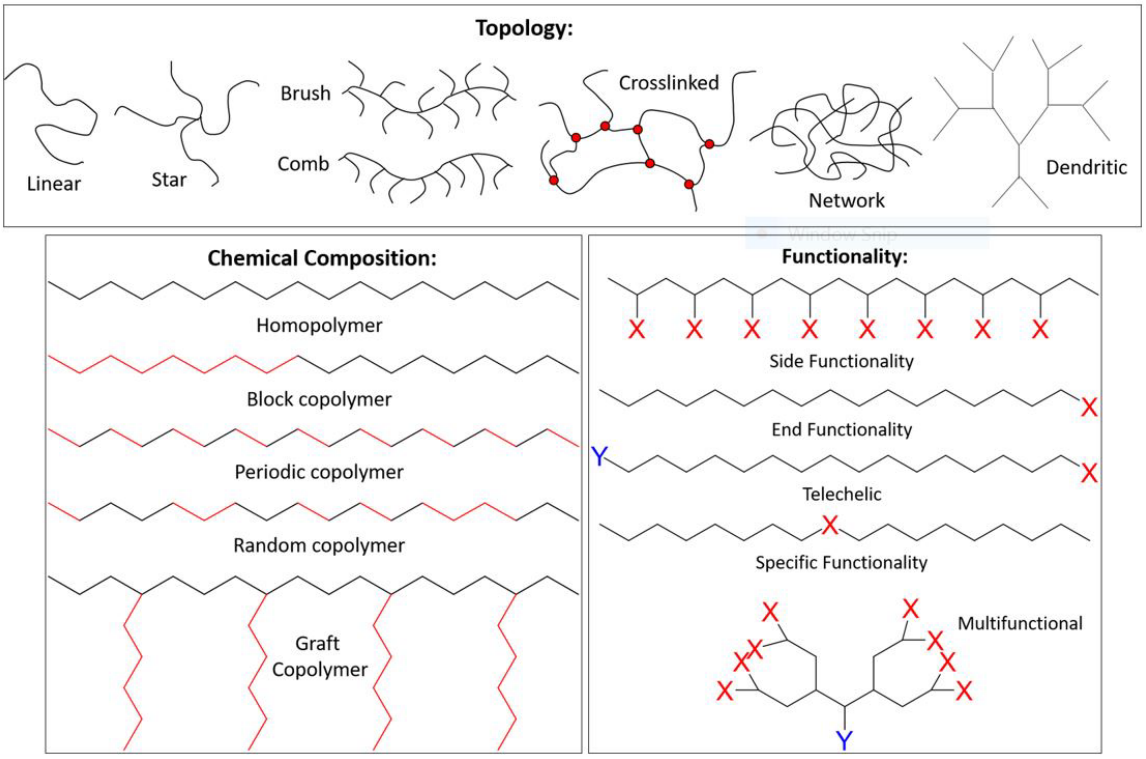

Figure 1. Types of polymer topologies, composition and functionality.

1.1.2 Electrolyte

An electrolyte is a substance such as sodium, potassium, chloride, phosphate, bromide and calcium that when dissolves into a polar solvent like water produces an electrically conducting solution. The dissolved electrolyte separates into cations and anions evenly throughout the solution. Unlike polymers, electrolytes are small molecules for which an example of this is sodium chloride in water:

$$NaCl \rightarrow Na^{+} + Cl^{-}$$

1.1.3 Polyelectrolyte Definition

Polyelectrolytes resemble both polymers and electrolytes and are a special class of chemical specie. We know they existed before life began on our planet, and we know that they must have played a pivotal role in the development of life because the fundamental process of life involves replicating complex information-containing charged polymers.

The IUPAC definition of a polyelectrolyte is a polymer composed of macromolecules in which a substantial portion of the constitutional units contains ionic or ionizable groups, or both.[41] Polyelectrolytes are polymers that contain electrolyte groups on their repeat units, that when dissolved in an appropriate polar solvent like water, these groups dissociate to form a polyion that bears one or more positive (polycation) and/or negative (polyanion) charges along with their associated counterions (Figure 2).[42-43]

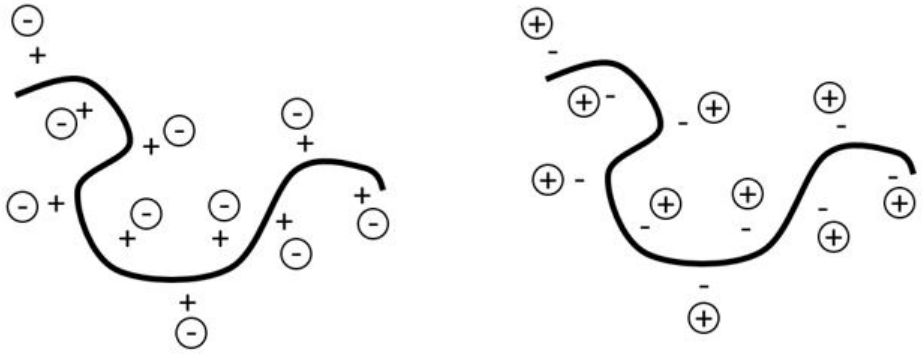

Figure 2. Polycation (left) and polyanion (right).

Typical anionic groups include carboxylate ($-COO^-$), phosphonate ($-PO_3H^-$ and sulfonate (SO_3^-), while the common cationic groups are the primary, secondary and quaternary ammonium ($-NH_3^+$, $=NH_2^+$ and $\equiv N^+$). Polyelectrolytes such as deoxyribonucleic acid (DNA), NaPSS and poly(acrylic acid) (PAA) dissociate into

polyanions, while poly(allylamine hydrochloride) (PAH), poly-L-lysine (PLL) hydrobromide are polycations.

Polyelectrolytes are classed as either synthetic or natural. Common natural polyelectrolytes include proteins, nucleic acids that make up proteins, polypeptides and polysaccharides (Figure 3).

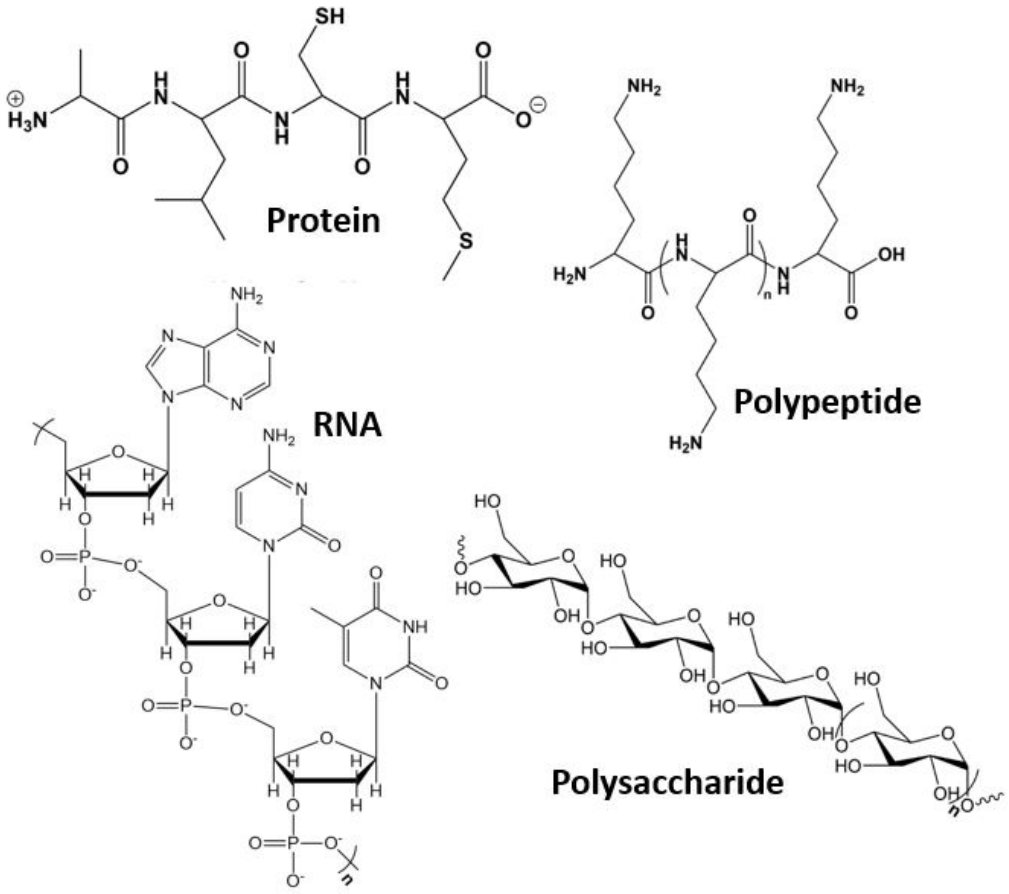

Figure 3. Natural polyelectrolytes, including clockwise from top left, several amino acids to make up a segment of a protein, the polypeptide polylysine, a polysaccharide and a segment of RNA.

Common synthetic polyelectrolytes include; PAA, NaPSS, polyacrylamide (PAM), poly(diallyldimethylammonium chloride) (PDADMAC) and poly(2-acrylamido-2-methyl-1-propanesulfonic acid) (PAMPS). Similar to acid/base classifications of strong and weak, polyelectrolytes are also divided into these types. The dissociation of polyelectrolyte chains is governed by pH and is classified depending on whether the dissociation is full or incomplete. Strong polyelectrolytes dissociate completely in solution, independent of the solution pH for most reasonable pH values. Examples include NaPSS and PDADMAC. Weak polyelectrolytes with pKa/pKb values in the approximate range of 2-10, only partially dissociate in solution at intermediate pH values, with the fraction of charge susceptible to pH, ionic strength and counter-ion concentration. PAA and PAM are examples of weak polyelectrolytes (Figure 4).

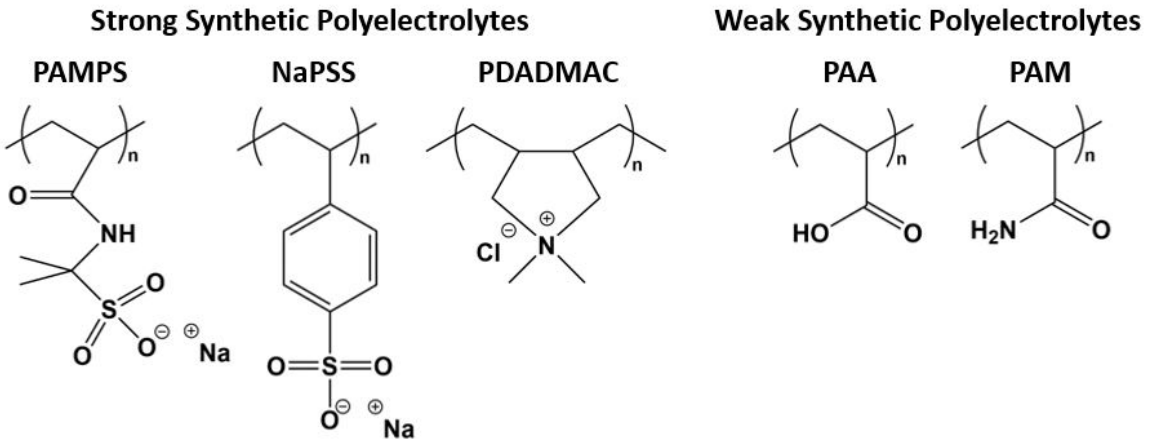

Figure 4. Strongly and weakly dissociating synthetic polyelectrolytes.

1.1.4 Polyelectrolytes vs Polymers

Polyelectrolytes display properties similar to both electrolytes and polymers, where the specific type of the ionic group, its counter-ion and the structure of the repeat unit

govern solution properties such as solubility in water and other polar and hydrogen-bonding liquids such as alcohols.

Due to charged groups and ensuing electrostatic forces, the solution properties of polyelectrolytes are significantly different to neutral polymers.[44] A simple example is the disparity in the solution viscosity between polyelectrolytes and neutral polymers at the same concentration. Dependence of solution viscosity on concentration for polyelectrolytes observes Fuoss' law which is given by: $\eta \sim C^{1/2}$ which is in contrast to neutral polymers that follow a direct dependence between solution viscosity and concentration.

Electrostatic interactions among and between polyelectrolyte chains results in an earlier onset of crossover between dilute and semidilute regimes. This crossover occurs at a much lower concentration for polyelectrolytes compared to neutral polymers because polyelectrolyte chains are expanded in polar solvents like water, and so chains overlap at much lower concentrations. Concentration regimes for polyelectrolytes are also more complex than their neutral counterparts because polyelectrolyte conformation is influenced by variables such as pH and ionic strength of the solution.

Counterions released by dissociating of polyelectrolyte chains in solution have a large effect on the osmotic pressure, which is typically several orders of magnitude higher than neutral polymers at the same concentration. These examples amongst others exemplify how the dynamics of polyelectrolyte solutions are vastly different to that of neutral polymer solutions.

1.1.5 Polyelectrolyte Applications

Polyelectrolytes display a variety of unique properties such as the ability to impart a charge onto neutral surfaces, to tune rheological behavior in response to external stimuli or to regulate and exchange salt ions and induce precipitation. These unique properties of polyelectrolytes permit their use in a variety of applications that can range from flow modification to inducing stabilization in aqueous colloids or gels. Polyelectrolytes are used as dispersants for ceramic slurry processing to increase stability and temperature resistance,[45] and also incorporated as a superplasticizer additive in concrete mixtures.[16] A range of weak and strong cationic and anionic materials are used as ion-exchange resins in the home for water softening or on industrial scales for removal of ionic impurities.[13-14, 46] PAM and PDADMAC are often used as flocculation agents to destabilize a colloidal suspension and to initiate flocculation and precipitation in waste water treatment. [47] NaPSS is used to minimize surfactant adsorption to enhance oil recovery,[48] and as a medicine to lower blood potassium levels in the treatment of hyperkalemia.[33] PAMPS along with types of acrylic and methacrylate polyelectrolytes are used as thickeners in adhesives and personal care detergent and cosmetic products to improve surface appearance and feel.[32, 49] Carboxymethyl cellulose, in its sodium salt form, is extensively used as a viscosity modifier and emulsion stabilizer many food products such as ice cream as well as in other products including toothpaste, water-based paint and diet pills.[50-51] Carrageenan, a sulfonated polysaccharide extracted from red seaweed, is used extensively in many dairy products like creams, yoghurts and milks as well as in some infant formulas.[52] Polyelectrolytes display an ability to take up large amounts of water and as such a class called super absorbent polymers, which are typically made from lightly crosslinked sodium

polyacrylate-polacrylamide, have found applications in hygiene products such as diapers and sanitary napkins.[53]

Various other polyelectrolyte based systems including polyelectrolyte multilayers, complexes, coacervates, and brushes, in solution or thin-film form also offer a range of potential uses. Polyelectrolyte multilayers are ultrathin films made from the alternating deposition of water soluble positive and negatively charged polymers on a substrate. These multilayer materials offer a variety of potential uses in a range of applications in areas such as active and passive protective coatings,[54] selective functional membranes,[55] and biological substrates.[56] Polyelectrolyte complexes are the association complex formed from the electrostatic interaction of two oppositely charged polymers. These materials are highly suitable for complexing with drugs and as such have found a variety of uses in pharmaceutical applications such as delivery vehicles for gene therapy or for controlled drug release.[57-59] Polyelectrolyte brushes are a class of material where the polyelectrolyte is grafted or localized at a surface at a high enough density to force alignment of the chains due to repulsive electrostatic interactions.[60] Identified as providing a smart surface characteristic this class of material has potential applications in the biological field for protein affinity separation and as switches in microfluidic devices.[61-62]

One synthetic polyelectrolyte in particular, NaPSS, has a wide range of uses and is used extensively in polyelectrolyte multilayers and complexes,[34-35] as well as a component in the PEDOT:PSS macromolecular salt mixture for a variety of applications such as flexible organic solar cells,[36] polymer electrolytic capacitors,[18-19] and organic light-emitting diodes.[37]

1.1.6 Limitations of polyelectrolyte processing

A polyelectrolyte melt state is often difficult to achieve because of the typically high ionic content that the counterions impart in the material. Therefore solution processing is the most attractive option for charged macromolecules. In most cases polyelectrolytes are processed from aqueous solutions where parameters such as the nature of the polyelectrolytes functional group, the charge density, molecular weight and size, polyelectrolyte concentration and concentration of added electrolyte have significant effects on the process-ability of these solutions. It is therefore critical that each parameter is precisely known beforehand. But experimental observations on solutions of polyelectrolytes have shown that these systems exhibit a range of perplexing behaviors. Some of which are counterintuitive to the laws of diffusion observed for neutral polymer solutions. A fundamental understanding of these inexplicable observations is necessary in order to implement characterization techniques, such as light scattering for size and molecular weight, to quantify the properties of charged macromolecular solutions. None of the well-established laws of diffusion for neutral polymer solutions can be implemented for polyelectrolyte solutions and this significantly inhibits the development of solution processing for polyelectrolyte materials in various applications.

1.2 Polyelectrolyte solutions

Polyelectrolyte solutions are complex systems of which we still lack understanding about many aspects of their behavior. Consider the most simplistic scenario of a single polyelectrolyte molecule situation; the system consists of a solvent (water), a polymer chain with its ionizable repeat units, counter-ions to balance these charges and co-ions in

solution in the form of an added salt. If the ionic strength of the solution is decreased by removing added salt the conformation of the polymer chain becomes extended due to intra-chain repulsion between charged repeat units. But upon addition of salt to increase the ionic strength, the co-ions electrostatically screen the charged repeat units to enable the polymer chain to adopt a more compact random coil conformation (Figure 5).

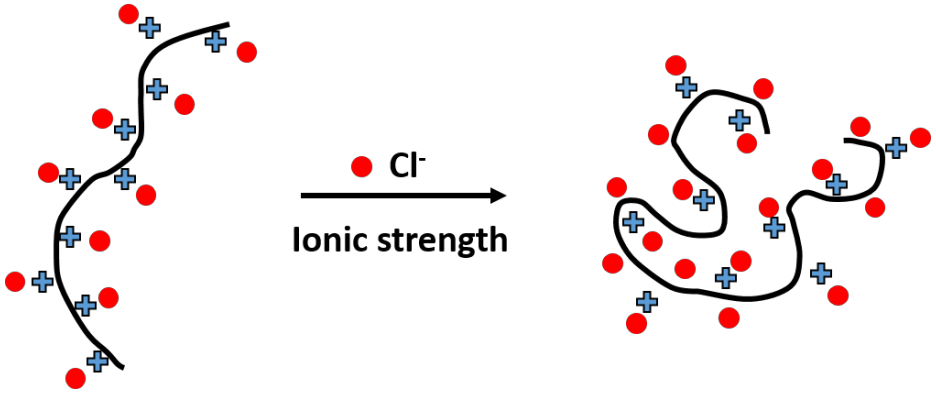

Figure 5. Effect of ionic strength on polyelectrolyte conformation.

This view simplifies the system by showing the effect of a single variable, ionic strength, on a single property, the polymer conformation of a single chain. In reality there are many variables governing polyelectrolyte phenomena and these variables can be linearly or non-linearly coupled, synergistic or antagonistic on the end result and also be time dependent and completely reverse. Consider a single chain of NaPSS in a saline solution of NaCl. The system is endowed with many forces from long-ranged electrostatics due to the charges (sulfonate groups, sodium counterions and salt co-ions), to hydrogen-bonding between water and sulfur along with dipolar interactions with water, as well as van der Waals forces, excluded volume effects and chain connectivity (Figure 6). The system becomes much more complex to understand when multiple chains are present and even furthermore when multiple chains of different kinds of polyelectrolytes exist.

Experimentally it is difficult to probe a system with so many variables with potentials and inhomogeneity's, and conceptually it is difficult to understand a system where all the chains are strongly correlated both topologically and electrostatically, where every molecule knows every other one in the system.

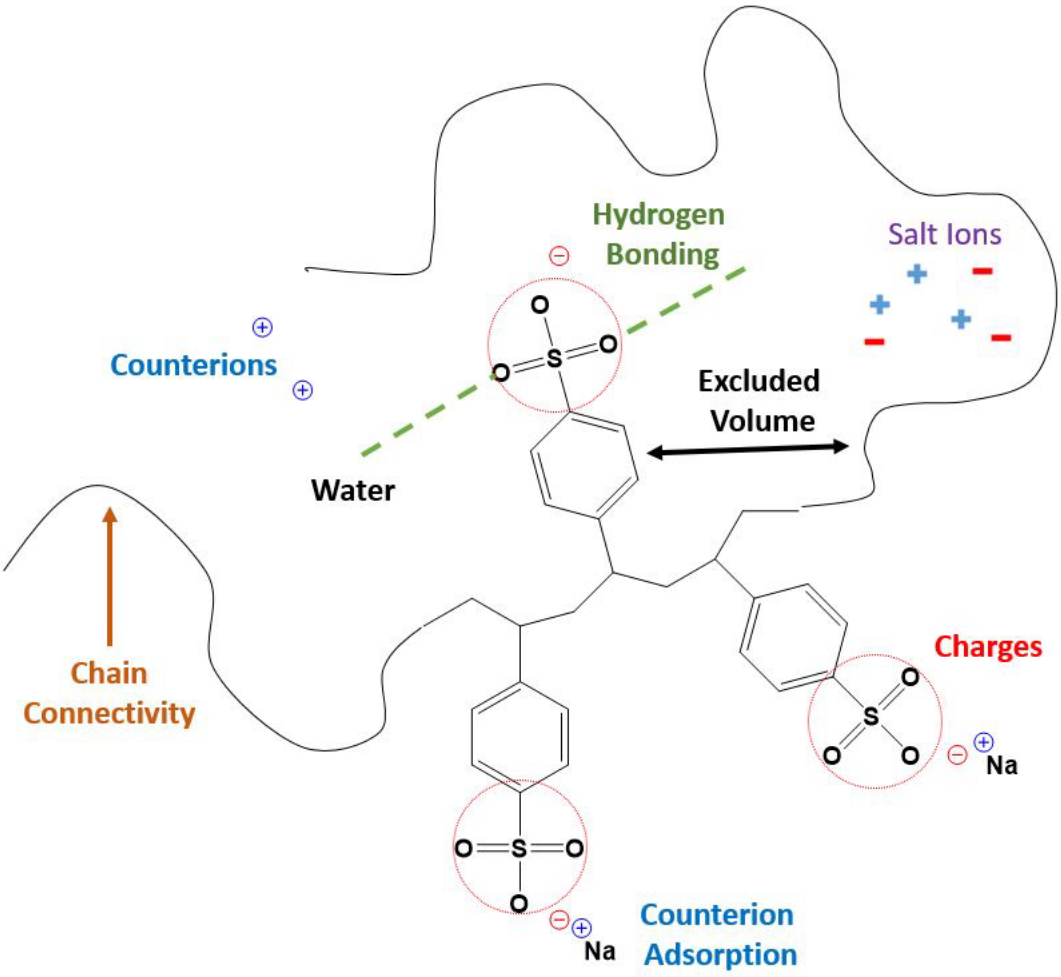

Figure 6. A simplified single chain NaPSS system showing the many forces that exist in polyelectrolyte solutions.

The literature on polyelectrolyte solutions is vast and encompasses work based on experiments, theory and simulations. For the scope of this thesis a theoretical summary on single polyelectrolyte type homopolymers in solution of monovalent salts will be

addressed. An introduction to energy and length scales, polyelectrolyte chain size in single and multiple chain systems, and the structures and properties that arise from multiple chain systems is warranted. These areas of polyelectrolyte science have been developed in the literature over many decades and are critical in providing a fundamental understanding of the behavior of polyelectrolyte solutions while also giving insight into the ordinary-extraordinary transition.

1.2.1 Energy and length scales

Two ions with charges $z_i e$ and $z_j e$ separated by a distance r_{ij} in a medium with a uniform dielectric constant ϵ experience an electrostatic interaction energy U_{ij} that is described by Coulombs Law:

$$\frac{U_{ij}}{k_b T} = z_i z_j \frac{e^2}{4\pi\epsilon_0 \epsilon k_b T} \frac{1}{r_{ij}} \tag{1}$$

where $k_b T$ is the product of absolute temperature and the Boltzmann constant, e is the electronic charge, ϵ_0 is the permittivity of a vacuum. The Bjerrum length l_B is described by the middle factor in the above equation as its dimension of length describes the separation distance r_{ij} at which the electrostatic interaction between two elementary like charges is comparable to the thermal energy $k_b T$:

$$l_B \equiv \frac{e^2}{4\pi\epsilon_0 \epsilon k_b T} \tag{2}$$

For opposite elementary charges that are separated by a distance shorter than l_B this results in an attraction that is stronger than $k_b T$, and so in the context of a polyelectrolyte solution

the charges that exist an ions are likely to be in an ion pair rather than dissociated. For aqueous solutions at 25 °C where the value of ϵ is approximately 80 then $l_B \approx 0.7\ nm$.

The Debye length is a fundamental length scale in polyelectrolyte solutions as it is the thermodynamic description of systems of mobile charges. Two ions of charge $z_i e$ and $z_j e$ in an electrolyte solution experience a pairwise interaction energy given by the screened Coulomb energy:

$$\frac{U_{ij}}{k_b T} = z_i z_j l_B \frac{e^{-\kappa r_{ij}}}{r_{ij}} \tag{3}$$

where:

$$\kappa^2 = \frac{e^2}{\epsilon_0 \epsilon k_b T} \sum_i {z_i}^2 n_{i0} \tag{4}$$

where n_{i0} is the average number concentration of the ith ion. The Bjerrum length describes the strength of the electrostatic interaction between ions and the Debye length determines the range over which the interactions act, given by $\kappa^{-1} \equiv \xi_D$ (Debye length).

$$\xi_D = \left(\frac{e^2}{\epsilon_0 \epsilon k_b T} \sum_i {z_i}^2 n_{i0} \right)^{-1/2} \tag{5}$$

This range decreases if $\epsilon k_b T$ is reduced and/or the external electrolyte concentration C_s is increased. Consider monovalent salt in water at 25 °C the Debye length is:

$$\xi_D \approx \frac{0.3}{\sqrt{C_s}} nm \tag{6}$$

If a counterion is a distance less than the Bjerrum length from a charge unit on the polyelectrolyte then the counterion can bind to the polymer and form a temporary dipole. This binding energy is high due to the effective dielectric constant near the polymer chain being low, furthermore this binding and dipole formation results in a total polyelectrolyte charge that is never fully realized at equilibrium. While these dipoles are temporary, they exist long enough to interact with other dipoles along the chain contour, with a dipole-dipole interaction being attractive and strong compared to $k_b T$. This attraction causes a smaller portion of the segments along the polyelectrolyte chain to cling together due to quadrupole formation while the rest of the chain segments would repel each other, resulting in non-uniform structures and potential attraction between like charged polymers (Figure 7).

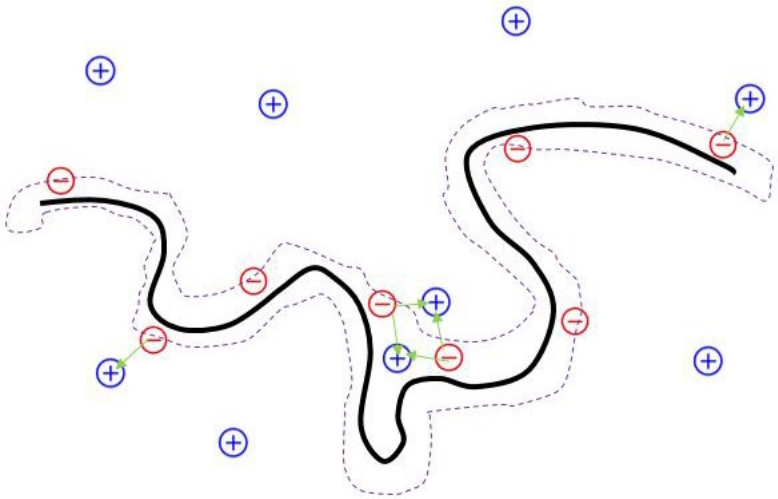

Figure 7. Quadrupole formation along a polyelectrolyte chain segment.

1.2.2 Polyelectrolyte size

In 1950 Katchalsky, Künzle and Kuhn proposed a model to determine the size of a single polyelectrolyte chain in water without the presence of counterions or co-ions from added salt.[63] Consider a flexible chain of N segments, each with length l and charge αz_p, where α is the degree of ionization and z_p is the number of ionizable groups per segment. The authors denoted the end-to-end distance of the polymer chain as R with an even distribution of charge along the chain and obtained:

$$\frac{R}{l} \sim \left(\frac{\alpha^2 {z_p}^2 l_B}{l}\right)^{1/3} N \quad \text{(salt free)} \tag{7}$$

This relation showed a direct proportionality between the end-to-end distance and the number of segments ($R \sim N$), which means that flexible polyelectrolyte chains adopt a rod-like conformation in water.

In a high salt case the electrostatic interactions in a polyelectrolyte solution are sufficiently screened. In 1953 Flory stated that intersegment electrostatic repulsion of a polyelectrolyte chain is accounted for by adding the term $4\pi\alpha^2 {z_p}^2 l_B$ to the two-body excluded volume parameter w which is related to the Flory-Huggins parameter χ by $w = (1/2 - \chi)$.[64] At the high salt concentration limit when excluded volume interactions are strong the radius of gyration R_G of a polyelectrolyte chain is given by:[64] _ENREF_34

$$R_G \sim l\left[w + \frac{4\pi\alpha^2 {z_p}^2 l_B}{\kappa^2 l^3}\right]^{1/5} N^{3/5} \quad \text{(high salt)} \tag{8}$$

A significant consequence of this finding relate to the arguments that Alfrey et al.[65] and Fuoss et al.[66] put forth in 1951 that describe the counterion distribution around a

polyelectrolyte chain to monotonically decrease in concentration as the distance from the chain increases. These arguments are contrasted to a later theory proposed by Manning in 1969 who introduced the phenomenon of counterion condensation around a rod-like polyelectrolyte.[67] In this model, the number of counterions inside a cylinder of radius r_0 around a thin rod-like chain diverges at a particular distance from the chain according to $z_p z_c l_B / l_p \geq 1$, where $z_p e$ is the charge of the polymer group, $z_c e$ the charge of the counterion and l_p is the distance between charged groups on the polymer chain. For many polyelectrolytes this theory is relevant as l_B is 0.7nm while l_p is typically 0.2-0.3 nm for most polymers, which means that in the region around the chain the charge distribution adheres to counterion condensation while outside this region the uncondensed mobile charges are treated with Debye-Hückel approximations.

1.2.3 Electrostatic blobs and scaling laws

_ENREF_34Physical scaling laws were introduced and applied to polyelectrolyte solutions in 1976 by De Genne et al.[68] For a salt-free polyelectrolyte solution where $R \sim N$ and the dimensionless variable for the strength of the electrostatic repulsion is $\alpha^2 {z_p}^2 l_B N^{3/2} / l$ where this interaction is weak if it has a value less than 1. A chain in this solution contains N segments that are further made up of grouped sections whereby the electrostatic interactions within each section are weak but beyond which the interaction is significant. These sections, defined as electrostatic blobs of size ξ_e where each blob contains g segments (Figure 8). It is assumed that the electrostatic energy inside the blob is comparable to the thermal energy:

$$\frac{l_B(az_p g)^2}{\xi_e} \approx 1 \tag{9}$$

Since the electrostatic interactions between blobs is strong it is expected to adopt a rod-like conformation with N/g blobs so the end-to-end distance of the chain is:

$$R \sim \left(\frac{N}{g}\right)\xi_e \sim l\left(\frac{a^2 {z_p}^2 l_B}{l}\right)^{1/3} N \tag{10}$$

This is same result obtained in (Equation 7).

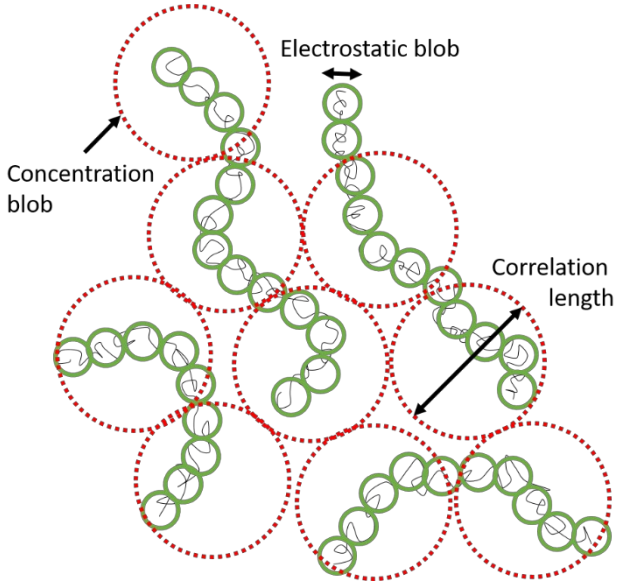

Figure 8. Schematic of electrostatic blobs along a polyelectrolyte chain and correlation lengths that arise from scaling arguments.

Scaling laws have been generalized to systems with good or poor solvation, a range of ionic strength, polymer concentration and molecular weight amongst other variables with a scaling potential.[5] For instance, a salt-free semidilute polyelectrolyte solution, where the polyelectrolyte concentration is above the overlap concentration C^* (when chains begin

to interact), the scaling laws for osmotic pressure Π, correlation length ξ and radius of gyration R_G are as follows:

$$\Pi \sim C^{3/2}; \quad \xi \sim C^{-1/2}; \quad R_G \sim C^{-1/4} \tag{11}$$

1.2.4 Net effective charge and size

A fundamental quantity that influences all properties of polyelectrolyte solutions is the net effective charge per polymer. Even for strongly dissociating polyelectrolytes where every ionizable repeat unit can fully ionize the net effective charge is always lower than the full chemical charge. This is because we are not dealing with two charges moving freely in a medium because often one charge is permanently attached to an oil-like non polar backbone. This causes the local dielectric constant to be significantly lower than in the bulk medium and with a lack of rigorous theoretical or experimental measurement of this local polarizability effect an early estimate that the dielectric constant changes from about 5 at the chain to about 80 at a distance 2 nm out.[69] It becomes clear that the degree of ionization of each repeat unit is less than 1, and in reality a homopolymer chain should be treated as a heteropolymer with ionized and un-ionized groups that change dynamically. It is best to assume the chain is uniformly charged with each repeat unit of degree of ionization α, a value that depends on all the chemical specifics of the polymer, counterion, salt co-ions, and solvent as well as the physical conditions such as temperature, and polymer and salt concentrations. Even as a chain conformation changes so does the value of α and so it is only ever a fixed number for unique set of specific experimental variables.

Rod-like conformation due to intrachain electrostatic repulsion may be reasonable from a theoretical standpoint, has not been observed experimentally for flexible polyelectrolytes. Relating the radius of gyration to the degree of polymerization DP requires the inclusion of an effective size exponent v_{eff}:

$$R_G \sim DP^{v_{eff}} \tag{12}$$

In salt-free solutions an expected v_{eff} value of 1 would be observed for a rod-like conformation but measured v_{eff} values are lower and typically range from 0.7-0.8, before dropping to 0.6 as soon as salt is added and its concentration exceeds about 0.001 M.[70] A further example to illustrate the complexity of polyelectrolyte solutions is how R_G is influenced by α. Consider the coil-to-globule transition of a flexible polyelectrolyte chain as the temperature or dielectric constant is lowered or salt concentration is increased.[71] As the chain collapses α will also decrease due to counterion adsorption, which in turn facilitates further chain collapse, decreasing R_G, due to less electrostatic repulsion and in effect a cascade occurs.[72] Experimentally it has been found that the ionic conductivity of a polyelectrolyte solution drops to zero when the chain adopts a globule conformation, indicating that all counterions were collected by the chain as the coil collapsed.[71]

For this reason there are often discrepancies between theory and experiment in many cases where theoretical arguments that use scaling theories, blobs or pearl-like and other structures, that are based on a fixed value of α across a range of different variables.

1.2.5 Electrostatically driven structure and correlation length

All chains in polyelectrolyte solutions are correlated topologically and electrostatically, even in very dilute solutions the chains are correlated as they position themselves at some distance at an energy minima due to the electrostatic repulsions between chains. As polyelectrolyte concentration increases, entropy is gained by forcing the chains to intertwine and modifying the repulsions between them. The scattering properties of polyelectrolyte solutions from light, X-ray and neutrons at low salt reveals the nature of these correlations.[9, 73-74] A scattering peak known as the 'polyelectrolyte peak' shifts position based on the polyelectrolyte concentration C as follows:

$$k_m \sim C^{\beta} \tag{13}$$

where k_m is the scattering wave vector at the peak position and the value of β changes from 1/3 for dilute solutions to 1/2 for semidilute solutions. At sufficient salt concentration the presence of the polyelectrolyte peak disappears (Figure 9).

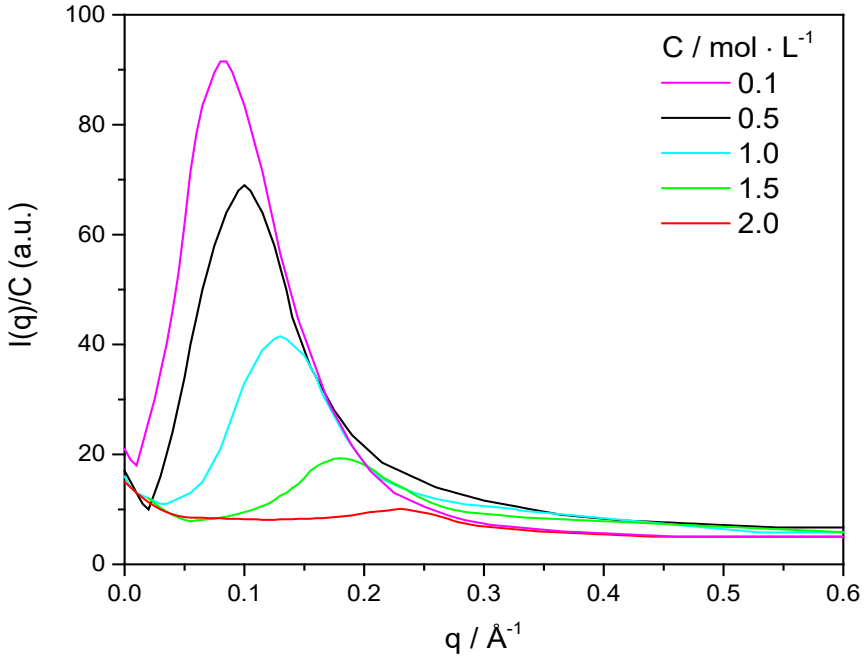

Figure 9. Dependence of polyelectrolyte scattering peak on salt solution concentration.

For a system of many chains in a volume V the correlation length scales with polyelectrolyte concentration differently in salt-free compared to high salt conditions:

$$\frac{F_{fl,p}}{k_B T} = \begin{cases} \frac{V}{24\sqrt{2}\pi}\frac{1}{\xi^3} & \text{(salt free)} \\ \frac{V}{24\pi}\frac{1}{\xi^3} & \text{(salty)} \end{cases} \tag{14}$$

For salt-free solutions at semidilute conditions $\xi \sim C^{-1/2}$ but crosses to $\xi \sim C^{-1/4}$ in concentrated conditions. In salty solutions at semidilute conditions $\xi \sim C^{-3/4}$ but crosses to $\xi \sim C^{-1/2}$ in concentrated conditions which is a similar property for neutral polymers.[75]

Theoretical predictions for radius of gyration values in polyelectrolyte solutions where salt and polymer concentration is varied for molecules with high degrees of polymerization DP are given as:

$$R_G \sim \begin{cases} \sqrt{DP}\left(w + \frac{w_c}{\kappa^2}\right)^{1/8} C^{-1/8} & \text{semidilute} \\ \sqrt{DP} & \text{concentrated} \end{cases} \quad (15)$$

under salty conditions, and:

$$R_G \sim \begin{cases} \sqrt{N} {w_c}^{1/12} C^{-1/4} & \text{semidilute} \\ \sqrt{N} & \text{concentrated} \end{cases} \quad (16)$$

for salt-free solutions.[75-76]

1.2.6 Polyelectrolyte concentration regimes

Using double screening theory and experimental results obtained about the polyelectrolyte peak from scattering it has been determined that there are five regimes of structure for salt-free polyelectrolyte solutions (Figure 10).[77]

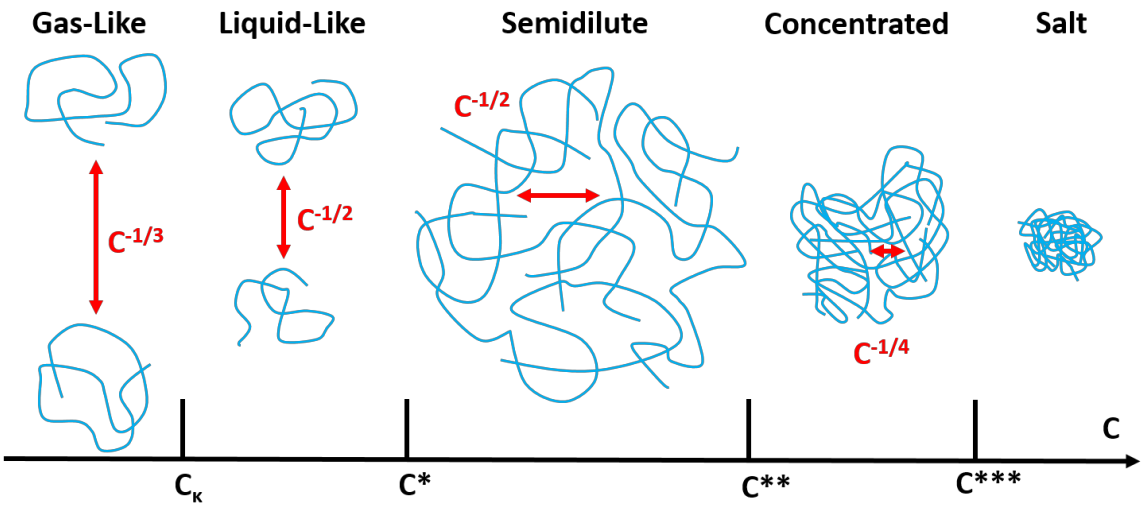

Figure 10. The five concentration regimes in polyelectrolyte solutions.

1. Electrostatically Uncorrelated Dilute "Gas-Like" Regime ($0<C<C_\kappa$)

At extremely low concentrations the average separation distance between chains Λ is so large that the strength of the electrostatic interactions between them is very small. The polyelectrolyte concentration C_κ is defined as the point at which the concentration causes the average distance between chains to be equal to the Debye length:

$$k_m \sim \frac{1}{\Lambda} \sim C^{1/3} \qquad C_\kappa \sim N\kappa^3 \tag{17}$$

2. Electrostatically Correlated Dilute "Liquid-Like" Regime ($C_\kappa < C < C^*$)

In this regime the average distance between chains Λ is shorter than the Debye length, yet the chains have not physically overlapped and so $2R_G < \Lambda < \kappa^{-1}$ before reaching the overlap concentration which is defined by $C^* = 3M/4\pi {R_G}^3$ where M is molecular weight.

The general result obtained from the polyelectrolyte scattering peak in dilute solutions with electrostatic correlations is:

$$k_m \sim \sqrt{C} \quad \text{dilute} \tag{18}$$

3. Semidilute Regime ($C^* < C < C^{**}$)

The polyelectrolyte concentration is above the overlap concentration but there are still significant concentration fluctuations throughout the entire solution. These fluctuations produce a correlation length which as measured from scattering is proportional to concentration as $\xi \sim C^{-1/2}$. A numerical prefactor difference separates the dilute from the semidilute regime as the exponent β for the concentration dependence of k_m for the two regimes is the same.[7]

4. Concentrated Regime ($C^{**} < C < C^{***}$)

Concentration fluctuations become weak as most of the chains become entangled and the polyelectrolyte scattering peak position is directly proportional to the correlation length as given by:

$$k_m \sim \xi^{-1} \sim C^{1/4} \quad \text{concentrated} \tag{19}$$

5. Hydrated Melt ($C^{***} < C$)

At concentrations above C^{***} exists the hydrated melt regime where chains are compact and entangled and there is no measurable or theoretical proportionality between the correlation length/polyelectrolyte peak and the polyelectrolyte concentration.

1.2.7 Effective interaction

Calculations that account for the simultaneous screening of topological and electrostatic correlations in the theoretical determination of the effective interaction Δ show that $\Delta(r)$ can be attractive under certain conditions. At intermediate distances of chain separation, comparable to the correlation length ξ, in solutions of low salt concentration, an attraction emerges between like charged chains that are interacting. At the infinitely dilute limit the interaction is purely repulsive but as the polyelectrolyte concentration is increased an attraction emerges due to topological correlations (Figure 11). It has yet to be determined if this intersegment attraction leads to the clumping of similarly charged polyelectrolyte chains but it is known that the spontaneous formation of dipoles and their mutual attraction to form quadrupoles can account for the aggregation of multiple chains that is observed in DLS.

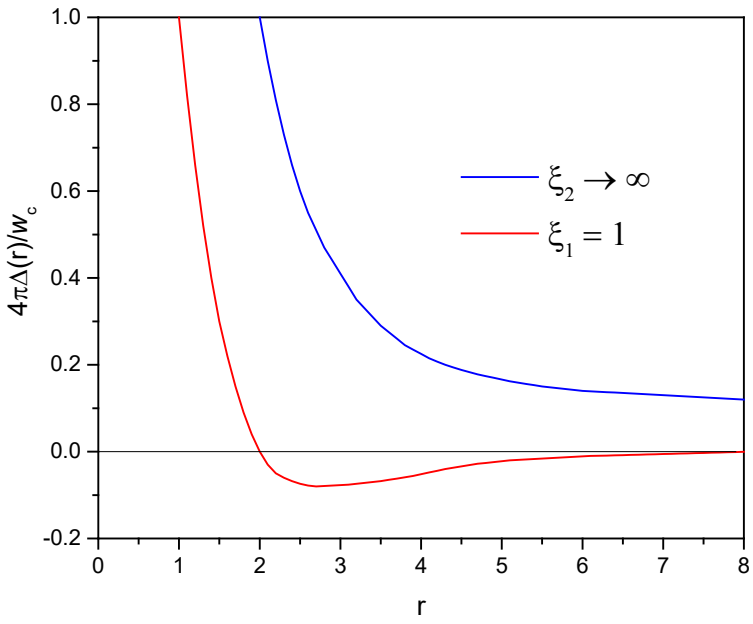

Figure 11. Net effective attractive interactions at inter and intra polyelectrolyte chain segment distances that are comparable to the correlation length.

1.2.8 Polyelectrolytes of all sizes move with the same speed

The electrophoretic mobility μ of a polyelectrolyte chain in solution under a constant electric field $\boldsymbol{E}$, is defined through

$$v_p = \mu \boldsymbol{E} \tag{20}$$

where v_p is the velocity of the polyelectrolyte chain, is independent of its molecular weight, $\mu \sim N^0$, at all salt concentrations.[78-79] This experimental result is in contradiction with the relation, based on isolated ions, that:

$$\mu = QD/k_BT \tag{21}$$

where Q is the charge and D is the diffusion coefficient of the molecule. The discrepancy between the measured molar mass independence of μ and the Einstein-Smulochowski relation is because the polyelectrolyte chain is not an independent entity but is constantly coupled to its oppositely charged counterion cloud. During a measurement the polyelectrolyte will move toward its favored electrode but the counterion cloud, being oppositely charged and attracted toward the other electrode, pulls the polyelectrolyte in the opposite direction resulting in compromised dynamics (Figure 12).

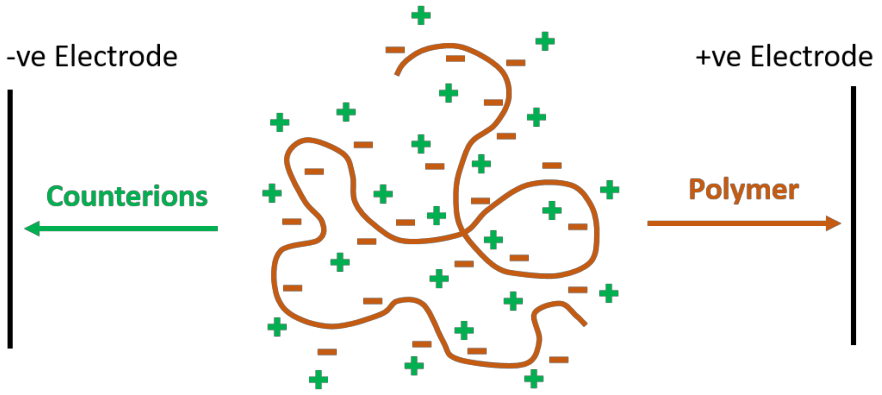

Figure 12. Counterions contribute to electrophoretic mobility leading to molecular weight independence of PE mobility in solutions.

1.3 Polyelectrolyte characterization with light scattering.

1.3.1 Origin of light scattering

Electromagnetic waves upon interaction with atomic matter induce an electric dipole moment by exerting an equal and opposite force on the charge centers of electrons and protons. The oscillatory nature of electromagnetic waves cause the induced dipole moments to fluctuate with the incident beam. Any oscillating dipole moment will give rise to secondary radiation in all directions called the scattered radiation. When dipole moments

oscillate with the same frequency as the incident beam then the scattered radiation will also be of the same frequency, a process called elastic scattering. When not in frequency the scattered radiation is called inelastic scattering.

1.3.2 Wave vector

The scattering wave vector or probing length is a key parameter in deciding which type of scattering technique to use in the characterization of macromolecules. Consider a sample which scatters incident radiation in all directions which is measured by detectors positioned at different angles all at a large distance from the scattering center.

The wave or propagation vector $\left|\overrightarrow{k_\iota}\right|$ of scattered light is related to the wavelength of the incident beam by the relation: $\left|\overrightarrow{k_\iota}\right| = 2\pi/\lambda$ where the wavelength of radiation in a medium is related to its wavelength in a vacuum λ_0 and the refractive index of the medium n via $\lambda = \lambda_0/n$. The scattering wave vector q is related to the propagation vector by:

$$q = 2\left|\overrightarrow{k_\iota}\right| \sin\theta/2 \tag{22}$$

where θ is the scattering angle. Substituting in for the propagation vector we obtain:

$$q = \frac{4\pi n}{\lambda_0} \sin\frac{\theta}{2} \tag{23}$$

The inverse of the scattering vector gives an estimate of the length scales that are being probed by the incident radiation beam being used. Light scattering for instance is able to cover a range of distances from 1 – 1000 nm. Since most macromolecules fall in this range,

light scattering is a suitable technique to probe size, structure and dynamics as long as the sample is transparent to the incident beam.

1.3.3 Static light scattering

In a continuous medium, light interacts with matter as it propagates and the degree to which it is affected by the medium is quantified by the index of refraction. The index of refraction is directly related to the polarizability of a material and thus the amount of light it will scatter. Light scattering, due to its non-invasive technique and scattering vector, is routinely used to study macromolecules, colloids and nano materials in solutions. Instead of the index of refraction, these solute-solvent systems are better analyzed using a specific refractive index increment dn/dc, which is the change in the index of refraction with the change in concentration of the solute, and is used to determine how much the solute will scatter ($I_{scattered}$):

$$I_{scattered} \propto \left(\frac{dn}{dc}\right)^2 \tag{24}$$

Consider a solute-solvent system containing many scattering centers, each with the same scattering properties and mass. If two or more scattering centers are connected to a larger entity there is a phase relation between the light scattered from each center because the larger unit is moving together as a whole and so the scattered light adds coherently. But if scattering centers are separated, then each are moving around differently in the system and so the phase relationship changes with time for the scattered light between each center. Therefore a time average incoherent sum of scattered light intensity occurs. So the difference between the coherent and incoherent addition of the fields leads to an observed

scattering intensity that is proportional to the mass of the system. If the specific refractive index increment dn/dc and concentration of the solute C is known then the total amount of measured light scattered directly determines the molar mass:

$$I(\theta)_{scattered} \propto MC\left(\frac{dn}{dc}\right)^2 \tag{25}$$

Not only is the total light scattering intensity an important observable but so too is the angular dependence of the scattering intensity. Isotropic scattering occurs for centers that are much smaller than the wavelength of the incident light. For this case the scatterer can be viewed as a point source of scattered radiation and will produce no measurable angular variation in the light scattered in the plane defined perpendicular to the polarization axis of incident light. For a red laser beam the particle must have physical dimensions smaller than 10 nm to scatter light equally into all angles. As particle size increases relative to the wavelength of light the effects of intramolecular interference lead to a variation in scattering intensity as a function of angle. At zero degrees there is no attenuation but the scattering intensity reduces further as scattering intensity increases (Figure 13).

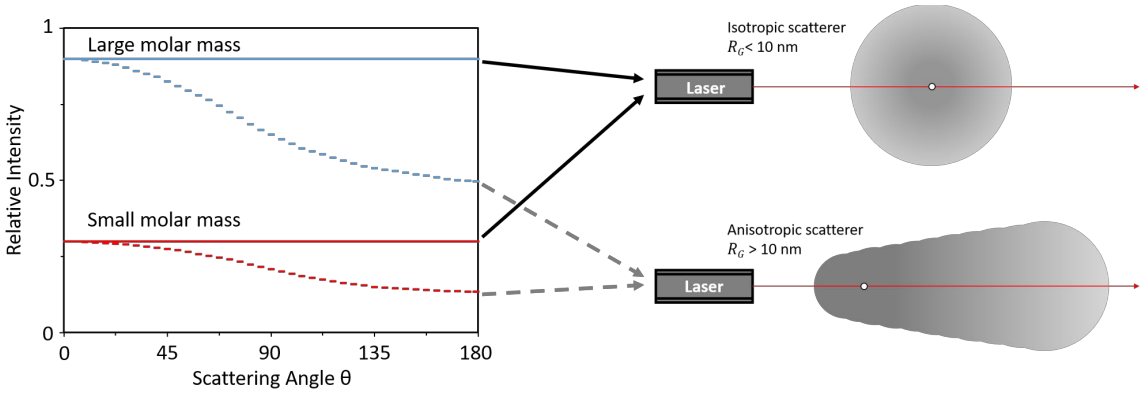

Figure 13. Variation of scattering intensity with scattering angle for scatterers above and below a critical size for incident red light.

The mathematical relationship describing the variation in scattering intensity is called the particle form factor $P(\theta)$ which depends on the size of the particle, the wavelength of incident light λ and the scattering angle θ. Therefore size information can be retrieved from the angular dependence of the scattering intensity alone. No information of the concentration or dn/dc of the solute is needed to determine size.

$$I(\theta)_{scattered} \propto MC\left(\frac{dn}{dc}\right)^2 P(\theta) \tag{26}$$

A macromolecule or larger extended type particle can be viewed as being composed of many small isotropic scattering centers. To calculate the total amount of light scattered at each detected angle its necessary to integrate over all contributions from all these scattering centers:

$$P(\theta) = 1 - \frac{16\pi^2 {n_0}^2}{3{\lambda_0}^2}\sin^2\left(\frac{\theta}{2}\right)\langle {R_G}^2\rangle + \ldots \tag{27}$$

The final term R_G is the radius of gyration or mean square radius, which is defined as the mass distribution about the center of mass, weighted by the square of the distance from the center of mass.

$$\langle {R_G}^2 \rangle = \frac{\sum {r_i}^2 m_i}{M} \tag{28}$$

where M is the center of mass, m_i are small points of mass distributed over a distance r_i from the center. So integrating over a particle means an integration over the entire mass distribution.

The actual measurement of scattered light depends on several factors, including the angle, sample to detector distance, incident beam intensity, and the volume of sample illuminated. The excess Rayleigh ratio $R(\theta)$ takes all of these factors into account. By definition it is the intensity of the scattered light from the solute alone, essentially quantifying the ratio of the scattered and incident light intensity.

$$I(\theta)_{scattered} \propto R(\theta) = K^* MCP(\theta) \tag{29}$$

where the constant K^* is composed of constants that must be known in order to determine mass or size by light scattering:

$$K^* = \frac{4\pi^2 {n_0}^2}{N_A {\lambda_0}^4} \left(\frac{dn}{dc}\right)^2 \tag{30}$$

where N_A is Avogadro's number.

The second virial coefficient A_2 is the second term of the virial expansion of the osmotic pressure and is a measure of solute-solvent interaction. It enters the light scattering equation as a correction factor for concentration effects where coherent intermolecular scattering affects the light scattering intensity. This term is only considered for conducting scattering experiments on polyelectrolyte solutions of concentrations exceeding the dilute regime.

$$R(\theta) = K^*MCP(\theta)[1 - 2A_2MCP(\theta)] \tag{31}$$

Typically the virial expansion is used to describe thermodynamic non-ideality where the first order correction A_2 is used to measure any attractive or repulsive interactions in the sample as a function of the solute concentration (Figure 14).

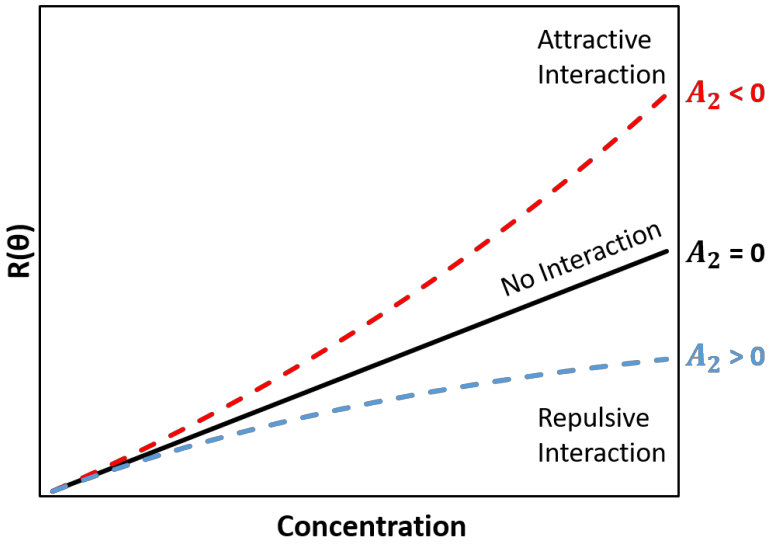

Figure 14. Relationship between solute concentration and excess Rayleigh ratio to determine intermolecular forces within a sample.

A Zimm plot is a graphical representation of light scattering data measured at several angles for many concentrations for a specific polymer in solution to produce values for R_G, A_2 and weight-average molecular weight M_w. The expression is defined as:

$$\frac{K^*C}{R(\theta)} = \left(\frac{1}{M_w} + \frac{2A_2}{k}kC\right)\left(1 + \frac{16\pi^2}{3\lambda^2}\langle {R_G}^2\rangle \sin^2\frac{\theta}{2}\right) \tag{32}$$

where $K^*C/R(\theta)$ is plotted on the y-axis and $\sin^2\frac{\theta}{2} + kC$ is plotted on the x-axis and is repeated for many concentrations and scattering angles. The scaling constant k is chosen to give the scattering vector and concentration values comparable importance, rendering both effects to be clearly visible on the plot. Measuring at many angles and concentrations produces a grid of straight lines, which when connected will show extrapolation of the left-most line $C = 0$ and lower line $\theta = 0$ to join at the lower left hand corner of the plot. The slope as a function of concentration equals $2A_2$ and the intercept of the extrapolated lines equals $1/M_w$. Substituting these values back into Zimm's expression at a constant concentration allows the calculation of $\langle {R_G}^2\rangle$, which when square rooted equals the root mean square radius of gyration or R_G (Figure 15).

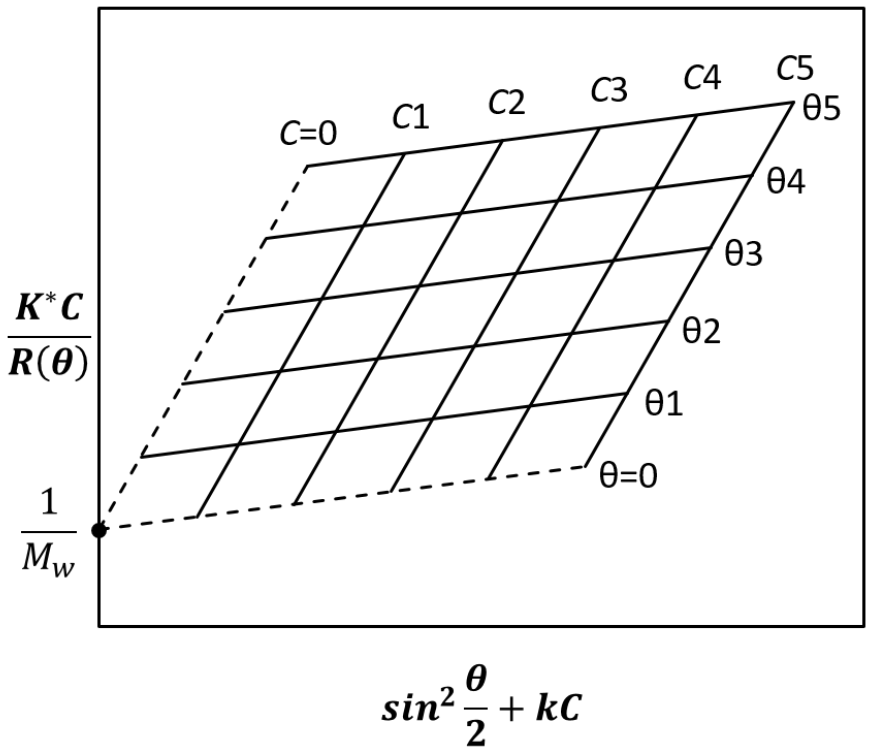

Figure 15. Example of a Zimm plot to determine M_W and R_G.

A major limitation of a batch style static light scattering measurement is that the macromolecule of interest have not been fractionated. This means the different molecular weight species have not been separated from one another and no information about dispersity of the sample can be obtained.

1.3.4 Size Exclusion Chromatography

Size-exclusion chromatography (SEC) is a chromatographic method that separates molecules based on their hydrodynamic volume. An SEC column contains a mobile phase, to transport the injected molecules, and a stationary phase, containing porous beads that alter the flow of the molecules through the column. The bead material and pore sizes can vary but the basic principle is that smaller sized molecules will enter the pores but those

too large to enter pores will flow around the bead. This has the effect of altering the flow time through the column for smaller molecules as they become entrained in more pores than larger molecules. When a mixture of molecules dissolved in mobile phase enters the column under pressure induced flow, the smaller molecules are distributed through a larger volume of solvent than is available to the larger ones. Consequently, larger molecules move more rapidly through the column, and in this way a sample is fractionated into its size components, produces a measurable distribution as each component elutes from the column. Typically a concentration detector such as a differential refractive index (dRI) detector or UV-Vis spectrophotometer is used to measure the signal of molecules eluting from the column (Figure 16).

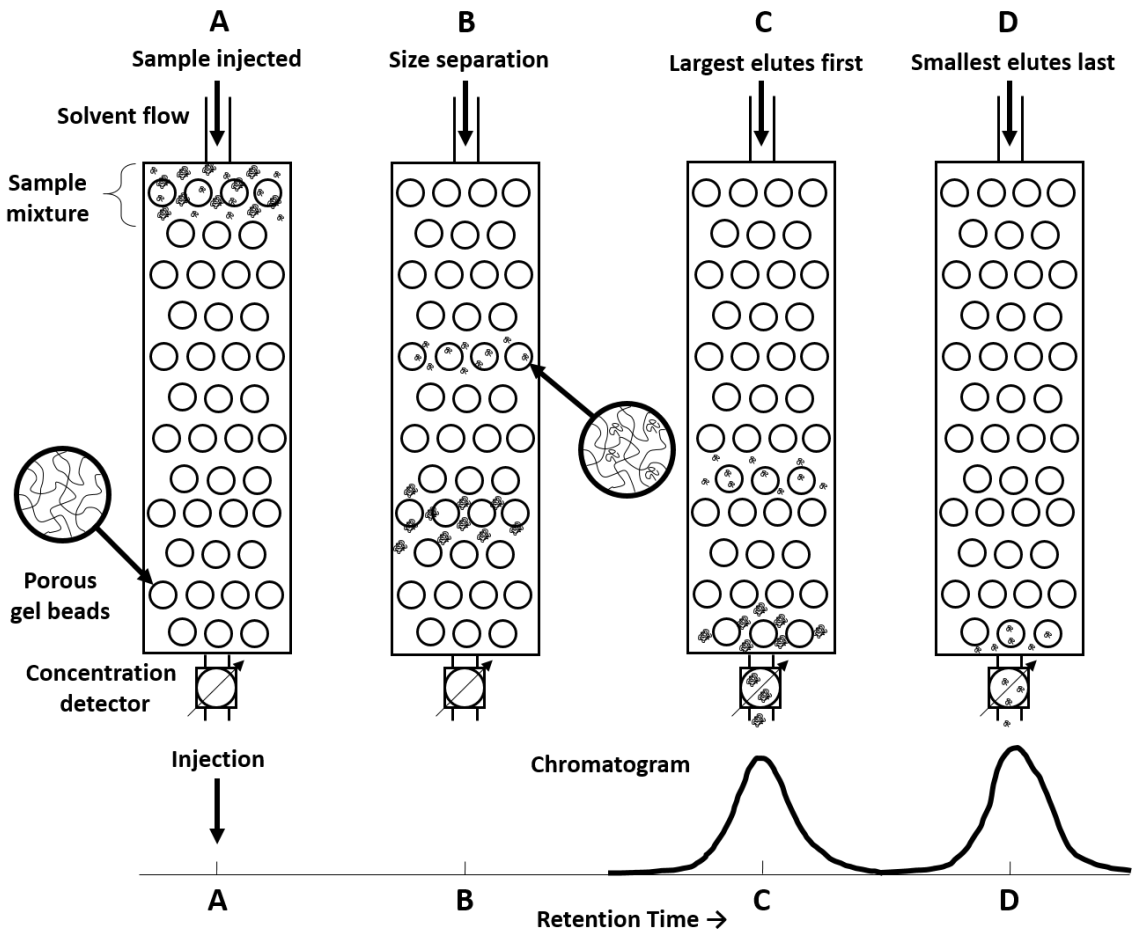

Figure 16. SEC separation of different sized polymers through a column packed with porous beads and the resulting chromatogram as each size elutes at a different rate.

The signal from the concentration detector determines the elution time of known molar mass standards under specific chromatographic conditions. A plot of molar mass vs elution time is generated to estimate the molar mass of unknown samples. By this method the elution time of a molecule is related to its hydrodynamic volume, which can then be related to molecular weight of calibrated standards. Hence this technique is a relative measurement and will fail if the standard molar mass and unknown standard have a different conformation or compactness in solution, a different density, dissimilar column interaction

and changes in elution time with injection volume. Polymers with different architectures such as branching cannot be accurately measured by comparison to calibrated linear polymer standards.

1.3.5 Size-Exclusion Chromatography coupled Multi-angle static light scattering

Coupling static light scattering with multi-angle light scattering (MALS) detection to an SEC column with a concentration detector enables the measurement of absolute molar mass of each eluting fraction of the sample and calculates the molar mass moments of the distribution to determine sample dispersity (Figure 17). The molar mass calculations are independent of the shape and density of the macromolecules and additional radii moments are also determined to provide more information about the sample.

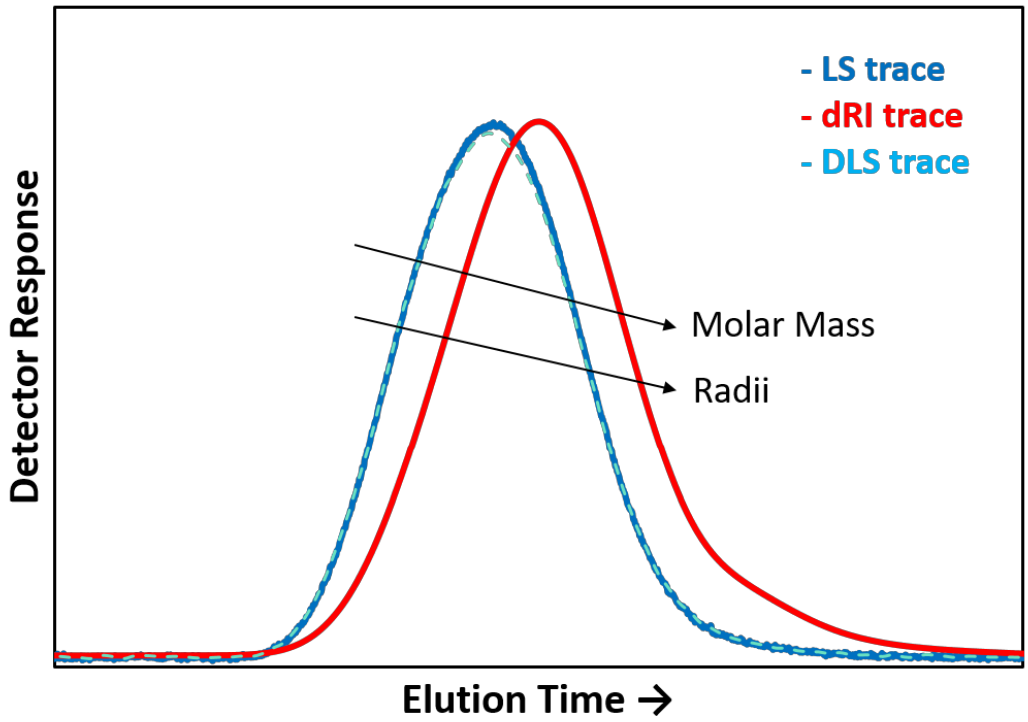

Figure 17. Chromatogram showing concentration dRI detector, static and dynamic light scattering detector responses to a macromolecule as it elutes through an SEC column.

Most macromolecular samples, especially polymers, do not exist as a single collective molar mass but instead as a distribution of many masses which are then measured by scattering in solution. Different weight averages are used to describe a population of N_i polymers of M_i mass:

$$M_n = \frac{\sum M_i N_i}{\sum N_i}, \qquad M_w = \frac{\sum {M_i}^2 N_i}{\sum M_i N_i}, \qquad M_z = \frac{\sum {M_i}^3 N_i}{\sum {M_i}^2 N_i} \tag{33}$$

where M_n is the number average molecular weight, M_w is the weight average, and M_z is the Z average. Each term is related to one another in a typical molar mass distribution curve

by: $M_n < M_w < M_z$ and the dispersity $Đ$ of mass is defined by: $Đ = M_w/M_n$ where a value of 1 represents a monodisperse sampe.

SEC-MALS also provides the same moments for radii. This information allows for the construction of a conformation plot where R_G moments eluting from the column are plotted against the simultaneous M values in a log-log format (Figure 18). A conformation plot of R_G versus M, with each axis plotted on a logarithmic scale, is based on the Flory relationship $R_G \sim M^{\nu}$, which when expressed in logarithmic fashion provides the equation of a straight line with slope ν. The relationship between ν and the fractal dimension of a polymer, d_f, defined as $d_f = 1/\nu$, describes the solution conformation of that polymer.[80] Theoretical slope values ranging from 1/3 to 1 describe architectures from a hard sphere through to a rigid rod, respectively, with linear random coil polymers adopting values of 0.5 in theta solvent conditions and range from 0.5 to 0.6 for good solvent conditions.[81] For samples with R_G < 10 nm which cannot be determined from light scattering, radius measurements from intrinsic viscosity or hydrodynamic radii (R_H) from DLS can be used in the conformation plot.

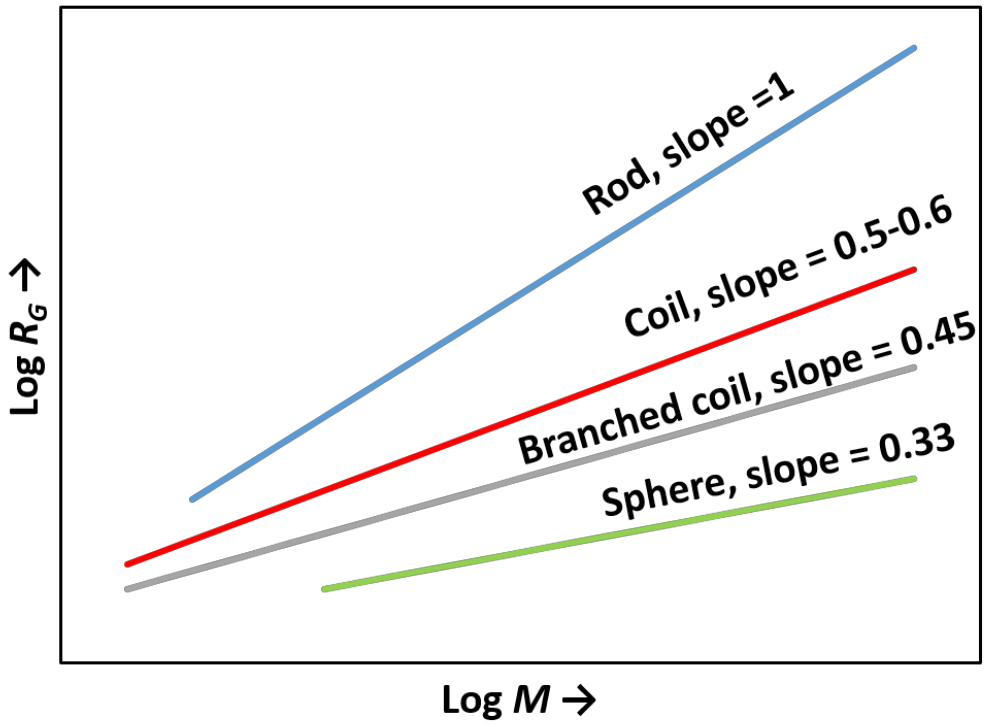

Figure 18. Conformation plot showing the relationship between *M* and R_G depends on the sample architecture.

A SEC-MALS system equipped with DLS capability permits the measurement of R_H and R_G simultaneously to obtain further polymer conformational information. The dimensionless radii ratio, $\rho \equiv R_G/R_H$, has been calculated for a number of polymeric architectures with values that range from $(3/5)^{1/2} = 0.778$ for a homogenous hard sphere to in excess of 4 for a rigid rod.[82-83]

1.3.6 Dynamic Light Scattering

DLS differs from static light scattering in that one is probing the motions of particles by analyzing the correlation in fluctuations of light scattered intensity, which gives information about the dynamics of the system.

A solution of scatterers undergo Brownian motion, which is the random fluctuations in movement due to collisions with solvent molecules. A result of Brownian motion is that the position of the fluctuating dipole moments of the scatterers is continuously shifted from its mean position with time. Thus when incident photons interact with the sample there is constructive and destructive scattering because the relative distance between scatterers changes with time. The constructive and destructive interference patterns are observed as a speckle pattern whereby the fluctuating light intensity in this speckle pattern is directly correlated to the motion of particles in solution (Figure 19).

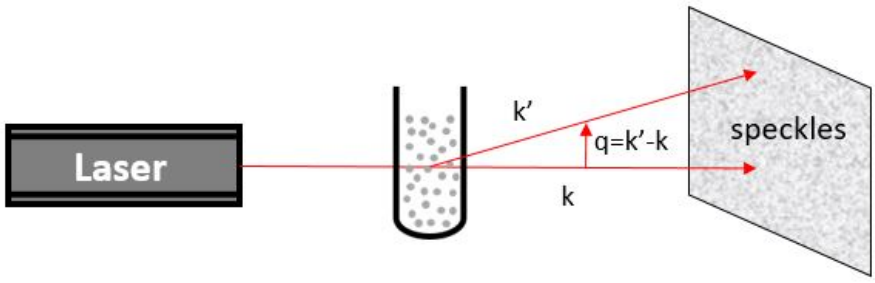

Figure 19. Speckle pattern created by the scattered light from particles in solution undergoing Brownian motion.

DLS relies on measuring the temporal intensity fluctuations arising due to the constant displacement of particles about their mean position. Dynamic information is then derived from the exponentially decaying mutual behavior of the particles with time. The first order field – field correlation function measured at time t and a later time $t + \tau$ is given by:[84]

$$g_1(q,\tau) = \frac{\langle E(t)E(t+\tau)\rangle}{\langle |E(t)|^2\rangle} \tag{34}$$

Since detectors are unable to measure the electric field E due to the square law principle, the detectors instead experimentally measure the intensity – intensity autocorrelation function $g_2(q,\tau)$:

$$g_2(q,\tau) = \frac{\langle I(t)I(t+\tau)\rangle}{\langle |I(t)|^2\rangle} \tag{35}$$

At short time delays the measured intensity correlation is high as particles do not have much time to move far from their initial positions, thus their mutual behavior is similar. As the time delay increases, the intensity correlation decays exponentially, consequently decaying to zero at long times, meaning there is no correlation between the scattered intensity at the initial and final states. The Siegert equation approximates the second order autocorrelation function in relation to the first order autocorrelation function as follows:

$$g_2(q,\tau) = 1 + \beta|g_1(q,\tau)|^2 \tag{36}$$

where β is a correction factor that depends on the light scattering set up and is typically the inverse of the speckle pattern and so is generally less than or equal to 1. An estimate of the diffusion coefficient is done by determining the relaxation time τ which is measured by DLS. The first order autocorrelation function is related to the decay constant by a single or sum of exponentials taking the form:

$$g_1(q,\tau) = Ae^{-\Gamma\tau} \tag{37}$$

where Γ is the decay rate and is related to the relaxation time by $\Gamma = \tau^{-1}$ and is related to the mutual diffusion coefficient D_m and scattering vector q by:

$$\Gamma = q^2 D_m \tag{38}$$

This relationship follows Fick's second law of diffusion where the first derivative of concentration with time equals diffusion times the second derivative of concentration with distance. This results in the calculation of the particles hydrodynamic radius R_H using the Stokes-Einstein equation:

$$R_H = \frac{kT}{6\pi\eta_0 D_m} \tag{39}$$

Depending on polydispersity or anisotropy of the probed species a plot of Γ/q^2 vs q^2 may show an angular dependence of the scattered intensity. If the system contains monodisperse spheres then no angular dependence is observed and the Stokes-Einstein relation provides an accurate hydrodynamic size measurement but if otherwise then the intercept of Γ/q^2 vs q^2 will equal D_m. This is important because a random coil polymer will have different values of R_H from DLS and R_G from static scattering, both providing physically different meaning. Compared to R_G, the hydrodynamic radius is the radius of a hard sphere diffusing through a single solvent, it is not a direct physical measurement because it relies on the sample/solvent interactions and particle shape.

The time dependent scattering intensity fluctuations are correlated over different time scales for larger slower-moving particles compared to smaller faster moving ones (Figure 20).

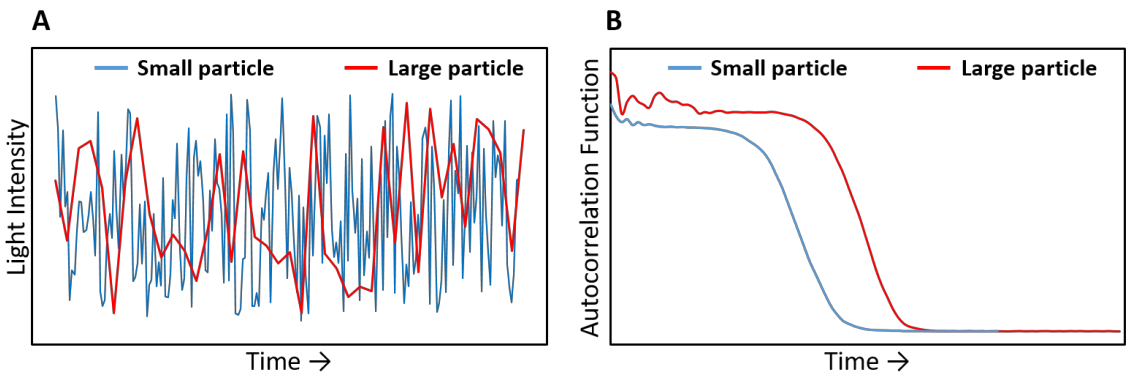

Figure 20. (A) Time dependent intensity fluctuations for small and large particles and, (B) different autocorrelation functions as motions are correlated at different time scales.

1.4 Ordinary-Extraordinary Transition

1.4.1 Fickian and Stoke-Einstein diffusion

The first quantitative description of the diffusive process was proposed in 1855 by Adolf Fick. According to Fick's first law of diffusion, the steady state flux J varies with solute concentration C given by:[85]

$$J = -D\left(\frac{\partial C}{\partial x}\right) \tag{40}$$

where the diffusion coefficient D describes how far the entity of interest moves in a given time owing to its diffusive motion and is expressed as distance^2/time, where x is the one dimensional space coordinate.

Fick's second law describes the rate of change of solute concentration:

$$\frac{\partial C}{\partial t} = D\left(\frac{\partial^2 C}{\partial x^2}\right) \tag{41}$$

In 1905 Albert Einstein provided a solution for Fick's second law for one dimensional diffusion:[86]

$$C(x,t) = \frac{c_0}{\sqrt{4\pi Dt}} e^{-x^2/4Dt} \tag{42}$$

where the probability density function for free diffusion in one dimension is described by letting $c_0 = 1$ and the expansion of the density function leads to a second moment denoted by mean square displacement, which is related to a diffusion coefficient by:

$$\langle x^2 \rangle = 2Dt \tag{43}$$

Extending the solution to a three dimensional situation leads to the representation $\langle r^2 \rangle = 6Dt$ where, $r^2 = x^2 + y^2$. The diffusion coefficient is related to a particles mobility v by:

$$D = k_B T v \tag{44}$$

where $k_B$is the Boltzmann constant, T is the absolute temperature. Particle mobility is related to the friction coefficient f by the relation: $v = 1/f$ which is strongly correlated to the size and shape of the diffusing particle. But for spherical particles the friction coefficient is described by Stokes law:

$$f = 6\pi\eta R_H \tag{45}$$

where η is the solution viscosity and R_H is the hydrodynamic radius of a diffusing particle. Combining these equations leads to the Stokes-Einstein law which relates the diffusion coefficient to the particles radius by:

$$D_{SE} = \frac{k_B T}{6\pi\eta R_H} \tag{46}$$

This equation assumes that the particle is diffusing through a homogenous media of solvent molecules that are much smaller than the solute of interest.

1.4.2 Breakdown of Stokes-Einstein diffusion

In a solution of neutral polymer the hydrodynamic radius of a single chain is proportional to the degree of polymerization N, and the diffusion coefficient D_{SE} of that chain is described by the Stokes-Einstein equation. And so it is expected that polyelectrolyte chains in salt-free solutions should also obey the same relation whereby $D_{SE} \sim \frac{1}{R_H} \sim \frac{1}{N}$ but this is not observed experimentally in measurements obtained using DLS. None of these well-established laws of diffusion for neutral polymers are observed for polyelectrolytes,[7] which presents a significant problem in using the DLS technique to successfully characterize charged macromolecules. Simply put the implementation of the Stokes-Einstein law, which is the routine methodology for characterizing uncharged polymers, is impractical for charged macromolecules.

In the four decades since the DLS experiments on low-salt solutions of PLL and subsequent discovery of the experimentally observed phenomenon termed the "ordinary-extraordinary" transition,[1] no aspect in the field of polyelectrolyte physics has proven to

be more confusing and controversial to understand.[2-4] Ordinary and extraordinary refer to the diffusional behavior of each mode, which are also called the fast D_f and slow D_s diffusive modes, respectively.

1.4.3 Ordinary diffusive mode

The ordinary diffusive behavior, represented by a comparatively faster mode of dynamics, displays a measured diffusion coefficient D_f from DLS that is independent of molecular weight M_w and polymer concentration C_p over several orders of magnitude of each variable. Essentially, $D_f \approx \left(C_p M_w\right)^0$ which is unlike neutral polymer solutions where D_f depends on M_w and C_p.[5-6] The intriguing aspect of the "ordinary" transition is that the measured D_f value from DLS increases above the expected D_{SE} value from the Stokes-Einstein law for dilute polyelectrolyte solutions. This increase only occurs if the molecular salt in the solution, such as NaCl is removed, and so as the salt concentration C_s is decreased from a value sufficiently high enough to screen interactions we observe a rise in D_f. As C_s is further decreased it is expected that due to less charge screening the polymer chain will swell in size from stronger intrachain electrostatic repulsion and thus D_f should decrease according to Stokes-Einstein law, but the observed D_f actually increases. Remarkable observations of polyelectrolytes with molecular weights around 1 million g · mol^{-1} will display fast mode diffusion coefficients only 4 times slower than that of a small ion such as K^+ or Na^+.[87-88] As previously mentioned the dynamic behavior of the fast mode only occurs when C_s is sufficiently low, at which point the measured D_f is several orders of magnitude higher than the expected D_{SE} value based on chain size from Stokes-Einstein. But the fast mode is called the ordinary transition because as C_s is continuously increased

then D_f decreases continuously and eventually reaches D_{SE} at the point where there is enough salt to sufficiently screen all charged polymer groups.

1.4.4 Extraordinary diffusive mode

Diffusive behavior associated with the extraordinary transition is altogether unlike the ordinary mode. The slow diffusion coefficient of the extraordinary mode D_s is orders several orders of magnitude smaller than both D_{SE} and D_f, and unlike the fast mode D_s depends on M_w and C_p, showing a strong decrease as either variable is increased.[7] Such small D_s values suggests the presence of very large aggregates, which is strange for like charged, and hence electrostatically repulsive, polyelectrolytes. Clustering similar to this is also observed in suspensions of charged colloidal particles and micelles,[89] and further evidence to support aggregates is the divergence of scattering intensity at very small angles when the slow mode emerges.[90] The emergence and deviation of D_s away from expected D_{SE} values toward much smaller diffusion coefficients only occurs as C_s is decreased. Simply put the extraordinary mode does not exist in a screened solution and only emerges beyond a sufficiently low value of C_s. This phenomena like the ordinary mode is also reversible with salt, as C_s is increased the value of D_s will increase and approach diffusion coefficient values that are expected, eventually reaching D_{SE} at high enough C_s. It is surprising then that aggregates would form at all under low salt conditions and then break apart when electrostatic interactions are screened (Figure 21).

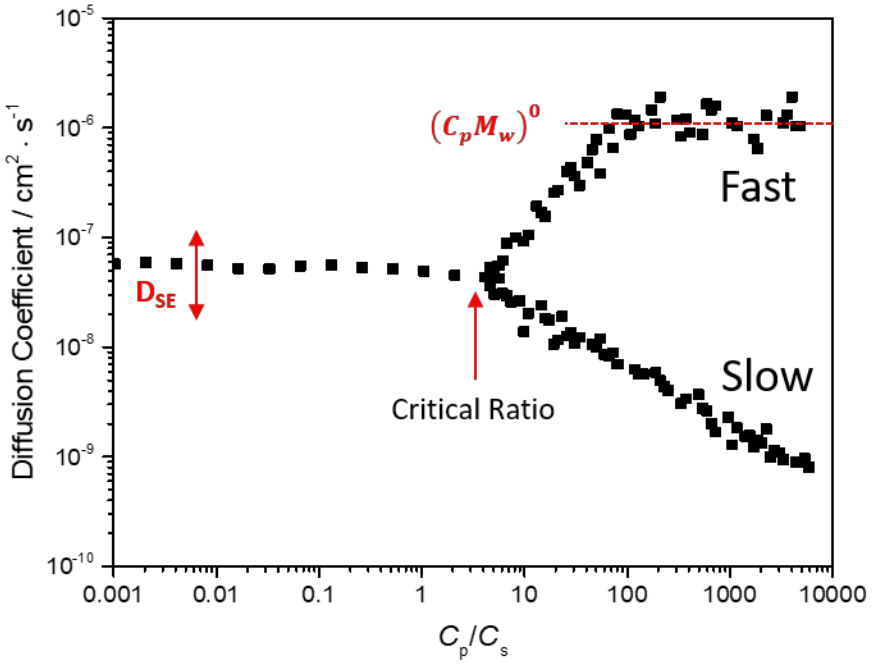

Figure 21. Diffusion coefficients for the fast ordinary mode and the slow extraordinary mode showing where each emerges at a threshold polymer and salt concentration value.

1.4.5 Role of polymer and salt concentration on the diffusive transition

It must be made clear that the phenomenon of the ordinary-extraordinary transition has been observed from DLS experiments on a wide range of solutions of charged macromolecules such as DNA, PLL, NaPSS, poly(methacrylic acid), polyvinyl pyridine, PAM and even charged colloids.[10, 91-100] So it is a phenomenon that appears to be universal for charged macromolecular solutions.

The simultaneous existence of the ordinary fast diffusive mode and extraordinary slow diffusive mode clearly relies on the presence and concentration of low molecular weight salt in the polyelectrolyte solution. Drifford and Dalbiez[9-10] proposed that the emergence

of the ordinary-extraordinary transition occurs at a particular threshold value of the ratio of polymer concentration C_p to salt concentration C_s:

$$\frac{C_p}{C_s} \approx 5.7 \tag{47}$$

This ratio is to be applied solely to the NaPSS-NaCl system, which is considered to be the model polyelectrolyte system for fundamental studies. In addition to suggesting that both the slow and fast modes are only observed at $C_p/C_s > 5.7$ the Drifford-Dalbiez ratio is also argued to be independent of molecular weight.[9-10] The quarternized poly(2-vinylpyridine)-potassium bromide system investigated by Förster et al. [87] displayed a splitting transition from the high salt mode that can be described by D_{SE} into the ordinary and extraordinary modes that occurred at an order higher magnitude of C_p and C_s where the ratio was closer to unity. Regardless of the specific ratio value there is a threshold that depends on C_p and C_s for all systems that display the ordinary-extraordinary transition.

1.4.6 Counterions as the cause for the ordinary-extraordinary transition

Resolving this puzzling ordinary-extraordinary phenomena observed in DLS lies in the ubiquitous cloud of counterions surrounding every polymer chain.[101] There is a net amount of counterions adsorbed around each polymer chain resulting from an optimization between translational entropy and force of attraction between counterions and polymer charged groups.[8] Now the effective charge of the polyelectrolyte is reduced from its chemical charge and as a result the chains no longer undergo independent motion but rather dynamics that are coupled to that of the counterion cloud.

For the fast mode the observed D_f is not simply the mutual diffusion coefficient but is attributed to a collective relaxation arising from electrostatic coupling between the fluctuations in the polyelectrolyte concentration and the counterion concentration.[23, 102-105] The counterions generate a local electric field on the chain segment which contributes to the chain mobility. Therefore the direct implementation of the Stokes-Einstein law for charged macromolecules is not allowed because it does not take into account the independence of electrophoretic mobility on the molar mass of these charged species.[75, 106] Upon the addition of salt the electrostatic correlation between the chain and counterions is now broken and as a result D_f approaches D_{SE} as expected for uncharged systems.

The slow diffusive mode is attributed to the spontaneous formation of aggregates due to the ability of counterions to adsorb onto a chain to form a strong dipole. Although dipole formation is transient, the simultaneous occurrence of several dipole-dipole pairings to form quadrupoles, can result in microgel-like aggregates.[8, 107-109] Such dipole-mediated aggregates, originating from adsorbed counterions, are responsible for the extraordinary behavior of the slow mode and their impermanent nature has led them to be termed temporal aggregates (Figure 22).[110]

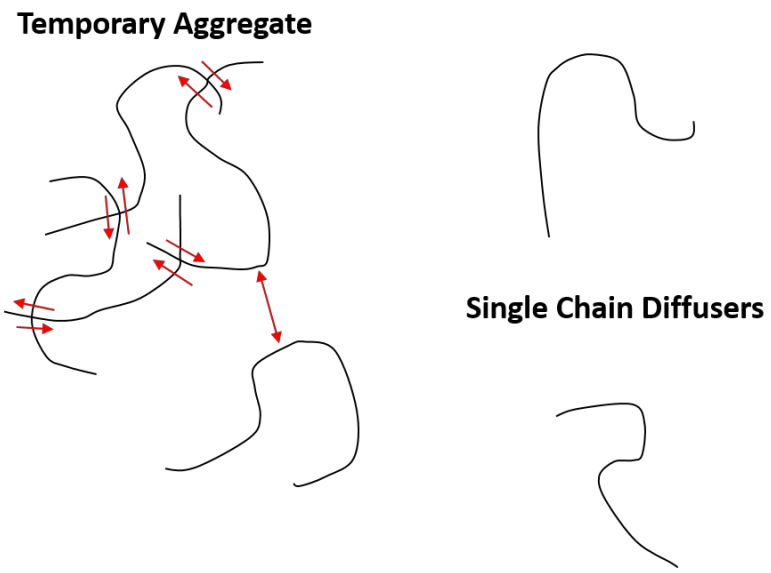

Figure 22. Red arrows indicate the formation of a dipole due to a counterion adsorbed on the polymer backbone. This results in the formation of a temporary aggregate where single chain diffusers in close proximity can enter and exit the aggregate as dipoles form.

1.4.7 Debate over the electrostatic origin of the slow mode

There is evidence to suggest that solvent quality, and not solely electrostatic interactions, are also cause for the slow DLS mode. A DLS examination by Li et al. of semidilute and concentrated neutral polymer solutions of PS in two solvents, toluene, an athermal solvent for PS, and in cyclohexane, a less good/θ solvent in the range of 34–50 °C, showed that solvent quality led to the appearance of a slow mode.[111] Across a range of concentrations only a fast diffusive mode was observed for PS in toluene but in cyclohexane at 45 °C an additional slow mode appeared. This slow mode was also found to be dependent on polymer concentration *C*. When concentration was only a few times larger than the overlap concentration *C**, when chains start to weakly interact with few entanglements, only some of the chains are entangled together to form large transient clusters which coexist with individual chains in solution (Figure 23A). This occurs in a less

good solvent where segment-segment interactions are stronger and the result is a temporal interaction between chain segments to form these larger clusters/aggregates. When the polymer concentration significantly exceeds the entanglement concentration C_e all chains become entangled together in one large network to form a single giant cluster. A visual representation of this is shown in Figure 23B. Each chain is confined inside a "tube" made from its surrounding chains that form the lattice network within a short time frame. The chain is divided into a number of segmental blobs whose size is governed by the correlation length of the neighboring chains i.e. the tube diameter. Each segment blob fluctuates under Brownian motion due to the thermal energy k_BT. In an athermal solvent these thermal blobs have no interaction with the tube and so they experience a single diffusive mode. In a less good solvent the segment-segment interactions near the entanglement points is stronger, therefore the blobs at these tube intersections should move slower than blobs in between these points of entanglement. This is schematically shown by the darker shaded blobs in Figure 23B.

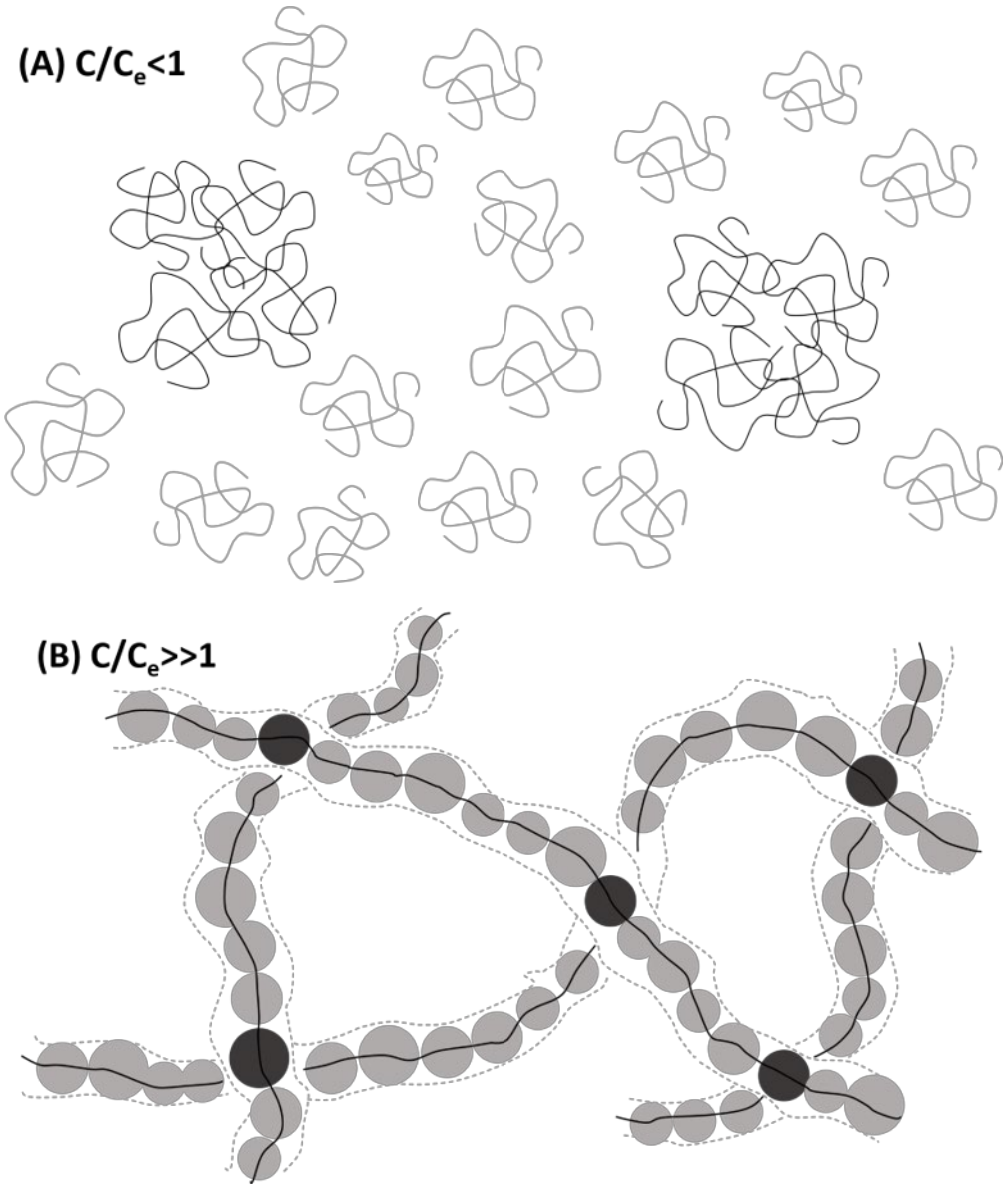

Figure 23. Schematic of diffusion of a neutral polymer in a less good solvent in different concentration regimes: (A) semidilute C/C_e<1 where individual chains and clusters/aggregates coexist in same environment but have different sizes and (B) concentrated C/C_e>>1 where polymer segmental blobs have similar sizes but different environment at entanglement points.

1.4.8 Debate over the origin of temporal aggregates

While there can be no doubt that some sort of attractive interaction exists between like-charged macroions, the argument for temporal aggregates has yet to be met with an

overwhelming consensus. For instance Ghosh et al.,[107] argued that the extraordinary phase is due to the presence of stable polyelectrolyte aggregates and other particulates such as dust. They showed that these entities were removed via filtration through a sufficiently small pore sized membrane and do not appear or grow-back after filtration and postulated that the aggregates are present in the dry polymer material and their existence depends critically on how the dry material is prepared. Another proposed cause for aggregation finds its origins in purity of NaPSS which is the model polyelectrolyte most commonly studied to investigate the ordinary-extraordinary transition. The disadvantage of this polymer is that researchers rarely synthesize it in house, but rather commercially obtain, whereby it is made by the sulfonation of PS, an imperfect procedure that leaves unwanted hydrophobic patches along the chain to act as sources for aggregation.[28, 112] Li et al.,[113] concluded that there is no decisive evidence to differentiate whether the slow relaxation mode is attributed to temporal aggregates formed from overlapping counterion clouds between chains or to the self-diffusion of individual chains retarded by surrounding chains (interchain friction). Their experimental results supported the idea that the slow mode was due to hindered motions of interacting polymer chains. Zhou et al. also supported this conclusion with a DLS study of poly(*p*-azidomethylstyrene)-co-polystyrene (PAMS-co-PS) which could undergo a reversible neutral-charged-neutral transition in DMF when the solution is alternatively bubbled with CO_2 and N_2.[114] They argue that the slow mode is attributed to some scattering objects with a dimension of approximately 20 nm, which is similar to the interchain distance. A cage model was put forth because the slow mode is related to the self-diffusion of the center of mass of individual chains under long-range electrostatic interaction-induced constraints of surrounding chains. At low salt electrostatic

interactions from neighboring chains occur over greater distances and thus create a cage for which an individual chain is restricted to move within.

1.4.9 Experimental DLS evidence to support multiple diffusive modes

Strong evidence for the existence of temporal aggregates was discovered by DLS measurements on binary mixtures of NaPSS of vastly different molecular weights. Sedlak,[115] found three diffusive modes of which the fast and slow mode were present along with an intermediate diffusive mode. The significant finding was that only one slow mode was measured, in spite of the fact that polyelectrolytes with appreciably different molecular weights give slow modes on different time scales, therefore the slow mode cannot be identified with a single-chain property.[116] This confirms that the slow mode is due to some multi-chain character which fits the description of temporal aggregates. To further reinforce and better understand the appearance of the third diffusive mode Jia and Muthukumar,[117] also detected a third mode on single molecular weight NaPSS solutions and found that molecular weight, not just C_p and C_s as previously postulated, also had an effect on the three diffusive modes. They showed that when a small amount of added salt is present there should be more than just one relaxation mode observed (the fast mode) in addition to the slow mode. This is because in the presence of salt there are three charged species present: polyelectrolyte, counterion and co-ion. Hence there is electrostatic coupling between three components; polymer segments to counterions to co-ions and so three decay rates are expected to be observed. One of these decays is the plasmon mode, which is nondiffusive as it represents the relaxation of ion clouds surrounding the many charged species and is too fast to be measured in DLS.[118] The other two decay rates correspond to two faster diffusive modes in salty solutions between the polymer chain and

counterion and co-ion respectively. Jia and Muthukumar,[117] detected these two faster diffusive modes, in addition to the slow mode, and showed that both $C_p\ /C_s$ along with $C_p\ /C^*\ (M_w)$, where C^* is the overlap concentration, control the nature of dynamical couplings among the polyelectrolyte chains, counterions, and co-ions (Figure 24).

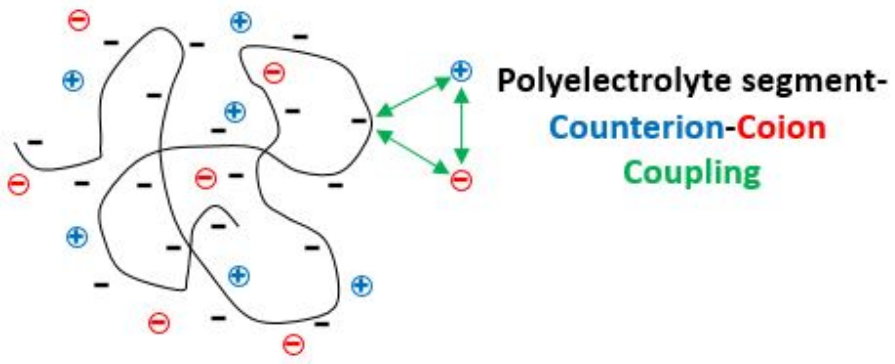

Figure 24. Three electrostatic interactions occur in polyelectrolyte solutions with added salt, each producing a dynamic mode.

The presence and amount of salt in a polyelectrolyte solution strongly effects the DLS signal intensity. With little to no salt the scattering signal is weak and therefore the amplitude of the slow mode is small, allowing for impurities and dust to easily corrupt the measurement. Sedlak,[109] revealed that the slow mode is present over a broad range of ionic strengths, there is no abrupt transition where it appears, but rather the absolute scattering intensity associated with the slow mode increases upon increasing ionic strength. This means that the multi-domain structures responsible for the slow mode form in solution and are not accounted for by some stable aggregate. Furthermore, domain dimensions also increase upon increasing ionic strength. Cong et al.,[38] performed DLS measurements on NaPSS solutions in dialysis equilibrium with an exchange fluid whose salt and pH could be altered without introducing dust to the cell. They observed that several cyclic salt

concentration changes did not affect the overall dynamics of the slow mode. This reversible behavior suggests the slow mode is representative of a polyelectrolyte state in thermodynamic equilibrium.

Evidence for the ordinary-extraordinary transition obtained by DLS is plentiful and sufficient but is completely lacking when measured using other techniques that probe dynamics such as FPR, Fluorescence Correlation Spectroscopy (FCS) and pulsed gradient field NMR or diffusion ordered spectroscopy (DOSY). It is critical to observe the ordinary extraordinary phenomena with a technique other than DLS.

CHAPTER 2. A CONTROLLED SYNTHESIS OF NAPSS OVER A RANGE OF MOLECULAR WEIGHTS WITH LOW DISPERSITIES VIA AQUEOUS ATRP

2.1 Introduction

2.1.1 Reversible deactivation radical polymerization

2.1.1.1 Definition and types

Defined by IUPAC a RDRP is a type of living polymerization where the active polymer chain end is a free radical. Propagation of the chain occurs by these radicals deactivating reversibly which brings them into one or more states of active/dormant equilibrium.[119] Examples of RDRP include: stable free radical mediated polymerization (SFRP) such as nitroxide-mediated polymerization (NMP),[120] ATRP,[121] reversible addition-fragmentation chain-transfer (RAFT) polymerization,[122] and telluride-mediated radical polymerization (TERP).[123]

There are several widely accepted features of an RDRP which define whether or not the polymerization is controlled.[124-126] A controlled polymerization refers to reaction conditions where chain breaking processes are insignificant compared to chain propagation which permits the synthesis of polymers with predetermined molecular weights, low dispersity and selective site functionalities.

2.1.2 Features of controlled polymerizations

2.1.2.1 First order kinetic behavior

The rate of polymerization R_p with respect to the log of the monomer concentration $[M]$ is linear as a function of reaction time. Due to the negligible contribution of non-reversible termination events the concentration of active propagating species $[P^{\cdot}]$ is constant.[127]

$$R_p = -\frac{d[M]}{dt} = k_p[P^{\cdot}][M] \tag{48}$$

$$ln\frac{[M]_0}{[M]} = k_p[P^{\cdot}]t \tag{49}$$

where k_p is the propagation constant. The above relationship and the effect of changes in $[P^{\cdot}]$ can be visualized through a semilogarithmic plot of $ln\frac{[M]_0}{[M]}$ vs t. A straight line depicts a constant $[P^{\cdot}]$ during the reaction time, which represents a balance of activation and deactivation rates of the propagating chain ends. An upwards curvature represents an increase in $[P^{\cdot}]$ due to a slow initiation, and a downwards curvature or a decrease in $[P^{\cdot}]$ is owed to termination reactions (Figure 25).

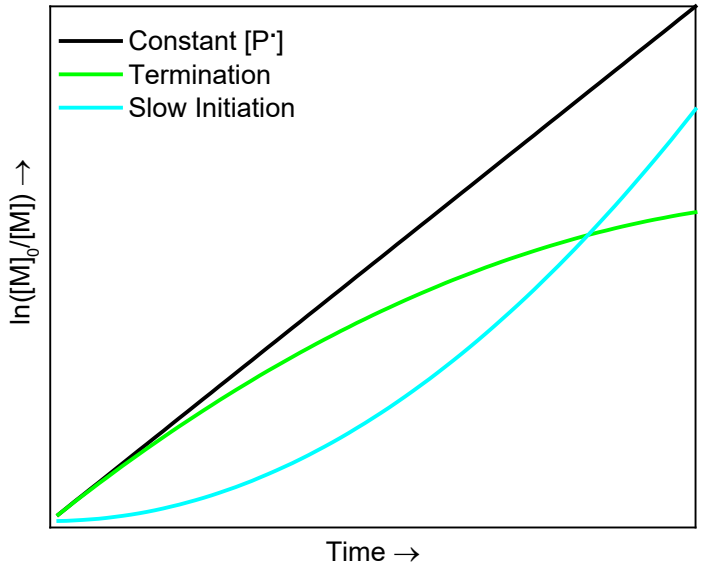

Figure 25. Dependence of ln([M]₀/[M]) on reaction time.

2.1.2.2 Pre-determinable degree of polymerization

The ability to target a specific molecular weight implies that the number average molecular weight M_n increases as a linear function with monomer conversion. A targeted degree of polymerization is set by the initial monomer $[M]_0$ and initiator $[I]_0$ concentrations.

$$DP_n = \frac{M_n}{M_0} = \frac{[M]_0}{[I]_0}(conversion) \tag{50}$$

A constant number of chains must exist for this condition to hold. Hence initiation should be fast, so all chains propagate at the same time before the reaction stops, and chain transfer must be negligible, otherwise the number of chains will increase during the reaction. Ideal

growth of molecular weight with conversion is shown below along with non-desirable cases (Figure 26Figure 26).

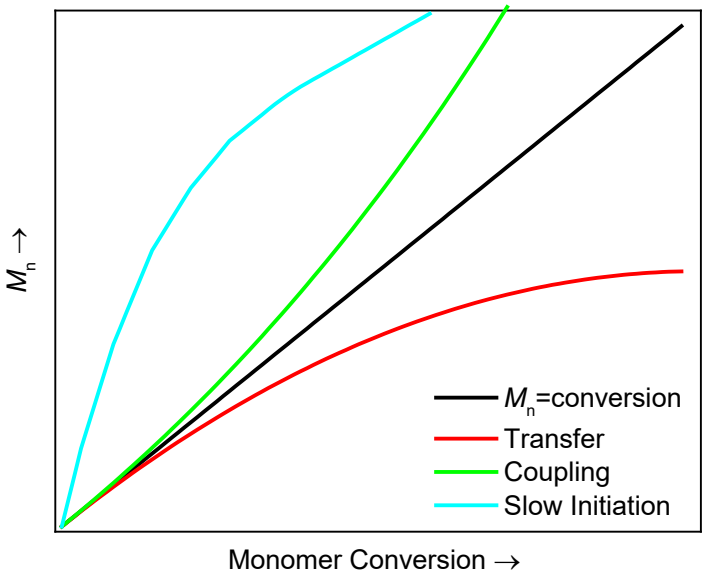

Figure 26. Dependence of molecular weight on monomer conversion.

2.1.2.3 Obtaining a narrow molecular weight distribution

Several factors have been identified for reactions that produce narrow molecular weight distributions.[128-129] The following criteria must be satisfied to achieve a low dispersity.

1. The rate of initiation is fast compared to the rate of propagation so that all chains grow simultaneously.

2. The rate of radical exchange between different species is fast compared to the rate of propagation. This permits monomer addition to active chain ends to be equally probable amongst all chains so that uniform growth occurs.

3. Chain transfer and termination processes are negligible.

4. The rate of depropagation is negligible so the polymerization is irreversible.

A controlled RDRP typically produces polymers with dispersities below 1.3.

2.1.2.4 Long-lived polymer chains with preserved end-functionalities.

When all monomer is consumed the chain ends will retain their active chain ends as long as termination and chain transfer is negligible. Introduction of more monomer will then allow the chains to recommence propagation. Chain end fidelity permits the sequential addition of block copolymers and polymers with segments of varying architecture.

2.1.3 Atom transfer radical polymerization

Discovered by Krzysztof Matyjaszewski in 1994 and developed by his research group at Carnegie Melon the ATRP process is one of the most widely used and effective types of RDRP.[130]

2.1.3.1 Main components of ATRP

The general ATRP reaction requires four components to work:

1. An initiator or macro initiator molecule (R-X) which contains at least one transferable atom or group X, typically a halogen such as Br or Cl.

2. A transition metal compound, Mt^m, that can undergo a one electron redox reaction, typically copper is used.

3. A ligand, L, that complexes the transition metal to form a catalyst which has tunable solubility and activity depending on ligand choice.

4. At least one radically polymerizable monomer.

The focal point of an ATRP reaction involves the formation of a dynamic equilibrium between the activation of a dormant species and the deactivation of the growing polymer chain end. The transfer of a radically exchangeable atom or molecule from an initiator to a lower oxidation state transition metal complex must occur to enable activation and deactivation states. For a successful ATRP the equilibria must be pushed to the left hand side so that there is a large fraction of dormant chains and the concentration of radicals is low, which reduces the probability of radical-radical termination reactions.

The lifespan of radicals during an ATRP are described by four rate constants. Active radicals form at a rate constant of activation given by k_{act}, propagate at a rate constant given by k_p, reversibly deactivate given by k_{deact} and can terminate given by k_t. Thus the rate of polymerization depends on the radical concentration ($R^{\cdot}$) and the equilibrium constant for the ATRP reaction.

$$R_p = k_p K_{ATRP} \frac{[RX][Cu^I L_n]}{[Cu^{II} L_n X]} [M] \tag{51}$$

2.1.3.2 ATRP reaction mechanism

The ATRP mechanism involves an inner sphere electron transfer process,[131] specifically a reversible homolytic halogen transfer occurs between a dormant species, which is the initiator (R-X) or dormant propagating polymer chain end ($R\text{-}P_n\text{-}X$), and a transition metal complex in its lower oxidation state (Mt^n/L). Due to the transfer an active radical chain end forms, which permits polymer propagation ($R^{\bullet}$), and the transition metal complex occupies a higher oxidation state due to the coordination of the halide-ligand ($X\text{-}Mt^{n+1}/L$). The reversible reaction between Mt^n/L and the initiator/dormant polymer chain to form $R^{\bullet}$ is highly unfavored compared to the reverse reaction. Radical propagation at the active chain end, adding monomer, is a short lived process and is rapidly deactivated as the transferable atom from $X\text{-}Mt^{n+1}/L$ reacts to form a dormant chain end capped by X. If the active radical state is long lived a higher concentration of $R^{\bullet}$ ensues which further increases the likelihood of termination events and reduces reaction control. It is worth noting that the R-X molecule called an initiator in ATRP is unlike a free radical initiator, it is a thermally stable entity that is fully incorporated as a molecule into the final polymer material (Figure 27).

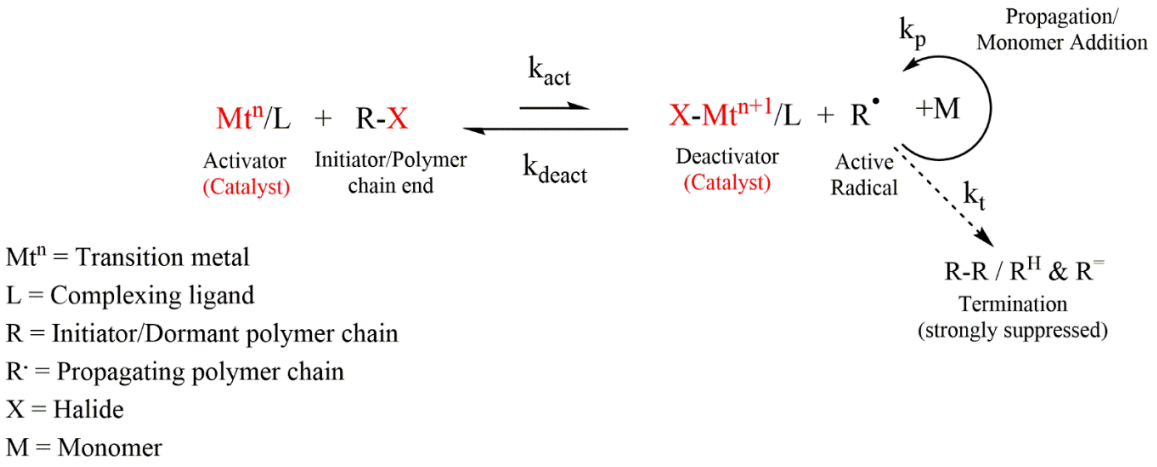

Figure 27. Mechanism of metal complex-mediated ATRP.

There are many types of ATRP reactions which focus on a range of capabilities from low catalyst concentrations to polymerization from surfaces to light activated initiators along with much debate over the specific mechanisms of disproportionation and comproportionation that describe a reaction under various solvent conditions. To reduce complexity the focus here will solely be on normal ATRP reactions using a copper transition metal catalyst.

ATRP can be performed in a variety of media such as bulk, solution, dispersions and various types of emulsions. Media choice depends primarily on solubility and heat transfer but many other considerations must be taken into account to perform a successful reaction on a desired monomer. As previously mentioned the balance between activation and deactivation is critical for a controlled ATRP reaction. The catalyst complex chosen is integral to optimizing this balance as the relative activity of a catalyst complex can vary over seven orders of magnitude.[132] Activity is heavily dependent on ligand and initiator structure in a given solvent system. For example it was found that activity decreased from tetradentate to tridentate to bidentate ligands in Cu catalyst systems and complexes made

of bridged ligands are more active than corresponding linear ligands.[132] Selection of the appropriate initiator is also critical as activation rate constants can vary by a factor of one million depending on type.[133] Choice of catalyst, ligand and initiator are just some considerations to make. Selection of halogen or transferable atom, suitable solvent for the desired monomer, and in addition the concentrations of all species relative to one another further increases the complexity of reaction parameters. Addition of a small fraction ~20% of Cu^{II} relative to Cu^{I} has also proven to provide greater reaction control in some ATRP systems as polymers were produced with lower dispersities and molecular weights closer to theoretical values.[134] There is not a one size fits all for polymerizable monomers via ATRP. Control over the reaction process to ensure the reaction isn't too fast or slow, doesn't start or stops prematurely and has desired molecular weights and low dispersities $Đ$<1.3 requires planning and tuning of reaction conditions.

2.1.4 ATRP in protic media

An initial challenge of ATRP was expanding the range of polymerizable monomers to those which were ionic and soluble in protic media with the desire to design functional materials in aqueous systems. Unwanted side reactions involving the catalyst complex became a major problem associated with the polar nature of such solvents. Ultimately these side reactions affected the deactivation efficiency of the system which resulted in a loss of reaction control.[30]

Reaction control is typically evaluated from the value of $Đ$, which depends on the deactivator concentration according to the following equation:[135]

$$Đ = \frac{M_w}{M_n} = 1 + \left(\frac{k_p[RX]_0}{k_{deact}[Cu^{II}L_nX]}\right)\left(\frac{2}{conv} - 1\right) \quad (52)$$

where $[RX]_0$ is the initial initiator concentration and $conv$ is the fraction of monomer conversion. Higher deactivator concentrations lead to lower dispersities but in protic media this concentration strongly depends on electron affinity and halidophilicity of the deactivator species which are expected to be high as halide anions formed are stabilized in protic solvents. Dissociation of the ATRP deactivator thus reduces the overall deactivator concentration and dispersity increases as a result.

2.1.4.1 Competing side equilibria in aqueous ATRP

There are several side reactions that occur when ATRP is carried out in protic solvents such as alcohols or aqueous media (Figure 28). All of which contribute toward reduced deactivation efficiency and loss of chain end fidelity. But protic and especially aqueous solutions, in comparison to organic solvents, offer the ability to adjust reaction variables such as pH, ionic strength and polarity, which along with temperature provides many avenues to adjust reaction conditions for an ATRP.

1. Disproportionation of the ATRP activator [Cu^I/L_n] catalyst complex (k_{disp})

2. Disproportionation or hydrolysis of the initiator or dormant chain end

3. Reduction in the deactivator concentration [X-Cu^{II}/L_n] via dissociation of the halide ligand (k_x)

4. Complexation of dissociated catalyst complex or halide ligand with polar solvent or monomer ($k_{CU,\,aq}$) or ($k_{X,\,aq,\,j}$)

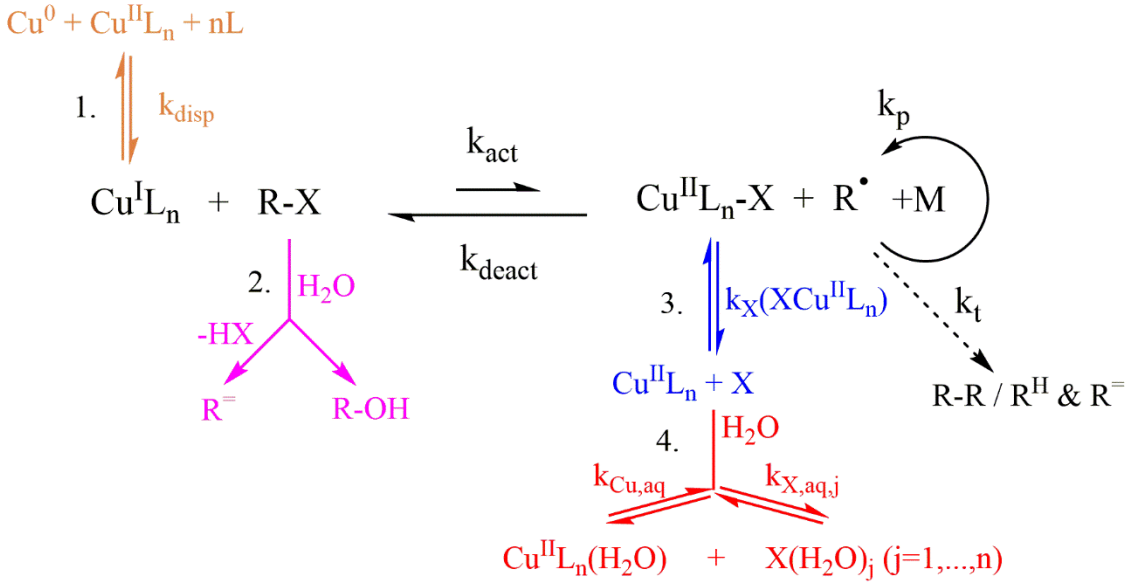

Figure 28. Competing unwanted side reaction equilibria when ATRP is conducted in protic solvents like water or alcohols.

Compounds of Cu^{I} are generally unstable in aqueous media and tend to disproportionate because this process relies on the dielectric constant of the solvent and the preferential ability to solvate Cu^{II} over Cu^{I}.[136] But the disproportionation constant k_{disp} is significantly affected by the choice of ligand to complex with Cu^{I} and Cu^{II} and so catalyst activity and propensity to disproportionate can be easily tuned.[137] There is debate over the role of disproportionation as a way to lead to a faster and more controlled polymerization due to the activation of an alkyl halide initiator by a highly active Cu^{0} species. Disproportionation of the generated Cu^{I} into Cu^{0} and Cu^{II} in protic solvents followed by deactivation of the propagating radical by the created Cu^{II} generates a stable equilibrium between active and dormant chains.[138] In an effort to quantify disproportionation it was

shown in a variety of protic solvents that comproportionation of Cu^0 into Cu^I and Cu^{II} was dominant by comparison, and it is generally accepted in the ATRP community that stopping or reducing disproportionation is the most effective way to attain reaction control in protic media.[139-140]

In aqueous media the hydrolysis of X-Cu^{II}/L_n is extensive because the halidophilicity of Cu^{II} towards halide ions such as Br^- and Cl^- is several orders of magnitude lower in water compared to conventional organic solvents.[30] A result of hydrolysis is an increased concentration of Cu^{II}/L_n which subsequently cannot deactivate radicals and reaction control is lost. Halide ions are significantly more soluble in water than organic solvents and so the degree of reversible dissociation of the halide ion from the higher oxidation state catalyst complex is more significant in aqueous media. Coordination of water to Cu^{II} further reduces the probability of halide ion re-complexation with the Cu^{II}/L_n catalyst. ATRP reactions are typically faster and less controlled in aqueous conditions.

2.1.4.2 Ways to negate unwanted side reactions

Several steps can be taken to reduce the occurrence of side reactions and maintain reaction control when conducting ATRP in aqueous media.

1. Choosing ligands such as 2,2'-bipyridine (bpy), 1,1,4,7,10,10-hexamethyltriethylenetetramine (HMTETA), and tris(2-pyridylmethyl)amine (TPMA) because their Cu^I complexes are significantly less prone to disproportionate while also being highly active which favors reaction control.[31]

2. Having a high initial concentration of deactivator catalyst species [X-Cu^{II}/L_n] relative to the whole catalyst concentration.[141]

3. Addition of halide salts to the system to negate the effect of hydrolysis and halide ion solvation by increasing the likelihood of extra chloride or bromide to form deactivator species.[30, 142]

4. Adjustment of solvent polarity and pH.[143-144]

2.1.5 ATRP of NaPSS

NaPSS, has a variety of applications such as multilayer polyelectrolyte membranes for controlled drug delivery,[11] medicines to treat abnormally high potassium or lithium levels in blood (hyperkalemia),[12] ion-exchange resins for metal ion selectivity and separation,[13-*14*] cosmetics,[17] proton exchange membranes for fuel cells,[18-19] and dopants for conducting polymers.[20-21] As a model polyelectrolyte, NaPSS has been used for fundamental experimental studies for several decades.[10] Parameters investigated have included osmotic pressure and viscosity,[22] chain conformation and counterion condensation,[23] and multilayer swelling and uptake of free ions.[24] Investigation of polyelectrolyte dynamics in solution are of particular interest to our research, specifically the "ordinary-extraordinary transition" measured by dynamic light scattering,[145-146] which is a concentration and molecular weight dependent observation of multiple diffusing modes of charged macromolecules in solutions of low salt. Investigation of this phenomenon requires the preparation of a broad range of molecular weight NaPSS of low polydispersity. The extensive interest and use of NaPSS for many of these applications is associated with two key factors: it is easily obtained from commercial sources; and, it is available in a wide

range of molecular weights. Despite these attributes, the available samples of NaPSS are not without problems. For accurate experimental results, the polymer must be perfectly and completely substituted with sulfonate groups, yet this is not always the case. Whether commercially obtained or synthesized in-house, NaPSS displays significant variations in purity, stated molecular weights and polydispersity.[28-29]

The commercial synthesis of NaPSS is achieved through the post-modification of PS (Figure 29) via treatment with either concentrated sulfuric acid,[147] concentrated sulfuric acid in the presence of catalyst,[148] acetyl sulfate,[149] chlorosulfonic acid,[150] or sulfur trioxide.[151] "Harsh" sulfonation methods lead to either degradation of the polymer through oxidation,[150] chain scission and sulfoxide crosslinks,[152] whereas "gentle" methods result in incomplete polymer sulfonation,[112] which leaves unwanted hydrophobic patches along the chain that lead to polymer aggregation in solution.[153] Coughlin et al. demonstrated significant progress towards complete PS sulfonation without chain degradation but at the expense of regioselectivity of the pendant sulfonate group.[29]

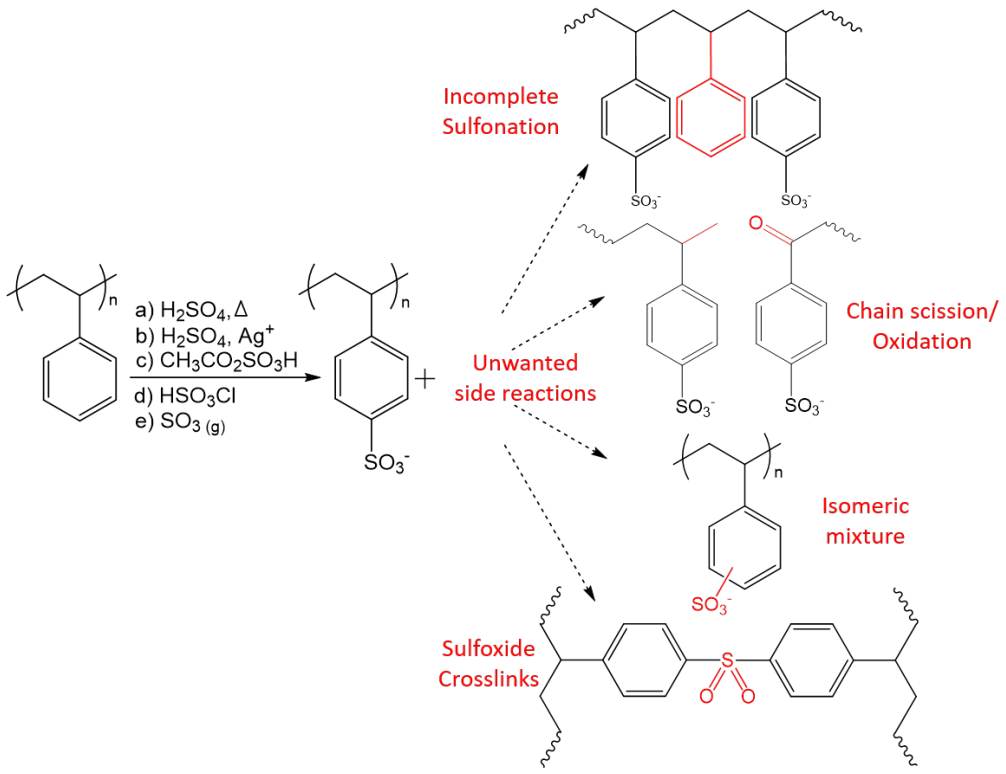

Figure 29. Unwanted products from the sulfonation of polystyrene.

Polymerization of NaPSS from styrene sulfonate monomer circumvents incomplete sulfonation and other post-modification problems, resulting in "patchless" NaPSS, but conventional free radical polymerizations of styrene sulfonate in water do not permit control over molecular weight and lead to *Đ* values that exceed 2. Several RDRP methods including RAFT,[154] NMP,[155,156] and ATRP[157,143] have been used to produce NaPSS. Reported syntheses of NaPSS via ATRP show limited ability to achieve high molecular weights (>50 000 g·mol^{-1}), low dispersities and overall reaction control. Choi et al. reported significant deviation from living polymer behavior, with multimodal SEC traces and high *Đ* values of (1.45-1.6) in pure water.[157] Through addition of a MeOH cosolvent and Cu(II)Br_2, the SEC high molecular weight shoulder was eliminated and *Đ* reduced to 1.21 for molecular weights ~20 000 g·mol^{-1}. Tsarevsky et al. showed that a pure water synthesis

at 30 °C resulted in high $Đ$ values, but incorporation of 50% pyridine by volume decreased $Đ$ to 1.26 for low M_n targets (~10 000 g·mol^{-1}).[158] Iddon et al. demonstrated room temperature syntheses of NaPSS in a mixed H_2O/MeOH solvent, but the molecular weights did not exceed 25 000 g·mol^{-1} and $Đ$ values were high (1.26-2.03).[143] Huberty et al. produced NaPSS via an aqueous ATRP with molecular weights of 30 000 to 2×10^5 g·mol^{-1} and $Đ$ values in the range of 1.01-1.24 but the reaction was reported to lack reproducibility.[159]

Copper-mediated RDRP in protic media has proved challenging to understand and implement due to the potential for many reactions to occur, such as disproportionation of the ATRP activator (Cu(I) complex), reduction of deactivator concentration via halide dissociation (Cu(II)L_mX), complexation of either dissociated species with solvent and/or polar monomers, and disproportionation of the initiator or hydrolysis of the chain end.[30, 160] The complexity that arises from the many potential Cu/ligand/solvent/initiator/monomer combinations, in addition to the order in which each component is introduced to a reaction, has a significant effect on the proposed polymerization mechanism. Percec et al. have conducted many investigations that provide evidence for disproportionation of the Cu(I) that is formed in situ to Cu(0) and Cu(II) in polar solvents as the mechanism in an outer sphere single-electron transfer living radical polymerization (SET-LRP) to produce polymers of low dispersity.[138, 161-164] Haddleton et al. extended the SET-LRP mechanism in an aqueous synthesis where full disproportionation of CuBr/tris(2-methylaminoethyl)amine (Me_6TREN) was permitted prior to addition of monomer and initiator to produce well defined multiblock copolymers.[165] The group also synthesized polyelectrolytes via SET-LRP[166-168] and further

discussed the mechanism in depth, highlighting the importance of ligand and catalyst compatibility for many systems.[169] Matyjaszewski et al. first used Cu(0) in 1997 for supplemental activator and reducing agent atom transfer radical polymerization (SARA-ATRP) which proposed Cu(I) is the major activator rather than "nascent" Cu(0).[170-172] While both models describe the same components to explain the rapid polymerization of monomers in polar solvents in the presence of active copper complexes, it has been pointed out that the contribution from every reaction is different.[173] Furthermore, several unexpected and counterintuitive experimental data sets reported in the literature suggest a more complex mechanism.[174]

The goal of this study is not to contribute further mechanistic understanding, but to apply knowledge from previous reports to arrive at convenient procedures to produce well-defined "patchless" NaPSS across a wide range of molecular weights. Several reaction variables have been shown to effect control in aqueous RDRP and guided the choice of our preliminary reaction variables for synthetic optimization (Figure 30). Acidity has been reported to have a considerable effect on the catalyst complex and the overall polymerization in water because it can change the coordinating ligand in the deactivated state.[175] Adjustment of solvent polarity with a miscible cosolvent can suppress deactivator hydrolysis and provide better polymerization control.[31, 176-177] The addition of a halide salt promotes efficient deactivation which permits greater control over the dispersity of the final product.[178-179] A chlorine-capped chain is approximately ten times less active than a bromine-capped chain and results in slower polymerizations, but the carbon-chlorine bond is more stable and produces more controlled reactions leading to narrow molecular weight distributions.[132, 180]

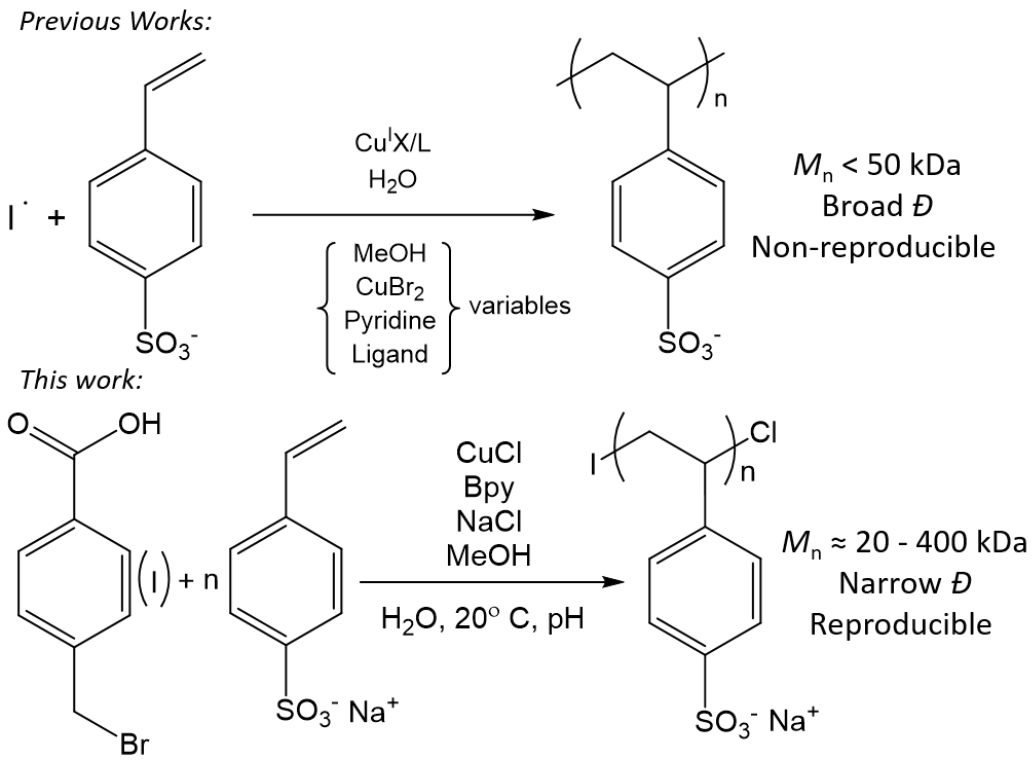

Figure 30. Progress in the RDRP of NaPSS.

In the remainder of this report, the synthesis of perfectly sulfonated NaPSS on gram scales in a reproducible manner via RDRP is described. It will be seen that pH, MeOH cosolvent and NaCl addition directly affect the molecular weight distribution, monomer conversion and overall reaction control. The end result is a pragmatic approach to perfectly sulfonated NaPSS with low polydispersity over a molecular weight range of 20 000 – 400 000 g·mol^{-1}.

2.2 Experimental

2.2.1 Materials

Sodium 4-vinylbenzesulfonate, 2,2'-bipyridine (bpy) (> 99.0%), copper (I) chloride (CuCl) (>99.995%), sodium chloride (NaCl) (>99.0%), copper (II) chloride ($CuCl_2$) (97.0%), 4-

(bromomethyl)benzoic acid (97.0%), sodium hydroxide (NaOH) (>97.0%), and pyridine (>99.0%) were purchased from Sigma Aldrich and used as received. Ethanol (>99.5%, KOPTEC) and methanol (>99.8%, BDH) were purchased from VWR. Sodium nitrate ($NaNO_3$) (>99.0%) was purchased from J. T. Baker. Sodium phosphate monobasic (NaH_2PO_4) (99.9%) was purchased from Fisher Scientific. Hydrochloric acid standard solution 5 M (HCl) was obtained from Fluka Analytical. Deionized water (18 MΩ·cm) was drawn from a Millipore Milli-Q Type I source.

2.2.2 Preparation of ATRP Catalyst Complex

In a round-bottom flask (1 L), 500 mL water was added and the flask was sealed. Subsequently, three cycles of degassing under vacuum and purging with dry argon were performed to deoxygenate the system. The flask was placed in a glove box under an argon atmosphere. CuCl (0.50 g, 5 mmol) and bpy (2.50 g, 16 mmol) were added to the degassed water under magnetic stirring. The CuCl was a white crystalline powder that did not dissolve, but upon bpy addition the entire flask content turned dark brown and the CuCl powder visibly dissolved. The sealed flask was kept under stirring in a glovebox.

2.2.3 Procedure for synthesis of NaPSS

Sodium 4-vinylbenzenesulfonate (4.00 g, 20 mmol), NaCl (vary), water (vary) and MeOH (vary) such that total solvent volume was always 45 mL, were added to a 100 mL round-bottom flask under magnetic stirring for 10 min. The initiator, 4-(bromomethyl) benzoic acid (0.02 g, 0.09 mmol) was added along with 1 M NaOH solution with continuous stirring. The pH was adjusted using solutions of 1 M NaOH or 1 M HCl. The round-bottom flask was sealed with a septum and underwent two cycles of 30 min degassing and 30 min

argon gas purging. Cu/bpy solution (5 mL) was drawn via syringe in the glovebox and transferred to the reaction solution turning it a dark brown color. An additional cycle of degassing and purging was conducted before the flask was sealed using Parafilm. Reaction time was varied but reaction temperature was kept at room temperature ~20 °C. A slight exothermic effect ~1–3 °C was observed with an infrared thermometer, indicating radical chain propagation, and the reaction mixture color remained a dark non-transparent brown. Aliquots were taken throughout the reaction and quenched by dissolving into cold MeOH. Quenched reactions turned transparent blue vitriol and were noticeably more viscous than the initial reagent solution.

Once quenched, all NaPSS reaction solutions were split into two portions, one crude and one purified. The crude portions underwent rotary evaporation and vacuum drying to yield a green/blue material of varying consistency. All NMR experiments to determine % monomer conversion were performed on crude samples. Purified portions were passed through a silica column using a 20% v/v MeOH/H_2O mobile phase to clear the sample of the copper complex catalyst. The catalyst-free sample was then dialyzed extensively in distilled water using 3500 molecular weight cut-off (MWCO) dialysis membrane tubing to remove excess monomer. Rotary evaporation followed by vacuum drying was performed on the purified samples to yield either a glassy and transparent solid or a white powder. These purified samples were analyzed by SEC-MALS.

2.2.4 Characterization

The SEC-MALS system consisted of a Gastorr BG-34 degasser, an Agilent 1100 series pump with an Agilent 1100 auto injector connected to an Agilent PL aquagel-OH 8 μm

guard column prior to two Agilent PL aquagel-OH Mixed-H 8 μm columns connected in series. The MALS system consisted of a Wyatt Dawn Heleos with a Wyatt Optilab rEX dRI detector operating at 658 nm. An Agilent 1100 series handheld control module was used to operate the SEC and data acquisition and analysis were done with Wyatt Astra 6.1 software. The mobile phase was a buffer solution of 0.3 M $NaNO_3$ + 0.01 M NaH_2PO_4 at pH 9 with 20% MeOH by volume. Polymer samples of concentration ~5 mg/mL were dissolved for 24 h prior to measurements to ensure complete dissolution. Solutions were filtered through Whatman Anotop 0.2 μm filters into Agilent 2 mL SEC vials. All chromatograms shown display the light scattering trace data taken from the 90° detector. Duplicate injections (100 μL) were performed for each sample measured by SEC-MALS and the resulting chromatography was found to be replicable in all cases.

Proton NMR experiments and data analysis were conducted with a Bruker DRX 500 MHz instrument and the Bruker TopSpin 3.2 NMR program. ^{1}H NMR data collected were obtained with 500 MHz field strength, probe temperate of 297 K and with a residual internal standard H_2O (δ 4.70). A T1 relaxation experiment was performed to determine the appropriate pulse delay (D1) for quantitative integration of polymer peaks. Setting D1 to five times T1 in all cases gives >95% integration accuracy. The largest T1 was 5.074 s and thus D1 was set to 25 s for all subsequent ^{1}H NMR experiments. Monomer conversion calculations are explained below.

2.2.5 Monomer Conversion from ^{1}H NMR

Samples for NMR were prepared by dissolving 10 mg dried crude NaPSS in D_2O. The percent monomer conversion was calculated:

$$\%\, Conversion = \frac{H_p}{H_p + H_m} \times 100 \quad (53)$$

where H_p and H_m are the integrals of the polymer and monomer peaks respectively. This equation only holds for integrated peaks that represent the equivalent number of protons on the monomer molecule and polymer repeat unit. To calculate % monomer conversion the three polymer backbone protons on each NaPSS repeat unit, represented by a large broad peak on the spectra from around 0.5–2.5 ppm, are compared to a single vinylic proton, represented as a doublet at 5.32 ppm, on the sodium 4-vinylbenzenesulfonate monomer. The integral of the broad polymer peak is calculated relative to the normalized monomer peak which represents a known single proton. The equivalent proton ratios being represented by each peak are 1:3 for monomer:polymer and therefore the polymer integral value must be divided by 3 before it is substituted into the % monomer conversion calculation. Figure 31 illustrates this process by comparing monomer, purified NaPSS and crude samples that were analyzed to determine % monomer conversion.

(Monomer): ^{1}H NMR (D_2O, 500 MHz): δ 5.32 (d, 1H, J = 10 Hz, H^E), 5.83 (d, 1H, J = 15 Hz, H^D), 6.73 (d of d, 1H, J = 10, 15 Hz, H^C), 7.51 (d, 2H, J = 5Hz, H^B), 7.67 (d, 2H, J = 5 Hz, H^A)

(Polymer): ^{1}H NMR (D_2O, 500 MHz): δ 1.36 (s, 3H), 6.53 (s, 2H), 7.44 (s, 2H)

Broad peaks on the polymer spectra are denoted as singlets and integral values are taken to represent a single repeat unit.

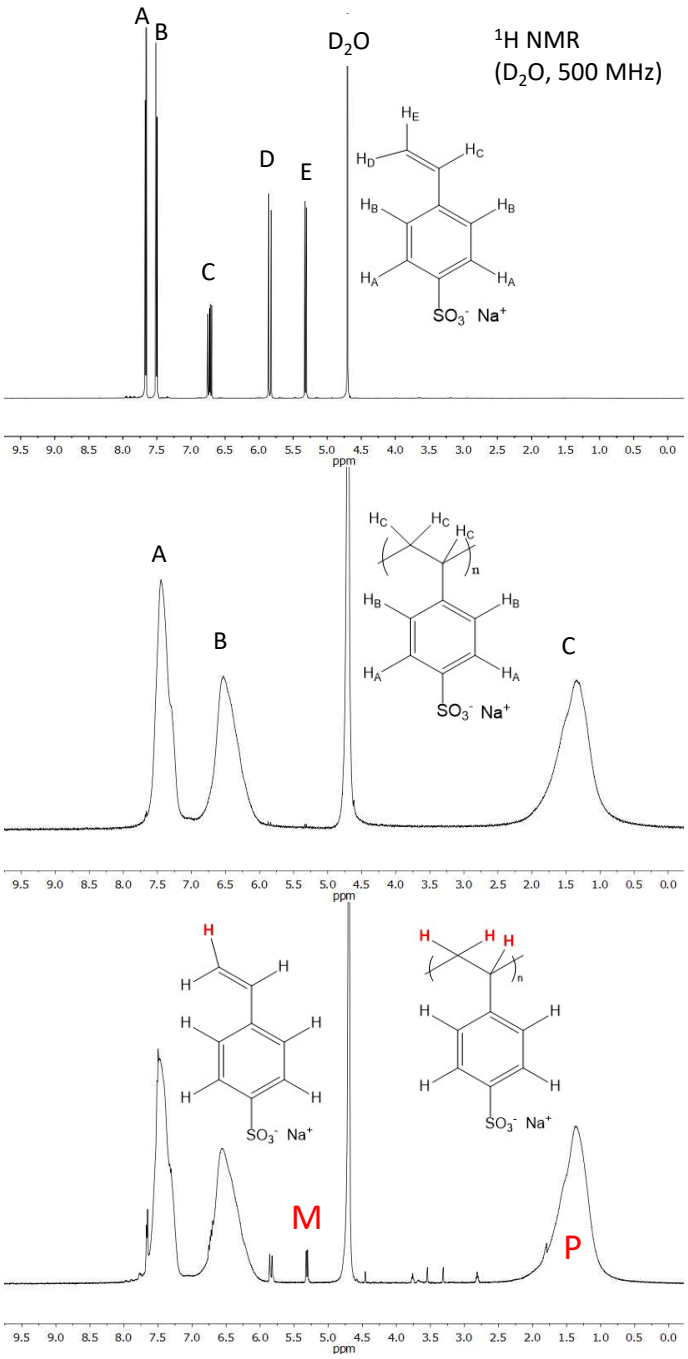

Figure 31. 1H NMR spectra of (A) sodium 4-vinylbenzenesulfonate monomer as obtained, (B) purified NaPSS and (C), crude NaPSS displaying how % conversion is taken as a ratio from the peak integral of three backbone polymer protons (P) to a single vinylic monomer proton (M).

2.3 Results and Discussion

The outset of the investigation into developing robust conditions to prepare NaPSS of high molecular weight and low dispersity focused on the effects of added halide salts, ligand: catalyst ratio, pH, and cosolvents. While each of these parameters has been shown to play a significant role in the radical polymerization of NaPSS and other aqueous monomers, a comprehensive evaluation of these variables has not been reported to date.

The appropriate choice of ligand and its concentration is critical to achieve both an acceptable reaction rate and control over the molecular weight distribution.[181] Bpy is a commercially available N-containing ligand suitable for aqueous conditions. It forms an active complex for ATRP yet remains stable toward disproportionation.[31, 169, 182] The Cu/bpy system has been previously reported for the synthesis of NaPSS,[159, 183] and has recently been shown to be a relatively stable active catalyst system in an aqueous environment.[184] A higher deactivation rate constant than expected results in narrow molecular weight distributions.[185-186] A slight molar excess of bpy has also been shown to exhibit molecular weight control for anionic monomers compared to other ligands commonly used in RDRP.[187]

Polymerizations were carried out with a fixed [M]/[I]/[bpy]/[CuCl] of [222]/[1]/[1.5]/[0.5]. The ratio of bpy ligand to copper was 3:1 to ensure a suitable excess. The target degree of polymerization of 222 (~46 000 $g \cdot mol^{-1}$) at 100% monomer conversion was selected as an appropriate benchmark for the study as it is a high molecular weight target for traditional RDRP systems. The reaction showed no visible signs of disproportionation, which would be indicated by coloration change to a green/blue solution or precipitation of a Cu(0) powder to the bottom of the reaction flask. Previously it was found that comproportionation dominates disproportionation when all Cu species are stabilized, i.e. when the

concentration of ligand exceeds that of copper,[188] and in our case we used an excess of bpy to Cu.

2.3.1 Effect of pH

Initial experiments showed that pH variation had a significant effect on the reaction viscosity. Under identical reaction conditions the solutions were adjusted to the pH ranges of 12-13 or 6-7. The contents of the pH 12-13 experiments appeared considerably more viscous after a short reaction time. An attempted polymerization in the pH 2-3 range did not permit complete initiator dissolution. ^{1}H NMR spectra showed that monomer conversion was considerably higher as a function of reaction time in the pH 12-13 experiment compared to the pH 6-7 experiment (Figure 32).

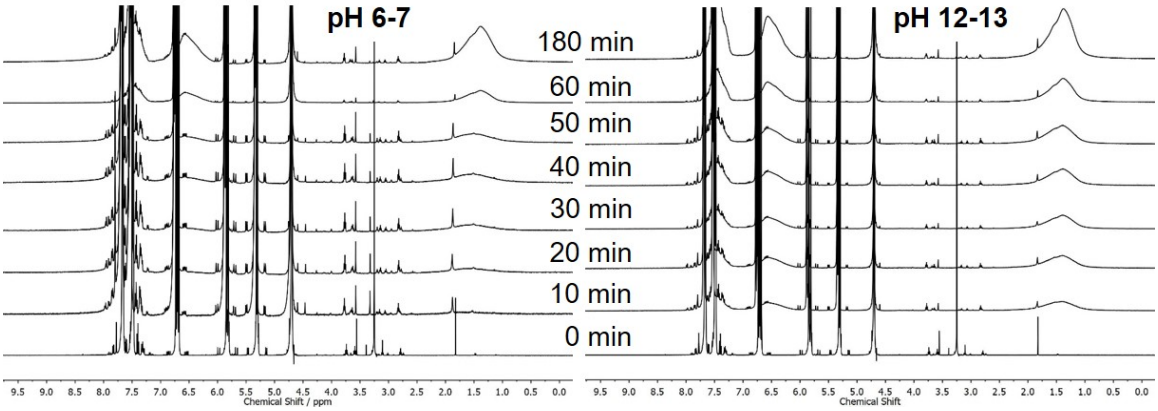

Figure 32. ^{1}H NMR spectra of NaPSS synthesized at different reaction pH as a function of reaction time.

The elution times and molar mass distributions were also significantly different at a 3 h reaction time for the pH 6-7 experiment (Figure 33A and C) compared to the pH 12-13 experiment (Figure 33B and D). The SEC-MALS data is reported as concentration (obtained from dRI and specific refractive index increment) vs molar mass plots by

combining raw data from two traces (concentration and molar mass from Figure 33) to provide a true representation of the molar mass distribution of each sample. The peak shape of these plots provides better visual representation of a molar mass distribution and dispersity compared to commonly presented chromatograms of the light scattering or refractive index trace.

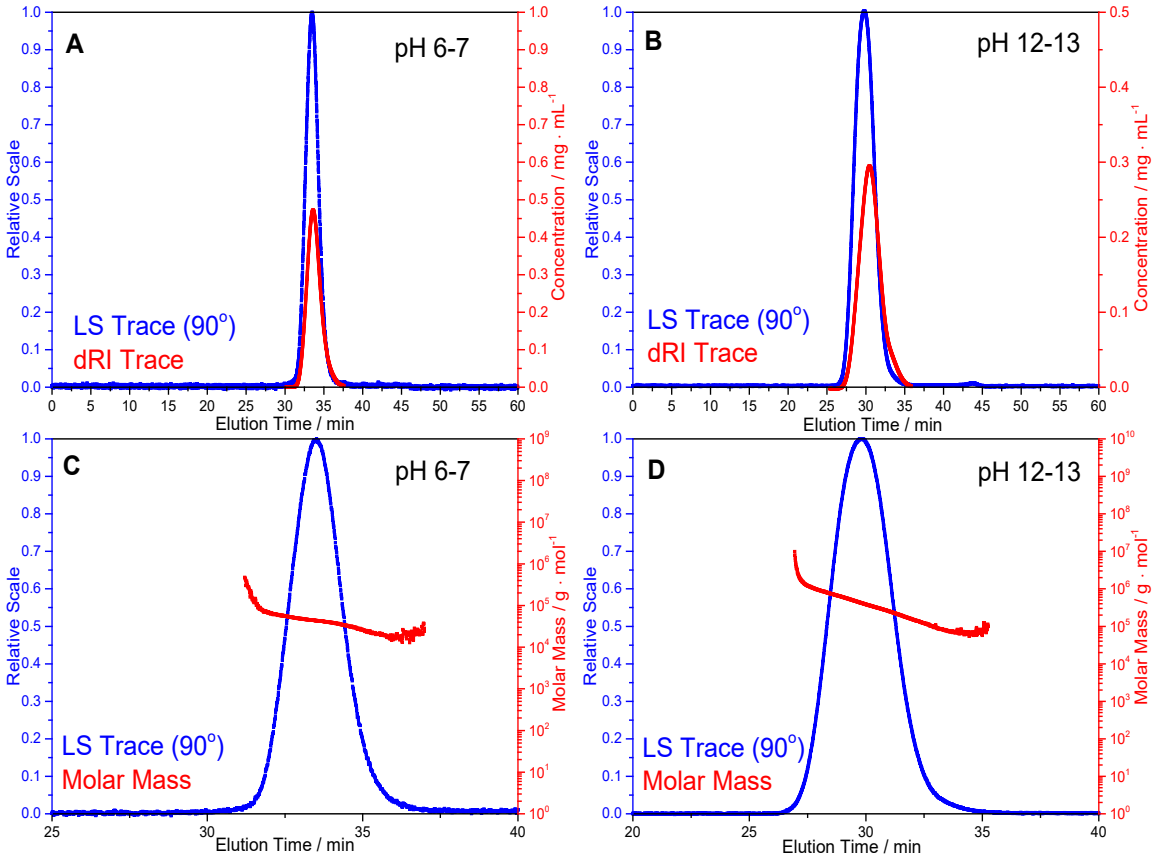

Figure 33. SEC-MALS chromatograms with overlaid concentration traces determined from the dRI detector and molar mass traces determined from the light scattering detector.

The variation in molar mass distributions, reaction rate and monomer conversion with time for the RDRP of NaPSS at reaction pH of 6-7 and 12-13 is shown in Figure 34. Experimental agreement with the targeted M_n is observed in the molar mass distribution

for reaction pH 6-7 but a near order-of-magnitude increase in the molar mass distribution is observed when the reaction pH is 12-13 (Figure 34A). Semi-logarithmic kinetic data, obtained by plotting $\ln([M]_0/[M]_t)$ vs time, where $[M]_t$ is the monomer concentration after a particular reaction time, showed the reaction rate at pH 12-13 was consistently 4-10 times higher than at pH 6-7 in all cases (Figure 34B). Linear first-order kinetic behavior was followed over a reaction time of 200 min at pH 6-7 (Figure 34B) with monomer conversion nearly reaching 80% over that time span (Figure 34C). By comparison, a deviation from linear first order kinetics is observed at pH 12-13 (Figure 34B) but complete monomer conversion (>98%) occurred after 200 min (Figure 34C). Furthermore, monomer conversion always exceeded 90% for reactions at pH 12-13, while at pH 6-7 monomer conversion did not reach that value at the same reaction time. A minimal increase in monomer conversion was observed when the pH 6-7 experiment was reacted to about 12 h. Evolution of number average molecular weight with monomer conversion showed a linear progression that extrapolated through the origin for the pH 6-7 experiment but the pH 12-13 experiment exhibited a degree of deviation from linearity (Figure 34D). There is a substantial pH-dependent difference in the growth of M_n with conversion and the dispersities are consistently lower under pH 6-7 reaction conditions (Figure 34D inset), but overall the pH 12-13 experiment shows low dispersities ($Đ$ <1.3) and a deviation from linear progression of M_n with conversion.

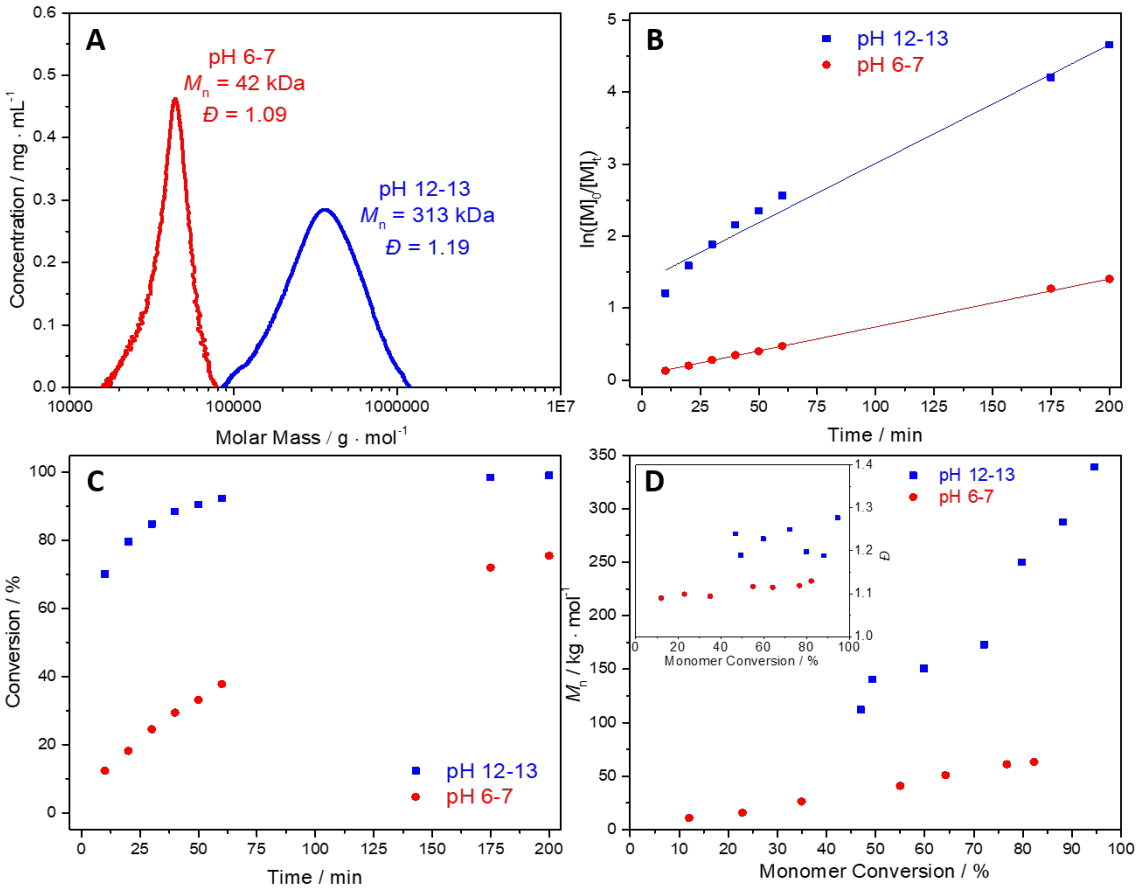

Figure 34. Concentration vs molar mass trace (A), semi-logarithmic kinetic data (B), monomer conversion with reaction time (C), and M_n vs conversion with inset of corresponding *Đ* for NaPSS synthesized at pH 12-13 and pH 6-7 as indicated (D).

Living polymerization conditions dictate that higher conversions lead to higher molecular weights which is only qualitatively consistent with the trend observed here. A 20% increase in monomer conversion does not account for such a significant increase in the molar mass distribution observed at basic pH. We hypothesize that a significant degree of reductive initiator coupling is occurring at high pH which effectively increases the monomer:initiator ratio. Raw data SEC-MALS traces support controlled reaction conditions under both pH ranges. Both the scattered light (90° detector) and dRI (converted to concentration via the specific refractive index increment) traces show monomodal distributions without any

indication of high or low molecular weight shoulders (Figure 33A and B). The molar mass traces across each scattering peak followed a slight linear decrease, indicative that no significant unwanted termination occurred and that the samples had a relatively low dispersity (Figure 33C and D).

The large deviation from the targeted M_n may point to pseudo living conditions under basic conditions, a result that aligns with previous reports stating that aqueous ATRP at high pH should be avoided;[175] nonetheless, when coupled with a relatively low dispersity we come to a result that conveniently provides a new method to produce NaPSS in a large range of molecular weights. This approach may lack obvious reaction control, but further experiments will demonstrate that useful polymers are attained reliably at high pH.

Depending on other reaction variables, the NaPSS produced had M_n values that were obtained in the range of around 20 – 60 kDa, and 200 – 400 kDa, for a reaction pH of 6-7 and 12-13, respectively. The high-pH products have molecular weights that are amongst the highest found in the field of RDRP that don't require specialized reaction conditions such as high pressure or heterogeneous conditions.[189-190]

2.3.2 Effect of MeOH

Addition of a less polar cosolvent to an aqueous ATRP system is a technique commonly used to slow reaction kinetics and increase reaction control.[160] Iddon et al. and Choi et al. separately and independently reported the synthesis of NaPSS in protic conditions via ATRP and showed that addition of MeOH gave the best control over the target molecular weight and $Đ$.[183] Here we explore the effect of added MeOH (as a volume percentage relative to the whole solvent volume) on the reaction kinetics, monomer conversion,

molecular weight distribution and dispersity. As expected, the reaction proceeded more slowly with increasing MeOH content as described by semi-logarithmic kinetic data, which was consistently linear for all MeOH compositions tested under pH 6-7 reaction conditions (Figure 35A). The effect of increasing MeOH composition at pH 12-13 did not lead to linear first-order kinetics but the reaction rate also decreased (Figure 36A). At 3 h reaction time the monomer conversion showed a decreasing trend as MeOH composition was increased from 0 to 41.5 % by volume. Monomer conversion decreased significantly, from about 80 to 45 %, and to a lesser extent, about 99 to 90 %, for a reaction pH of 6-7 and 12-13, respectively (Figure 35B). Little change in conversion occurred when reaction time was increased to 12 h. A clearly decreasing shift in the molecular weight was observed as MeOH composition was increased in the reaction, Figure 35C for pH 12-13 and Figure 36C for pH 6-7. Plotting M_n vs monomer conversion showed that reaction control was more evident at a higher MeOH composition of 27 compared to 0 (v/v %), due to the closer match between experimental and targeted M_n at higher monomer conversions (> 70%) and lower dispersity values found at the higher MeOH composition (Figure 35D).

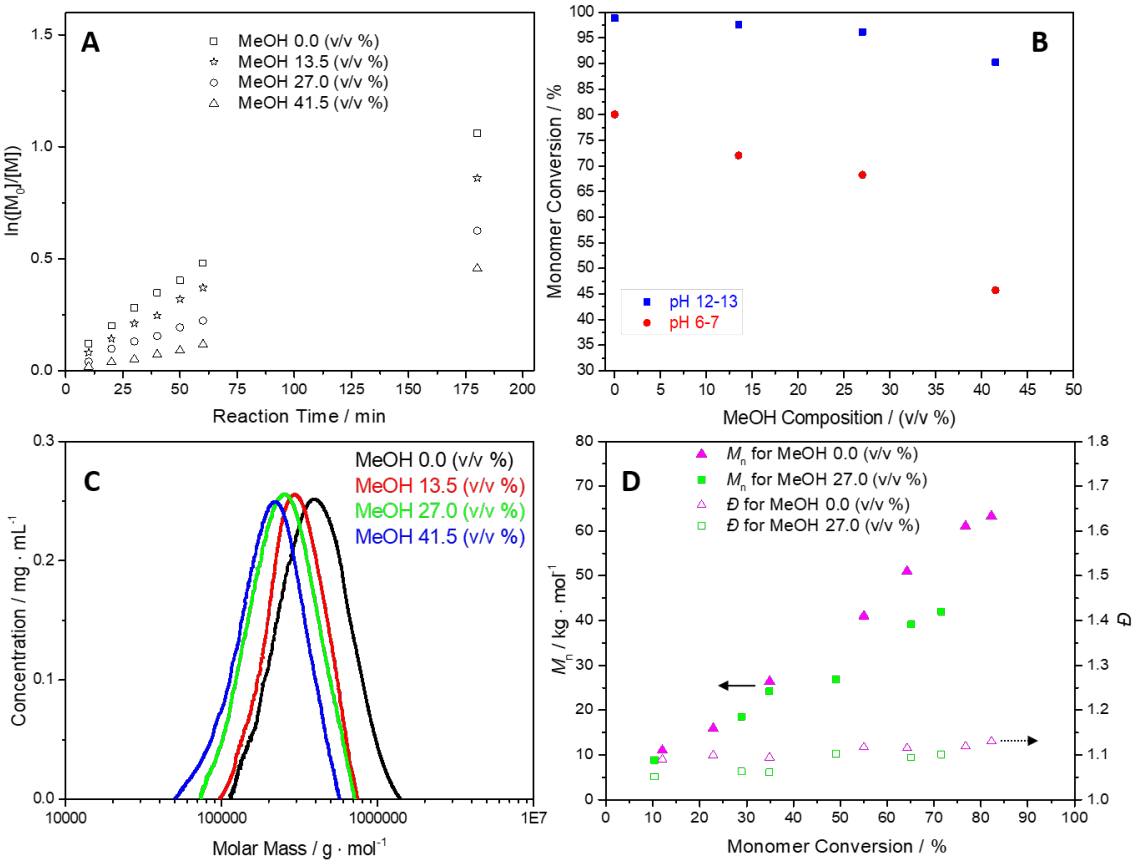

Figure 35. (A) The effect of cosolvent MeOH composition on reaction rate at pH 6-7, (B) effect of MeOH on monomer conversion and, (C) molecular weight distributions at pH 12-13 and, (D) effect of MeOH on *Đ* and the growth of M_n with monomer conversion for NaPSS synthesized at pH 6-7 pH 12-13.

The relationship between slowed reaction kinetics, as evidenced in Figure 35A and Figure 36A, and an increase in reaction control is further highlighted in Figure 36B and D. For both reaction pH ranges investigated the dispersity and measured M_n decrease somewhat with added MeOH. At higher reaction pH, although the theoretical M_n is not matched by the measured M_n, it is further approached, and the dispersity values also decrease as the MeOH composition is increased to 41.5 (v/v %) (Figure 36D). More reaction control is achieved with less added MeOH at a reaction pH of 6-7, as dispersity plateaus and measured M_n reasonably matches its theoretical value at a MeOH composition of 13.5%

by volume (Figure 36B). These findings confirm previous reports that witnessed greater reaction control in a mixed aqueous media.[157, 183]

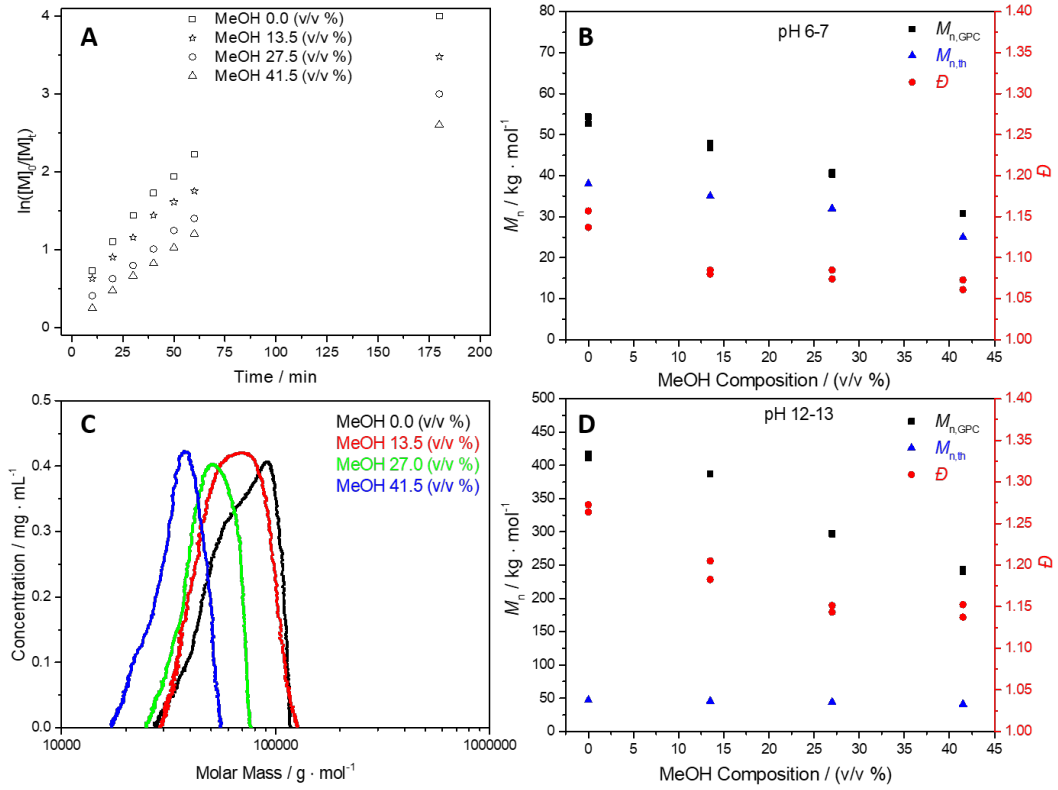

Figure 36. Semi-logarithmic kinetic plots for NaPSS synthesized at pH 12-13 with varying MeOH composition (A), effect of MeOH composition on M_n and $Đ$ (B and D), and molar mass distribution of NaPSS synthesized at pH 6-7 with varying MeOH composition (C).

2.3.3 Effect of NaCl

It has been shown that addition of external halide salts can improve the control over a polymerization as extra halide ions combat halide dissociation and increase the achievable range of molecular weights.[30, 191] Subsequently, NaCl was used as the halide source for all reactions and is reported as an equivalent concentration relative to the total copper

concentration ([NaCl]/[CuCl]). SEC-MALS measurements reveal that added salt had a lesser effect on the molecular weight distribution compared to MeOH or pH. Over a range of [NaCl]/[CuCl] values investigated, from 0.1 to 100 at both pH ranges, the highest M_n values observed after 3 h reaction time were at [NaCl]/[CuCl] values of 1-10 (Figure 37A). Increasing the external halide concentration from [NaCl]/[CuCl] = 0.1 to 10 produced well-defined polymers with $Đ$ = 1.16 and 1.07 for pH 12-13 and 6-7 respectively, but no significant reduction in dispersity was observed as [NaCl]/[CuCl] was further increased beyond 10 to 50 and 100 (Figure 37B), a result that points to moderate external halide concentrations being required to gain greater reaction control.

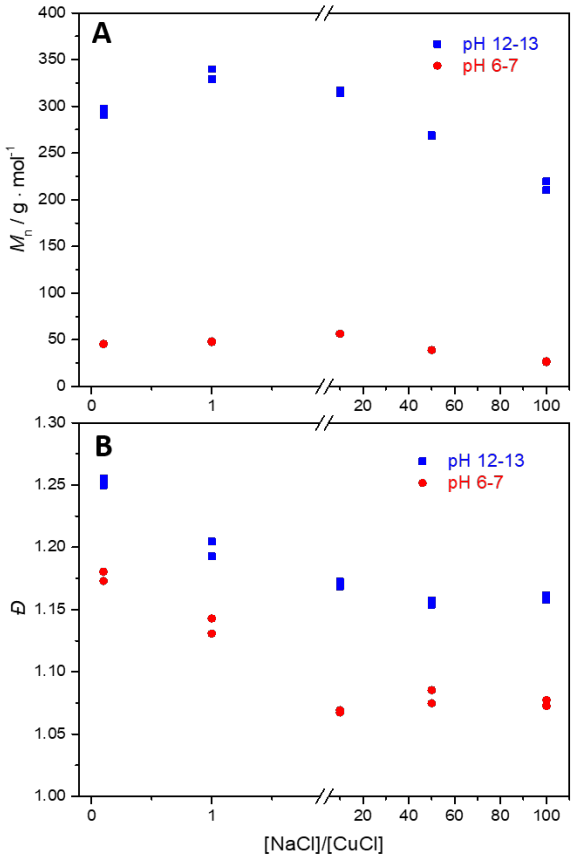

Figure 37. The effect of [NaCl]/[CuCl] on M_n (A), and $Đ$ (B) at two reaction pH ranges tested.

When the [NaCl]/[CuCl] ratio was lowered to 0.1 or raised to 50 or 100, M_n decreased in both pH regimes, a trend found to be in agreement with previous reports of the effect of NaCl concentration on molecular weight.[180] Reaction kinetics results also followed the trend between [NaCl]/[CuCl] and M_n (Figure 38), which is a result that is consistent with controlled radical polymerizations. The control over molecular weight appeared to depend on rate, as monomer conversion continued at higher NaCl concentrations when reaction times extended beyond 3 h.

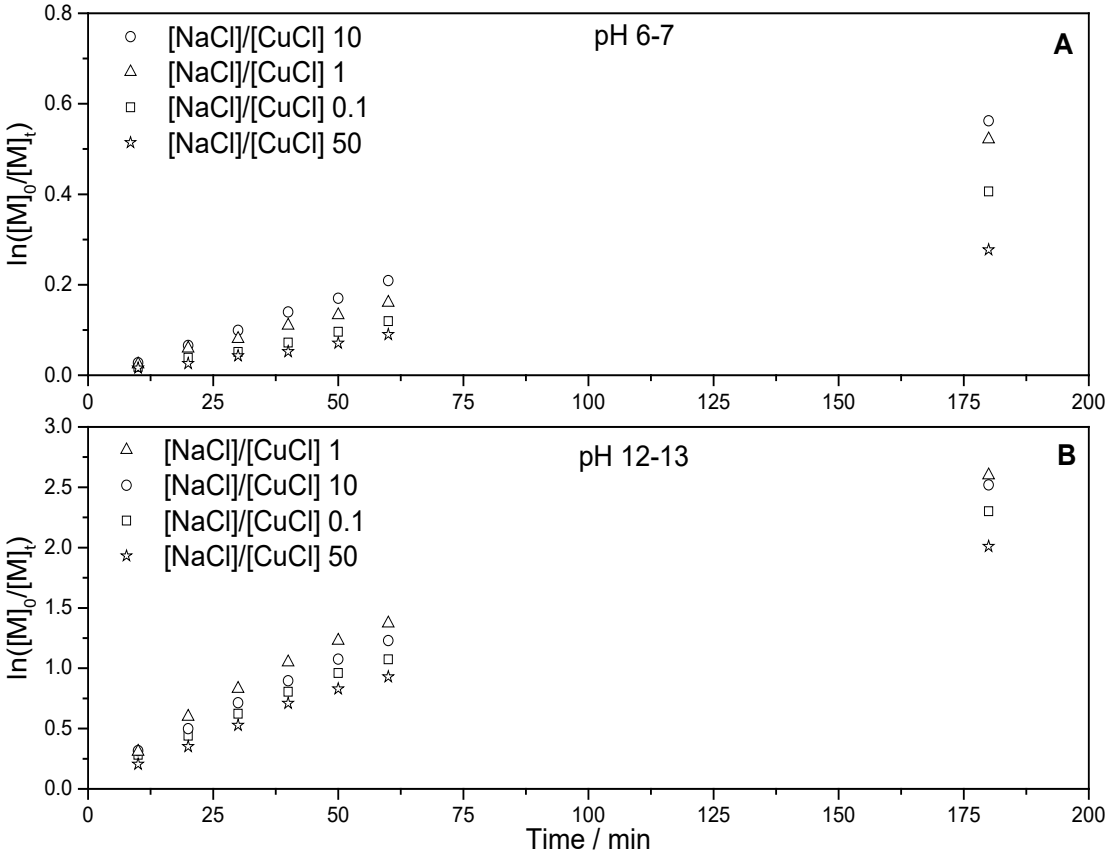

Figure 38. Semi log kinetic plots showing the effect of added NaCl on the reaction rate of NaPSS at pH 6-7 (top) and pH 12-13 (bottom).

We also found that reaction rate at the lowest salt concentration of [NaCl]/[CuCl] = 0.1 slowed again, which contradicts what has been previously observed.[180] This result could in part owe the nature of the ionic monomer used here.

Although we conducted the above studies by targeting a molecular weight of 46 000 g·mol^{-1}, it was our goal to attempt higher M:I ratios and to increase control and repeatability via optimization of reaction conditions. Instead, we discovered that the modulation of three reaction variables surprisingly resulted in the ability to target molecular weight. This unconventional parametric approach to synthesize a variety of molecular weight NaPSS materials is summarized in Figure 39. Variation of reaction conditions permitted the

synthesis of NaPSS from 22 000 to 372 000 g · mol^{-1} (summarized in Table 1), some of which are among the highest for an RDRP approach.

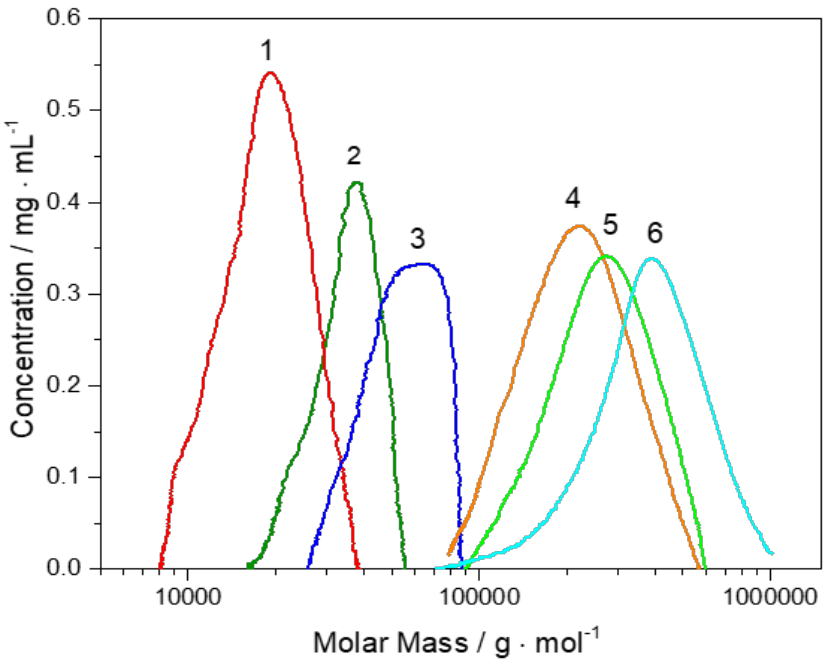

Figure 39. Concentration vs molar mass plots of NaPSS synthesized at varying pH, MeOH composition and NaCl concentration but with a fixed monomer to initiator ratio.

Table 1. Reaction conditions and physical data for each sample shown in the above figure.

Sample	pH	MeOH (v/v %)	NaCl ([NaCl]/[CuCl])	NaCl (mmol)	M_n kg · mol^{-1}	$Đ$
1	6-7	41.5	10	5.6	22	1.06
2	6-7	27	1	0.56	38	1.11
3	6-7	0	0.1	0.056	59	1.14
4	12-13	41.5	0.1	0.056	214	1.16
5	12-13	27	10	5.6	289	1.19
6	12-13	0	1	0.56	372	1.29

2.3.4 Reaction repeatability and chain end fidelity

In general, the activation and deactivation rates are hindered by the presence of a strong ligand. Because OH^- is a stronger ligand than Cl^-, the halide coordination site is occupied and Cu(II) will be present as $[Cu(II)L_m(OH)]^+$ rather than $[Cu(II)L_m(Cl)]^+$.[175] Experimentally we find the opposite is true. Instead of a slowed reaction rate we observe faster reaction kinetics under basic conditions. Mincheva, R. et al. reported an aqueous ATRP of the anionic monomer sodium 2-acrylamido-2-methylpropanesulfonate, which showed multimodal SEC traces and dispersity values ranging from 2.37 to 7.31 when reaction pH ranged from 8.5 to 12.[187] In addition, the reaction rate was faster at high pH with 100% monomer conversion at pH 12.0 compared to just 54% at pH 7.5. The authors acknowledged they could not fully explain this phenomenon, but suggested that the coordination of OH^- to Cu(II) lowered the deactivator concentration and led to a faster and more uncontrolled polymerization. While this trend between reaction pH and rate agrees

with our kinetic results, the reported molar mass data does not align with our observations because the SEC traces found here were monomodal and produced relatively low dispersity values in all cases ($Đ$ < 1.35). Reductive initiator coupling would have the effect of lowering the initiator concentration and thus increasing the theoretical M_n. As previously stated, it is not the goal of this work to delve into mechanistic details, yet some description is warranted as to why the dispersity is lower than comparable studies of RDRP done in aqueous media.[187, 192]

If dissociation of the halide from Cu(II) is sufficiently suppressed, the recombination and disproportionation termination events should theoretically be insignificant as is typical of a successful RDRP. Experimentally it has been found that many controlled radical polymerization processes attribute termination to occur by recombination and specifically by coupling of long chains with lower molecular weight radicals.[193-194] Coupling of already-long propagating chains is a plausible reason for the unexpectedly high molar mass seen at high pH, but a high dispersity would also be anticipated with these termination events. Carmean et al. reason that the high viscosities present in the aqueous RDRP synthesis of ultra-high molecular weight polymers reduce the probability of chain-chain interaction.[195] In the concentrated solution regime polymer chains become entangled leading to a significant reduction in translational diffusion while monomer diffusion remains fast.[196] As a result the probability of termination by chain coupling is reduced. We can determine the NaPSS reaction solution is in the entangled regime from a random coil model. The overlap concentration (C^*) from the semidilute to the entangled regime is defined as[197]:

$$C^* = 0.77/[\eta] \quad (54)$$

Having substantial molecular weight information, we can approximate the intrinsic viscosity $[\eta]$ from the Mark-Houwink relation:

$$[\eta] = KM^a \quad (55)$$

For NaPSS in a buffer of moderate ionic strength (0.3 M) at 25 °C, the Mark-Houwink parameters are approximately 0.2×10^{-3} mL·g^{-1} and 0.7 for K and a respectively[198-200]. For a polymer molecular weight of 1.5×10^5 g·mol^{-1}, which is at the low end of molar masses found under pH 12-13 reaction conditions, c^* occurs around 5 wt%, which is below the reaction concentration used here of 8 wt%. At high reaction pH the solution is in the entangled regime which could be cause for the lower than expected termination events and a relatively low dispersity. To further probe the possibility of chain coupling we conducted chain extension reactions to assess chain end fidelity.

Living chain end functionality at both neutral and basic pH conditions was confirmed by chain extension of the NaPSS homopolymer after addition of a deoxygenated monomer solution at 3 h reaction time. The experiments were designed to increase the targeted degree of polymerization from 222 to 272 (from ~46 000 to ~56 000 g·mol^{-1}). A clear increasing shift in molecular weight was observed for NaPSS synthesized under both pH ranges after chain extension, but the expected low dispersity and target M_n were only met under pH 6-7 reaction conditions (Figure 40A). The targeted M_n was not obtained for NaPSS synthesized at pH 12-13 after a chain extension reaction and the dispersity also increased from 1.26 to 1.44 but the molecular weight still increased. The higher dispersity indicates that transfer reactions could be taking place and thus a high degree of end group fidelity is

not present. This may be because additional monomer was added 3 h into each reaction vessel, at which point monomer conversion was at near completion for the pH 12-13, a time where there is a higher potential for chain end hydrolysis of the Cl atom. This issue has been identified previously for a copolymerization in aqueous media with additional halide salts.[191]

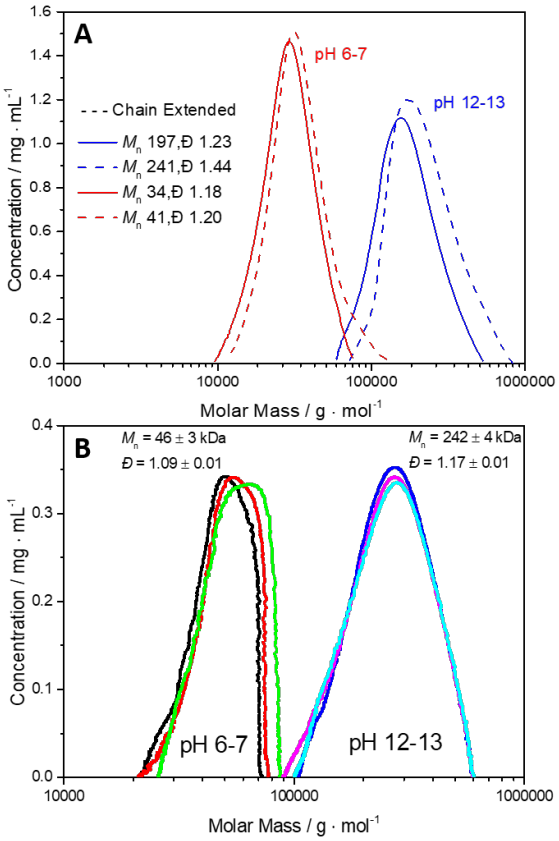

Figure 40. Chain extension of NaPSS under different pH ranges (A), and concentration vs molar mass traces from triplicate syntheses with repeated reaction conditions (B).

Evidence such as semi-logarithmic kinetic data and non-linear growth of M_n with monomer conversion points to a lack of reaction control at pH 12-13, but nevertheless we find excellent synthetic reproducibility present under these reaction conditions (Figure 40B). The six concentration versus molar mass traces shown represent two sets of triplicate

syntheses under the same conditions and reaction times (3 h). The only difference is the pH. The three traces at pH 6-7 show experimental agreement with the theoretical M_n of approximately 39 000 g · mol^{-1} at approximately 80% monomer conversion. When the reaction pH was 12-13 the almost 10× increase in the molar mass distributions was found to be consistent upon repeated syntheses, proving that high molecular weights could be reliably targeted. From a pragmatic perspective, the NaPSS product is obtained in gram scales, is perfectly sulfonated, can come in a wide range of molecular weights and low dispersities, and is well suited for further polyelectrolyte-based studies. Contrary to previous reports, this study finds that monomodal SEC-MALS traces along with reaction control, repeatability and relatively low dispersities are found under basic reaction conditions in aqueous media.[175, 187]

2.4 Conclusions

The most effective polymerization of NaPSS via aqueous RDRP to date has been performed. Synthesis of perfectly sulfonated NaPSS over a range of molecular weights in gram-scale quantities allows for broader applications in experimentally modelling polyelectrolyte systems with greater ease and accuracy. An unconventional approach to molecular weight control was achieved by parametric variation rather than changes in monomer to initiator ratio. Both pH and MeOH cosolvent affected the reaction rate and molecular weight of the NaPSS product, whereas NaCl concentration only affected dispersity. Variation of pH produced molecular weights ranging from approximately 1.5–4 × 10^5 g · mol^{-1} for the same monomer: initiator values, and dispersities remained low ($Đ$ < 1.3). Increasing MeOH slowed reaction kinetics, lowered molecular weight and dispersity, increased overall reaction control. Chain extension reactions confirmed the end

group fidelity for NaPSS synthesized at both neutral and basic pH, but significantly higher dispersities ensued at pH 12-13 conditions. In spite of evidence pointing to reduced reaction control at basic pH, triplicate synthesis proved the reaction was reproducible.

2.5 Acknowledgements

We would like to acknowledge Dr. Rafael Cueto for his guidance and training on polymer characterization, particularly SEC-MALS. This work made use of the equipment and resources of the NMR facility at Georgia Tech and the Polymer Analysis Laboratory at Louisiana State University. We are grateful for the contributions and expertise provided by Dr. Will Gutekunst in construction of a manuscript for this research project. We would like to acknowledge The Georgia Tech Hightower Family and STAMI for their support of this work.

CHAPTER 3. COMPARISON OF PERFECTLY SULFONATED NAPSS MADE FROM ATRP TO COMMERCIALLY OBTAINED NAPSS MADE FROM POST TREATMENT OF POLYSTYRENE

3.1 Introduction

3.1.1 Polyelectrolyte type and uses

NaPSS is a synthetic polyanion that in aqueous solution bears a fully charged sulfonate repeat unit balanced by a sodium counterion. NaPSS is widely regarded as a model polyelectrolyte, and it occupies a focal role in the fundamental and applied sciences of polyelectrolytes. NaPSS has a variety of applications such as multilayer polyelectrolyte membranes for controlled drug delivery,[11] medicines to treat abnormally high potassium or lithium levels in blood (hyperkalemia),[12, 33]_ENREF_129 ion-exchange resins for metal ion selectivity and separation,[13-*14*] cosmetics,[17, 32]_ENREF_131 proton exchange membranes for fuel cells,[18-19], flocculants,[15] and concrete additives[16]. It is used extensively in polyelectrolyte multilayers and complexes,[34-35] dopants for conducting polymers,[20-21] as well as a component in the PEDOT:PSS macromolecular salt mixture for a variety of applications such as flexible organic solar cells,[36] polymer electrolytic capacitors,[18-19] and organic light-emitting diodes.[37]

As a model polyelectrolyte, NaPSS has been used for fundamental experimental studies for several decades.[10] Polyelectrolyte properties understood at a fundamental level through the study of NaPSS include osmotic pressure,[22] chain conformation and counterion condensation,[23] multilayer swelling and uptake of free ions,[24] viscosity,[201-202]

electrophoretic mobility,[203] conductivity,[204] solvent interactions,[205] chain conformation,[206] and many other concentration-scaling properties.[23] The extensive interest and use of NaPSS for many of these applications is associated with two key factors: it is easily obtained from commercial sources, and it is available in a wide range of known molecular weights. Furthermore, NaPSS is a strong polyelectrolyte, remaining fully charged in solution over a broad pH range with every repeat unit considered to bear a charged anionic substituent. Despite these attributes, NaPSS is not without problems. For accurate experimental results the polymer must be perfectly and completely substituted with sulfonate groups, yet this is not always the case. Whether commercially obtained or synthesized in-house, NaPSS displays significant variations in purity, stated molecular weights and polydispersity.[28-29]

The most enigmatic phenomenon in the field of polyelectrolyte science is the "ordinary-extraordinary" behavior of diffusion of charged macromolecules,[100, 117] where the "slow mode" of polyelectrolyte dynamics as measured by DLS in low salt solutions has gained significant research interest.[145-146] The use of NaPSS as a model polyelectrolyte to better understand this problem has raised controversy due to the imperfect nature of most NaPSS samples.[109, 153] In particular, NaPSS is reported to have sulfonation levels that range from 85 to 99%, depending on its source.[28, 207] Imperfect sulfonation translates to chemical heterogeneity along the polymer chain whereby unsulfonated repeat units are essentially hydrophobic patches on the polymer that leave it prone to aggregation.[38] Regardless of the source, one cannot assume the purity of commercially available NaPSS, even calibration standards.

3.1.2 Commercial production of NaPSS

The reason for its use as a model polyelectrolyte to study the ordinary-extraordinary transition is that NaPSS is one of the few polyelectrolyte standards that is commercially available over a wide range of molecular weights with narrow dispersities. Limited availability of polyelectrolyte standards is due to an inability of the living anionic polymerization mechanism to link charged monomers.[208-209] Polymer standards prepared by anionic polymerization are derived from neutral monomers. In particular, NaPSS is typically prepared by post-treatment sulfonation of anionically polymerized styrene. The post-treatment methods have been categorized as either "hard' or "soft" as a way to distinguish between aggressive sulfonation reagents that yield higher sulfonation but more unwanted side reactions and mild reagents that produce lower degrees of sulfonation but with less impurities. Several "hard" sulfonation methods include treating PS with fuming sulfuric acid,[148, 210] chlorosulfonic acid,[150] or sulfur trioxide,[211] which can lead to degradation of the polymer through oxidation,[150] chain scission and sulfoxide crosslinks.[152] "Soft" methods include the use of sulfuric acid with a catalyst,[212-213] the use of sulfuric acid with phosphorous pentoxide,[214] acetyl sulfate,[149] sulfur trioxide,[151] and combining sulfur trioxide with triethyl phosphate.[215] These "soft" methods result in incomplete polymer sulfonation,[112] which leaves unwanted hydrophobic patches along the chain that lead to polymer aggregation in solution.[153] Regardless of treatment choice, the final polymer properties are compromised.

3.1.3 Progress toward ideal NaPSS

Literature reports often fail to mention the degree of sulfonation or the existence of side products. Even if they do, the most popular methods are elemental analysis and titration, both of which report the amount of sulfur present in a NaPSS sample but lack

information pertaining to the location of the atom on the polymer. These techniques cannot discern a perfectly sulfonated material from one with sulfur-containing impurities, such as sulfoxide crosslinks or sulfonation at the meta position. Coughlin et al. demonstrated significant progress in achieving complete PS sulfonation without chain degradation but at the expense of introducing a small degree of undesired meta-position ring substitution of the pendant sulfonate group.[29] It is known that incomplete sulfonation effects the measured physical properties of NaPSS solutions. For instance, Kim and Peiffer calculated the overlap concentration from viscosity measurements in DMF of polystyrenes sulfonated at a variety of levels.[216] They showed that the scaling of the overlap concentration with sulfonation level followed a slope value of -2 when C^*M^2 was plotted against the mole % of sulfonated monomer. The ideal polymer would carry a sulfonate charge in the para position of every styrene repeat unit (100% sulfonated) without any crosslinking or sulfonation on other parts of the polymer chain. These issues can be avoided by polymerization of NaPSS directly from pure 4-styrene sulfonate sodium salt monomer, but typical free radical methods result in much broader molecular weight distributions.

A synthetic method that avoids trivial and uninteresting causes of temporal aggregation, such as incomplete sulfonation, incomplete redissolution of polymer and incorporation of impurities, was implemented in the mid-2000s. Synthesis of "patchless" and never-dried NaPSS was achieved through radical polymerization of monomeric styrenesulfonate.[207] Direct polymerization was found to ensure 100 % sulfonation of the NaPSS polymer. Centrifugation with a Centricon YM-3 cell of molecular weight cutoff 3000 $g \cdot mol^{-1}$ removes unwanted smaller impurities and concentrates the NaPSS sample. This approach ensures that the polyelectrolyte sample is never dried and avoids forcing the

polyelectrolyte through small pore-sized filters to remove dust.[146] While this approach rules out many factors sometimes associated with temporal aggregate formation, it is limited due to the lack of synthetic control permissible by free radical polymer chemistry. Obtaining high molecular weights with narrow dispersities by free radical chemistry is achievable with the use of SEC fractionation. But even with preparative scale SEC, it would be difficult to obtain a gram of material at each specific molecular weights and dispersity. The development of controlled living radical polymerization techniques has enabled the synthesis of water soluble polymers with defined molecular weights and dispersities.

We previously reported a convenient synthesis of perfectly sulfonated NaP4SS, directly from para-functionalized styrene sulfonate monomer, and produced samples over a molecular weight range of approximately 20,000 – 400,000 $g \cdot mol^{-1}$ with relatively narrow dispersities, $Đ \approx 1.05–1.3$.[217] The availability of this perfectly sulfonated material warrants a re-investigation of select physical properties and a comparison to commercially obtained (C-NaPSS) samples. The commercial samples were chosen because they were used in recent fundamental PE studies,[117, 218-219] because they are available in sufficient quantities for lab-scale application, and because the PS sulfonation process was reasoned to be just as effective for these larger industrial batches as for NaPSS standards (which usually lack a specification for degree of sulfonation). In the present work we explore reliable avenues to characterize the completeness of sulfonation of both NaP4SS, prepared in-house, and C-NaPSS, purchased commercially. We assess the significance of NaPSS imperfections on solution and bulk properties, and provide the first reported case of how refractive index increments, partial specific volume, glass transition temperature and

decomposition temperature vary across a broad range of molecular weights for perfectly sulfonated NaPSS.

3.2 Experimental

3.2.1 Materials

_ENREF_217 A range of molar masses of completely sulfonated NaPSS was synthesized using an ATRP technique that has been previously described.[217] Polystyrene sulfonate with stated molecular weights of 70 kDa (Catalog # 243051, Lot # 0001445584) and 1000 kDa (Catalog # 434574, Lot # MKAA3419V) were purchased from Sigma Aldrich (St. Louis, MO). Polystyrene sulfonate with stated molecular weights 70 kDa (Catalog # 574, Lot # 510827022), 500 kDa (Catalog # 576) and 6000 kDa (Catalog # 575) were purchased from Scientific Polymer Products (SP^2) (Ontario, NY). Sodium chloride (NaCl) (>99.5%) and sodium azide (NaN_3) (>99.0%) were purchased from Sigma Aldrich (St. Louis, MO). Sodium nitrate ($NaNO_3$) (>99.0%) was purchased from J. T. Baker (Phillipsburg, NJ). Sodium phosphate monobasic (NaH_2PO_4) (99.9%) was purchased from Thermo Fisher Scientific (Waltham, MA). Hydrochloric acid standard solution 5 M (HCl) was obtained from Fluka Analytical (Munich, Germany). Deionized water (18 MΩ·cm) was drawn from a Millipore Milli-Q Type I source.

3.2.2 Preparation of NaPSS for testing

All NaPSS samples were dissolved in water and dialyzed using 3500 g/mol MWCO dialysis membrane tubing against pH 7 water with 1000 times the sample volume of

dialysis liquid used. Water was evaporated and the NaPSS powder was vacuum dried until no further mass reduction was measured.

3.2.3 FTIR Spectroscopy

FTIR spectroscopy was performed with a Thermo Scientific Nicolet iS5 instrument using an iD7 Attenuated Total Reflectance (ATR) accessory equipped with a diamond crystal. The instrument was controlled with Thermo Scientific OMNIC^{TM} software. Dried and ground powder samples were used with a constant pressure applied to the sample on the diamond crystal using a hand-tightened anvil. All FTIR spectra represent an average of 256 scans with a frequency resolution of 1 cm^{-1} and a frequency range of 4000 to 500 cm^{-1}.

3.2.4 Thermogravimetric Analysis Measurements

Thermogravimetric analysis (TGA) was performed using a PerkinElmer Pyris 1 Thermogravimetric Analyzer. Samples were pre-dried and ground into a powder before being oven-dried at 70 °C under vacuum for 12 h. Approximately 5-10 mg of sample was placed in an aluminum pan on the balance hook and tested in a flowing nitrogen gas environment. The TGA protocol was as follows: sample held for 10 min at the starting sample temperature of 30 °C, and then ramped at 10 °C·min^{-1} from 30 - 650 °C.

3.2.5 Size Exclusion Chromatography coupled Multi-Angle Light Scattering

The SEC-MALS system consisted of an Agilent 1260 infinity II with online degasser, an ISO pump and 1260 vialsampler connected to an Agilent PL aquagel-OH 8 µm guard column in front of two Agilent PL aquagel-OH Mixed-H 8 µm columns connected in series. The MALS system consisted of a Wyatt Dawn Heleos-II with a Wyatt Optilab T-rEX dRI

detector. Agilent OpenLab software was used to operate the SEC and data acquisition and analysis were done with Wyatt Astra 7.1 software. The mobile phase was a buffer solution of 0.3 M $NaNO_3$ + 0.01 M NaH_2PO_4 + 0.02% NaN_3 at pH 9. Polymer samples of concentration ~5 mg/mL were dissolved for 24 h prior to measurements to ensure complete dissolution. Solutions were filtered through Whatman Anotop 0.2 μm filters into Agilent 2 mL SEC vials. All chromatograms shown display the light scattering trace data taken from the 90° detector. Duplicate injections (100 μL) were performed for each sample measured by SEC-MALS and the resulting chromatography was found to be replicable in all cases.

A second system consisted of a Gastorr BG-34 degasser, an Agilent 1100 series pump with an Agilent 1100 auto injector connected to an Agilent PL aquagel-OH 8 μm guard column prior to two Agilent PL aquagel-OH Mixed-H 8 μm columns connected in series. The MALS system consisted of a Wyatt Dawn Heleos equipped with a single angle quasi-elastic light scattering (QELS) photometer, and a Wyatt Optilab rEX dRI detector, also operating at 658 nm. An Agilent 1100 series handheld control module was used to operate the SEC and data acquisition and analysis were done with Wyatt Astra 6.1 software. The mobile phase was 0.3 M $NaNO_3$ + 0.01 M NaH_2PO_4 + 0.02% NaN_3 at pH 9.

3.2.6 Differential Refractometer

Calculation of the specific refractive index increment ($\delta n/\delta c$) for light scattering was conducted using a divided cell differential refractometer equipped with a helium lamp and four filter lenses (C. N. Wood). The instrument was calibrated using dried KCl solutions. NaP4SS and C-NaPSS samples were vacuum dried, weighed, and then dialyzed against Millipore water at pH 7 or an aqueous solution of 0.3 M $NaNO_3$ + 0.01 M NaH_2PO_4 +

0.02% NaN_3 at pH 9. Polymer concentrations that ranged from approximately 0.1 - 10 mg/mL were measured at 25 ± 1 °C at four different wavelengths (488.0, 514.5, 589.0 and 632.8 nm) in order to develop Cauchy style plots.

3.2.7 NMR

Both ^1H and ^{13}C experiments and data analysis were conducted on a Bruker Avance IIIHD 700 MHz instrument and the Bruker TopSpin 3.5 NMR program. ^1H and ^{13}C NMR data collected was obtained with 700 MHz field strength, probe temperate of 297 K and with a residual internal standard H_2O (δ 4.70). Both ^1H and ^{13}C spectra were recorded in D_2O at concentrations of approximately 50 mg/mL. Quantitative integration of ^1H spectra was performed following a T_1 relaxation experiment to determine the appropriate pulse delay (D1). Setting D1 to five times T_1 in all cases gives >95% integration accuracy. The largest T_1 measured was 5.074 s and thus D1 was set to 25 s for all subsequent ^1H NMR experiments. The ^{13}C spectra were measured using a 90° pulse and a delay of 2 s. At least 8000 scans were averaged.

3.2.8 Differential Scanning Calorimetry

To assess the glass transition temperature (T_g) of the samples, differential scanning calorimetry (DSC) was performed using a TA Instruments Discovery DSC with aluminum Tzero Hermetic Pans in a flowing nitrogen gas environment. Vacuum dried samples of mass 2-4 mg in powder form were tested. Samples were equilibrated at 30 °C for 5 minutes before being heated to 420 °C at a rate of 10 °C/min, held at 420 °C for 5 minutes, cooled to -70 °C at a rate of 5 °C/min, held at -70 °C for 5 minutes, then heated to 420 °C at a rate of 5 °C/min. The first heating profile was used to eliminate any thermal history from the

sample and T_g was calculated from second heating step using the TA instruments Trios version 4.5 analysis software.

3.2.9 Partial Specific Volume

Partial specific volume values were calculated from density measurements obtained from an Anton-Paar 5000M Density and Sound Velocity Meter. The instrument determines density from the high frequency oscillations of a solution-filled U-shaped tube. Samples were dialyzed extensively in water then dried under vacuum before being carefully dissolved to desired concentrations in aqueous solutions for 24 hours. Density measurements accurate to six significant figures were recorded at 20 °C (±0.1 °C). High precision densitometry measurements were conducted on NaP4SS and C-NaPSS in both water and increasing concentrations of NaCl solution.

3.3 Results and Discussion

3.3.1 Characterization of NaPSS via FTIR

The FT-IR spectra of C-NaPSS and NaP4SS are compared in Figure 41A and B, respectively. Complete absorption band assignments for many different hydrated and salt forms of PSS can be found in the literature.[220] The OH stretching vibration of H_2O in the frequency region of 3700 – 3000 cm^{-1} and H_2O scissor vibration around 1650 cm^{-1} were clearly evident in both sets of spectra across all molecular weights. The characteristic SO_3^- group antisymmetric and symmetric vibrational absorption peaks are located at 1178 and 1037 cm^{-1}, respectively, while the in-plane skeletal vibration and in-plane bending vibration of the benzene ring are assigned to peaks located at 1125 and 1008 cm^{-1},

respectively.[220] Comparison of NaP4SS and C-NaPSS spectra reveals minor differences, which have been previously recorded for a range of partially- to fully-sulfonated NaPSS spectra.[221]

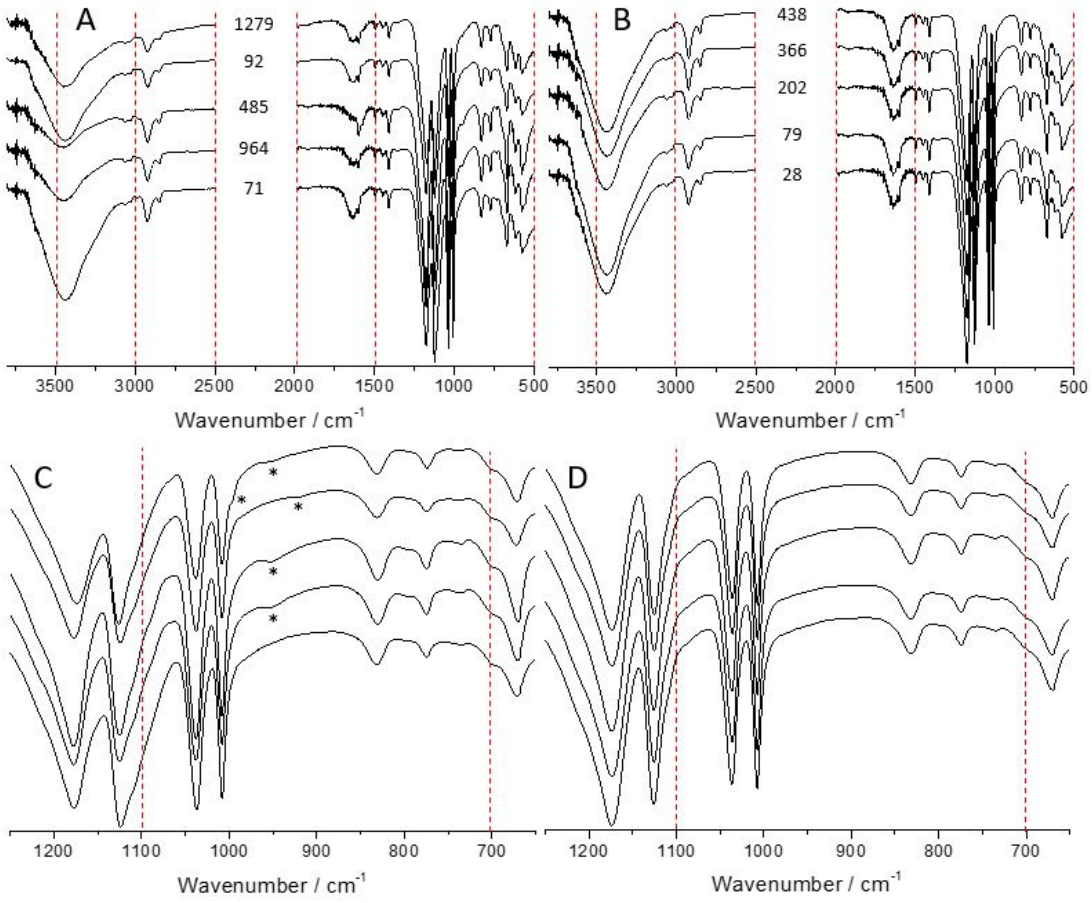

Figure 41. FT-IR spectra of (A) C-NaPSS and, (B) NaP4SS of varying molecular weights, along with the observed discrepancies (starred) between the spectra in the wavelength range from 1100 to 700 cm^{-1} for (C) C-NaPSS and (D) NaP4SS, respectively.

Yang et al. noted that a sample with 50% degree of sulfonation displays a very similar FT-IR spectrum to a 100% sulfonated material rather than an intermediate spectrum between NaPSS and PS. Overlaid NaP4SS and C-NaPSS spectra normalized to the characteristic SO_3^- band at 1178 cm^{-1} show that the peak is more intense for all NaP4SS compared to C-

NaPSS, indicating a greater sulfonate content (Figure 42A). In addition, the characteristic 1125 cm^{-1} band was broadened toward lower wavenumbers for all C-NaPSS samples compared to NaP4SS. This may be a convoluted peak due to the appearance of a peak at 1097 cm^{-1} which has been noted to appear when syndiotactic PS is sulfonated and could indicate a degree of incomplete sulfonation.[222] Other differences were highlighted by spectral bands occurring at 950, 699 and 620 cm^{-1} for C-NaPSS but were absent on NaP4SS spectra (Figure 41C and D). There is a correlation between the peak intensity and sulfonation degree where a lower sulfonation degree causes a greater band intensity at 699 cm^{-1},[222] and the peak shoulders observed were of greater intensity for all the C-NaPSS spectra compared to the NaP4SS spectra (Figure 42B). Tangents to these shoulder peaks are drawn to guide the eye (Figure 42C and D).

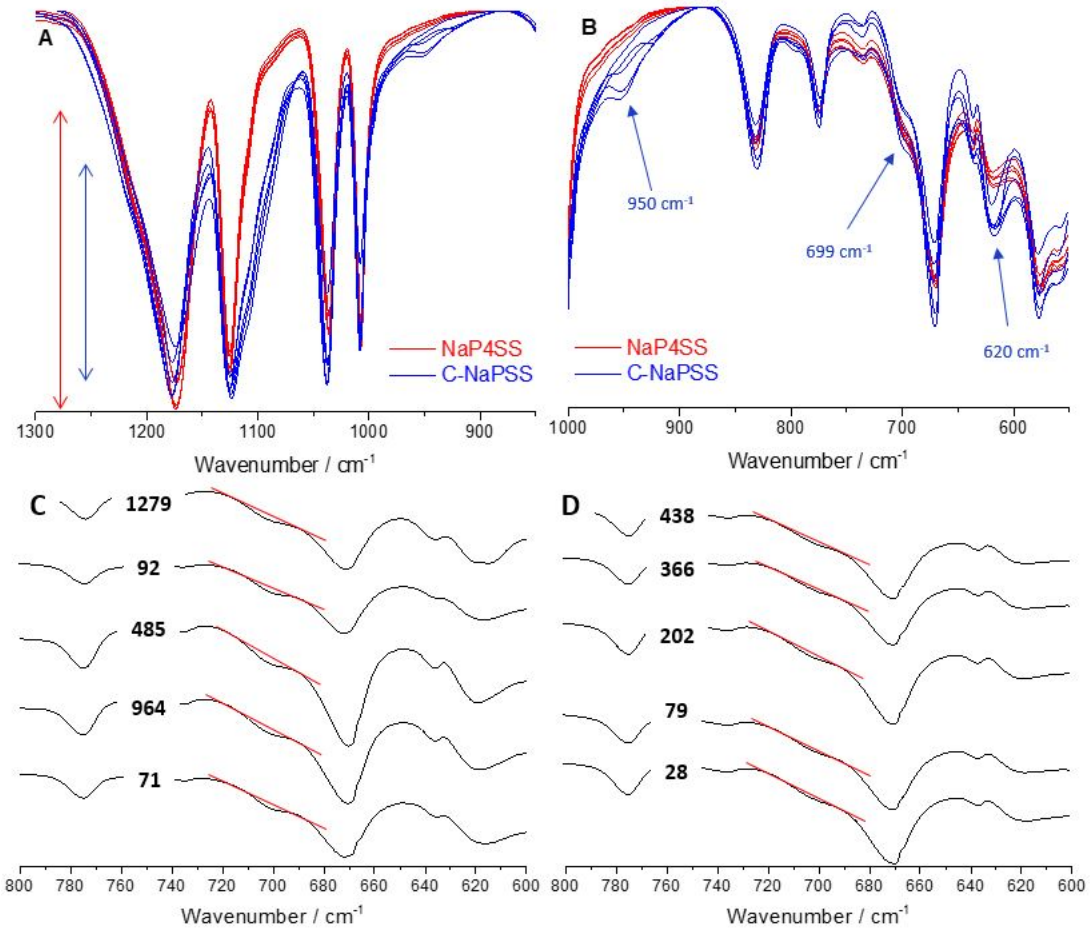

Figure 42. (A) Characteristic SO_3^- group observed by the peak at 1178 cm^{-1} is more intense for NaP4SS than C-NaPSS, arrows show qualitatively average peak high difference, (B) spectral bands at 950, 699 and 620 cm^{-1} only found for C-NaPSS. Spectra in (A) and (B) are normalized at 880 cm^{-1} to highlight intensity differences. (C) Shoulder peak at 699 cm^{-1} for C-NaPSS, not seen for (D) NaP4SS, spectra are offset for clarity and numbers indicate sample molecular weight in kDa.

3.3.2 Characterization of NaPSS via NMR

NMR spectroscopy has proven particularly useful in the investigation of varying degrees of sulfonation of PS and related polymers.[29, 223] Both ^1H and ^{13}C NMR spectroscopies were used to detect differences between NaP4SS and C-NaPSS in regards to potential incomplete and nonspecific sulfonation as well as other potential side products. C-NaPSS

spectra displayed signals that disappeared following sufficient dialysis with 3500 g/mol MWCO tubing, identifying their source as non-covalent impurities (Figure 43).

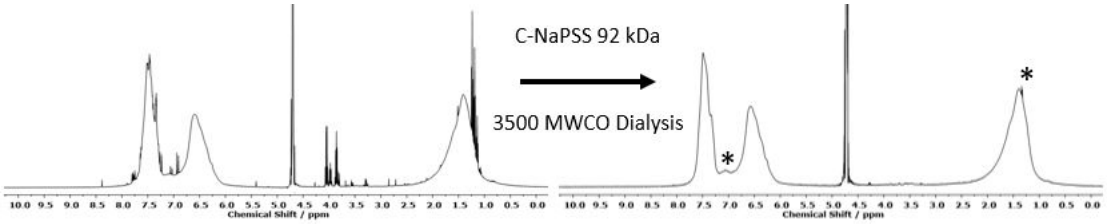

Figure 43. Proton NMR spectra showing dialysis purification with 3500 g/mol MWCO tubing of C-NaPSS samples exhibiting the impurity peaks that are chemically bound to the polymer structure.

3.3.2.1 Determination of degree of sulfonation by ^{1}H NMR

Samples for NMR were prepared by dissolving 10 mg dried crude NaP4SS in D_2O. The percent of non-sulfonated repeat units was calculated according to:

$$\%\, para\ protons\ = \frac{3H_p}{H_b} \times\ 100 \tag{56}$$

where H_p and H_b are the integrals of the para protons and backbone proton peaks respectively, which are designated in Figure 44. To calculate the % of non-sulfonated repeat units the three polymer backbone protons on each NaPSS repeat unit, represented by a large broad peak on the spectra from around 0.5–2.5 ppm, are compared to a single para benzylic proton, shown at 7.02 ppm. The integral of the broad polymer peak is calculated relative to the normalized monomer peak which represents a known single proton. The equivalent proton ratios being represented by each peak are 1:3 for backbone:para proton. The peak at 7.02 ppm is not baseline resolved which introduces error into the calculation. To minimize this error the integral value from the same region on a spectra for NaP4SS, which does not display a peak at 7.02 ppm and is also not

completely baseline resolved between the two large peaks at 6.53 and 7.44 ppm, is subtracted from the C-NaPSS H_p integral value. Brukers TopSpin3.5 software has a peak deconvolution tool which produced similar integral values for the 7.02 ppm C-NaPSS peak to what was achieved when it was subtracted with the NaP4SS integral.

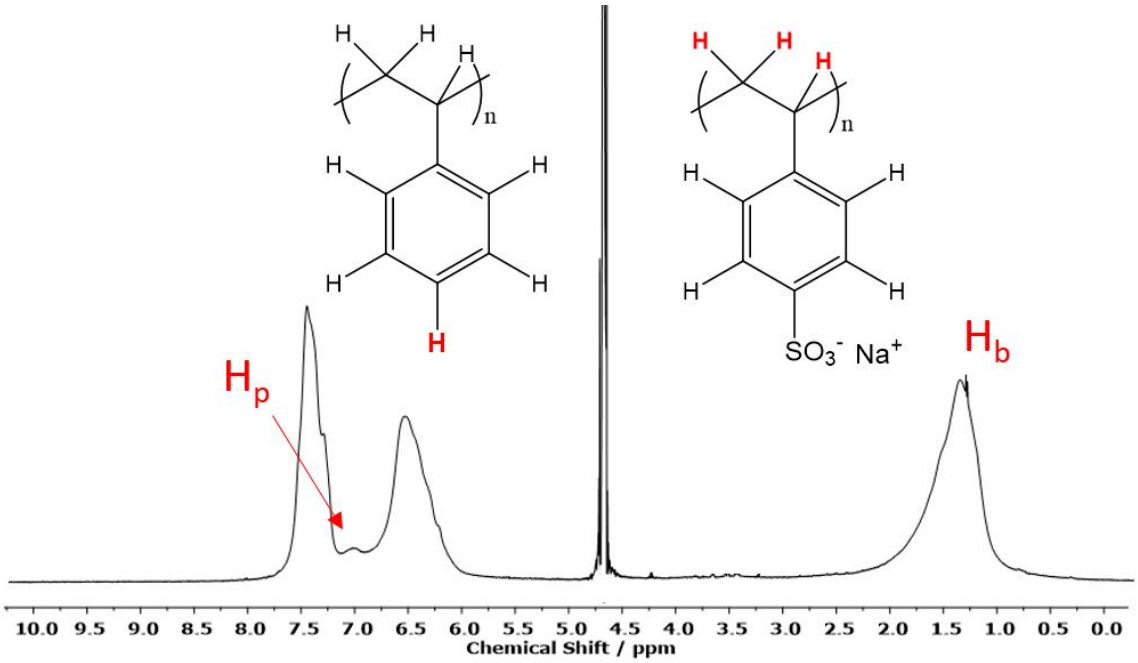

Figure 44. ^{1}H NMR spectra of C-NaPSS displaying how % non-sulfonated repeat units are calculated from the ratio of benzylic para proton peak integral (H_p) to the three backbone polymer protons (H_b).

(Monomer): ^{1}H NMR (D_2O, 500 MHz): δ 5.32 (d, 1H, J = 10 Hz, H^E), 5.83 (d, 1H, J = 15 Hz, H^D), 6.73 (d of d, 1H, J = 10, 15 Hz, H^C), 7.51 (d, 2H, J = 5Hz, H^B), 7.67 (d, 2H, J = 5 Hz, H^A)

(Polymer): ^{1}H NMR (D_2O, 500 MHz): δ 1.36 (s, 3H), 6.53 (s, 2H), 7.44 (s, 2H)

To differentiate impurities from potential starting monomer, spectra for NaP4SS monomer, partially converted NaP4SS reaction product, and post dialysis/purified NaP4SS are also provided (Figure 45).

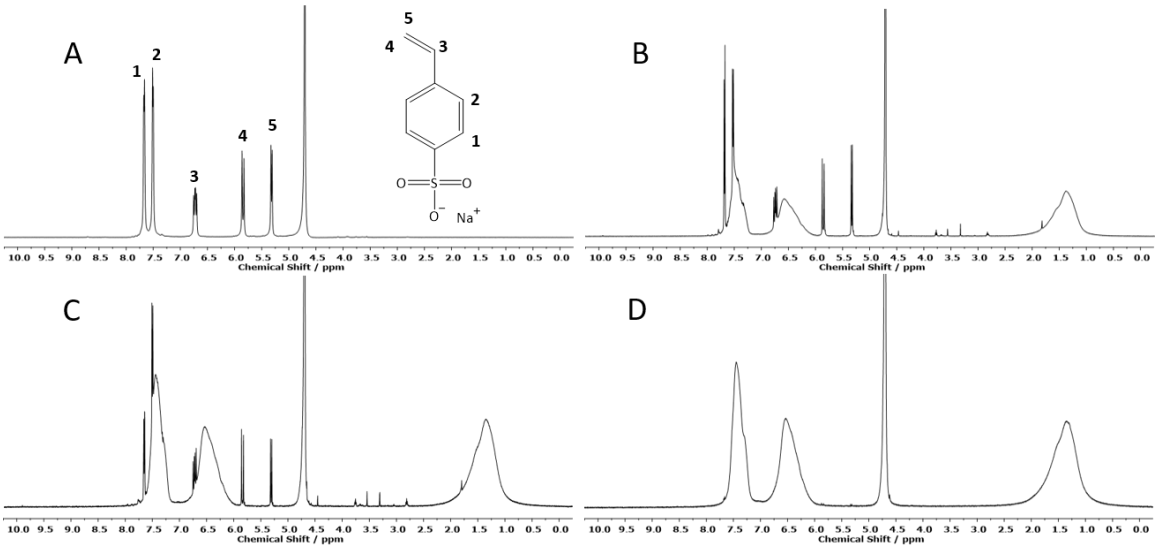

Figure 45. Proton NMR spectra of, (A) 4-styrene sulfonate monomer, (B) both monomer and polymer peaks during the course of polymerization and, (C) unpurified NaP4SS obtained post-polymerization, and (D) NaP4SS after purification by dialysis.

Minor discrepancies were observed in the ^{1}H NMR spectra for the C-NaPSS samples compared to NaP4SS spectra. Three large and broad signals centered at 7.45, 6.55 and 1.35 ppm were observed in all spectra, which corresponded to protons labeled 2, 3, and 5 and 6, respectively, on the NaPSS repeat unit (Figure 46A). Focusing on the peak regions from 8-6 ppm and 2.5-0.5 ppm revealed pronounced shoulders on all C-NaPSS spectra at 7.32, 6.30 and 6.24 ppm and, in some instances, small sharp signals around 1.24 and 1.11 ppm. These were not observed for NaP4SS, or at least not as pronounced, as shown on the bottommost spectra. Sulfonation leading to unwanted side reactions or differences in PS stereoregularity could be indicated by such signals.[224] In addition, the consistent

appearance of a small, broad peak at 7.02 ppm, convoluted by the presence of the larger two aryl resonances, was found in all of the C-NaPSS spectra. This signal represents the para proton aryl resonance of a PS spectrum, thus providing evidence for incomplete sulfonation.[29, 225] While baseline resolution between the large, broad aryl signals attributed to the ortho and meta protons was not achieved, quantitative integration of the small broad peak at 7.02 ppm provided an estimate of the amount of repeat units with para proton signals (calculations using above equation). It was assumed there was no substitution of backbone protons as a result of any post-treatment process. As such, the broad peak at 2.5-0.5 ppm, corresponding to the three backbone protons on the repeat unit, was set to a relative intensity of 1 (Figure 44). Peak integral values for the 7.02 ppm signal corresponding to the para proton composition were computed to range from 6 to 11.1 ± 1% across the C-NaPSS samples (Figure 46B). To account for a lack of baselines resolution between the peaks at 7.45 and 6.55 ppm, the equivalent ppm region on a NaP4SS spectra, where no 7.02 ppm peak was observed, was also integrated to provide an error estimate. A value equivalent to approximately 1% of non-sulfonated repeat units was calculated. ^{1}H NMR analysis indicates that the C-NaPSS samples were not completely sulfonated and there is a possibility that sulfonate groups exist on either the meta or ortho aryl ring positions.

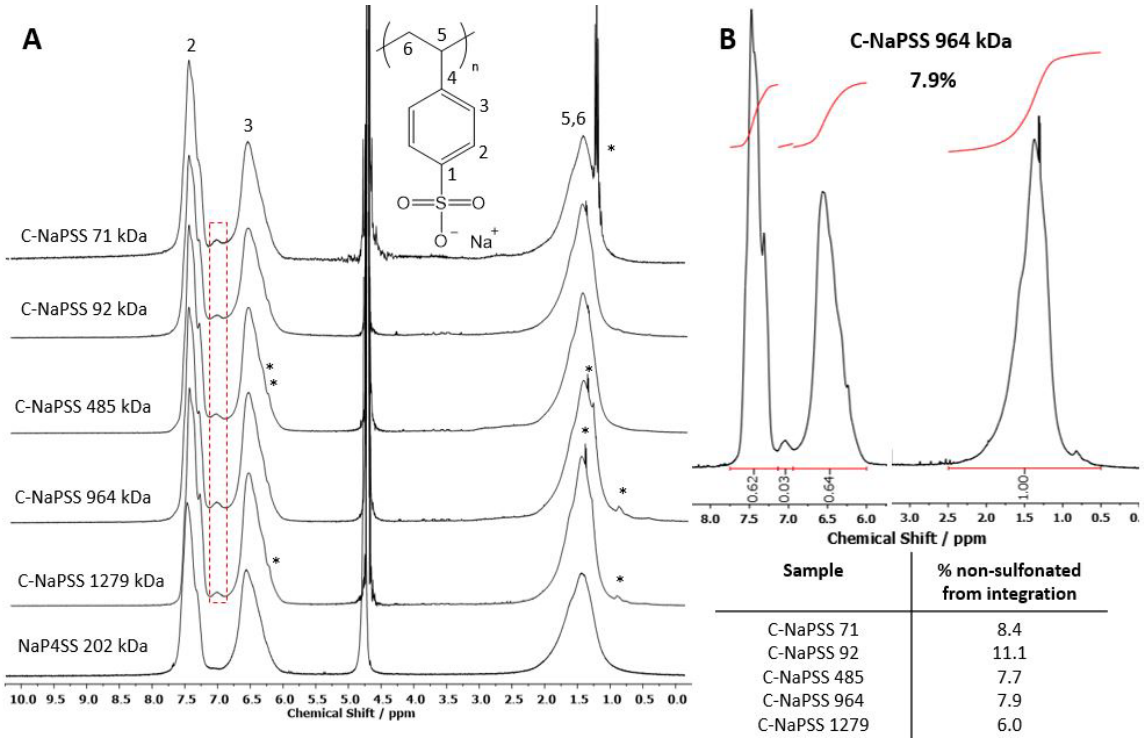

Figure 46. (A) Stacked ^{1}H NMR spectra highlighting impurity peaks (starred) associated with C-NaPSS compared to NaP4SS; and, (B) integration of peak observed at 7.02 ppm for C-NaPSS 1279 representing the % degree of non-sulfonated repeat units and also included calculations for other C-NaPSS samples.

The ^{13}C resonances for 4-styrene sulfonate monomer to make NaP4SS (Figure 47), along with resonances for NaP4SS and C-NaPSS, matched expected and previously observed data.[226-228]

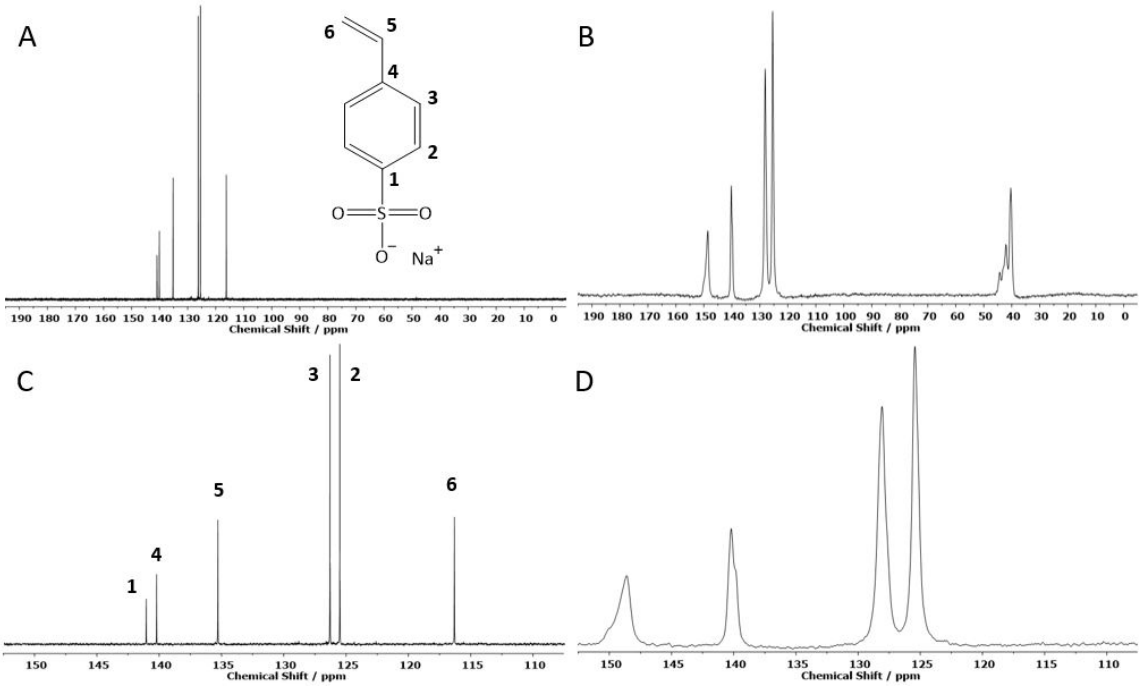

Figure 47. Carbon spectra of 4-styrene sulfonate monomer in (A) and (C). Carbon spectra for NaP4SS in (B) and (D).

Peaks at 148.6, 140.2, 128.1 and 125.5 ppm corresponded to carbons 1, 4, 3 and 2, respectively, on the NaPSS repeat unit, and a broad multiplet at 46-38 ppm was observed which corresponded to carbons 5 and 6 (Figure 48).

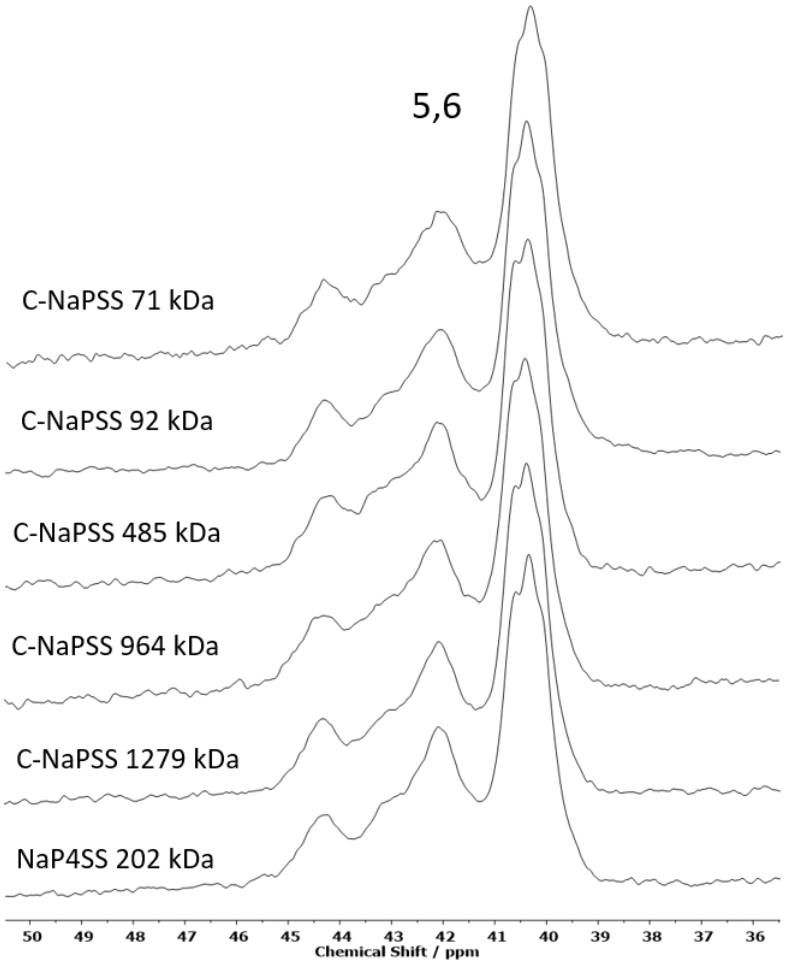

Figure 48. Stacked carbon spectra of the peaks assigned to the polymer backbone.

Coughlin et al. performed an in-depth study of the sulfonation kinetics of PS, and revealed through ^{13}C analysis, with a comparison to polymerized NaP4SS, that sulfonated PS was essentially 100% sulfonated but contained extra spectral peaks that quantitatively totaled to 6% of SO_3^- groups being in the meta position.[29] We also observed these same several small additional peaks in many of C-NaPSS spectra that accounted for meta SO_3^- groups. A small, broad peak at 146 ppm, one at 142.5 ppm, and peaks at 130 and 123 ppm (Figure 49). These signals confirm the results obtained by Coughlin et al. and show that post-treatment sulfonation processes are not regiospecific, in addition to being incomplete.

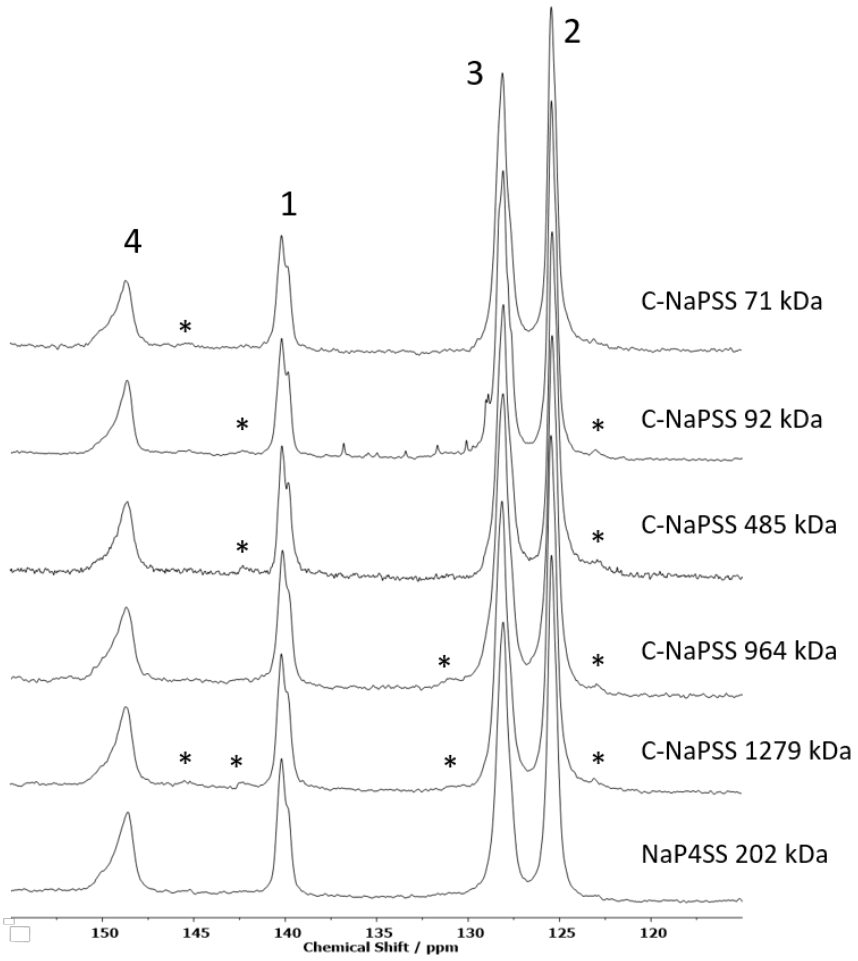

Figure 49. Stacked ^{13}C spectra confirming the presence of small shoulders on all C-NaPSS materials indicating meta-substitution of sulfonate groups; such signals were not observed for NaP4SS. Points of special interest are starred (see text).

3.3.3 Solution Properties of NaPSS

With evidence suggesting ample differences between the chemical structure of NaP4SS and NaPSS produced by the post-treatment sulfonation methods typically used by most commercial vendors, there is a need to revisit and re-measure some physical constants for NaP4SS in solution.

3.3.3.1 Specific refractive index increment

Deviation of light through the split cell of the refractometer, solvent on one and solution on the other side, was measured as a function of the polymer concentration, and the value of the non-weighted linear least squares fit to the plotted data equal to $\delta n/\delta c$ (Figure 50A). Measurements at the four different wavelengths enabled Cauchy plots to be developed, thus providing $\delta n/\delta c$ values across the visible spectrum (Figure 50B).

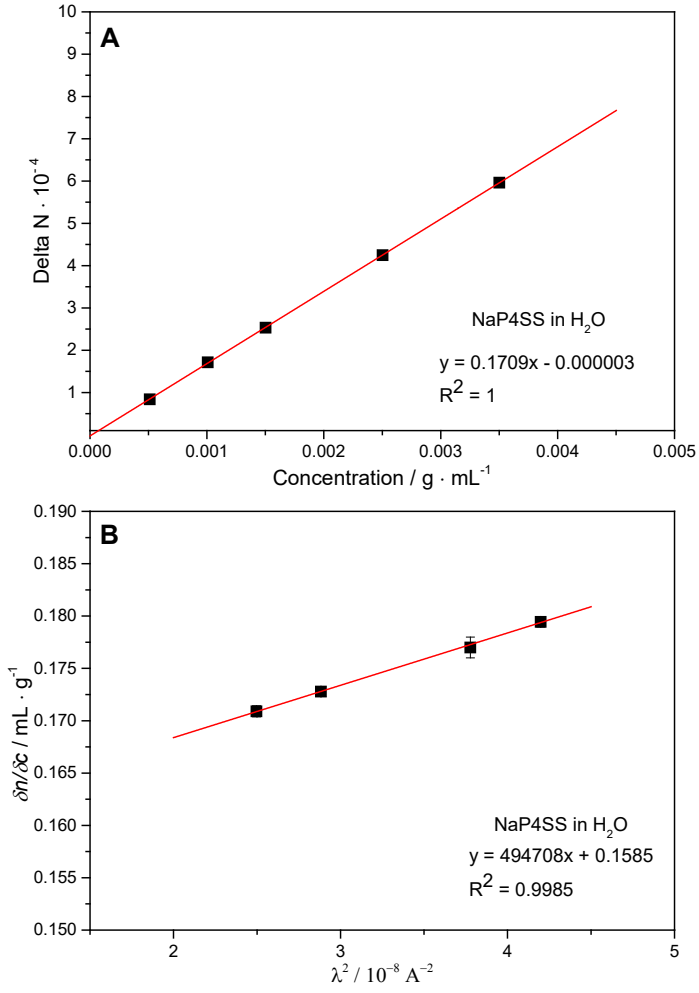

Figure 50. (A) Determination of specific refractive index increments as the slope of the plot of the degree of light deviation through a split cell as a function of polymer concentration. (B) Cauchy plot showing the relationship between $\delta n/\delta c$ and wavelength of light used to probe the samples.

Factors that affect refractive index also affect $\delta n/\delta c$; these include temperature, wavelength of the radiation source, molecular weight, and the chemical identity of the solvent and analyte.[229] Sulfur increases the refractive index of polymers,[230-231] and as a result any differences in the degree of sulfonation between NaP4SS and C-NaPSS would translate to a difference in $\delta n/\delta c$. The Cauchy plots in Figure 51A of NaP4SS and C-NaPSS of similar molecular weights, 79 and 71 kDa, measured in water, confirm this difference across the entire range of wavelengths displayed. Furthermore, we observed the discrepancy in $\delta n/\delta c$ between samples to be consistent across a wide range of molecular weights, with NaP4SS tracking slightly higher at about 0.175 ± 0.001 mL/g compared to 0.172 ± 0.001 mL/g for C-NaPSS. Limited reports of $\delta n/\delta c$ values for NaPSS in water vary from 0.166 to 0.23 mL/g.[42, 218] For most homopolymers the $\delta n/\delta c$ is constant across a broad range of molecular weights but begins to vary at lower molecular weights. This is due to a greater contribution of end group units to the polymer's overall chemical identity. Neither sample displayed a significant relationship between $\delta n/\delta c$ and wavelength or molecular weight (Figure 51C and D), but C-NaPSS varied randomly from sample to sample, which we take as an indicator of varying sulfonation levels. NaP4SS exhibited a very minor downturn in $\delta n/\delta c$ for the 28 kDa sample, which is at a degree of polymerization where end groups account for approximately 2% of the total polymer chain by mole.

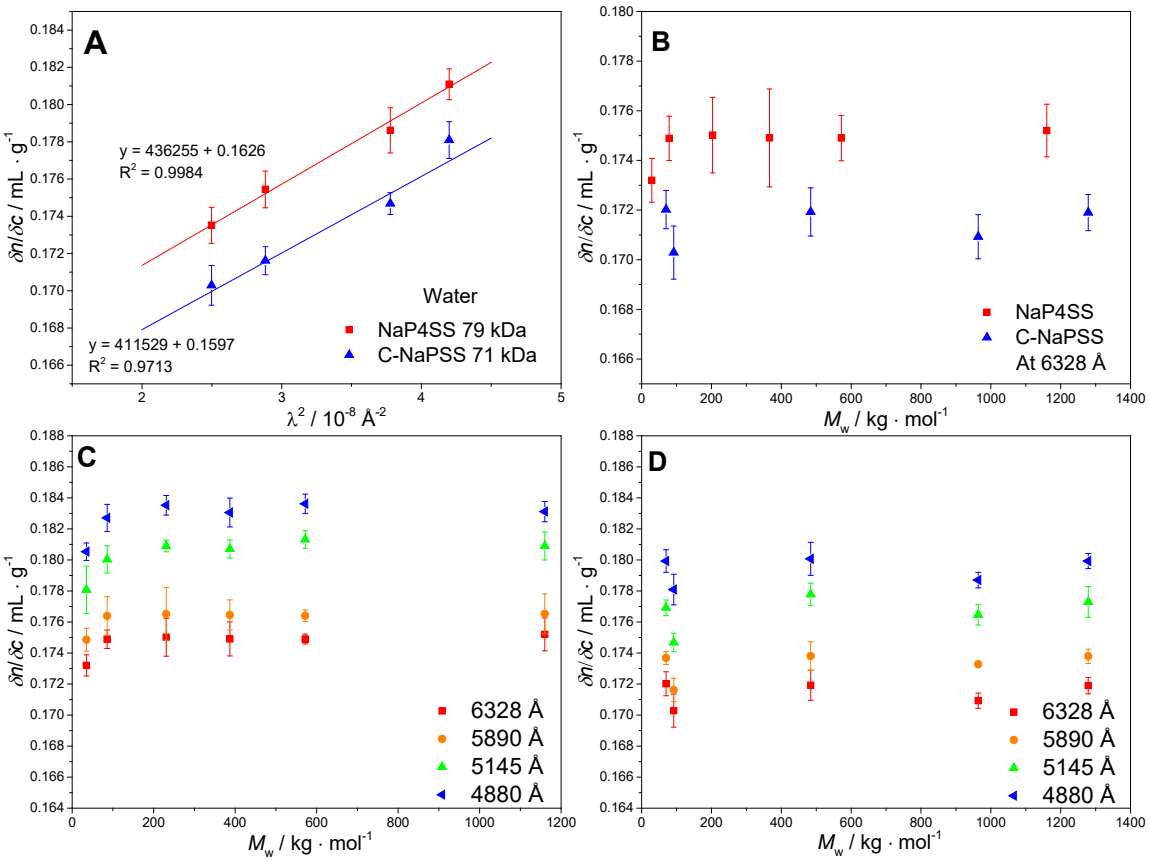

Figure 51. (A) Cauchy plots for NaP4SS and C-NaPSS of comparable molecular weights, (B) *δn/δc* values at a single wavelength for NaP4SS and C-NaPSS over a range of molecular weights and, (C) *δn/δc* values as a function of wavelength and molecular weights for NaP4SS and, (D) for C-NaPSS. All measurements were conducted in nanopure water adjusted to pH 7.

In contrast to the *δn/δc* results observed for NaP4SS and C-NaPSS in water, there was no statistically significant deviation between samples measured in a SEC-relevant solution for anionic polyelectrolytes, 0.3 M $NaNO_3$ + 0.01 M NaH_2PO_4 + 0.02% NaN_3 at pH 9. The Cauchy plots for NaP4SS and C-NaPSS were nearly identical and the *δn/δc* values as a function of molecular weight were within 0.001 mL/g of each other (Figure 52A and B). Similar to the results observed in water, there was also a slight dip in the *δn/δc* values for NaP4SS at the lowest molecular weight (Figure 52C) as well as variation in *δn/δc* for C-NaPSS as a function of molecular weight (Figure 52D).

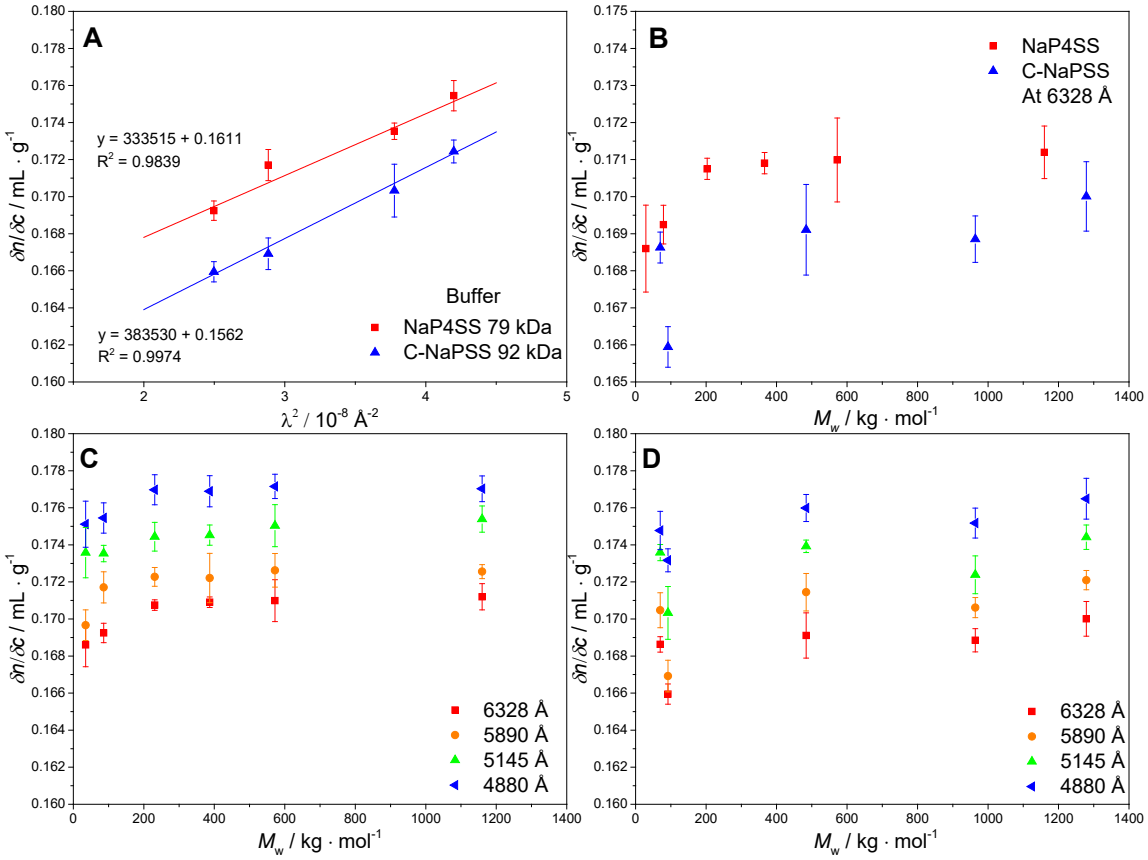

Figure 52. (A) Cauchy plots for NaP4SS and C-NaPSS of comparable molecular weights, (B) *δn/δc* values at a single wavelength for NaP4SS and C-NaPSS over a range of molecular weight and, (C) *δn/δc* values as a function of wavelength and molecular weight for NaP4SS and, (D) for C-NaPSS. All were measured in 0.3 M $NaNO_3$ + 0.01 M NaH_2PO_4 + 0.02% NaN_3 at pH 9.

3.3.3.2 Molar mass, Radii and polymer architecture

SEC-coupled MALS with dRI detection was used to determine molar mass distributions (M_n and M_w), root mean square (RMS) radius (synonymous with radius of gyration R_G), and polymer architecture from conformation plots for several NaP4SS and C-NaPSS samples. Table 2 details the number and weight average molecular weights as well as the dispersity and degree of sulfonation as measured by ^{1}H NMR for all NaP4SS and C-NaPSS samples.

Table 2. Molecular weight and dispersity data obtained by SEC-MALS, and degree of sulfonation obtained by ^{1}H NMR.

Sample	M_n (kDa)	M_w (kDa)	$Đ=(M_w/M_n)$	Sulfonation % (^{1}H NMR)	Source/ Catalog Number
NaP4SS	340	438	1.29	100	Synthesized from Ref 39
NaP4SS	286	366	1.28	100	Ref 39
NaP4SS	208	260	1.25	100	Ref 39
NaP4SS	158	202	1.28	100	Ref 39
NaP4SS	67	79	1.18	100	Ref 39
NaP4SS	47	51	1.09	100	Ref 39
NaP4SS	26	28	1.08	100	Ref 39
C-NaPSS	521	1279	2.45	94.0	SP^2/575
C-NaPSS	426	964	2.26	92.1	Sigma Aldrich/434574
C-NaPSS	222	485	2.18	92.3	SP^2/576
C-NaPSS	53	92	1.74	88.9	SP^2/574
C-NaPSS	48	71	1.48	91.6	Sigma Aldrich/243051

Chromatograms composed of the normalized light scattering traces at 90° for NaP4SS and C-NaPSS are shown in Figure 53A and B, respectively. Symmetrical monomodal traces without significant shoulders or high or low molecular weight tailings were observed for all NaP4SS samples across a broad range of molecular weights. The C-NaPSS

chromatograms show a greater degree of asymmetry. This is exemplified by a high molecular weight shoulder on samples 964 and 485 kDa, a low molecular weight shoulder on samples 1279 and 71 kDa, and high and low molecular weight tails on samples 92 and 1279 kDa, respectively. A more meaningful representation of a polymer's molar mass distribution can be visually displayed with a concentration vs molar mass plot, which quantifies each molar mass slice across the distribution. These distributions, shown in Figure 53C and D, for NaP4SS and C-NaPSS, respectively, reveal that NaP4SS samples are monomodal with only slight low molecular weight tails observed for samples 438 and 257 kDa. By comparison the C-NaPSS samples have broader molar mass distributions with high molecular weight tails observed for samples 1279, 964 and 485 kDa, in addition to a small degree of peak multi-modality seen for samples 71 and 92 kDa. These findings correlate with the higher $Đ$ values calculated for all C-NaPSS samples. Total mass recovery from SEC-MALS exceeded 83% for all samples.

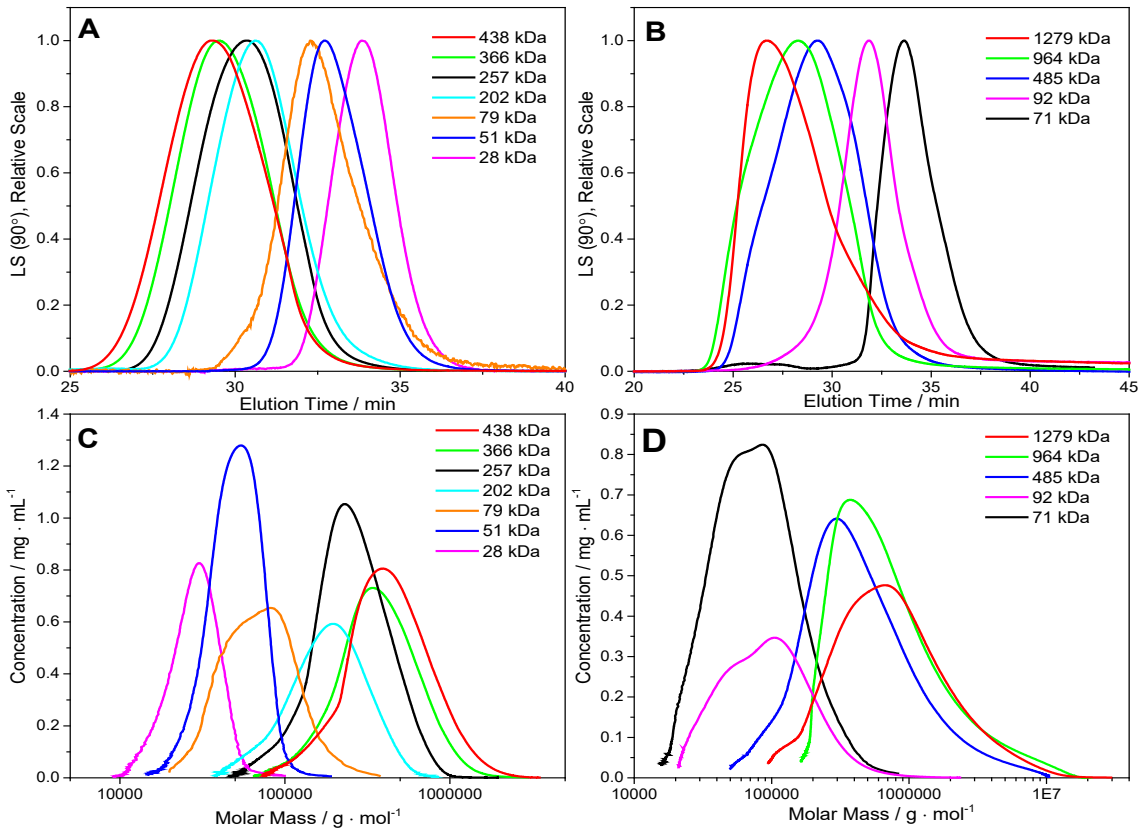

Figure 53. Normalized light scattering traces for a range of molecular weights of (A) NaP4SS and, (B) C-NaPSS, along with the corresponding concentration vs molar mass plots to show a true molar mass distribution for each (C) NaP4SS and, (D) C-NaPSS.

Conformation plots of R_G vs M, with each axis plotted on a logarithmic scale, are designed to explore the Flory relationship $R_G \sim M^{\upsilon}$. Conformation plots for select NaP4SS and C-NaPSS samples, sufficient to span a wide M range, are displayed in Figure 54A and B, respectively. The relationship between υ and the fractal dimension of a polymer, d_f, defined as $d_f = 1/\upsilon$, describes the solution conformation of that polymer.[80] Theoretical slope values ranging from 1/3 to 1 describe architectures from a hard sphere through to a rigid rod, respectively, with linear random coil polymers adopting values of 0.5 in theta conditions to 0.6 for good solvent conditions.[81] The slope values from conformation plots

were constant at 0.6 ± 0.02 for all NaP4SS samples across a broad *M* range. By contrast, v values for C-NaPSS were 0.5 ± 0.01, also across a broad *M* range. The lower slope values of 0.5 for C-NaPSS suggest a more compact coil relative to NaP4SS, where the higher v = 0.6 value indicates the adoption of a more extended coil conformation by comparison. These results are consistent with the notion that C-NaPSS contains self-attracting hydrophobic patches.

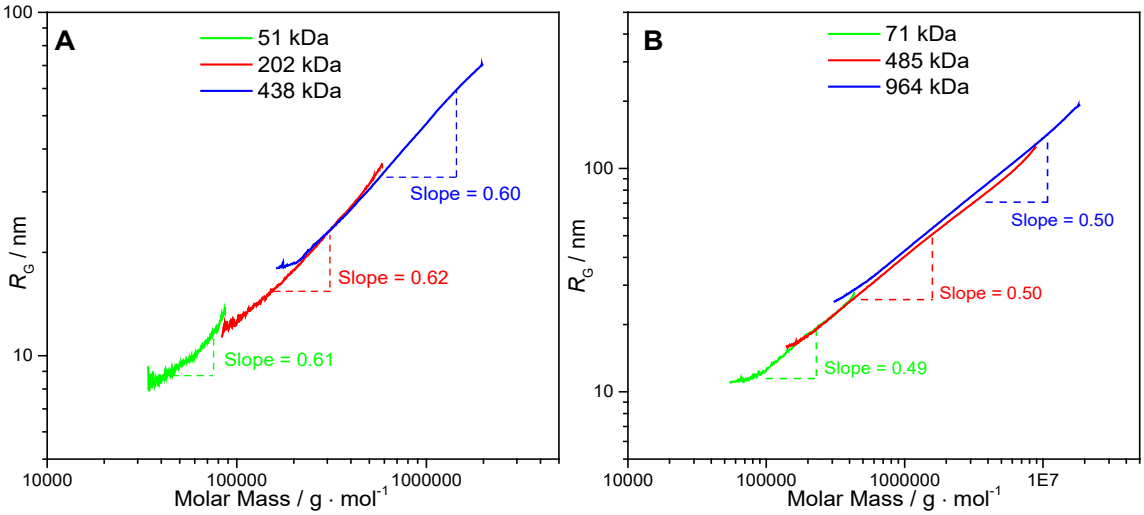

Figure 54. Log-log conformation plots of root mean square radius of gyration vs molar mass for (A) NaP4SS and, (B) C-NaPSS samples spanning a broad molar mass range.

For reference, the evolution of molar mass and root mean square radius across the elution time for all NaP4SS and C-NaPSS samples are shown in Figure 55.

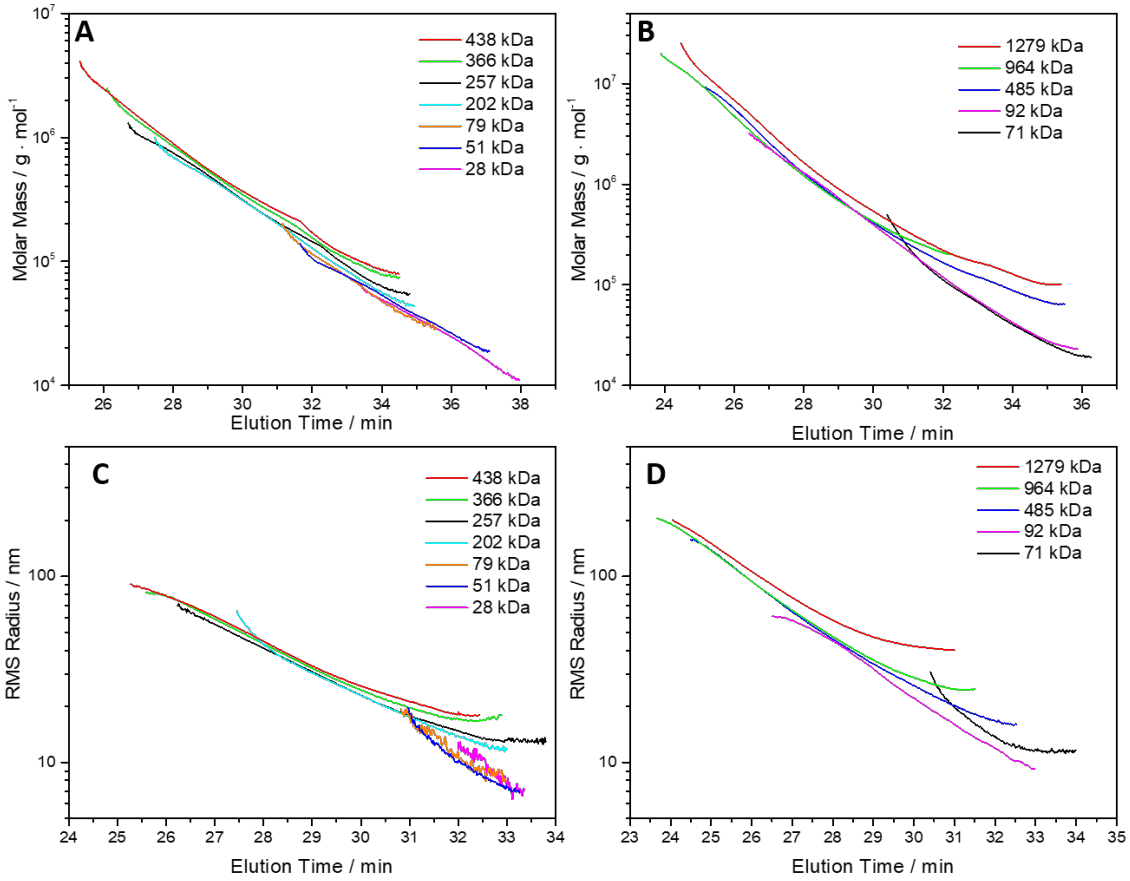

Figure 55. Plots of molar mass for NaP4SS (A) and C-NaPSS (B) as functions of elution time. RMS radius of gyration as a function of elution time for NaP4SS (C) and C-NaPSS (D). SEC-MALS eluting solvent was 0.3 M $NaNO_3$ + 0.01 M NaH_2PO_4 + 0.02% NaN_3 at pH 9.

A separate online SEC-MALS system equipped with QELS capability was used to measure R_H and R_G simultaneously, thus revealing further polymer conformational information for the perfectly sulfonated NaP4SS samples in solution. The dimensionless radius ratio, $\rho \equiv R_G/R_H$, has been calculated for a number of polymeric architectures with values that range from $(3/5)^{1/2} = 0.778$ for a homogenous hard sphere to values in excess of 4 for a rigid rod.[82-83] Our results are best understood after reviewing the response of light scattering and quasielastic light scattering experiments to polydisperse samples. Batch measurements on

unfractionated samples yield for R_G the square root of the z-average of squared radii of gyration:

$$R_G = \sqrt{\frac{\sum C_i M_i \langle {R_G}^2 \rangle_i}{\sum C_i M_i}} \tag{57}$$

where $\langle {R_G}^2 \rangle_i$ is the conformational average of the squared radius of gyration of polymers having i subunits, which is assigned by the light scattering experiment a weighting proportional to $c_i M_i$. In comparison, for R_H one obtains the inverse of the z-average of the inverse hydrodynamic radii, modified by the particle form factor P_i ($0 < P_i < 1$):[232]

$$R_H = \left(\frac{\sum C_i M_i \left(\frac{1}{R_H} \right)_i}{\sum C_i M_i} \right)^{-1} \tag{58}$$

In these expressions, subscript i usually represents an individual polymer species with degree of polymerization i. ASTRA uses Equation 57 with subscript i representing the results from a single slice, assumed to be monodisperse (the assumption is more likely valid for MALS slices than for QELS slices, as the latter require a longer observation time, in our case 10 s which can be compared to 0.5 s for MALS).

We report R_G/R_H values in two separate ways. In Figure 56A, we used the whole polymer chromatogram in calculating R_G and R_H according to Equation 57 and Equation 58, respectively, and plotted the ratio as a function of M_w, also determined from the whole chromatogram. This approach shows that ρ increases in value from about 1.5 for smaller M_w NaPSS to about 1.8 for larger M_w NaPSS, meaning these polymers are linear random coils in good solvent conditions. Each data point is labeled with the sample's $Đ$ because

polydisperse linear random coils have ρ values that range from 1.7 to 2 which is higher than the ρ values of 1.5 to 1.75 for the monodisperse case.

In the second way is shown in Figure 56B, where we report R_G/R_H slice-by-slice for two chromatograms for two different NaPSS samples than span a broad molar mass range. The slice time is set by the QELS measurement. About 20 MALS slices were averaged for each QELS slice and the R_G/R_H ratio was plotted against the corresponding molar mass value at that same time slice. Here ASTRA calculates R_G at each slice from a Zimm method according to:

$$R_G = \sqrt{\frac{3sM_w\lambda^2}{16\pi^2}} \tag{59}$$

where $s = d[K^*C/R_\theta]/d[\sin^2\theta/2]$ using the optical constant K^*, excess Rayleigh factor R_θ, sample concentration C, scattering angle θ and laser wavelength in vacuo λ_0. While there is a proven correlation between $Đ$ and ρ,[233] determination of R_G and R_H across the molar mass distribution of NaP4SS during a SEC experiment shows that ρ tends toward larger values with increasing molar mass (Figure 56B). This data further points toward NaP4SS being in an expanded random coil conformation, especially at higher molar mass.

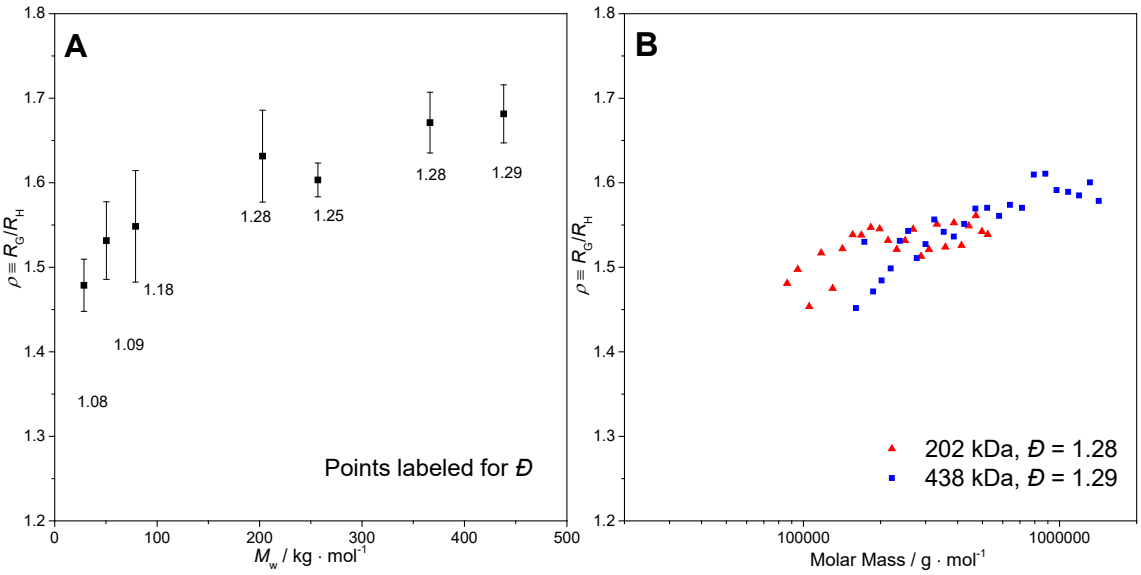

Figure 56. (A) Ratio of z-averages of R_G and R_H vs M_w over a whole polymer chromatogram for a range of NaP4SS samples and their labeled dispersities. (B) Ratio of R_G to R_H taken at slice intervals along the chromatogram for two NaP4SS samples as a function of the corresponding molar mass at that slice.

3.3.3.3 Partial Specific Volume

The partial specific volume ($\tilde{v}$) of a polyelectrolyte in solution is an important thermodynamic property that is useful in the identification of solvent-solute and solute-solute interactions. It is also used in analytical ultracentrifugation experiments. There are two methods used to calculate partial specific volumes ($\tilde{v}$) from experimental density data.[234] If the partial specific volume value at infinite dilution does not depend significantly on polyelectrolyte concentration, then the value can be obtained directly by plotting density vs concentration according to:

$$\rho_D = \rho_0 + (1 - \tilde{\nu}\rho_0)C \tag{60}$$

where ρ_D designates the solution density, ρ_0 the solvent density, and C the polymer concentration in g/cm^3.[235] This approach yields an approximation because, in practice,

density measurements are taken over a limited range of polymer concentrations, so the concentration influence on $\tilde{v}$ is not fully considered. An absolute thermodynamic approach (method of intercepts) is carried out by plotting the inverse solution density ($1/\rho_D$) against solute weight fraction (w) and extrapolating a linear least squares fit to w=1, where the y-intercept value equals $\tilde{v}$.[236] The linear least squares fit at w = 1 with a confidence interval of 95% was used to determine the error in $\tilde{v}$ at the y-intercept (Figure 57).

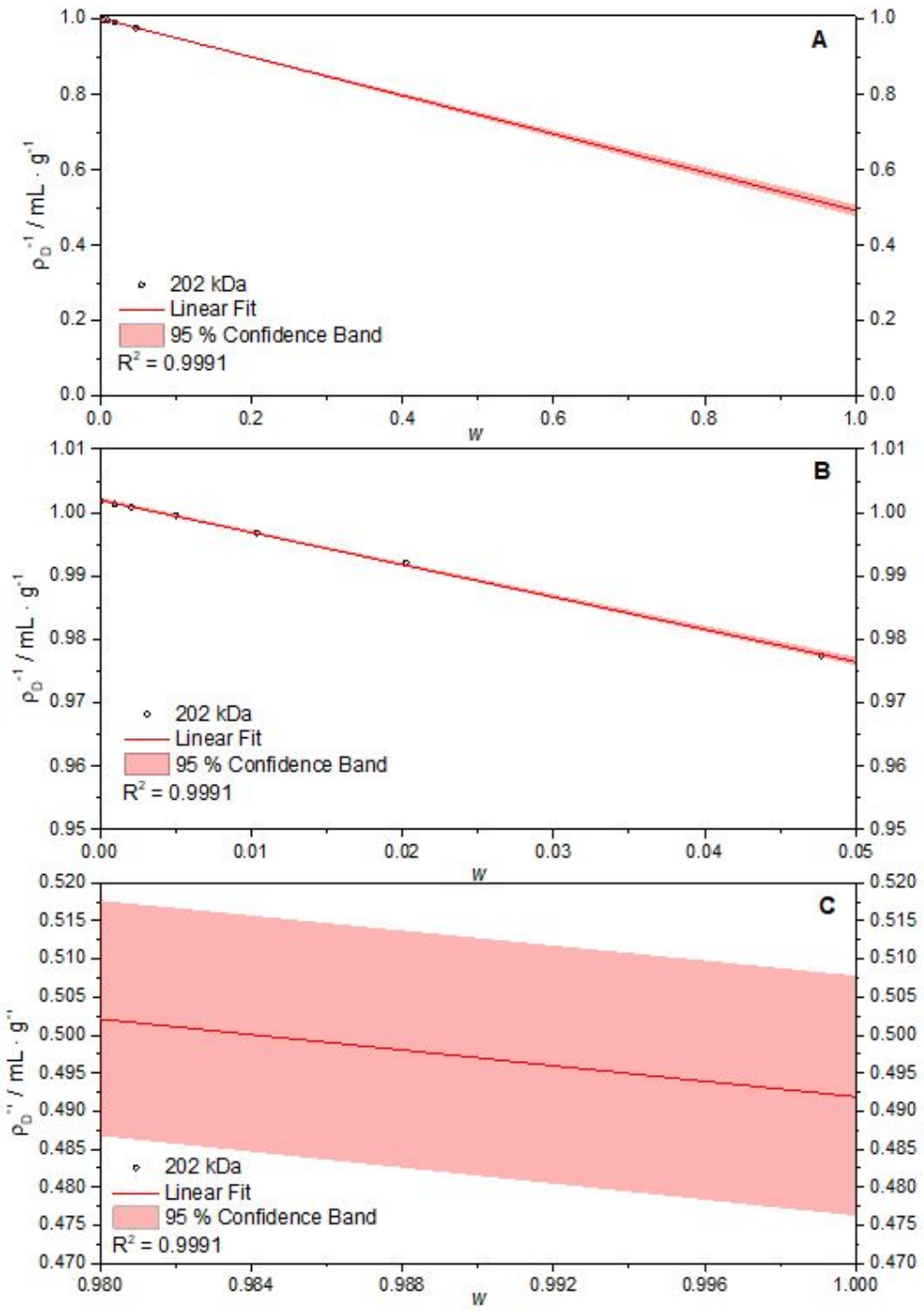

Figure 57. (A) Plotting inverse density versus weight fraction in a polymer-solvent system showing the extrapolation to the secondary y-axis to determine partial specific volume. (B) Data values only span a small region of the entire weight fraction axis, but nevertheless result in a well-defined intercept at $w = 1$ (C) which was used to determine the partial specific volume and associated uncertainty. Solvent was nanopure water adjusted to pH 7.

Values of $\tilde{v}$ for C-NaPSS in both water and the SEC relevant buffer used were in the range of 0.53-0.56 cm^3/g, and were slightly higher than the range of approximately 0.51-0.54 cm^3/g for NaP4SS (Figure 58A and B). Values for C-NaPSS agreed well with previously reported data for NaPSS while NaP4SS exhibited slightly lower values.[234] Discrepancies between the two sample data sets are justified by several factors including analysis method, and polyelectrolyte purity or the degree of ionic substitution. Wandrey et al. determined that highly sulfonated anionic polyelectrolytes had a smaller $\tilde{v}$ compared to their less negatively charged counterparts.[234] Salamanca et al. reported that $\tilde{v}$ increased with the hydrophobic content of anionic polyelectrolytes.[237] These prior findings contribute to our deduction that incomplete sulfonation of C-NaPSS samples affects the polymer's solution properties. In addition, NaP4SS displayed a molecular weight dependence, as $\tilde{v}$ slightly but consistently decreased as M_w increased, contrary to the observed independence of $\tilde{v}$ on M_w for C-NaPSS (Figure 58A and B). The trend was visible for NaP4SS in both water and buffer solution. Typically, the molar mass of polyelectrolytes does not affect the partial specific volume as long as it is sufficiently high.[238] While this molar mass independence was observed for C-NaPSS, the phenomenon also depends on the measured concentration range; specifically, whether it spans the dilute-to-semidilute regime or even higher concentrations where entanglements occur.[239] Chemical differences between NaP4SS and C-NaPSS could affect these regimes, as polyelectrolyte conformation in dilute solution depends on the fraction of charged groups on the polymer and the ionic strength of the solution.[240-241]

Measurements of $\tilde{v}$ over several concentrations of NaCl were conducted to observe the effect of ionic strength for NaP4SS and C-NaPSS samples of similar molecular weight

(Figure 58C). Both samples showed a decrease in $\tilde{v}$ as ionic strength increased, representing a contraction of the chain in the presence of greater electrostatic screening. C-NaPSS displayed $\tilde{v}$ values that were approximately 0.01-0.02 cm^3/g higher than NaP4SS at corresponding salt concentrations.

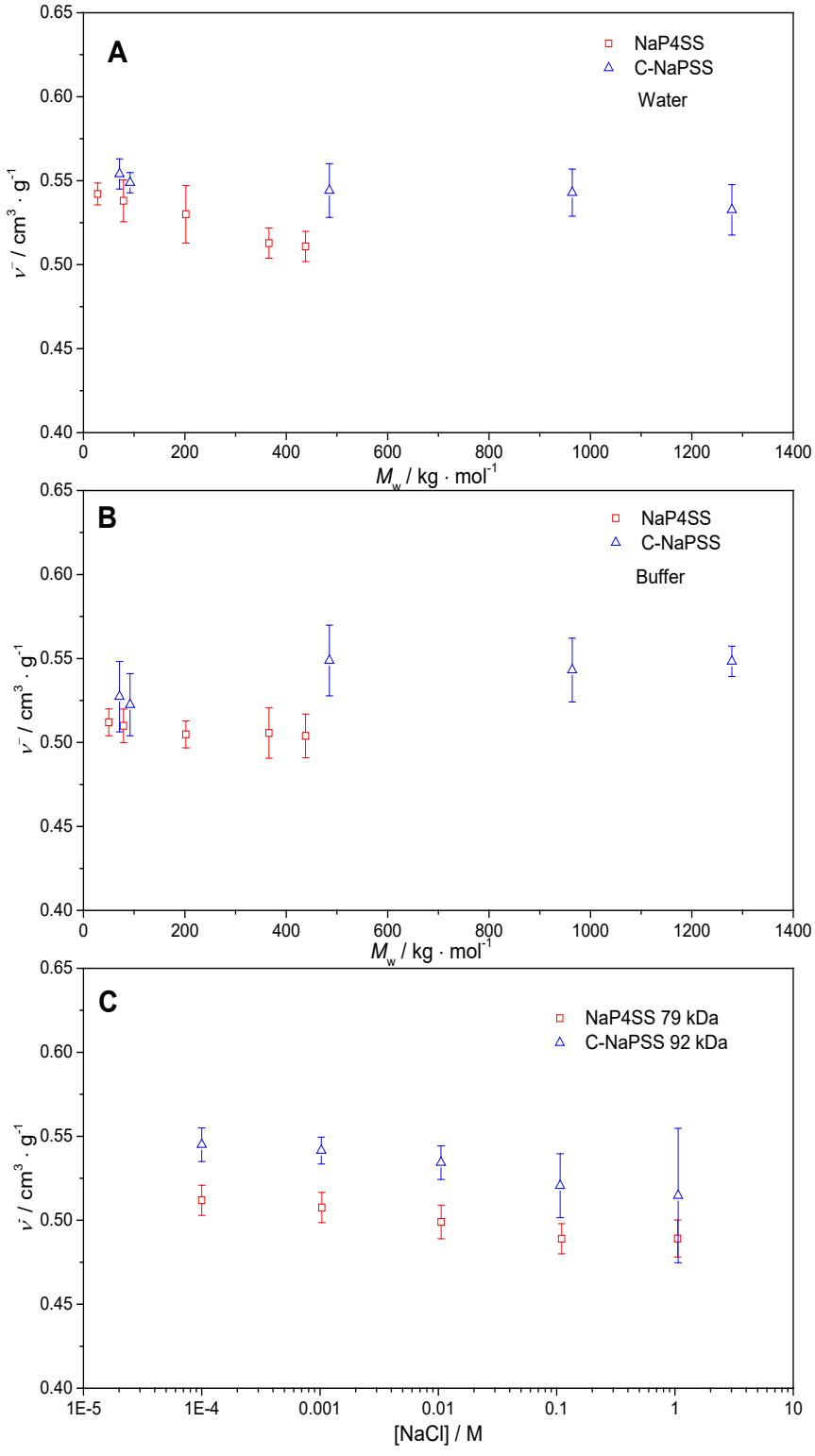

Figure 58. (A) Effect of molar mass on partial specific volume in water and, (B) in 0.3 M $NaNO_3$ + 0.01 M NaH_2PO_4 + 0.02% NaN_3 at pH 9. (C) Effect of salt concentration on partial specific volume for NaP4SS and C-NaPSS.

3.3.4 Bulk Thermal Properties of NaPSS

3.3.4.1 Thermal Stability

TGA curves for a number of C-NaPSS and NaP4SS samples of different molecular weights, along with the first order derivatives, are shown in Figure 59 below. Thermal properties extracted from these curves are shown in Table 3. The decomposition onset temperature, T_d, is usually defined as the temperature at which 5% mass loss occurs. Because over 50% of NaPSS is non-volatile at 800 °C, we use $T_{70\%}$ instead, which is the temperature at which 70% of mass loss has occurred.[242] We also define the weight loss percent that occurred at 700 °C as $W_{700\,°C}$. NaPSS displays a single, prominent degradation step at a temperature T_{max} which corresponds to the maximum rate of mass loss. Both C-NaPSS and NaP4SS exhibit a T_{max} at approximately 450 °C.

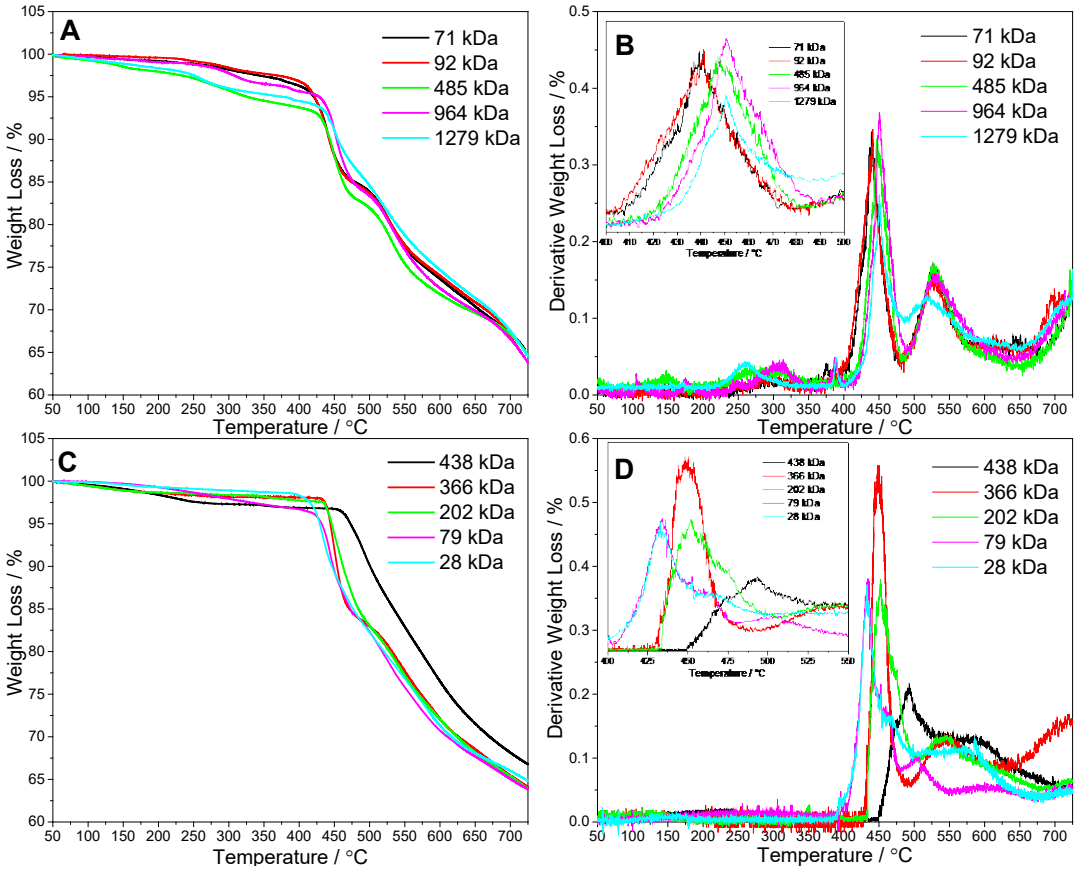

Figure 59. (A) TGA traces for C-NaPSS and, (B) corresponding differential traces. (C) TGA traces for NaP4SS and, (D) the corresponding derivative curves.

Inconsistencies in the relationship between T_d and molecular weight for NaP4SS and C-NaPSS were observed. T_d was found to increase with molecular weight for the NaP4SS sample set. This trend was not observed for C-NaPSS, as exemplified by the lower T_d values for the 485 and 1279 kDa samples. Furthermore, the T_d values for NaP4SS were consistently higher than those for C-NaPSS samples of similar molecular weights. Yao et al. conducted TGA studies of the copolymer poly(styrene-co-styrene sulfonate), and found that T_d occurred at lower temperatures for copolymers with higher PS components, in addition to a greater net mass loss over the temperature testing range up to 800 °C.[243] Unlike its unsulfonated PS counterpart, the degradation of NaPSS occurs at high

temperatures, 450-500 °C vs 350-400 °C, and produces a significant amount of non-volatile char, containing the inorganic salts sodium sulfate and sodium sulfite. Small peaks on the derivative traces for C-NaPSS around 250-300 °C could be indicative of weight loss attributed to a PS component in the polyelectrolyte. Both $T_{70\%}$ and T_{max} are increased for NaP4SS compared to C-NaPSS due to the higher content of inorganic salt.

Table 3. Thermal decomposition properties of NaP4SS and C-NaPSS.

Sample	M_w (kDa)	T_d (°C)	$T_{70\%}$ (°C)	$W_{700\,°C}$ (%)	T_{max} (°C)
NaP4SS	28	429.2	615.9	66.0	434.9
NaP4SS	79	431.8	619.1	65.5	437.9
NaP4SS	202	444.2	624.3	66.5	452.0
NaP4SS	366	446.1	632.7	67.9	453.9
NaP4SS	438	470.5	653.5	68.7	498.1
C-NaPSS	71	420.9	655.8	67.3	439.2
C-NaPSS	92	421.8	665.4	66.8	441.1
C-NaPSS	485	356.6	645.4	67.5	450.7
C-NaPSS	964	428.1	647.7	66.6	450.7
C-NaPSS	1279	399.4	671.3	67.5	450.4

3.3.4.2 Glass Transition Temperature

The T_g was calculated from the inflection point where a slope change occurred on the heat flow plot of the second heating scan in DSC measurements. Each of the C-NaPSS samples displayed a distinct slope change on both the first cooling and second heating scan but no

such transition was observed for NaP4SS over the measured temperature range (-70 – 420 °C) (Figure 60).

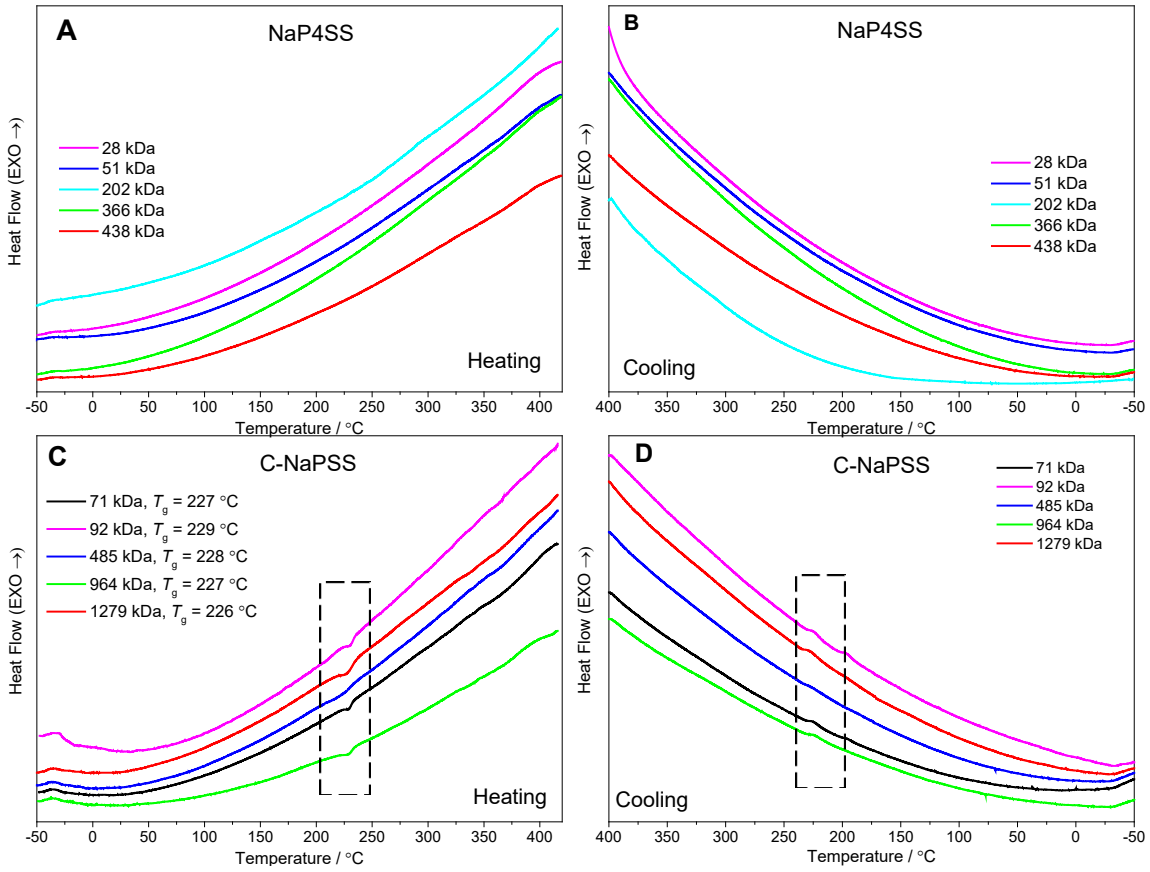

Figure 60. (A) DSC heating trace for NaP4SS and, (B) corresponding cooling trace with no visible transitions. (C) DSC heating trace for C-NaPSS and, (D) corresponding cooling trace with a highlighted glass transition signature observed for both.

Along with molecular weight and crosslinking effects, it has been shown that the T_g of sulfonated atactic PS (measured by a dilatometric technique) increases linearly with the degree of sulfonation.[244] The specific dependence of T_g, as measured for sulfonic acid weight fractions up to 0.15 in the copolymer, adhered to the following equation:

$$T_g = T_{g,B} + [190w_A/(1 - 0.45w_A)] \quad (61)$$

where $T_{g,B}$ represents the glass transition of the PS component (assumed to be 100 °C) and w_A is the weight fraction of monomer units bearing sulfonic acid groups. Assuming this relationship holds for higher sulfonic acid weight fractions, the C-NaPSS samples with T_g values of approximately 230 °C are therefore calculated to have degrees of sulfonation on the order of 60%, which is much lower than the values measured by ^{1}H NMR. The reliability of Equation 61 for copolymers with sulfonic acid weight fractions nearing unity is difficult to ascertain, as there are minimal data points made available by vendors that pertain to the T_g of commercial NaPSS. One vendor, which claims a degree of sulfonation in excess of 98% as determined by titration and elemental analysis, states a T_g of 210 °C for NaPSS with a molecular weight of approximately 200 kDa.[245] By this calculation, a fully sulfonated polymer would have a T_g of approximately 440 °C. Because the onset of decomposition for NaP4SS occurs close to 440 °C, we limited the heating scan to a maximum temperature of 420 °C, which potentially accounts for the lack of an observed T_g. Su. et al. studied the perturbation of T_g, as measured by DSC, for PS with varying degrees of sulfonation up to and in excess of 60%.[246] They similarly observed increases in T_g from neat PS with samples of higher degrees of sulfonation, but increases were associated with a diminishing signal size of the T_g transition. What can be deduced from previous reports and the data provided here is that if a NaP4SS material of 100% sulfonation possesses a T_g it must lie so close to the decomposition temperature as to be unmeasurable by DSC. In comparison, materials with degrees of sulfonation in the 90-99% range display a T_g around 210-240 °C. This finding suggests that if all repeat units bear a counterion then the high degree of ionic binding restricts the ability of pure NaPSS to enter

a rubbery state; however, with the introduction of a few unsulfonated, neutral repeat units, the carbon chains are able to move. Implications of this finding have relevance for NaPSS used in thin film and bulk material applications.

3.4 Conclusion

A comparison of perfectly sulfonated NaP4SS, obtained from polymerization of para-sulfonated monomer, to commercial samples produced by post-treatment processing of polystyrene has shown that the degree and specificity of sulfonation have real implications for the solution and bulk properties of this polyelectrolyte. Post-treatment processes to produce NaPSS are imperfect, as shown by ^{1}H NMR, ^{13}C NMR and FTIR, and in general no assumptions can be made about the purity or physical properties of commercially sourced NaPSS used in so many investigations. Solution properties such as specific refractive index increment, partial specific volume, and polymer conformation by SEC-MALS-QELS differ for NaP4SS and C-NaPSS over a range of molecular weights. The thermal bulk properties regarding polymer degradation as measured by TGA were comparable, but DSC analysis of both sample sets revealed the lack of a glass transition for NaP4SS over a range of molecular weights whereas C-NaPSS displayed a glass transition at T_g ~230 °C. Given the relative ease with which narrow-distribution NaP4SS can be produced over a wide range of molecular weights, fundamental studies should focus on pure materials as long as dispersity values of ~1.2 are tolerable. If even narrower dispersities are desired, researchers might consider preparative SEC of NaP4SS. The availability of pure NaP4SS also invites re-investigation of old applications and, perhaps, development of new ones.

3.5 Acknowledgements

We are grateful to Dr. Cameron Irvin and Alex Balzer for assistance with thermal measurements, to Dr. Graham Parkinson for help with density measurements, to Rachel Borrelli and Ron Volkovinsky for assistance with various aspects of measurements, writing and data analysis. We would also like to thank Dr. Rafael Cueto and Dr. Andre Striegel for insightful discussion on data interpretation. We thank Wyatt Technology for continual support and assistance with light scattering measurements. This work made use of the resources of the Mill at Georgia Tech and the thermal analysis laboratory of Dr. Meisha Shofner and Dr. Natalie Stingelin. This study was carried out with support from US Endowment and USDA Forest Service [E17-23].

CHAPTER 4. FLUORESCENCE PHOTOBLEACHING RECOVERY MEASUREMENTS OF BINARY MIXTURES OF SODIUM POLY(STYRENE SULFONATE)

4.1 Introduction

4.1.1 Fluorescence Photobleaching Recovery

4.1.1.1 Basics of fluorescence

Fluorescence signals are vital in microscopy because they provide excellent contrast between the details of interest and the dark background. Molecules and atoms in an electronic ground state can be excited to a higher energy level upon the input of sufficient energy. These temporarily excited species can then revert back to the ground state following radiative or non-radiative processes. A fluorescence signal is a radiative transition process that results from the relaxation of a molecule in an excited state back down to its ground state energy level. A Jablonski diagram illustrates the excitation and emission procedures involved in a fluorescent event through the various molecular energy levels and possible relaxation pathways (Figure 61).

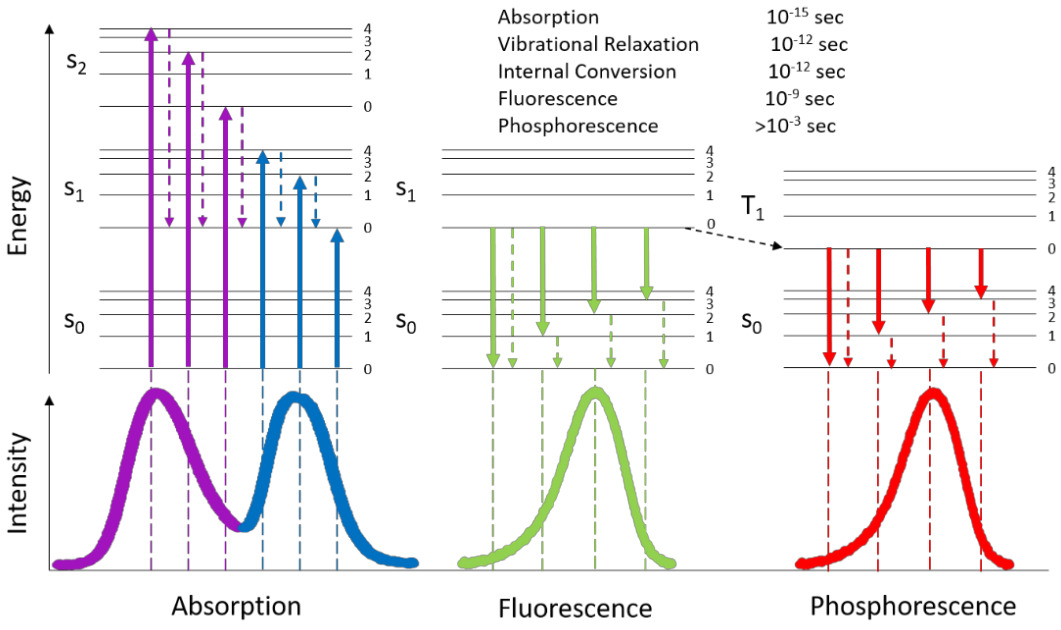

Figure 61. Jablonski diagram illustrating the single and triplet energy states of a fluorescent molecule and the possible excitation and relaxation pathways along with relative time scales for these processes.

An excited molecule will reach its ground energy state via a number of energy loss pathways. Rapid energy loss occurs as the excited molecule drops down to the lowest vibrational level of the excited state. Then a radiative transition from this level down to one of the vibrational levels of the ground state can occur. This is the process of fluorescence.

4.1.1.2 Introduction to Fluorescence Photobleaching Recovery

FPR is an experimental technique used to obtain the self-diffusion coefficient of entities that comprise a fluorescent sample. A routine FPR measurement can be divided into three distinct parts, firstly a pre-bleach phase, secondly a bleach phase, and finally a post-bleach phase. In the first phase a small select region of the fluorescent sample is illuminated with a beam of light, such as a low intensity laser beam, ensuring the incident

beam does not bleach the fluorophores but excites them to fluoresce consistently. Since the system is under equilibrium in this phase the obtained fluorescence signal F_i is almost constant in space and time, subject to minor variation due to thermal and laser intensity fluctuations. A pre-bleach essentially develops the baseline of the fluorescence intensity signal. In the second part, or bleach phase of the measurement, the beam intensity is rapidly increased, for a brief interval, to a magnitude sufficient to deliver enough energy to permanently destroy a portion of the fluorescent moieties. A photobleached dark area now occupies the selected sample region leading to a sharp drop in the fluorescence signal given by F_0. Defined as the ratio of F_0 to F_i the bleach depth is varied depending on sample characteristics. Deep bleaches obtain better signal to noise while shallow bleaches are less disruptive to the system and less likely to cause parasitic photobleaching. Optimization between the two to set upper and lower bleach limits is usually done by varying the bleach beam intensity or duration. The third and final part or post-bleach phase sees the intense beam quickly and heavily attenuated (same as the initial pre-bleach beam intensity), making sure this probing intensity does not further bleach the fluorophores as it remains focused on the photobleached region. Over time the return of fluorescence is observed, due to the exchange by diffusion of bleached molecules occupying the visibly dark region with healthy unbleached fluorescent moieties that originally lay outside the selected volume (Figure 62). This process is monitored photometrically, and the recovery rate of fluorescence of the dye-tagged or inherently fluorescent molecules by exchange with those that were destroyed/photobleached is analyzed. System kinetics are manifested by a recovery profile, changing the otherwise static pre-bleach signal into an exponentially varying one. Information attainable from fluorescence photobleaching recovery includes a

diffusion coefficient measurement, identification of the transport type whether it be random diffusion due to Brownian motion or under directed flow, and an estimate of the fraction of fluorophores that are mobile.

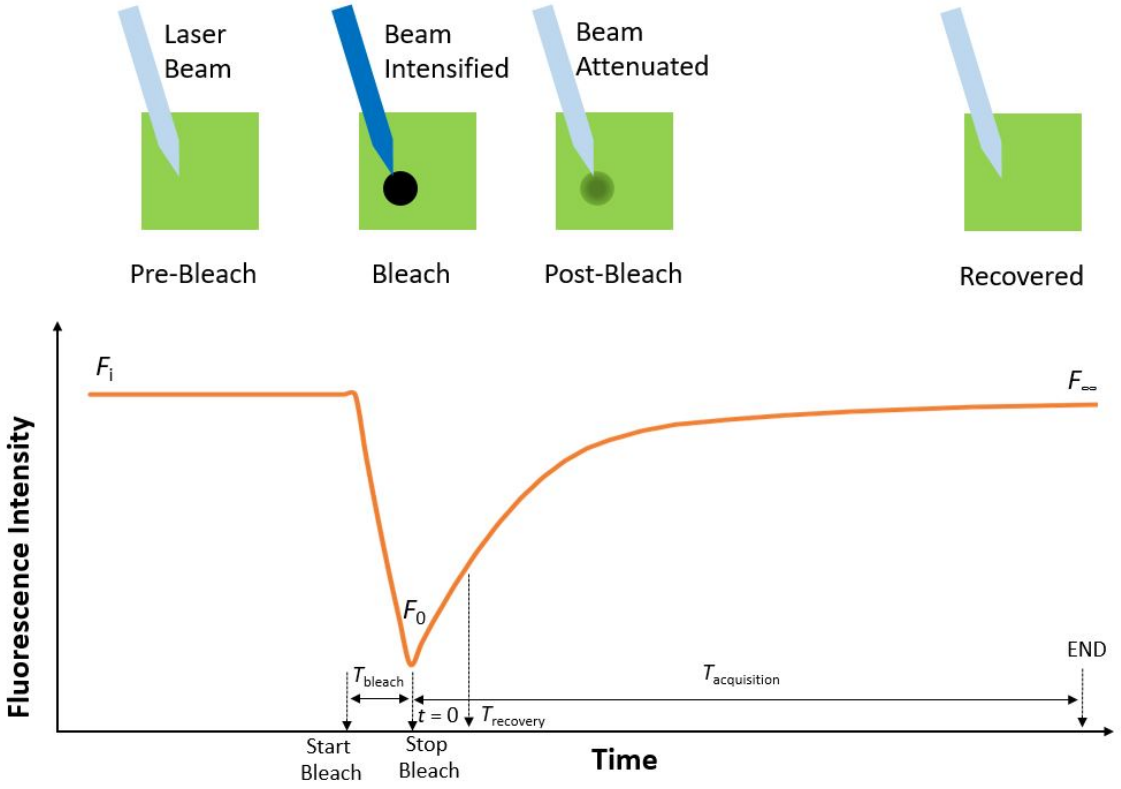

Figure 62. Typical FPR curve of the variation of fluorescence intensity with time for each phase of the experiment. The time stages are illustrated to show the phases of the experiment.

Pioneers of the FPR in the mid-1970s first described the technique as a method to measure the two-dimensional lateral mobility of fluorescently labelled molecules.[247-249] Although FPR was primarily developed for biological applications, such as protein movements through cell membranes,[250-251] great potential has been exhibited for many other systems. Smith at IBM laboratories used FPR to study the motion of small molecules in glassy films,[252] and Zero and Ware realized the capability of FPR to measure tracer

transport in complex media such as polyelectrolyte solutions and gels.[25-26] One of the key advantages of the FPR technique is the ability to conduct measurements in heterogeneous media, in which some structure on a microscopic or nanoscopic scale influences molecular motion. FPR diffusion measurements have been made in simple solutions of small and large molecules, and more complex media such as gels, liquid crystals, films, bulk polymers, cells and membranes.[27]

Consider a near perfect spherical molecule of radius r in a homogenous media of viscosity η, the Stokes-Einstein Law describes the diffusion coefficient D of this molecule by $D = \frac{kT}{6\pi\eta r}$. This relationship works well for homogenous solvents of low viscosity where the solvent molecules are significantly smaller than the solute of interest. If the media is heterogeneous on the molecular scale, where for instance chemical interactions are large or a polymer network exists, the diffusion coefficient depends on the molecular structure of the media rather than the bulk viscosity value.[253]

4.1.1.3 Comparison of FPR to other diffusion measuring instruments

FPR can measure diffusion coefficients from about 1×10^{-5} to $<10^{-14}$ $cm^2 \cdot s^{-1}$, which is a range that few other diffusion methods can match but other methods are more widely available than FPR. DLS can span a wider range of diffusion coefficients in a single measurement than any other competitor, pulsed field gradient NMR or DOSY excels at small rapid diffusers that do not scatter enough light for DLS, and analytical ultracentrifugation (AUC) can measure samples of very low concentration. These techniques, unlike FPR, do not require a sample to be inherently fluorescent or labeled with a fluorescent moiety. In exchange for labelling and verification of no deleterious effects

from labelling, FPR offers unmatched selectivity. One observes directly the diffusers that have been labelled, and this optical tracer self-diffusion value is not influenced by sample impurities such as dust or by thermodynamic interactions that provide the mutual diffusion coefficient obtained in DLS and AUC. The FPR self-diffusion coefficient is not the same as that obtained by DOSY because the concentration gradient between bleached and unbleached probes have an associated chemical potential, albeit very small in comparison to chemical potentials that arise from concentration fluctuations of the solute molecules themselves.[27] FCS, a close relative to FPR, is limited by a small sampling size, leading to inferior statistics, and it requires exclusion of background fluorescence, a feat often difficult to achieve in most heterogeneous samples.

If the molecule to be measured requires fluorescent labelling, a key consideration is determining which dye will react with available functional moieties on the molecule such as amino ($-NH_2$), hydroxyl (-OH), carboxyl (-COOH) and ester (-COOR) groups, among others. The fluorescent tag must have an absorption maximum at a wavelength (λ_{max}) close to the illumination wavelength of the laser line, such as a 488 nm blue, 514.5 nm green or 632 nm red. Furthermore, the dye must bleach at a higher illumination power but not undergo parasitic photobleaching during the recovery phase of the experiment, nor can a fluorescent electronic configuration be regained over the course of the measurement. FITC for blue light illumination and Rhodamine isothiocyanate (RITC) for green light illumination exhibit the necessary dye requirements for FPR experiments.[27] Degree of dye attachment is done on a case by case basis as too many can affect or induce structure of the macromolecule but since the FPR signal is directly correlated to the fluorophore concentration, not enough labelling can result in noisy data. Stoichiometry targeted at

adding enough dye to label one or ten or 100 macromolecules are worthy starting points or if an end functionalized polymer chain is used the dye labelling can be more specific and controlled. Not all dye will label the macromolecule of interest and so simple dialysis, chromatography, Soxhlet extraction or repeated precipitation and washings will remove unreacted dye. The degree of labelling can be determined by fluorescence or absorption and calibrate against solutions of free dye, assuming no shift in absorptivity or peak maxima when the dye is attached. Determination of any macromolecular conformational change from dye labeling is achieved by SEC-MALS to produce an R_G vs M plot.

4.1.1.4 General considerations

There are a wide range of FPR systems composed of different parts and analysis techniques e.g. photomultiplier tube (PMT) or a digital camera, spot or striped bleaches etc, but there is a general rule of thumb to ensure good results over a wide range of different FPR systems. That is, the photobleaching subsystem should meet the rule of 1000, meaning the bleach beam should be at least 1000 times brighter than the read beam used to monitor recovery.[254] This particular number is chosen as the product of three criteria that must be met. One factor of ten arises from the bleach duration having to be less than 10% of the recovery time; another factor of ten is needed because the acquisition time after bleaching needs to be 10 times longer than the recovery time; and the last factor of ten arises from parasitic photobleaching from the read beam during the recovery phase should not exceed 10%.[27] Further care must be taken into ensuring that any stray light from reflections or from laser mirrors does not strike the sample or if it does it must be stable and far less intense than the read beam.

In practice it is simple to increase the acquisition time and reduce the bleach time so it is far shorter than the recovery time, but it is not only the time of the photobleach that matters but also the laser intensity must be high enough to effect the bleach.[255] In FPR systems where an optical switch changes the bleach to the read beam and vice versa the intensity of each beam is proportional to one another. This means that you cannot simply turn up the laser intensity to accomplish shorter bleaches because this also increases the read beam intensity and therefore increases the probability of parasitic photobleaching during the recovery phase. Dissolved oxygen can affect the rate of unwanted spontaneous reversal of photobleaching and transferring significant amounts of energy to a sample from a laser can heat it significantly which thus effects the measured diffusion coefficients.[256] Furthermore it is vital to guard against fluorescence recovery not related to diffusion by measuring the sample at different diffusion lengths. Complete reversibility of photobleaching is simply detected because it displays length-independent recovery times.

4.1.2 Types of FPR instruments

4.1.2.1 Spot bleaching

The majority of FPR systems are constructed around an epifluorescence microscope as the core component, with the advantage being able to get visual feedback of a samples stability, bleach speed or problems such as inhomogeneity or bubbles. In addition, when equipped with a laser the microscope allows for beam spot size adjustments or allowing it to pass unhindered onto the sample, resulting in a Gaussian beam profile in the sample's plane (Figure 63). Axelrod et al., made early developments in FPR data

modeling to deduce the diffusive mechanism governing a single beam system with a Gaussian profile spot bleach.[247]

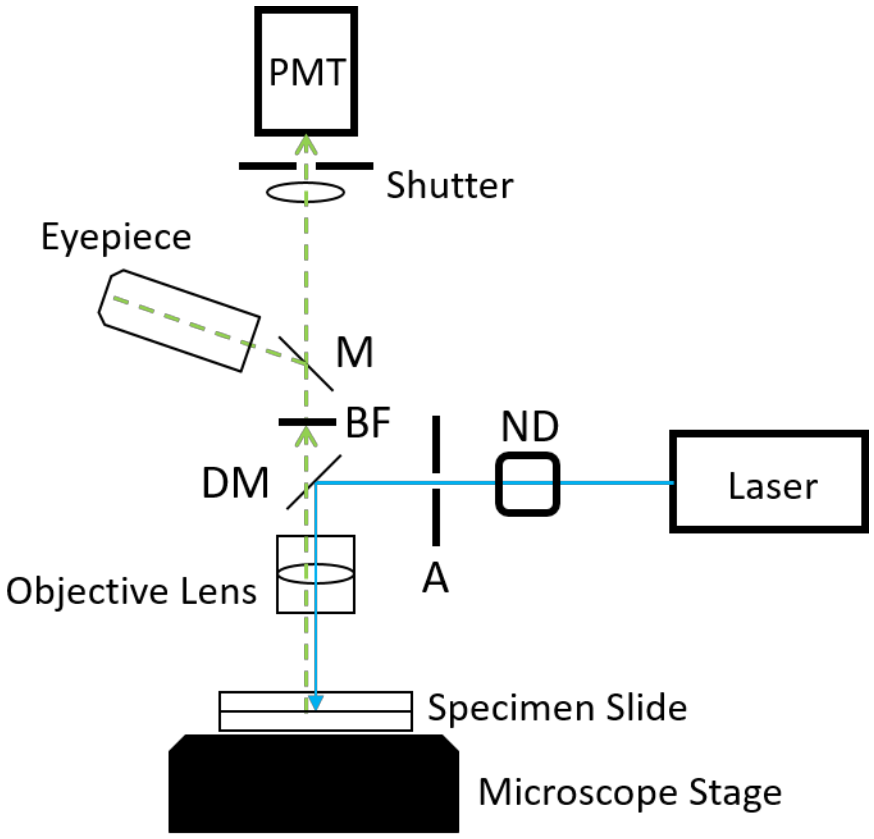

Figure 63. Simple spot bleach FPR experimental set up using an epifluorescence microscope showing the blue laser beam path to excite the sample and the fluorescent green light from the sample to the microscope eyepiece to view the bleached spot or to the detector. ND is neutral density filter, A is aperture which is in the rear image plane of the objective, DM is dichroic mirror, BF is barrier filter, M is mirror, and PMT is photomultiplier tube.

Consider a 2D spherical region of sample having a Gaussian cross-sectional profile as produced by an unimpeded laser beam operating in a usual transverse electromagnetic (TEM_{oo}) mode. Initially the system is under equilibrium because all fluorophores are evenly distributed throughout the sample and across the illuminated region. This gives rise to a time invariant fluorescence signal due to a concentration of unbleached fluorophores

$C(r,t)$ at a radial distance r from the center of the spot at a time t. Application of an intense bleaching beam $I(r)$ disrupts the equilibrium as some population of healthy fluorophores become irreversibly photobleached. Assuming the photobleaching reaction is a first-order reaction of rate constant $\alpha I(r)$, an estimation of fluorophore concentration at a given time is given by:

$$\frac{dC(r,t)}{dt} = -\alpha I(r)C(r,t) \tag{62}$$

where the intensity of an intense Gaussian bleaching beam is $(2P_0/\pi w^2)exp(-2r^2/w^2)$. The radial resolution w denotes the half-width of total laser beam radius at a height of e^{-2} and P_0 is the total power of the beam. The above equation is valid on the condition that no diffusion occurs during the bleaching process, which is a false assumption, but can be approximated by ensuring the bleach time is significantly less than the characteristic diffusion recovery time.

Immediately after bleaching for a short duration T the fluorophore concentration is expressed as:

$$C(r,0) = C_0 exp[-\alpha T I(r)] \tag{63}$$

the measurement time $t = 0$ and initial fluorescence signal C_0 prior to bleaching take on a constant value. An estimate of the bleach depth at the origin of the spot ($r = 0$), which depends on the bleach beam intensity and time applied, is given by $K_{depth} = \alpha T I(r)$.

Just as a chemical system has a tendency to regain equilibrium so will FPR after photobleaching. The time evolution of the original state, being the initial fluorescence intensity, is achieved again after bleaching by what is assumed to be solely a diffusional fluorophore transport mechanism. Then the change in fluorophore concentration can be related to a lateral diffusion coefficient given by Fick's second law:

$$\frac{\partial C(r,t)}{\partial t} = D\left(\frac{\partial^2 C}{\partial x^2}\right)C(r,t) \tag{64}$$

Solving $C(r,t)$, which will correspond to the fluorescence signal recovered, requires two conditions be assumed:

1) Boundary condition: $C(\infty,t) = C_0$, meaning the concentration of fluorophores at great distance from the bleach spot represents the concentration of all unbleached molecules which corresponds to a uniform fluorescence signal.

2) Initial condition: $C(r,0) = C_0 exp[-\alpha TI(r)]$

Because we are talking about spot bleaching the solution to Fick's equation $C_K(r,t)$ depends on the quantum efficiency q_e related to all absorption, emission and detection phenomena, and the factor A by which the bleach beam is attenuated to the read beam.

Fluorescence measured in the pre-bleach phase is invariant of the spatial and temporal configuration of fluorophores:

$$F_{K_{depth}} = q_e P_0 C_0 / A \tag{65}$$

The fluorescence signal measured immediately after bleaching is expressed as:

$$F_{K_{depth}}(0) = \frac{q_e P_0 C_0}{A} {K_{depth}}^{-1}(1 - e^{-K_{depth}}) \tag{66}$$

The recovered fluorescence signal at any time t after is written as:

$$F_{K_{depth}}(t) = \frac{q_e P_0 C_0}{A} v {K_{depth}}^{-v} \Gamma(v) P\left(\frac{2K_{depth}}{2v}\right) \tag{67}$$

where $\Gamma(v)$ is the gamma function, $v = (1 + \frac{2t}{\tau_D})^{-1}$ and τ_D is the characteristic diffusion recovery time of probe molecules which is defined by:

$$\tau_D = \frac{w^2}{nD} \tag{68}$$

Here n represents the spatial dimensionality which takes the value of 2, 4, 6 for one, two and three dimensions respectively. For FPR it is equal to 4 because it is assumed the diffusion is only measurable in two dimensions.

A series solution for $F_{K_{depth}}(t)$ which holds true for all values of K_{depth} and t was shown by Jacobsen et al.,[250] to be simplified to:

$$F_{K_{depth}}(t) = \frac{q_e P_0 C_0}{A}\left[1 - \frac{K_{depth}}{2\left(1 + \frac{t}{\tau_D}\right)}\right] \tag{69}$$

For spots that are uniformly illuminated, for instance when the diffuse center illumination from a bulb source impinges on a pinhole, the fluorescence intensity at a time t obeys:

$$f(t) = exp(-2\tau_D/t)\left[I_0\left(\frac{2\tau_D}{t}\right) + I_1(\frac{2\tau_D}{t})\right] \quad (70)$$

where I_0 and I_1 are modified Bessel functions,[257] and $f(t)$ is the normalized fraction of fluorescence recovered at the bleached spot which is given by:

$$f(t) = \frac{F(t) - F(0)}{F(\infty) - F(0)} \quad (71)$$

where $F(t)$ is the fluorescence intensity at any instant of time, $F(0)$ is the fluorescence intensity immediately after bleaching and $F(\infty)$ is the fluorescence signal at a sufficiently long time after bleaching. In this case of a uniformly illuminated spot $f(t)$ is independent of the bleaching depth parameter K and so the characteristic diffusion recovery time can be obtained by the half time $t_{1/2}$ the time required for half recovery:[257]

$$D = \frac{0.224w^2}{t_{1/2}} \quad (72)$$

4.1.2.2 Stripe bleaching

The simplicity of spot photobleaching is alluring but it is limited and the use of a periodic pattern for bleaching instead of a spot is advantageous.[249] Writing a pattern during the photobleaching phase is achieved by placing a mask, such as a Ronchi ruling, directly over the sample or in the rear image plane of the microscope (Figure 64). The pattern periodicity bleached into the sample is L and thus the spatial frequency of the pattern is $K = 2\pi/L$.

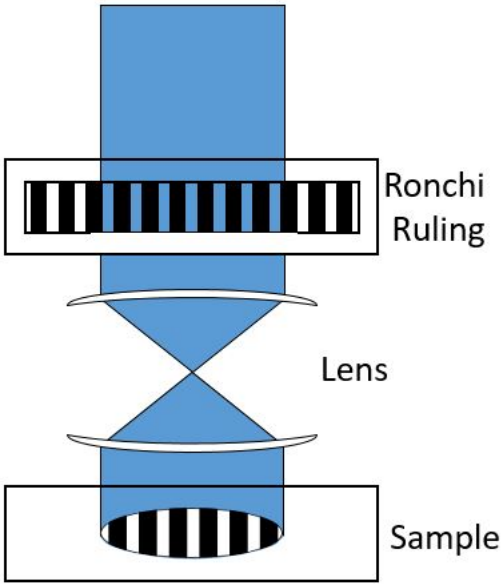

Figure 64. A Ronchi ruling placed in the rear image plane will cast a striped photobleached pattern into the sample when illuminated with a significantly intense laser beam.

Immediately after photobleaching ($t = 0$) the pattern amounts to a square wave of fluorescence intensity as a function of distance x in a direction perpendicular to the stripes which consist of bright and dark regions of equal width. A square wave can be represented by a Fourier series containing fundamental and off harmonics of diminishing importance:

$$F(x, t = 0) = F^0 - \frac{C}{2} + \frac{C}{2}\left[\frac{4}{\pi}\left(\sin(Kx) + \frac{1}{3}\sin(3Kx) + \frac{1}{5}\sin(5Kx) + \frac{1}{7}\sin(7Kx) + \frac{1}{9}\sin(9Kx) \ldots\right)\right] \quad (73)$$

where F^0 is the pre-bleach fluorescence intensity and C represents the initial contrast between the dark and bright striped regions immediately after photobleaching:

$$C = |F^0 - F_{min}(t = 0)| \tag{74}$$

where F_{min} is the minimum fluorescence intensity along the square wave pattern. The square wave representation neglects edge effects at the stripe boundaries and the circular or Gaussian illumination profile. Due to diffusion of fluorophores from the unbleached bright stripes into the dark bleached stripes the total contrast between stripes decays with time after photobleaching. This translates to a relaxation of the square wave pattern which amounts to multiple, simultaneous instances of diffusion in a sine wave boundary condition. Each component in the Fourier series decays exponentially, the first term or fundamental decays as $exp[-DK^2t]$, the third harmonic nine times faster as $exp[-D(3K)^2t]$, the fifth harmonic twenty-five times faster as $exp[-D(5K)^2t]$ and continues on. The first few terms of the Fourier series provide the boundary shape or sharpness of the square wave and these higher harmonics also decay quickly after photobleaching, and so the sharply defined square pattern quickly softens. Only the first few exponential terms are needed to represent the fluorescence recovery at any time integrated over all x:

$$F(t) = F^0 - \frac{C}{2} - \frac{C}{2}\frac{e^{-DK^2t} + \frac{1}{3}e^{-9DK^2t} + \ldots}{1 + \frac{1}{3} + \ldots} \tag{75}$$

When the illuminated region contains many stripes, the recovery caused by stripe-to-stripe probe transport will significantly outpace transport into and out of the spot itself, which is not a problem for a sample composed of single diffusers or multiple diffusers on similar time scales. But if the sample contains both significantly fast and slow diffusers then the

exchange of the slow component between the striped fringes may occur on the same time scale as the spot mode recovery caused by the fast component diffusing in the underlying Gaussian illumination pattern. The best solution to this issue is to separate the two recovery modes using a modulation detector to record the recovery associated with a selected Fourier component in the fringe pattern.[258]

Simple striped photobleaching is sufficient for single component monodisperse systems but becomes complicated and exhausting when analyzing multicomponent diffusers or polydisperse systems. This is because a single diffuser gives rise to multiple exponential terms. Another major problem with all FPR schemes presented so far is that they require deep bleaches, often exceeding 50%. A superior analysis technique was devised by Lanni and Ware,[259] and it involved modulation of the Ronchi ruling by translating it in a direction perpendicular to the stripes during recovery immediately after photobleaching is performed. The current, converted from fluorescence intensity at the detector first represents a triangle wave with a fundamental circular frequency ω that depends on the speed at which the Ronchi ruling is translated back and forth across the bleach pattern and the periodicity of the pattern. With time the triangle wave decays and is described by:

$$V(t) \propto C_1(t)\sin(\omega t) - C_3(t)\sin(3\omega t) + C_5(t)\sin(5\omega t) - C_7(t)\sin(7\omega t) + \ldots \quad (76)$$

Each exponentially decaying function represents the contrast decay associated with a particular Fourier component of the triangle wave:

$$C_n(t) \propto \frac{1}{n^2} e^{-n^2 K^2 D t} \tag{77}$$

In comparison to each component of the Fourier series for a square wave the contrast associated with the high harmonics of the above described triangle fade even faster due to the n^2 term. By simply using a lock-in amplifier or peak voltage detector after an amplifier tuned to the fundamental frequency, weakly oscillating signals can easily be detected. This permits shallow bleaches to be performed and each diffusing component produces a single exponential decay term instead of multiple ones which is the case for non-modulated systems (Figure 65A).

The exponentially decaying signals from FPR systems with modulation detectors can be analyzed in the same fashion as done by DLS. Analysis methods such as cumulants,[260] single or multiple exponentials with floating baselines, and Laplace inversion can be applied.[261] A common mistake in FPR experiments is measuring at spatial frequencies K that are too high. This is because the signal to noise improves as more photons are detected during the recovery period, which decreases as K increases. Probing long recoveries permits lower light levels, shallower bleach depths, reduced heating of the sample, reduced dye labelling, and associated artifacts from labelling. Measuring over a range of K values and obtaining respective characteristic diffusion recovery time τ_D values enables the calculation of the diffusion coefficient of probe molecules:

$$D = \frac{1}{K^2 \tau_D} \tag{78}$$

The diffusion coefficient obtained above represents an average self-diffusion of fluorophores in the sample. A plot of decay rate, Γ vs K^2 confirms the absence of non-diffusive recovery of fluorescence (spontaneous or chemical) if a linear least squares fit to the data passes through zero. The value of the slope of this plot is the diffusion coefficient (Figure 65B).

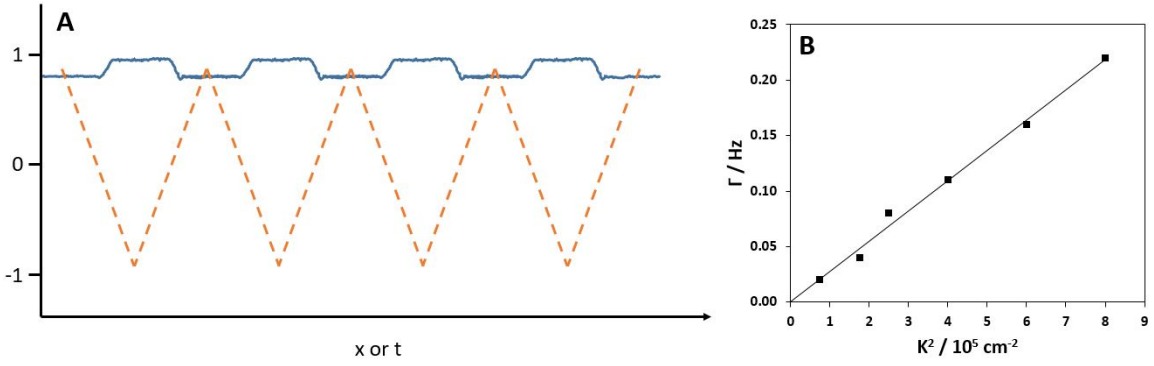

Figure 65. (A) The magnitude of fluorescence contrast (orange) between bleached and unbleached striped regions in the sample (blue) arises from when a Ronchi ruling is modulated perpendicular back and forth one half period to the striped pattern. This permits shallower bleach depths. (B) Linear dependency of Γ on K^2 with a linear least squares fit passing through the origin confirms that fluorescence recovery is purely diffusive.

4.2 Fluorescence Photobleaching Recovery Measurements of Binary Mixtures of NaPSS

4.2.1 Background

The diffusion of charged macromolecules in aqueous media is fundamental to understanding many processes that span applications in both industrial and biological areas.[262-264] From the DLS observations of PLL in low ionic strength solutions of NaBr in 1978 there has not been a greater challenge to further understanding this field.[93] The

discovery, since termed the “slow mode” or “ordinary-extraordinary transition”, describes the co-existence of a slow diffusive mode in addition to the fast mode of molecular motion. This observation has since been found in many other macromolecular systems that have been strong or weakly charged, biological or synthetic in nature. A strong polyelectrolyte is the subject of this work. A more comprehensive introduction and explanation of this controversial topic can be found elsewhere.[2, 4, 265]

The slower diffusive mode is attributed to large scale “heterogeneities” or “temporal aggregates” that form between like-charged macromolecules in the solution below a critical ratio of polymer to salt concentration (C_p/C_s). Attraction between like-charged polyelectrolytes has been owed to induced dipoles at intermediate length scales comparable to the correlation length and then the subsequent formation of quadrupoles to cause intra- and inter-chain binding.[266]

There is sufficient DLS evidence to substantiate the existence of the ordinary-extraordinary transition, but there are still many questions to be addressed. Little is known about the nature of temporary aggregates, for instance, how long do they persist in solution and maintain structural integrity, if and on what time scales do single chains exchange in and out of the aggregate, and what is the concentration ratio of aggregates exist relative to single diffusing chains and whether total polymer concentration and molecular weight will affect all of these processes.[117] In addition, only in DLS has the slow mode been observed and, as noted by earlier workers,[26] the problems associated with acquiring and interpreting DLS data on polyelectrolyte solutions provide strong motivation to try other methods, especially FPR[3, 38] and DOSY.[267]

FPR aims to provide further understanding of temporary aggregates and settle any debate over potential artefacts of the DLS technique. Sehgal and Seery investigated the effect of salt on the diffusion of NaPSS in NMF using FPR and found that measured self-diffusion coefficients were intermediate between the DLS fast and slow mode in the ordinary-extraordinary regime.[268] But the FPR and DLS comparison is imperfect because typical FPR length scales are maybe too long to capture the short existence of these temporary aggregates.[38] A single decay mode detected by FPR represents a weighted average of the multimacroion diffusion coefficient representative of temporary aggregates and the self-diffusion coefficient of a single polyelectrolyte chain, which may join and leave an aggregate many times during the much longer recovery time of FPR measurements.

In an attempt to overcome the shortcomings of acquisition time and distance scales one looks to the useful ability of FPR to measure the dynamics of a specific tracer molecule in a heterogeneous mixture. In 1997 Sedlak performed DLS measurements on mixed molecular weight systems of the same polyelectrolyte, NaPSS, to further understand the nature of the slow mode.[115-116] In an effort to test the residence time of probes in temporal aggregates Cong et al. performed FPR measurements on labeled NaPSS probes diffusing through an unlabeled NaPSS matrix of a single molecular weight and found no evidence of temporal aggregate formation.[146] We look to revisit FPR measurements of fluorescent NaPSS probes that encompasses a greater range of C_p/C_s in order to observe any diffusive transitions. In addition, we extend the mixed NaPSS system approach by exploring a greater range of matrix molecular weights and concentrations to determine if probes become entrained in matrix aggregates and adopt their dynamics, or remain free of them. In this study we developed several objectives and coupled them to testable hypotheses that

together reflect a plan that acknowledges the existence of temporal aggregates while respecting probe diffusion in multi-component systems.[23, 269-270]

The first is to measure the diffusion of single component solutions consisting of a range of fluorescent NaPSS (F-NaPSS) probe molecular weights as a function of the critical C_p/C_s ratio. Then we increase the probe concentration to see if aggregates become saturated and observe if the FPR decay signal moves from a single to double exponential. The second involves mixing F-NaPSS with an unlabeled matrix NaPSS (M-NaPSS) with the aim to increase matrix concentration for a series of probe molecular weights. If probes enter matrix aggregates and adopt their dynamics then probe diffusion becomes independent of probe molecular weight. Again using a mixed NaPSS system, the third approach aims to extend previous works by exploring a greater range of matrix molecular weights for a series of probe molecular weights and concentrations. If most probes remain outside the aggregates, the associated diffusion-coefficient should be independent of matrix molecular weight when high enough for entanglement to occur. Theoretical treatments of probe diffusion in the presence of matrix are also applied to better understand the forces that govern dynamics and elucidate whether temporal aggregates could be the cause for any non-Stokes-Einstein behavior. This is warranted as there is a lack of theoretical treatments for a model polyelectrolyte system at low salt where probe and matrix polymer are of the same chemical identity. Regardless of the reasons to examine ordinary-extraordinary dynamics it is important to study the diffusion of mixed polyelectrolytes at low salt for reasons ranging from polydispersity to biological function, as charged macromolecules are often found mixed with others.

4.3 Experimental

4.3.1 Materials

Sodium 4-vinylbenzesulfonate, 2,2'-bipyridine (bpy) (> 99.0%), copper (I) chloride (CuCl) (>99.995%), sodium chloride (NaCl) (>99.0%), copper (II) chloride ($CuCl_2$) (97.0%), 4-(bromomethyl)benzoic acid (97.0%), sodium hydroxide (NaOH) (>97.0%), fluorescein isothiocyanate isomer 1 (FITC) (>97.5%), and pyridine (>99.0%) were purchased from Sigma Aldrich and used as received. Ethanol (>99.5%, KOPTEC) and methanol (>99.8%, BDH) were purchased from VWR. Sodium nitrate ($NaNO_3$) (>99.0%) was purchased from J. T. Baker. 4-vinylaniline (90%), and sodium phosphate monobasic (NaH_2PO_4) (99.9%) were purchased from Fisher Scientific. Hydrochloric acid standard solution 5 M (HCl) was obtained from Fluka Analytical. Deionized water (18 MΩ·cm) was drawn from a Millipore Milli-Q Type I source.

4.3.2 Synthesis

Non-fluorescently labeled, perfectly sulfonated NaPSS across a range of molar masses was synthesized using an ATRP technique that has been previously described.[217]

Fluorescently labelled NaPSS was synthesized by incorporating a FITC-vinylaniline comonomer adduct at approximately a 1% ratio to the 99% sodium 4-vinylbenzesulfonate monomer before conducting the ATRP reaction.

Fluorescently labeled comonomer was synthesized by dissolving 38 mg of FITC in 8 mL of 200-proof ethanol under stirring in a sealed flask and purged with argon for 30 min. Via syringe, 10 μL of 4-vinylaniline was added and the reaction was heated at 50 °C for 1 h,

then removed from the heat and left to stir for 24 h under an argon atmosphere. The comonomer was obtained from rotary evaporation as a bright orange-yellow powder.

4.3.3 Purification of NaPSS

All NaPSS samples were dissolved in water and dialyzed using 3500 MWCO dialysis membrane tubing against pH 7 water with 1000 times the sample volume of dialysis liquid used. Water was evaporated and the NaPSS powder was vacuum dried until no further mass reduction was measured. Fluorescently labeled NaPSS samples were continuously dialyzed until unreacted fluorescent monomer ceased to be observed in the dialysate which was determined by observing no fluorescence when passing a hand held 2 W blue laser through the dialysate.

4.3.4 Molecular Weight Characterization

The SEC-MALS system consisted of an Agilent 1260 infinity II with online degasser, an ISO pump and 1260 vialsampler connected to an Agilent PL aquagel-OH 8 μm guard column prior to two Agilent PL aquagel-OH Mixed-H 8 μm columns connected in series. The MALS system consisted of a Wyatt Dawn Heleos-II with a Wyatt Optilab T-rEX differential refractive index detector operating at 658 nm. Agilent OpenLab software was used to operate the SEC and data acquisition and analysis were done with Wyatt Astra 7.1 software. The mobile phase was a buffer solution of 0.3 M $NaNO_3$ + 0.01 M NaH_2PO_4 + 0.02% NaN3 at pH 9 under a flow rate of 1.0 mL/min. Polymer samples of concentration ~5 mg/mL were dissolved for 24 h prior to measurements to ensure complete dissolution. Solutions were filtered through Whatman Anotop 0.2 μm filters into Agilent 2 mL SEC vials. All chromatograms shown display the light scattering trace data taken from the 90°

detector. Duplicate injections (100 μL) were performed for each sample measured by SEC-MALS and the resulting chromatography was found to be replicable in all cases. The specific refractive index increment $\delta n/\delta c$ was previously determined to be 0.172 mL/g for NaPSS in buffer solution of 0.3 M $NaNO_3$ + 0.01 M NaH_2PO_4 + 0.02% NaN_3 at λ_0 = 658 nm.

4.3.5 Viscosity

Viscosity measurements were conducted with a RheoSense microVISC portable viscometer equipped with an A05 chip which contains a 50 μm flow channel depth. M-NaPSS solutions were prepared in 1 mM NaCl and filtered through Whatman Anotop 0.2 μm filters. Measurements were made using approximately 100 μL of solution injected into the viscometer which was temperature controlled at 20 ± 0.05 °C. A minimum of 5 measurements were made for each reported viscosity value.

4.3.6 UV-vis

UV-vis spectra were recorded using an Agilent 850 UV-vis spectrometer. FITC and F-NaPSS solutions were prepared in 0.01 M NaCl and transferred into a disposable plastic cuvette (1 cm path length). The absorption peak maximum observed from the spectra was taken to be 492 nm for both FITC and F-NaPSS, indicating that the labelling procedure did not cause changes in the optical properties of the dye. The degree of dye labeling on the polymer chain was determined via construction of an FITC calibration curve, which was compared to the spectra of 2 mg/mL F-NaPSS solution. Conversion of F-NaPSS to moles by dividing by the monomer molar mass (206 g/mol) permitted the calculation of a molar ratio between F-NaPSS and FITC. This ratio was around 3200, meaning for every 3200

monomer units there was a FITC moiety. Using F-NaPSS with an M_w of 590 kDa, degree of polymerization approximately 2900, meant that the degree of dye labelling was approximately 0.8-0.9 labels per polymer chain assuming a random distribution of dye functionalized monomer addition throughout the reaction.

4.3.7 FPR Instrument

The fundamental aspects of the FPR instrument (Figure 66) are modelled around the modulation detection system designed by Lanni and Ware,[259] and Fong et al.[271] Ronchi rulings (Edmund Scientific) were mounted in the rear image plane atop a cradle fitted between two opposing 4 inch loudspeakers (Radio Shack), which operate inaudibly at 16 Hz and driven by an audio amplifier that is fed a triangle wave from a signal generator. The amplitude of the wave is adjusted to move the Ronchi ruling by one stripe width. The frequency of the triangle wave is locked in using a low noise preamplifier (Stanford Instruments) and discards any signal acquired at lower frequencies. A single diode laser (2W at 435 nm) produces both the bleaching and reading beams by switching the intensity through a TTL high to low intensity device. The beam illuminates the Ronchi ruling before hitting a dichroic mirror positioned above the objectives in an Olympus upright microscope with a majority of the light being directed to down to the sample and a portion into the eyepiece for viewing. Fluorescent light from the sample captured by the objectives moves up through a bandgap filter and shutter before entering a photomultiplier tube.

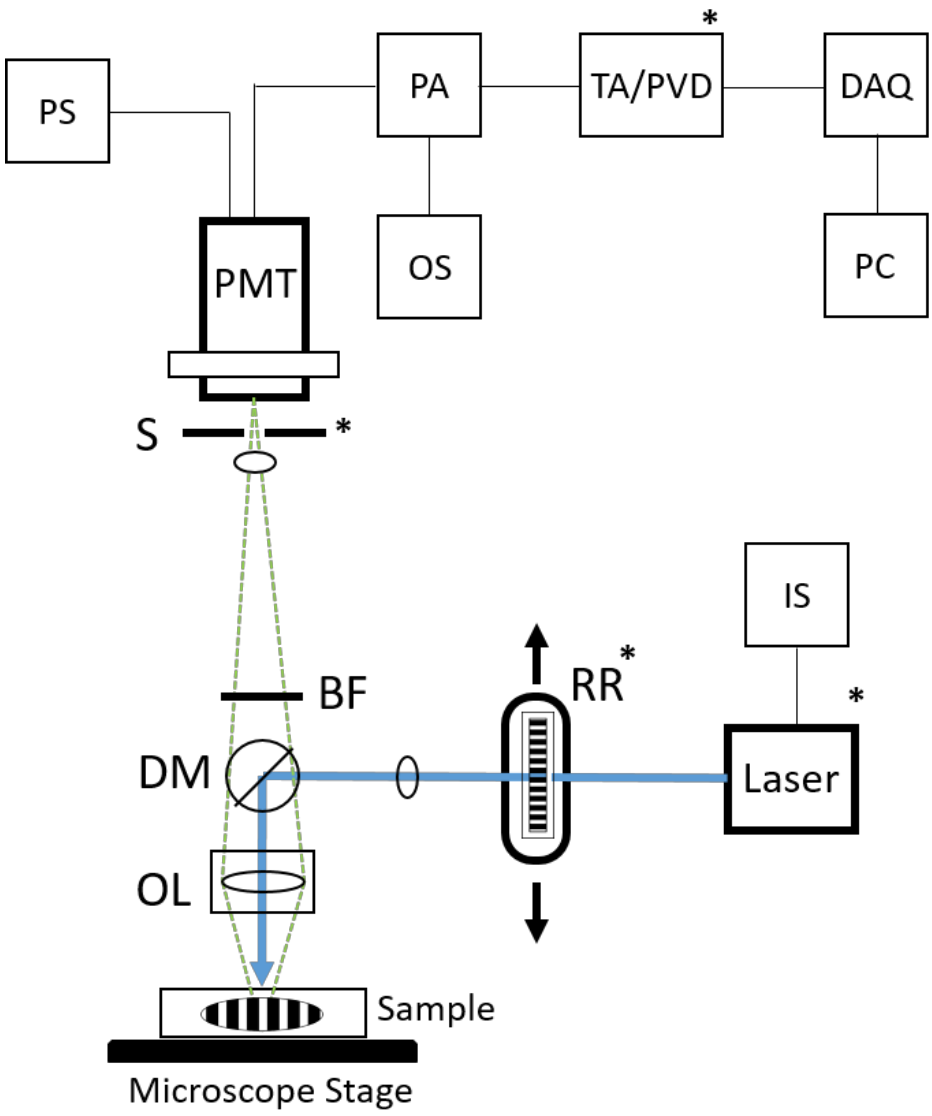

Figure 66. Schematic of the FPR device. RR = Ronchi ruling, DM = dichroic mirror, OL = objective lens, BF = barrier filter, S = shutter, PMT = photomultiplier tube, PS = power source, PA = preamplifier, OS = oscilloscope, TA/PVD = tuned amplifier/peak voltage detection circuitry, DAQ = data acquisition and control interface, PC = computer, IS = intensity shifter. The symbol * means that component is computer controlled.

4.3.8 FPR Operational and Analysis Details

All NaPSS samples were dissolved in NaCl solutions of varying concentrations and prepared at least 24 hours prior to being loaded into flame sealed rectangular capillary cells

of path length 100 μm (Vitrocom, Mountain Lakes, NJ). A range of spatial frequencies from 157 to 1170 cm^{-1} were selected for measurements and bleaching times ranged from 0.1-2 seconds, which were approximately 10-100 times shorter than the recovery time. Two Ronchi rulings (50 and 100 lines/inch) and four long working distance objectives (4, 7, 10 and 18X) were used to span the spatial frequency range. Single-exponential decay fits were used to analyze most of the FPR measurements and each diffuser in the multicomponent system (free polymer or bound in temporal aggregate) was assigned its own single decay term. Sufficient fits also reflect the low dispersity of the NaPSS samples. The control software for the instrument is written in LabView (National Instruments) and the data fitting and analysis was performed using a custom ANSCAN program written in Visual Basic (Microsoft).

4.3.9 FPR theory

For a single diffuser the change in fluorescence amplitude, representing the contrast created immediately after bleaching the striped pattern $C(0)$, fades with time $C(t)$ according to a single exponential:

$$C(t) = C(0)e^{-K^2Dt} \tag{79}$$

where $K = 2\pi/L$ is the spatial frequency and D is the tracer diffusion coefficient of the labelled species . A plot of K^2 versus FPR relaxation time Γ produces a slope equal to the self-diffusion coefficient according to the relation:

$$\Gamma = \mathrm{D}K^2 \tag{80}$$

When multiple types of diffusers are present the recovery of fluorescence signal is multiexponential:

$$C(t) = \sum_{i=1}^{M} F_i \, e^{-K^2 D_i t} \tag{81}$$

where F_i represents the fluorescence intensity of the i^{th} diffuser and M is their mass.

4.4 Results and Discussion

4.4.1 Calculation of degree of labelling by UV-Vis

In order to determine the degree of FITC dye labels per polymer chain, averaged by the weight average molecular weight, a calibration curve obtained by absorbance from neat sodium fluorescein in solution is developed and then compared to the absorbance profiles of F-NaPSS (Figure 67).

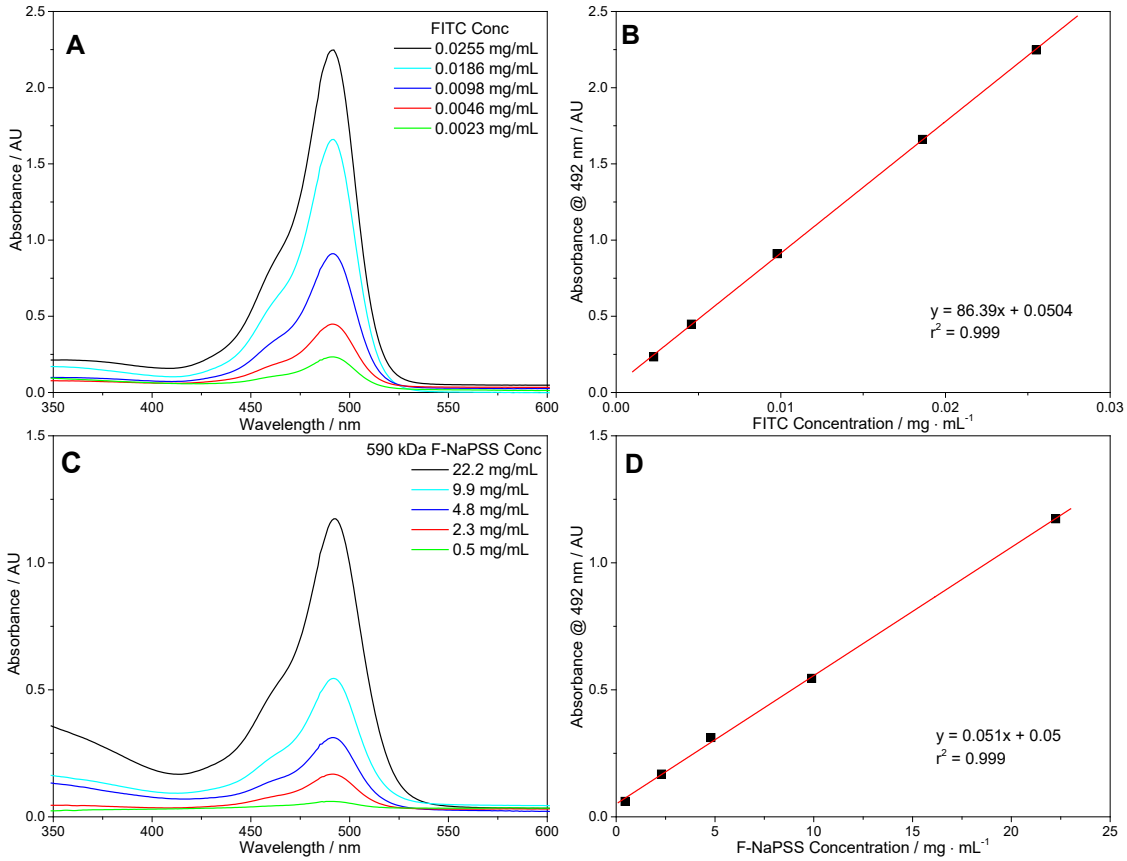

Figure 67. (A) UV-Vis spectra of sodium fluorescein in water at different concentrations, (B) calibration curve of sodium fluorescein between absorbance and concentration, (C) UV-Vis spectra of 546 kDa F-NaPSS in water at different concentrations and, (D) calibration curve of F-NaPSS showing dependence of absorbance on concentration.

The absorbance of 20 mg of 590 kDa NaPSS based on the calibration equation $y = 0.051x + 0.05$ equals 1.07, a value that corresponds to 0.0118 mg of FITC based on the calibration equation $y = 86.39x + 0.0504$ (Figure 67B). Hence the number of moles of FITC present in 20 mg of F-NaPSS sample is 3.034 x 10^{-8}. The number of moles of 20 mg of F-NaPSS, based on the monomer molar mass of 206 g · mol^{-1} for styrene sulfonic acid sodium salt, is 9.7087 × 10^{-5} moles. The molar ratio of F-NaPSS to FITC is 3200 and the number of repeat units on a polymer chain based on its weight average molecular weight of 590 kDa is 2864. Hence, assuming random incorporation of dye-functionalized

monomer during polymerization, there should be approximately 0.89 FITC units per F-NaPSS chain (2864/3200).

4.4.2 SEC-MALS Characterization

Molar mass distributions for F-NaPSS and M-NaPSS samples were obtained with SEC-MALS. All samples displayed monomodal and relatively symmetrical normalized light scattering traces from the 90° detector (Figure 68).

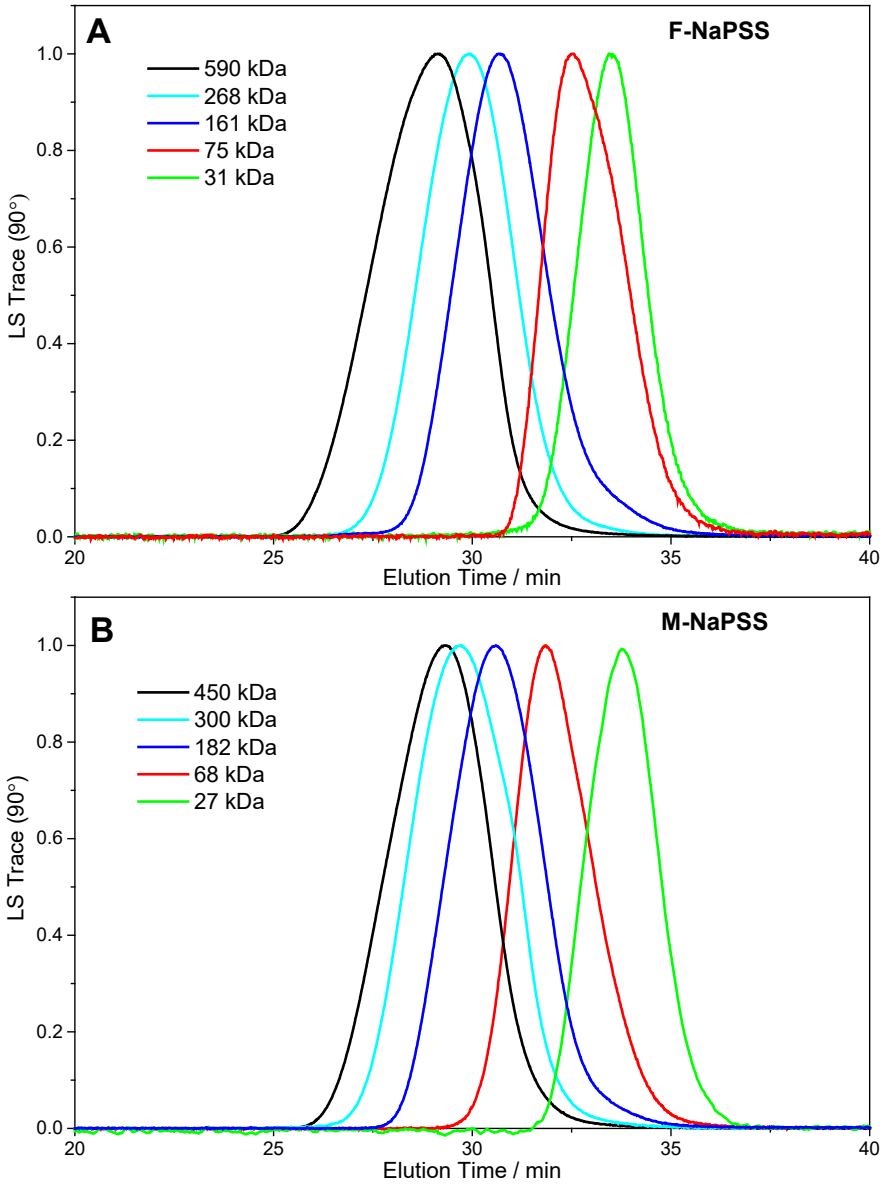

Figure 68. SEC-MALS chromatograms observed at the 90° detector for (A) F-NaPSS and, (B) M-NaPSS. The SEC eluent is 0.3 M NaNO3 + 0.01 M NaH2PO4 + 0.02% NaN3 and the corresponding Mw for each sample is stated. A δn/δc value of 0.172 mL/g was used.

Weight average molecular weights ranged from 31 to 590 kDa for F-NaPSS and 27 to 450 kDa for M-NaPSS, respectively, and dispersities ranged from 1.06 to 1.25 (Table 4).

Table 4. Molar mass and dispersity data for F-NaPSS and M-NaPSS.

Sample Code	M_n (kDa)	M_w (kDa)	$Đ$
F-NaPSS 31	29	31	1.06
F-NaPSS 75	64	75	1.17
F-NaPSS 161	129	161	1.25
F-NaPSS 268	228	268	1.18
F-NaPSS 590	481	590	1.22
M-NaPSS 27	26	27	1.04
M-NaPSS 68	60	68	1.13
M-NaPSS 182	145	182	1.25
M-NaPSS 300	252	300	1.19
M-NaPSS 450	369	450	1.21

Conformation plots of R_G versus M, with each axis plotted on a logarithmic scale, are based on the Flory relationship $R_G \sim M^v$, which when expressed in logarithmic fashion provides the equation of a straight line with slope v. The shape of the line and its slope describe the architecture of a polymer in solution. Conformation plots for three F-NaPSS and M-NaPSS samples of comparable molecular weights show no distinct differences which confirms that the dye labeling process does not impart significant conformational changes on the F-NaPSS materials (Figure 69).

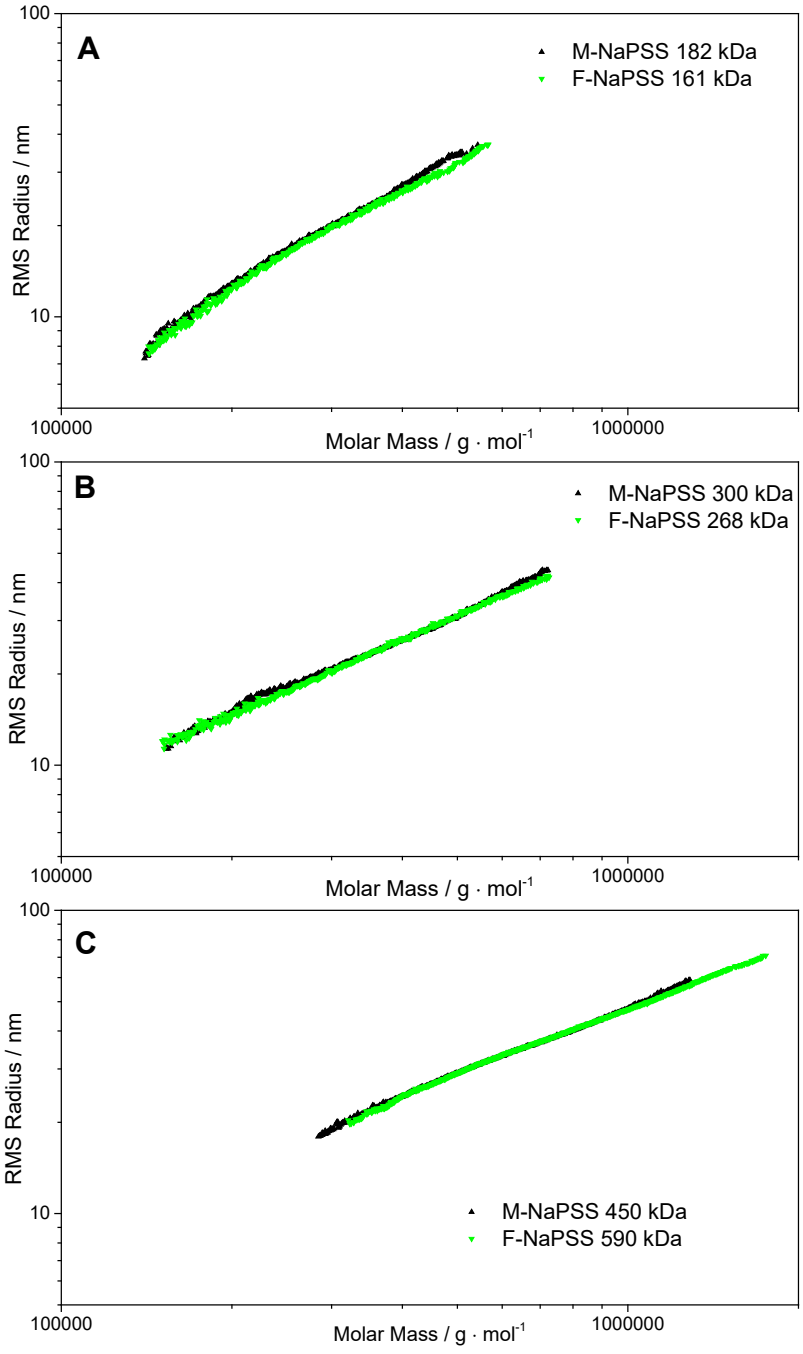

Figure 69. Conformation plots of M-NaPSS and F-NaPSS of similar molecular weights overlaid to demonstrate negligible conformation change from dye labeling for (A) 161 kDa F-NaPSS, (B) 268 kDa F-NaPSS and (C) 590 F-NaPSS. The SEC eluent is 0.3 M $NaNO_3$ + 0.01 M NaH_2PO_4 + 0.02% NaN_3 and the corresponding M_w for each sample is stated. A $\delta n/\delta c$ value of 0.172 mL/g was used.

4.4.3 Viscosity of matrix NaPSS

Viscosities of M-NaPSS polymers of a variety of molecular weights and concentrations in solution of 0.001M NaCl were obtained (Figure 70).

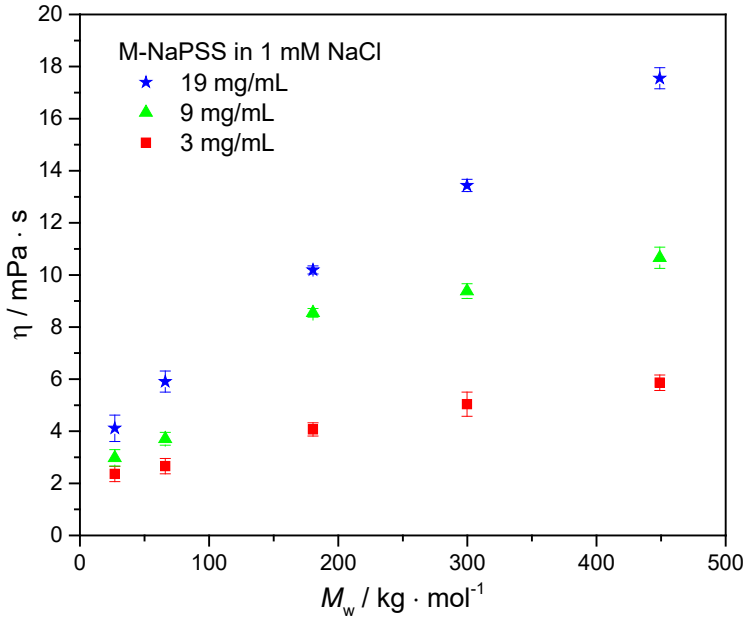

Figure 70. Viscosity versus M_w for M-NaPSS in 1 mM NaCl solution at polymer concentrations of 3, 9 and 19 ± 0.05 mg/mL.

4.4.4 Testing the FPR instrument with FITC in solution

The AC trace is the time-dependent magnitude of the contrast in fluorescence intensity between the bleached and unbleached stripes as the Ronchi ruling is modulated back and forth over the pattern (Figure 71A). The DC voltage is a measurement of the total fluorescence measured from the region. From the height of the AC trace the characteristic relaxation time (1/e = 0.37 of the height) is approximately 8 seconds which means the acquisition should be run at least 10 times that length for a reliable exponential fit. Shorter

acquisition times are acceptable for monodisperse samples. A logarithmic AC perspective shows a linear trend which shows the recovery of fluoresence is purely diffusion related (Figure 71B). Plots of Γ vs K^2 show data for FITC in solutions of varying NaCl concentration trend through the origin with no deviation in slope, hence the diffusion coefficients are independent of ionic strength as is expected for a nonionic molecule (Figure 71C and D).

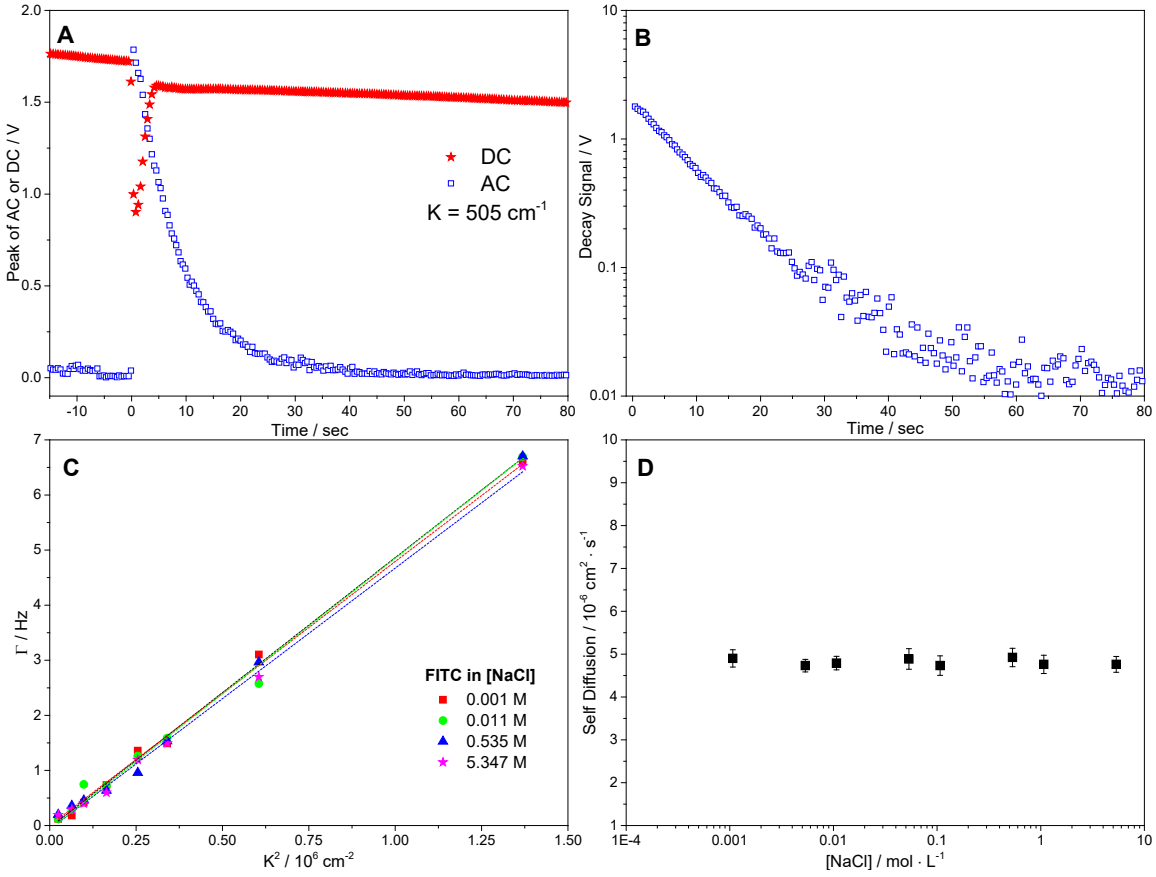

Figure 71. (A) Raw FPR signal for AC and DC voltage, (B) AC contrast decay plotted in logarithmic scale showing it is linear over the characteristic decay period, (C) Γ vs K^2 for FITC at different NaCl concentrations as stated, (D) no dependence of the self-diffusion coefficient was observed for the nonionic FITC molecule in salt solutions.

4.4.5 Expected onset of ordinary-extraordinary behaviour

Drifford and Dalbiez[9-10] showed that for the NaPSS-NaCl system the onset of the ordinary-extraordinary transition occurs at a critical ratio of polymer concentration C_p to salt concentration C_s:

$$\frac{C_p}{C_s} \simeq 5.7 \tag{82}$$

where for values above this critical ratio the simultaneous occurrence of both slow and fast modes are to be observed. This threshold ratio also depends on the concentrations of each component as the splitting of the diffusive transition is observed when C_p and C_s are shifted to higher values but now with a ratio at about unity.[7]

For the single component F-NaPSS system investigated here the polymer concentration remains fixed at about 10 mg/mL, where the $C_{p,monomer}$ equals 0.05 M (monomer = 206 g/mol). For a $C_p/C_s > 5.7$ the ordinary-extraordinary behavior should be exhibited, and so the NaCl concentration for this system must be lower than about 0.01 M.

4.4.6 Single NaPSS molecular weights

A typical recovery profile shows the DC trace (total fluorescence) and AC trace (fluorescence pattern contrast), which follows single exponential decay behavior (Figure 72A). A plot of Γ vs K^2, constructed from fluorescence recovery profiles of solutions of F-NaPSS 268 at varying NaCl concentrations and at varying spatial frequencies, shows that within uncertainty the data trends to the zero intercept (Figure 72B). This implies that fluorescence recovery is absent of convection and/or chemical recovery of the dye.

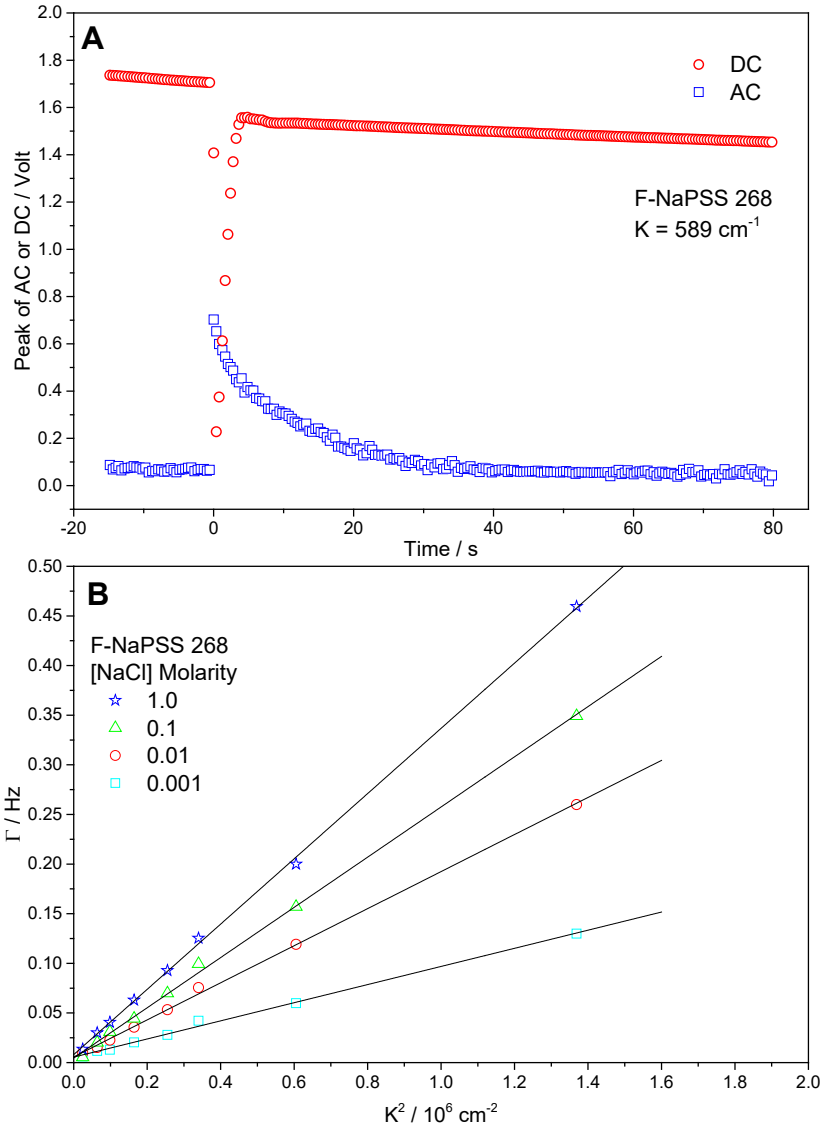

Figure 72. (A) FPR AC trace recovery profile for F-NaPSS 268 in NaCl solution; *K* = 589 cm^{-1}. (B) Plot of Γ vs *K*2 for F-NaPSS 268 at different NaCl concentrations and *K* values showing fits that trend through zero to indicate fluorescence recovery solely by diffusion.

Conclusive evidence for the existence of the ordinary-extraordinary transition has been routinely confirmed by the DLS technique on single molecular weight NaPSS solutions. But while FPR has been used to study polyelectrolytes at low salt, there has not been any evidence to suggest the existence of two diffusive modes. This is because the comparison

of FPR to DLS to probe the ordinary-extraordinary transition is imperfect for two main reasons. The first and more obvious is that DLS senses cooperative motion producing a mutual diffusion coefficient whereas FPR senses an optical tracer and produces a self-diffusion coefficient. The second, and key reason, is that FPR typically measures diffusion on long time and distance scales, with FPR ($2\pi/K \sim 50\text{-}100 \times 10^3$ nm) being orders of magnitude larger than DLS distance scales ($2\pi/q \sim 200\text{-}2000$ nm). Therefore the temporary aggregates responsible for the slow diffusive mode need only exist for a short time to relax the DLS correlation function but may not maintain integrity for the requisite 1000-10000 times longer in order to be sensed by FPR. The result is that the low spatial frequency FPR instrument will obtain a self-diffusion coefficient that represents the average collective motions of both the slow and fast diffusive modes of the ordinary-extraordinary transition. This then provides a tool to indirectly detect extraordinary diffusion in NaPSS solutions. Tracking diffusion below the threshold C_p/C_s value will return "normal" diffusive behavior of single chains, but above the threshold C_p/C_s the measured diffusion also has the contribution of much slower-moving temporary aggregates.

The first objective, variation of polymer concentration in a single component F-NaPSS probe system, is designed to explore qualitatively the equilibrium between polyelectrolytes that are contained in the temporal aggregates and those that are free of them. If the temporal aggregates can be saturated as probe concentration rises, we may expect additional probe molecules will lead to one of two effects. If two modes are detected, one for free probe and one for bound probe the amplitude of the faster mode might be expected to increase. If only one mode is seen, as we expect of FPR measurements on a long distance scale, it may mean that chains exchange in and out of aggregates quickly on the time scale of the experiment.

We tested this hypothesis by measuring diffusion of F-NaPSS at increasing polymer concentrations, passing through a dilute to semidilute regime, while staying above the C_p/C_s for all measurements. In salt-free solutions, fully sulfonated F-NaPSS 161 has a degree of polymerization of 780, which therefore has an overlap concentration of approximately 0.01 M (around 2 mg/mL).[23] With some salt it is expected to be a bit higher. We tested NaPSS concentrations from 0.93 – 30.93 mg/mL (0.004-0.15 M) at a fixed NaCl concentration of 0.01 M (Figure 73). This plot is counter-intuitive to what we expect from theory which states that diffusion in the dilute regime is independent of C_p and by comparison scales more greatly with concentration in the semidilute regime. We see a sharp decrease in diffusion in the dilute regime followed by a more gradual decrease in diffusion in the semidilute. This could be due to the ratio of C_s to C_p becomes significantly smaller relative to increasing the C_p. Therefore there is a variation of free ions in solution that can screen the increasing number of charged polyelectrolyte repeat units within each polymer concentration regime. This would have the effect causing the polyelectrolyte chain to expand as C_p increases.

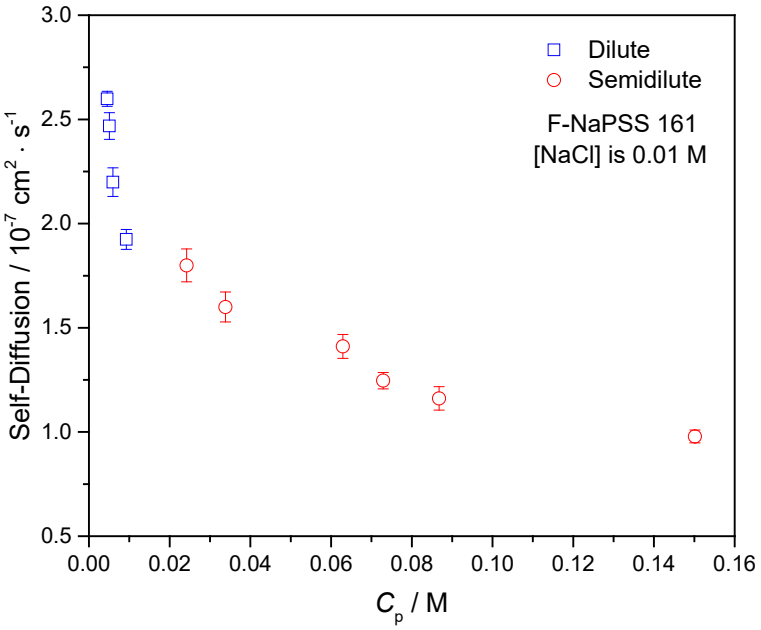

Figure 73. Self-diffusion coefficients for F-NaPSS 161 at increasing C_p with C_s fixed at 0.01 M. Dilute and semidilute concentrations regimes are indicated and calculated from theory for NaPSS under low salt conditions.

With the aim to encourage more chains to enter temporary aggregates to increase the amplitude of the slow mode, the measured FPR decaying contrast signal was inspected for biexponential behavior at various measured spatial frequencies as probe concentration was increased (Figure 74). As expected for a long-distance FPR measurement, the traces followed single exponential behavior, meaning that the chains exchange quickly in and out of the aggregates on the time scale of the experiment.

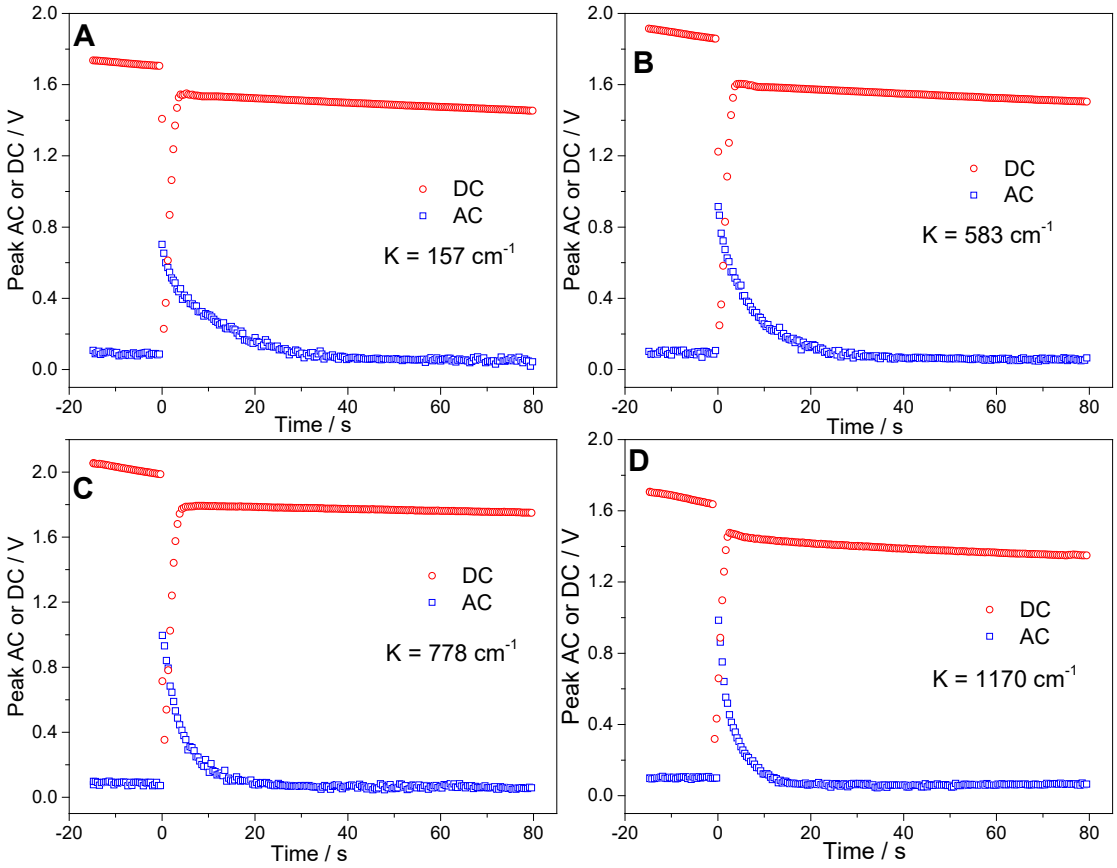

Figure 74. FPR AC decay traces for F-NaPSS 161 at a C_p of 0.09 M and increasing spatial frequencies from K = 157 cm^{-1} for (A), through K = 1170 cm^{-1} for (D).

While only a single diffusive mode was detected for F-NaPSS 161, this mode is qualitatively different if below or above the critical C_p/C_s threshold value. A decrease in diffusion above the critical C_p/C_s threshold is expected due to the contribution of formed aggregates to the system dynamics, which is now on average slower compared to faster moving probes that diffuse freely of aggregates below the C_p/C_s threshold. This was explored by measuring the diffusion coefficients of F-NaPSS samples of a range of molecular weights and over C_p/C_s ratio values that spanned four decades (Figure 75). Polymer interaction was expected at the semidilute concentrations measured across the varying C_p/C_s values. As expected the diffusion slowed as C_p/C_s increased and even more

so beyond the critical ratio threshold where diffusion appeared to decrease more substantially. A trend line fitted to the data points below the critical threshold was extended over the C_p/C_s region where ordinary-extraordinary behavior is expected to occur as a guide to the eye. The furthest right 3 data points, which are at C_p/C_s values above the critical ratio, deviate below the projected trend line, indicating that slow moving temporal aggregates could be contributing to the measured diffusion coefficient.

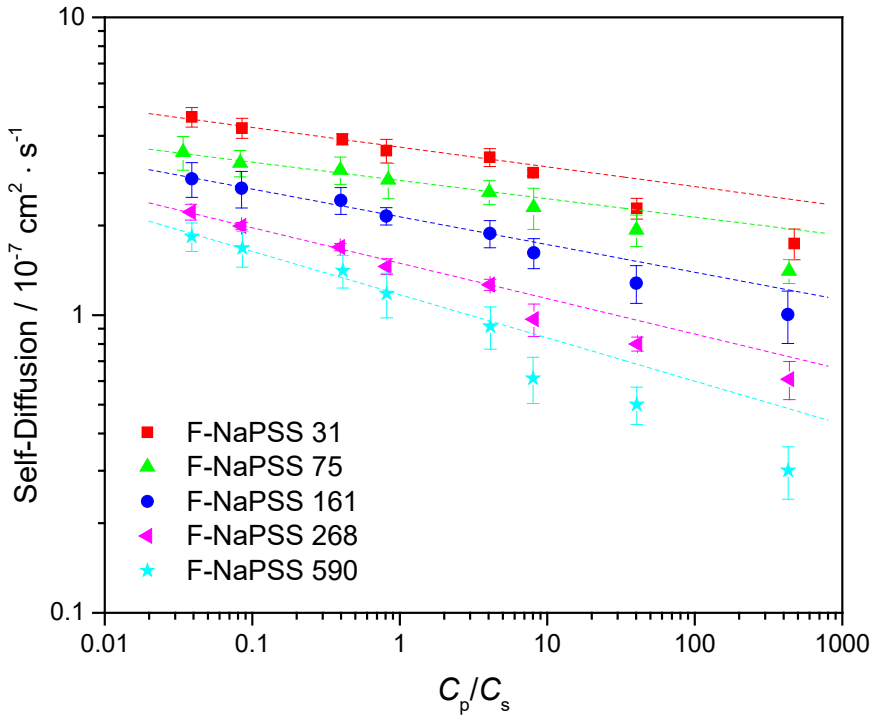

Figure 75. Self-diffusion coefficients as a function of the C_p/C_s ratio for F-NaPSS of varying molecular weight. Fits are made to the left 5 data points (below critical C_p/C_s threshold) to highlight a deviation for the right 3 data points (above critical C_p/C_s threshold) from the exhibited decreasing trend in diffusion.

F-NaPSS 268 had a self-diffusion coefficient of $8.0 \times 10^{-8} \pm 0.4$ cm$^2 \cdot$ s^{-1} at [NaCl] of 0.001 M ($C_p/C_s \approx 40$), which was comparable to the value of 7.7×10^{-8} cm$^2 \cdot$ s^{-1} for 200 kDa

NaPSS at similar polymer and NaCl concentrations obtained by Sehgal and Seery.[268] Similar to their findings, and unlike what is observed in DLS, we also did not observe a dramatic transition in the self-diffusion coefficient at the critical C_p/C_s ratio for the onset of the ordinary-extraordinary transition, which suggests there is no catastrophic change in the polymer conformation. A self-diffusion coefficient of $2.43 \pm 0.3 \times 10^{-7}$ cm$^2 \cdot$ s^{-1} for F-NaPSS 161 ($C_p/C_s \approx 0.085$) compared with measurements made by Cong et al.[38] for 167 kDa NaPSS of approximately 2.5×10^{-7} cm$^2 \cdot$ s^{-1} at a concentration of 0.09 M NaCl ($C_p/C_s \approx 0.09$). Theoretical arguments by Tanahatoe and Kuil using a wormlike chain model, taking into account persistence lengths, excluded volume and counterion condensation, calculated diffusion coefficients for NaPSS of 77 kDa at 0.1M NaCl of around 3×10^{-7} cm$^2 \cdot$ s^{-1}.[272] This agrees well with our F-NaPSS 75 which exhibits a diffusion coefficient of $3.07 \pm 0.03 \times 10^{-7}$ cm$^2 \cdot$ s^{-1} at a similar NaCl concentration ($C_p/C_s \approx 0.4$).

4.4.7 Scaling relations

The molecular weight scaling exponent for labeled NaPSS averaged over a variety of salt concentrations, β in $D_{probe} \sim M_{probe}^{-\beta}$ was found to be 0.54 ± 0.06 over a NaCl concentration range of 0.001 – 1 M, which is a typical value for random coil polymers in dilute solutions (Figure 76).[5] Cong et al. reported a β value of 0.67 ± 0.01 at low salt, consistent with an expanded random coil and in agreement with the increase of β to 0.65 ± 0.05 we observed at lower salt.[146] DLS results from Tanahatoe and Kuil of NaPSS at 0.1 M NaCl ($\beta = 0.61 \pm 0.04$),[272] and from Cong et al. at 0.2 M $NaNO_3$ ($\beta = 0.59 \pm 0.05$),[38] are consistent with our observations at lower salt. The average value is supported by diffusion scaling data obtained by other FPR practitioners. Bu and Russo[273] measured the diffusion of labeled

dextran in water, obtaining $\beta = 0.53 \pm 0.02$ over a molecular weight range similar to that tested in this study. Furukawa and Ware[274] reported $\beta = 0.52 \pm 0.01$ for the infinite dilution diffusion values for fluorescein labelled dextran in the presence of several matrix dextran molecular weights. Doucet et al.[275] also achieved similar results for fluorescently labeled pullulans in dilute solution: $\beta = 0.5$.

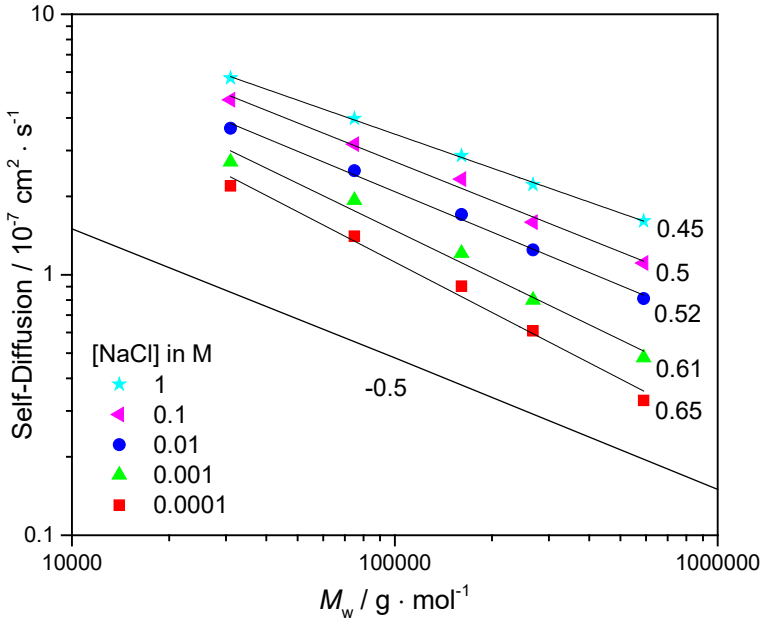

Figure 76. Self-diffusion coefficient as a function of F-NaPSS molecular weight at varying NaCl solution concentrations with provided slope β values and fits to the data to guide the eye. A line of slope of -0.5 is provided as a reference.

4.4.8 Diffusion of binary mixed NaPSS

Diffusion of mixed molecular weight polyelectrolytes is important for reasons ranging from polydispersity to biological function as charged macromolecules are often found with others. Transport of an F-NaPSS probe through M-NaPSS can offer insight into temporal aggregate behavior as well as mixed molecular weight diffusion.

The slow mode diffusive mode as observed by DLS has largely been shown to exhibit behavior independent of molecular with the size of the temporal aggregates to remain constant around 80 nm radius.[88, 265, 276] Contrary to this Jia and Muthukumar found that the slow mode disappeared as the molecular weight of NaPSS decreased to 126 kDa while still above the threshold ratio.[277] In a search for characteristics to better define temporary aggregates, Sedlak performed DLS measurements on binary mixtures of NaPSS having different molecular weights and found three diffusive modes.[115-116] It is difficult to interpret such results, especially when DLS is applied to solutions in which the scatterers interact strongly, which is the case for an osmotically stiff system. FPR offers the ability to separate the signals from a binary polyelectrolyte system and selectively track only the component that is fluorescently labeled. No change in overall concentration is induced by photobleaching and polymers with bleached dye labels are very similar to those with their dye moieties still intact. As a result FPR is insensitive to thermodynamic interactions amongst components which is in contrast to DLS. The self-diffusion coefficient of the fluorescently labeled component can be associated with the self-diffusion coefficient of unlabeled polymer if the dyes do not induce any conformational changes, which is the case for NaPSS,[278] and is evident from conformation plots in Figure 69.

The second objective rests on the observation[12;13;35] that the size of the temporal aggregates (typically 80 nm radius) depends weakly on molar mass. If probe particles are induced by rising matrix concentration to enter the temporal aggregates, and if they stay there for a time long compared to the acquisition time of the FPR measurement, then the associated diffusion coefficient will be that of the molecular-weight-independent aggregates. The usual molecular weight dependence of diffusion in dilute solutions would almost vanish as

matrix is added. A series of probes, at fixed concentration, but with molecular weights of 31, 161 and 590 kDa were separately mixed with a 450 kDa M-NaPSS of varying concentration (Figure 77). If rising matrix concentration encouraged a substantial amount of probes to enter aggregates then the probe diffusion coefficient should be independent of probe molecular weight. This would be evident if the diffusion coefficients at each probe molecular weight converged to equivalent values at high enough matrix concentrations. Instead we found that probe diffusion depended on molecular weight at all matrix concentrations tested and even at higher matrix concentrations (C_{matrix}) the different sized probes had distinctly different diffusion coefficients (Figure 77A). Failure of the hypothesis suggested that the probes spend much time independent of the temporal aggregates, their diffusion retarded by the usual mechanisms of entanglement or physical impediments imposed by the matrix. The scaling exponent β increased in the presence of a higher matrix concentration, rising from 0.64 ± 0.02 to 0.75 ± 0.05 for C_{matrix} of 3 and 20 mg/mL, respectively (Figure 77B). Cong et al. reported β = 0.95 ± 0.05 measured from three probe NaPSS molecular weights in the presence of a 990 000 g/mol matrix at concentrations an order of magnitude higher than used here.[146] It is to be expected that β climbs as matrix is added, with values of 1 resembling Rouse-like dynamics,[279] and the expectation for reptation at values of 2.[5, 270] This is evidence that entanglements are negligible at the matrix concentrations measured here.

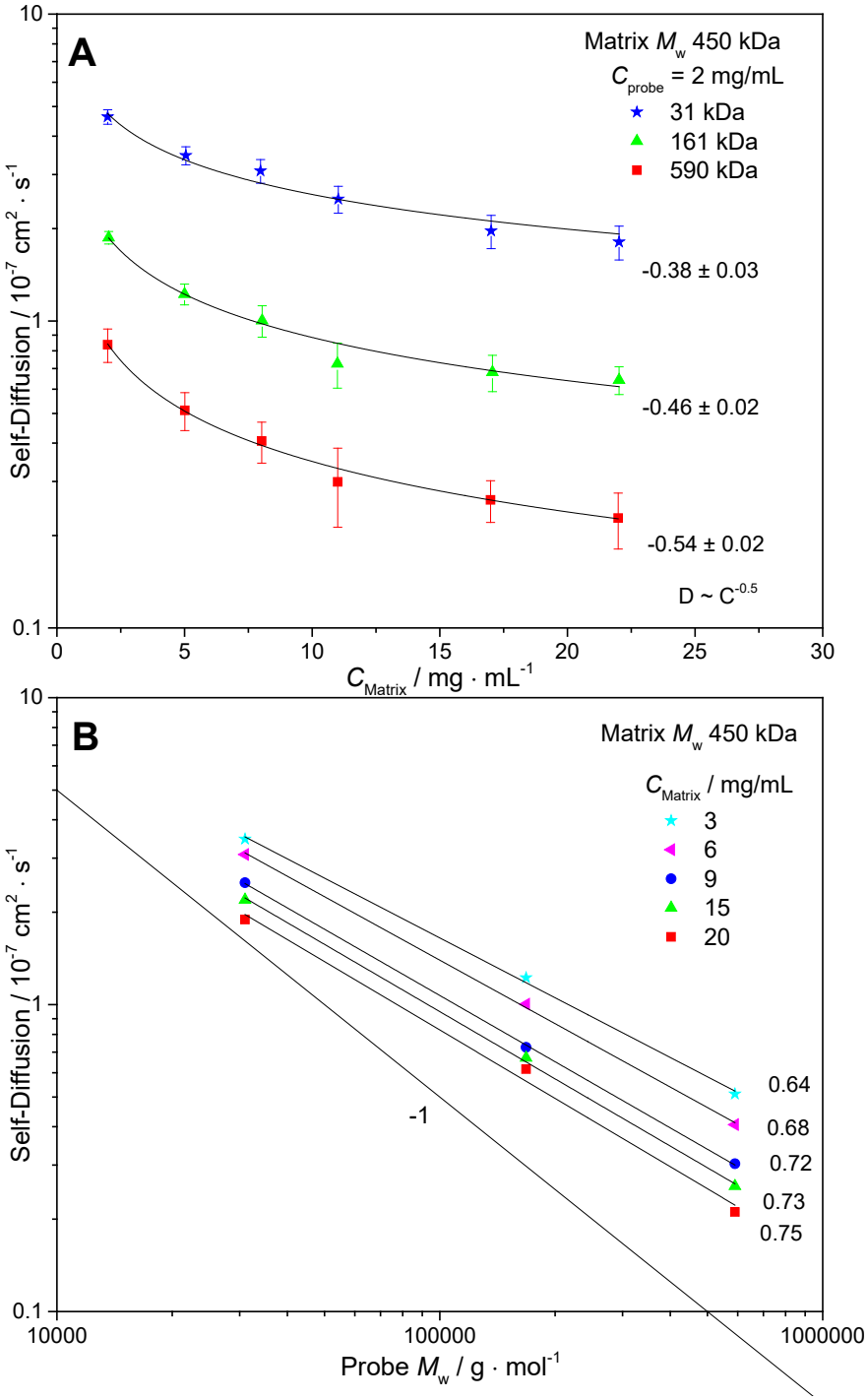

Figure 77. (A) Self-diffusion coefficients for F-NaPSS 31, 161 and 590 mixed with M-NaPSS 450 at varying Cmatrix. A dependence of diffusion on probe molecular weight is seen. A fit to the diffusion of each probe Mw as a function of Cmatrix is seen to adhere to the scaling relation $D \sim C^{-1/2}$ with the exponent values for each fit stated. (B) Self-diffusion coefficient as a function of F-NaPSS probe M_w diffusing

through M-NaPSS 450 at varying C_{matrix} with provided slope β values and fits to the data to guide the eye. A line of slope of -1 is provided as a reference.

The dependence of diffusion on probe M_w was greater at lower matrix concentrations as the difference in diffusion between each of the three probe molecular weights, was larger at lower matrix concentrations and became significantly smaller as matrix concentration increased. This result could be indicative of two things. One, is that smaller polymers are slowed more rapidly in an environment that is increasingly more crowded. Two, a portion of probes are entering aggregates as the average diffusion values become increasingly dominated by the aggregates dynamics.

The relationship between probe diffusion and C_{matrix} varied for each probe molecular weight in a similar fashion to what was observed by Cong et al.[146] According to the theoretical scaling of single component entangled polyelectrolyte solutions at low salt concentrations diffusion scales with concentration according to $D \sim C^{-1/2}$.[106] Applying this theory to mixed molecular weight systems the C_{matrix} exponent approached -0.5 as the probe and matrix molecular weights became increasingly equivalent from 31 to 161 to 590 kDa for the probes and 450 kDa for the matrix.

In the third objective, if the diffusion of a probe is controlled by the matrix correlation length, which is expected to be independent of matrix molar mass for sufficiently large matrix polymers at sufficiently high concentrations,[36] then probe diffusion should not depend on matrix molecular weight. It should depend on probe molecular weight, in contrast to Hypothesis 2. Also, the onset concentration for such behavior *would* depend on matrix molecular weight because longer chains entangle at lower concentrations.

Figure 78A shows the diffusion of three probes, F-NaPSS 31, 161 and 590, mixed with five different matrix molecular weights, M-NaPSS 27, 68, 182, 300 and 450 but the probe and matrix concentration are held constant at 2 and 6 mg/mL, respectively. Diffusion for each probe depends on probe and matrix molecular weight as we observe diffusion decreases monotonically with matrix molecular weight at these matrix concentrations. The scaling exponent β is found to increase for probes diffusing through higher molecular weight matrices (Figure 78B). Values of β = 0.64 ± 0.04, 0.65 ± 0.01 and 0.65 ± 0.02 were measured for probes diffusing in M-NaPSS 27, 31 and 161, respectively. Comparable to the F-NaPSS zero-matrix value at low NaCl, these values imply negligible effect of matrix polymer on the mode of probe dynamics but their presence certainly slows the probes. It is reasoned that the fixed matrix concentration is too low at these molecular weights because β increases to 0.71 ± 0.03 and 0.79 ± 0.04 for probes in the presence of M-NaPSS 300 and 450, respectively.

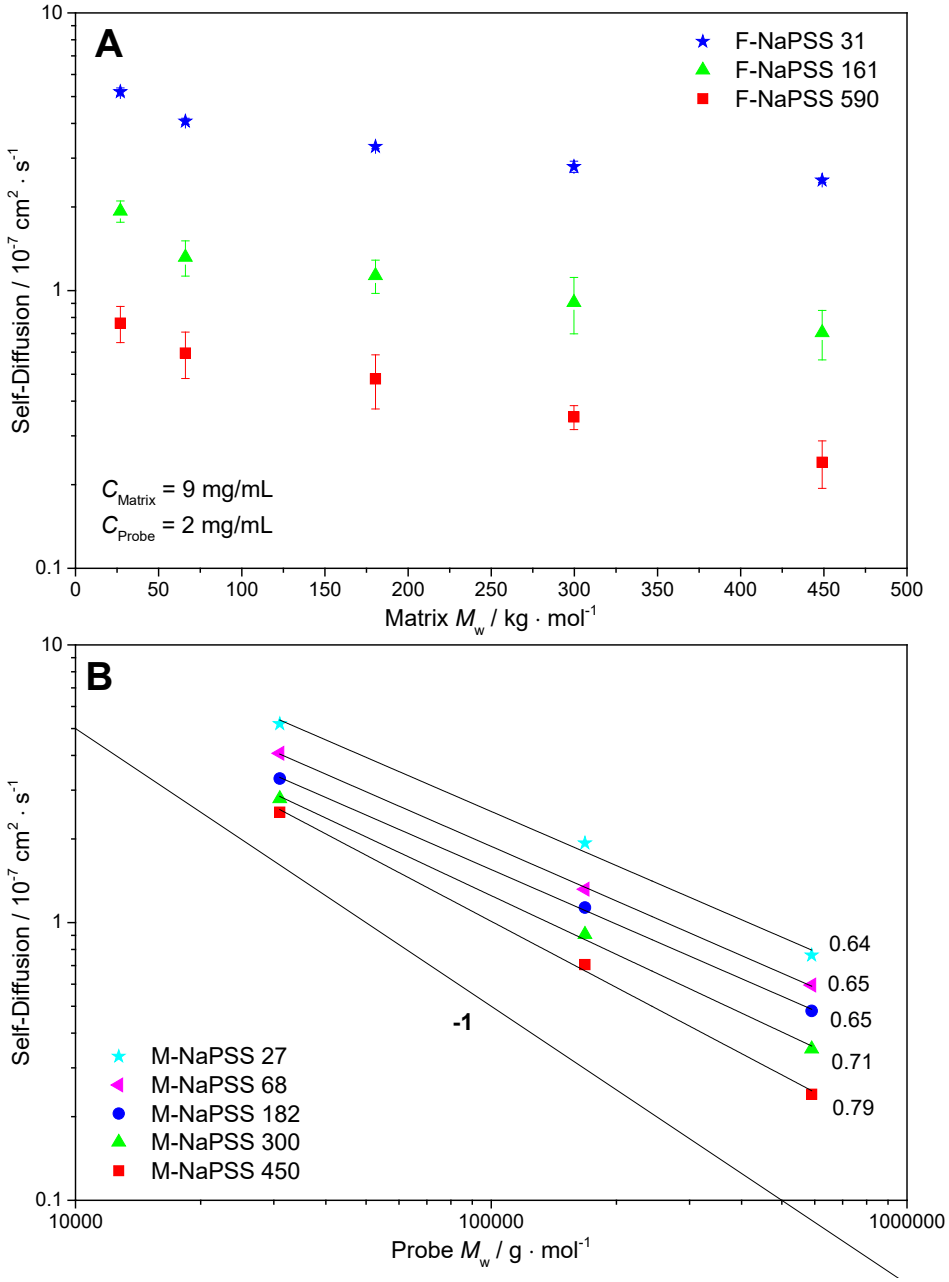

Figure 78. (A) Self-diffusion coefficients for F-NaPSS 31, 161 and 590 probes through M-NaPSS 27, 68, 182, 300 and 450 matrix polymers where probe and matrix concentrations held constant. (B) Self-diffusion coefficient as a function of F-NaPSS probe molecular weight diffusing through M-NaPSS of varied molecular weights with provided slope β values and fits to the data to guide the eye. A line of slope of -1 is provided as a reference.

A sufficient matrix concentration needed to be reached in order to determine if probe dynamics became independent of matrix molecular weight. Focusing on the F-NaPSS 31

probe, the matrix concentrations for M-NaPSS 27, 68, 182, 300 and 450, were varied. Diffusion of the smaller probe through the 5 different matrices was found to depend on matrix molecular weight at low matrix concentrations. With a fixed probe concentration at 1 mg/mL the matrix concentration was varied from 3-19 mg/mL. Probe diffusion decreased as matrix concentration and molecular weight increased, but above a threshold the dependence of diffusion on matrix molecular weight was less apparent. Above a matrix molecular weight of 161 kDa, and at sufficiently high matrix concentration above 9 mg/mL, the probe diffusion was independent of matrix molecular weight (Figure 79). In this more crowded matrix environment the probe diffusion was constrained.

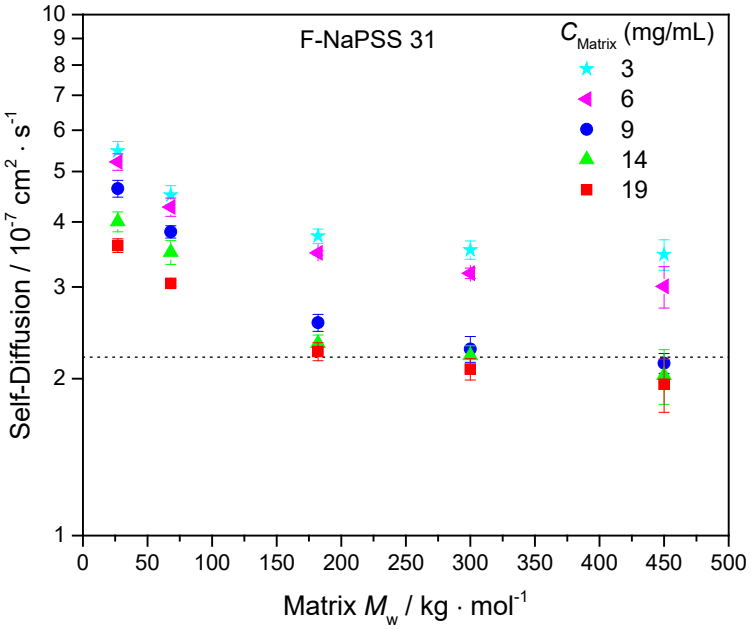

Figure 79. Effect of matrix molecular weight and matrix concentration on the self-diffusion coefficient of a smaller probe F-NaPSS 31. A horizontal reference line is drawn to indicate that above these matrix concentrations the probe diffusion becomes relatively independent of matrix molecular weight.

4.4.9 Comparison of results to selected theoretical treatments

Diffusion of a particle or polymer of hydrodynamic radius R_H in a simple fluid of viscosity η_0 at a constant temperature T is described by the Stokes-Einstein relation, $D = k_B T/6\pi\eta_0 R_H$, where k_B is the Boltzmann constant. A breakdown of Stokes-Einstein behavior is well documented for polyelectrolytes at low salt,[39] and further is not expect to hold for the description of small probe diffuses in a complex mixed polymer solution.[273] Theoretical arguments for diffusion in mixed media describe a system where a single polymer molecule, the probe chain, moves through a network of polymer chains, the matrix. There are two main models used to describe these systems, namely the reptation/scaling and hydrodynamic scaling model, with the key difference being the disagreement between which forces dominate the polymer dynamics. The reptation/scaling model asserts that at significant concentrations exceeding the overlap concentration it is the topological constraints from chain entanglements between polymers that are the dominant physical force.[6] The requirement for entanglements to occur means that there is a lowest concentration, the overlap concentration, below which this model is inappropriate. In contrast the hydrodynamic scaling model, an extension from the Kirkwood-Riseman model,[280] considers the solvent-meditaed hydrodynamic forces between the probe and matrix polymer are dominant.[281] There are no entanglement requirements in this model and therefore is valid extending up from the extreme dilute toward the melt.[282] The entanglement-focused reptation/scaling model assumes that on the time scales of interest, based on the smaller probe polymer and its comparatively faster chain dynamics, the matrix chains are effectively stationary. Much like the way a crosslinked gel constrains probe chain motions, forcing movement parallel to its own chain contour, the matrix chains in the polymer solution form a transient lattice or pseudogel. There is no concept of a matrix

lattice in the hydrodynamic scaling model, instead all chains are free to translate and rotate about their center of mass. When a probe chain moves up to and encounters matrix polymer the reptation/scaling model states that the probe polymer chain is brought to a stop by the matrix polymer; whereas the hydrodynamic scaling model asserts that the probe polymer will carry the matrix chain along to some degree so that they both move in parallel directions so as to not block each other's motions.[283]

The entanglement based reptation model also incorporates a second independent assumption which is that the polymer diffusion coefficient depends on solution properties via scaling laws:

$$D_{self}(C, M) = D_{cm} C^{v} M^{\gamma} \tag{83}$$

where self-diffusion D_s of a probe at a specific concentration C and molecular weight M depends on the scaling exponents v and γ.

The hydrodynamic scaling model instead makes predictions based on stretched exponentials:[282]

$$D_{self}(C, M) = D_0 exp(-\alpha C^{v} M^{\gamma}) \tag{84}$$

While topological and solvent-induced hydrodynamic forces are addressed, a major drawback of these models in describing the diffusion of mixed NaPSS at low salt is the lack of treatment of electrostatic forces that also govern polyelectrolyte diffusion. The concentration range examined in this mixed NaPSS study is focused in the semidilute regime. Lower and upper bounds are approximately around the overlap concentration

extending up to several times higher but do not reach the concentrated entangled regime according to the theory of Dobrynin, Colby and Rubinstein.[23] We expect the dynamics of matrix NaPSS to be on similar time scales as the probe, therefore the hydrodynamic scaling approach is a more appropriate treatment of this data. Langevin and Rondelez proposed a simple stretched exponential to describe the enhanced diffusion of small probes in semidilute solutions or gels.[284] In their model the diffusion normalized by its value in dilute solution absent of any matrix minus the quotient of viscosities depends on the probes radius and the matrix correlation length:

$$D_{self}/D_0 = \eta_0/\eta + exp\left[-(R/\xi)^{\delta}\right] \tag{85}$$

Here, D_{self} is the diffusion of a spherical probe of radius R through the mixed media solution of viscosity η, and D_0 and η_0 are the diffusion of the probe absent any retarding matrix and the viscosity of the pure solvent, respectively. It is assumed that $R = R_H$ as calculated from D_0 using the Stokes-Einstein equation at a temperature of 293 K. The equation is intended for semidilute solutions ($\xi \ll R_G$) which are the correlation length and radius of gyration for the matrix polymer, respectively. The parameter δ is expected to be 2.5 for rigid gel matrices but in solutions it should be less. The above equation has the linearized form $\log(-\ln(D_s/D_0 - \eta_0/\eta)) = \delta \log R_H - \delta \log \xi$ from which both δ and ξ can be obtained by applying unweighted linear fits to the linear regime, where the slope of the fit equals δ and the y-intercept is $-\delta \log \xi$. F-NaPSS 31, 161 and 590 probes diffusing through M-NaPSS of fixed concentration at 9 mg/mL but varied M_w (Figure 80A), and through M-NaPSS 450 of varied concentration (Figure 80B) were plotted using the Langevin-Rondelez analysis. Linear plots from the form of the above equation indicate

adherence of probe diffusion to Stokes-Einstein behavior. The function $y = \log(-\ln(z))$ diverges at $z = 0$ or 1, which corresponds respectively to the success and failure of the Stokes-Einstein relationship. Deviation from Stokes-Einstein behavior was more apparent for smaller probes diffusing through smaller matrices, as $z = 0.88$ for F-NaPSS 31 in M-NaPSS 27 compared to $z = 0.06$ for F-NaPSS 590 in M-NaPSS 450, and also at lower matrix concentrations, as $z = 0.68$ for F-NaPSS 31 in 3 mg/mL of M-NaPSS 450 compared to $z = 0.30$ when M-NaPSS concentration increased to 20 mg/mL. Values of δ ranged from 0.49 to 1.1 when 9 mg/mL M-NaPSS M_w was varied, and from 0.56 to 0.89 for M-NaPSS 450 of varying concentration. These values indicate the solution like nature of the matrix and compare somewhat to average values found in the literature; $\delta = 0.63$ for dextrans in hydroxyl-propyl cellulose,[273] $\delta = 0.59$ for bovine serum albumin in polyacrylamide,[285] and 0.58 for pullulans diffusing in dextran.[275] The higher δ values corresponded to when $y = \log(-\ln(z))$ diverged at $z = 1$.

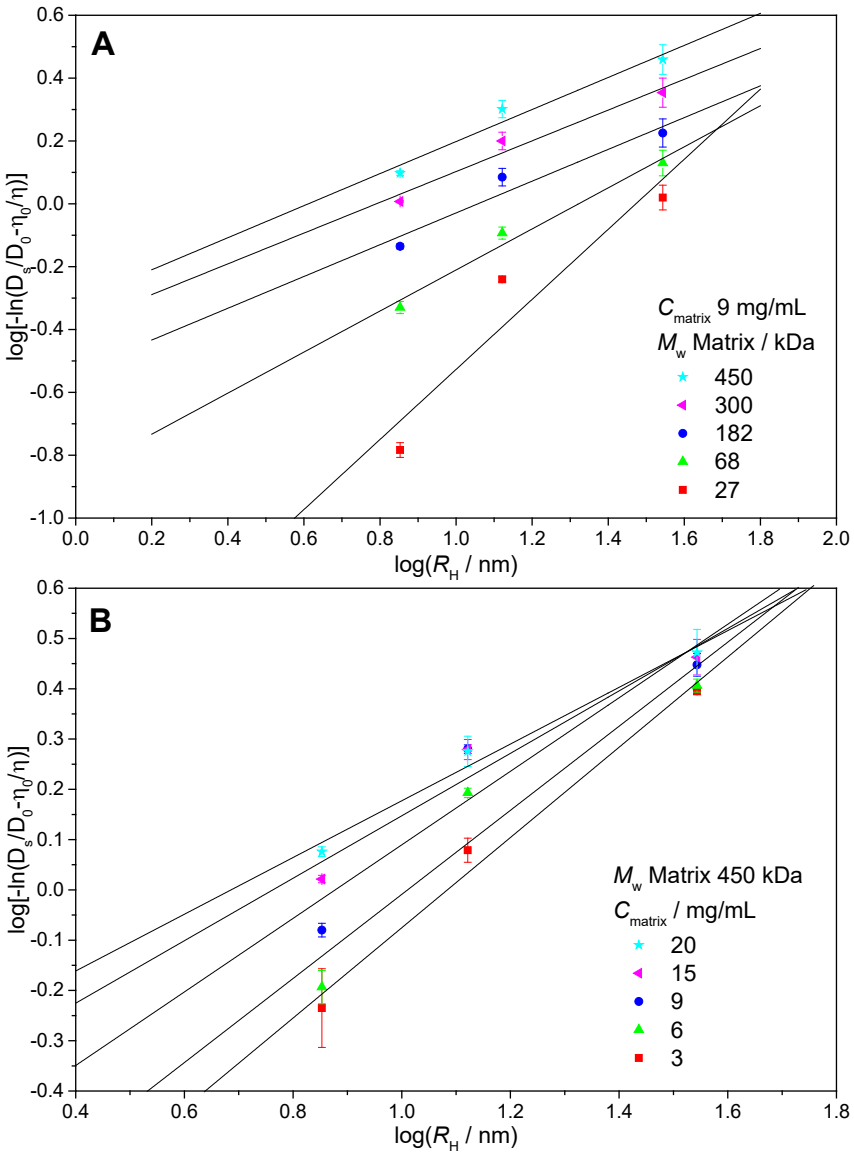

Figure 80. Langevin-Rondelez plots for F-NaPSS 31 probes in (A) matrices of fixed concentration (9 mg/mL) but varying M_w, and (B) matrices of fixed M_w (M-NaPSS 450) but with varying concentration. Unweighted linear least-squares fits to the data are shown and produce a slope value equal to δ.

Typically, a large uncertainty is associated with the values of δ and ξ when extracted from the linearized form of the Langevin-Rondelez equation. Therefore, an unweighted nonlinear least-squares fit to a more generalized expression of the Langevin-Rondelez equation is also used (Microsoft Excel 2016 Solver). Here, the viscosity dependence of

solid spherical diffusers is incorporated into the matrix concentration c and probe size R_H dependencies:

$$D_{self}/D_0 = exp(-\alpha C^{v}) \text{ at constant } R_H \quad (86)$$

$$D_{self}/D_0 = exp\left[-(R/\xi)^{\delta}\right] \text{ at constant } C \quad (87)$$

A v value of 0.5 is put forth in the theories of Cukier,[286] Tirrell,[287] and Ogston, [288] but according to the hydrodynamic scaling model put forth by Phillies[289] v can vary from 0.5 for large molecular weight probes to a value of 1 for low molecular weight probes. The hydrodynamic scaling model predicts that the concentration prefactor $\alpha \sim \left(M_p/M_m\right)^{1/2}$, for probe ($M_p$) and matrix molecular weight (M_m), which in our case produces v values that are slightly below 0.5. A result that is probably due to the inability of this model to predict the electrostatically dictated expanded rod-like nature of the probes and their lower than expected M_p values for the corresponding probe radius that was intended for hard spheres.

This study is primarily focused on detecting the presence of temporal aggregates and their effect on dynamics in mixed media, therefore it spans a limited probe molecular weight range with limited data points so we do not claim the δ and ξ values to be definitive; however we observe relative agreement with theory as the Langevin-Rondelez correlation length ξ_{LR} decreases with matrix concentration $\xi_{LR} \sim {C_{matrix}}^{-x}$ with x equal to 0.49 ± 0.03 and 0.55 ± 0.04 using the unweighted nonlinear least-squares analysis of Equation 86, and the linear least-squares fit to the Langevin-Rondelez plot, respectively (Figure 81A). The

expected exponent for a random coil in a good solvent is 0.75,[5] for a rod theoretically it's expected to be 0.5[68] but less experimentally.[290] As a function of matrix M_w at fixed concentration the ξ_{LR} values trended with slope values equal to 0.50 ± 0.04 and 0.56 ± 0.04 for the unweighted nonlinear least-squares fit to the generalized form of the equation and the least-squares linear Langevin-Rondelez plot fit, respectively (Figure 81B).

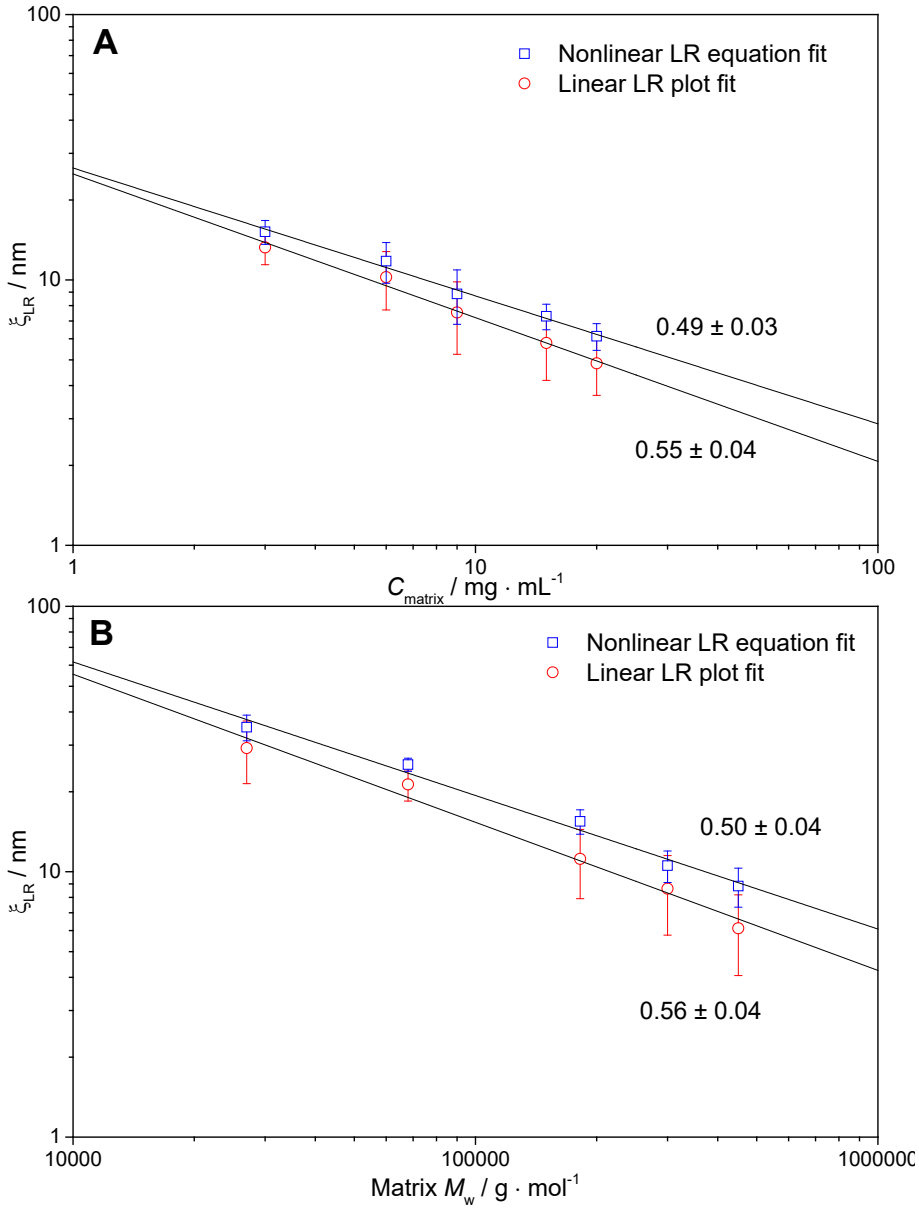

Figure 81. Correlation lengths determined from linear least-squares fits to Langevin-Rondelez plots and to unweighted nonlinear least-squares fitting to the generalized Langevin-Rondelez equation for probes diffusing through (A) M-NaPSS 450 at varying concentration, and (B) 9 mg/mL of matrix NaPSS of varying M_w. Fits to the data are made and the slope values are provided.

Using the calculated ξ_{LR} values from each fitting method and diffusion data in Figure 79 a plot of F-NaPSS 31 probe diffusion versus M-NaPSS correlation lengths was produced (Figure 82). Dependence of probe diffusion on ξ_{LR} was observed.

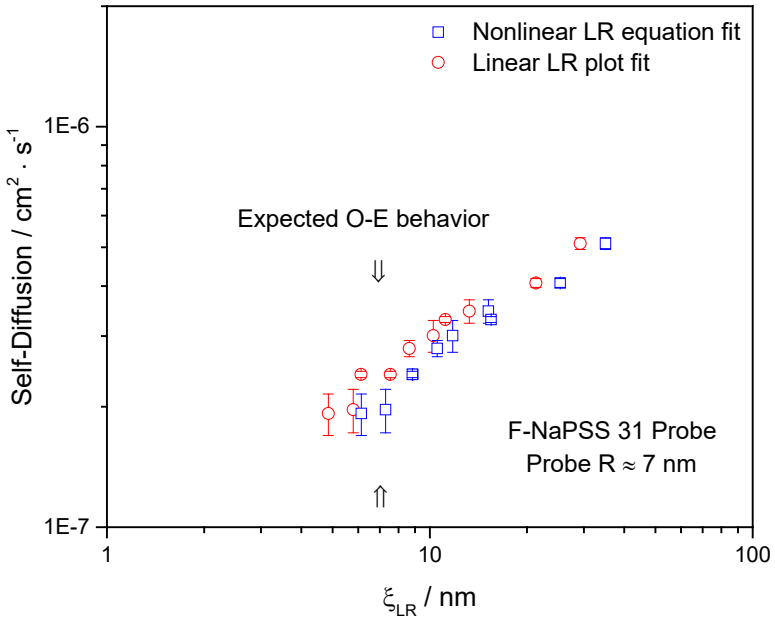

Figure 82. Relationship between probe diffusion and matrix correlation length determined from the two Langevin-Rondelez based analysis methods.

Temporal aggregate formation and the expected onset of the ordinary-extraordinary transition begins to emerge at intermediate distances of chain separation, comparable to the correlation length.[39] At the point where the matrix correlation length and the probe radius are equivalent there is no deviation from the trend between diffusion and matrix correlation length.

4.5 Conclusion

An investigation of both single component fluorescently labeled F-NaPSS and mixed F-NaPSS probe with unlabeled matrix M-NaPSS was done with FPR in order to detect and gain further insight into the nature of temporary aggregates that account for the "ordinary-extraordinary' slow mode that is routinely observed with DLS. Tracking diffusion as a

function of the C_p/C_s ratio showed a larger decrease above the critical threshold which could be owed to the formation of larger structures lowering the average self-diffusion coefficient. No evidence for bi-exponential decay of the FPR contrast signal was found, supporting the premise that NaPSS polymers enter and leave aggregates many times on the time scale of the FPR experiment, which is many times longer than DLS. A broader range of probe and matrix molecular weight and concentration was investigated than previously done. Mixed solutions were observed to display a dependence of probe diffusion on probe M_w as a function of C_{matrix} and matrix M_w, contrary to the hypothesis that probes of all sizes that were entrained in aggregates would diffuse equally, regardless of matrix conditions. The diffusion scaling exponent $D_{probe} \sim M_{probe}^{-\beta}$ increased from β to 0.65 ± 0.03 without the presence of matrix to 0.79 ± 0.04 in the presence of added M-NaPSS 450 matrix at 20 mg/mL. Probe diffusion became independent of matrix M_w above at high enough C_{matrix} suggesting deviation from Stokes-Einstein behavior. A Langevin-Rondelez treatment of the mixed NaPSS results also showed deviation from Stokes-Einstein behavior for smaller probes in smaller matrices, and revealed a dependence of probe diffusion on matrix correlation lengths.

4.6 Acknowledgements

I am grateful to Rachel Borrelli for conducting many of the FPR measurements and to Dr. Alyssa Blake for her assistance in the synthesis of fluorescently labeled NaPSS. We would like to acknowledge the support of OPALL, STAMI and The Georgia Tech Hightower Family.

CHAPTER 5. HOLOGRAPHIC FPR MEASUREMENTS ON LOW-SALT NAPSS SOLUTIONS AT SPATIAL FREQUENCIES COMPARABLE TO DLS IN ORDER TO INVESTIGATE TEMPORARY AGGREGATE FORMATION AND LIFETIME

5.1 Introduction

Diffusion of charged macromolecules in concentrated aqueous solutions and crowded environments is omnipresent in the biological world and in therapeutic medicines.[291-293] DLS is the premier technique to measure diffusion of these macromolecules and in turn characterize their size, but when solutions possess a low salt concentration relative to the macromolecule concentration, bizarre phenomena occur. The collective movements of charged macromolecules becomes elusive due to nonlinear couplings among long-range forces arising from electrostatics and hydrodynamics, and long-range topological correlation effects.[39] What results is the simultaneous occurrence of two diffusive modes, and the recent explanation of a third diffusive mode at uniquely high molecular weights and concentrations, which in turn falsely states that multiple sized species must be present in solution.[117] It is therefore necessary to determine if the same strange dynamic behavior is observed with a technique that, unlike DLS, does not sense the mutual diffusion of these charged macromolecules.

Experiments using traditional long-distance FPR instruments have failed to provide evidence of biexponential decay of the fluorescence contrast signal and thus unable to detect the separate slow and fast modes.[26, 38, 294] Small angle neutron scattering

experiments, though, provide compelling evidence in support of DLS measurements. A steep upturn in the scattering peak at low q values (below 0.01 $Å^{-1}$) substantiates the existence of clusters in solution and a proposed multi-chain domain structure.[265, 276, 295] The single FPR diffusive mode measured at low K (long-distance scale) lies in between the DLS fast and slow diffusive modes measured at high q (short distance scale). This single FPR mode is not the average of the two DLS modes.[38] With the FPR mode being faster than the DLS slow mode this suggests that chains may enter and exit a temporal aggregate, but when they leave they do not move as quickly as the diffusers responsible for the DLS fast mode (rates of diffusion similar to salt ions). The discrepancy here is due to FPR measuring the self-diffusion of an optical tracer whereas DLS is sensing strong thermodynamic interactions.

Temporal aggregates need maintain their structural integrity for only about 0.05 s to relax the DLS correlation function. If individual chains do exchange in these aggregates then there can be an upper bound placed on the residence time of a chain that has joined an aggregate. That upper limit is the FPR recovery time of about 20 s for the low K measurements made previously.

The objective of this research project is to reduce the FPR distance scale using a holographic FPR technique in order to reach high enough K values, somewhat comparable to the q values of DLS, and search for a split in the decay profile, one for free polymer and the other for those entrained in aggregates. Measurements will be conducted on single component fluorescent NaPSS solutions under semidilute concentrations above the critical C_p/C_s threshold. If the strategy proves successful at one molecular weight and concentration, it can be applied to others as well to observe scaling trends and their effect

on temporal aggregate behavior. The overall objective is broken into smaller achievable parts. The first is to determine if the holographic FPR can produce a striped pattern on a length scale equivalent to DLS. We then look to improve and simplify the FPR technique by implementing a high-speed camera to capture the decaying fluorescent pattern and using an image analysis algorithm to calculate the intensity of the contrast signal with time. This has the effect of eliminating the need for pattern modulation and fluorescence signal capture with a photodiode or PMT.

5.1.1 Background on holographic FPR

A major limitation to FPR systems is that they cannot probe very small distance scales. This renders the measurement of very low diffusion coefficients to be quite challenging. Probing small distance scales is performed by bleaching very small regions in the sample but for striped patterns there is a lower limit in the periodicity that can be achieved with a Ronchi ruling due to manufacturing constraints. This issue is circumvented through the use of an instrument in which two coherent laser beams are crossed on the sample to produce a spatial interference pattern much smaller than what can be projected by illuminating a Ronchi ruling (Figure 83). When two coherent beams are crossed the holographic intensity grating depends on beam location x and phase difference φ between the two beams according to:[296]

$$I(x,\varphi) = \frac{1}{2} + \frac{1}{2}\cos(Kx + \varphi) \tag{88}$$

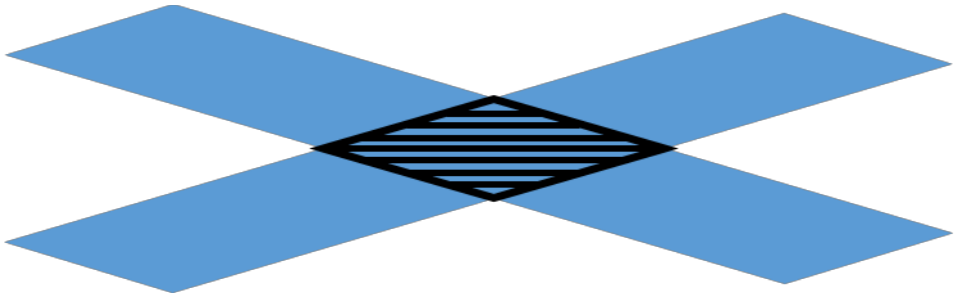

Figure 83. Holographic interference pattern created by two coherent crossed beams.

Two variations of these systems have been designed, each with a unique method to produce stripe modulation for enhanced analysis. Davoust et al.[297] used a mirror on a piezoelectric mount on one arm of the interferometer to oscillate the relative phase of the crossed beams. Cicerone et al.[40] produced the relative phase difference between the two beams by placing a Pockels cell along a branch of the interferometer. In each case, the piezo or Pockels cell devices, remained off until the photobleaching step has ceased, at which point the laser is attenuated to the read mode and the devices are switched on. The modulation devices are driven in a linear fashion with a triangle or sawtooth wave to produce the relative phase difference between the two beams. The result is that the interference pattern shifts spatially, in a direction perpendicular to the stripes, to scan across the dark and bright sample regions as caused by photobleaching. Regarding the measured oscillating, decaying exponential signal there is no difference in the analysis compared to an FPR system with a modulated Ronchi ruling, the fundamental terms are identical. But the fringe distance and spatial frequency are determined instead by the laser beam wavelength λ in the sample of refractive index n and crossing angle θ as described by:

$$L = \frac{\lambda_0/n}{2\sin\left(\frac{\theta}{2}\right)} = \frac{2\pi}{K} \tag{89}$$

A typical holographic FPR set up requires a laser to excite the fluorophores, a set of optics to split and then recombine the beam on the sample, a way to manipulate the beam intensity for fast switching between bleaching and reading beams, a device to modulate the reading beam, a microscope and stage to focus the crossed beams onto the sample region of interest, photon detection to collect the fluorescence signal and convert it to an electronic one, and a data processing card to collect and process the detector signal along with controlling the hardware components of the FPR experiment. A generic two beam holographic set up is shown below with each optical component to attenuate, modulate and align the beams on the fluorescent sample (Figure 84).

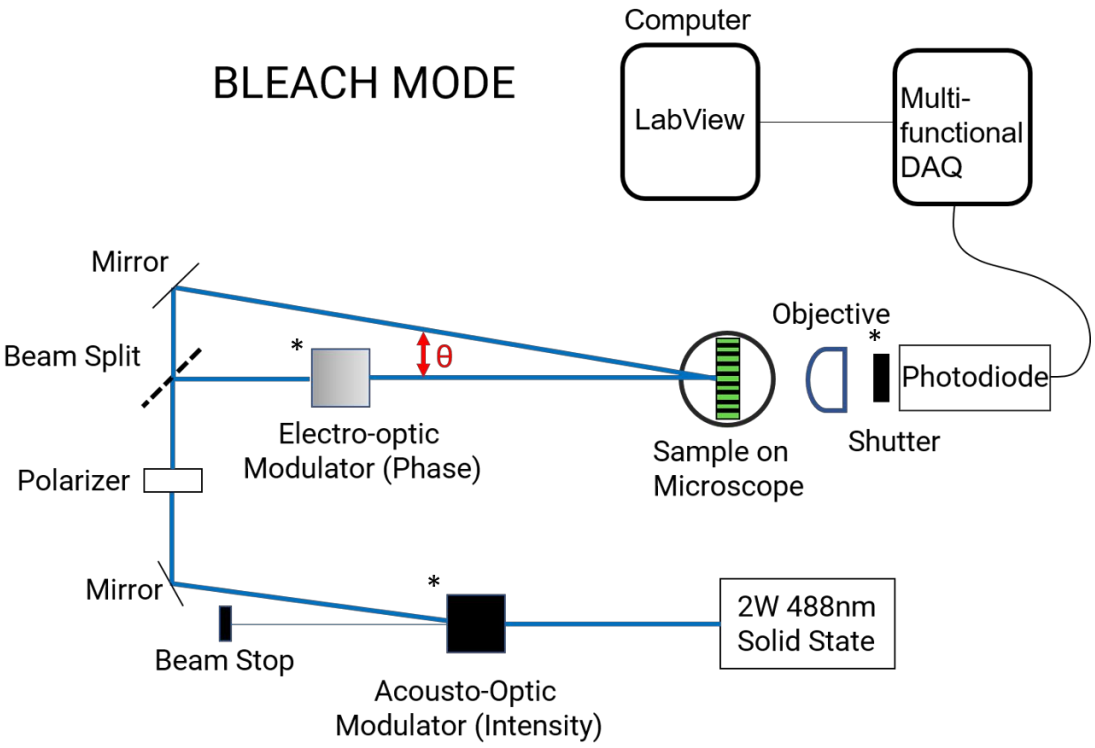

Figure 84. Diagram of a generic holographic FPR set up in bleach mode showing the crossed beams converging on the sample at an angle θ. One beam passing through an EOM which is switched on when the beams are switched to read mode to cause modulation of one beam which has the effect of moving the pattern across the sample. AOM is an intensity switch and EOM is a phase switch of the laser light. Fluorescence is collected at the photodiode with an option to protect it from the high light levels of the bleach phase using a shutter. The symbol * means that component is computer controlled.

An understanding of the key components of prior holographic FPR designs is warranted to aid in the development of a new instrument. A highly monochromatic intense laser beam with minimal divergence and a long coherence length is desired for a crossed-beam set up. This serves the purpose of producing a well-defined interference pattern and bleaching that pattern onto a small region of sample. The rapid switching of a beams intensity between bleaching and reading beam is critical because theoretically there should not be movement of healthy fluorophores from surrounding regions to the bleaching region over the duration

of bleaching. Practically this is impossible to achieve, and so to minimize error the bleaching time is kept as small as possible, in addition the time for beam switching must be kept to a minimum. Keeping the bleaching time at least ten times shorter than the characteristic relaxation time of a diffuser is the general rule of thumb. With this in mind the use of moving neutral density filters, piezo mirrors or liquid crystal switches, or in general any optics that rely on material movement or a mechanically driven action to attenuate a beam, have an associated lag time for moving a part to be dragged in and out of the beam path. Switching time for these devices is on the order of milliseconds, which will increase the bleaching time and permit a greater number of healthy fluorophores to move into the bleaching region. Switching time must be kept at a minimum, especially when trying to observe faster dynamics. An acousto-optic modulator (AOM) is a fast switching device that can attenuate a beam on the order of hundreds of nanoseconds. The radio frequency (RF) driver that drives the AOM creates a sound wave within the crystal to make it behave like a movable diffraction grating. An incoming laser beam then gets diffracted into several orders upon encountering the diffraction pattern within the crystal (Figure 85). Each order of diffracted beam can be intensity varied by tuning the Bragg angle of the crystal or the power output from the RF driver. Beam attenuation is achieved by turning the RF driver on, which switches the laser power between the first and zeroth order diffraction beams. In this way the first order beam can be switched between reading and bleaching beams.

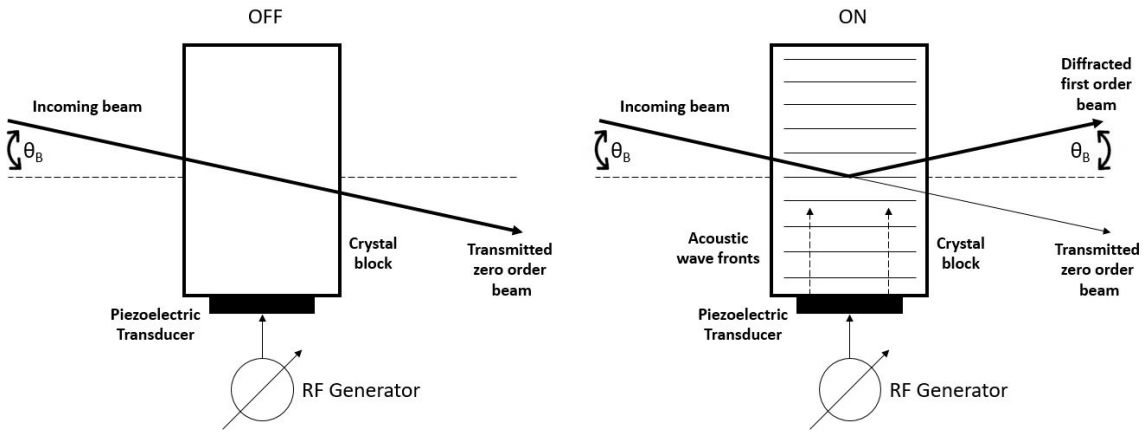

Figure 85. Schematic of an AOM showing the zero order beam being switched from low to high intensity when the RF driver is turned on and off, respectively.

The lateral translation of the striped interference pattern created by the crossed beams during the reading phase is done to enhance the signal acquired at a lower bleach depth thus allowing for a lower bleaching beam intensity and bleaching time. The desired modulation of the pattern is achieved by passing one of the crossed beams through an electro-optic modulator (EOM) to phase modulate the beam. A Pockels cell is essentially a voltage-controlled wave plate that rotates the polarization of a beam (Figure 86). This is achieved by applying a strong electric field across a crystal which lacks inversion symmetry, such as lithium niobate, which has the effect of changing the crystal lattice spacing and thus produces birefringence. A high voltage driver is required to produce the strong electric fields required to produce a Pockels effect within the cell. A signal generator can be used to control the phase rate and pattern at which the polarization is varied as a beam exits the cell. By rotating the polarization through 180° the interference pattern created on the sample will alternate back and forth one full period across the stripes.

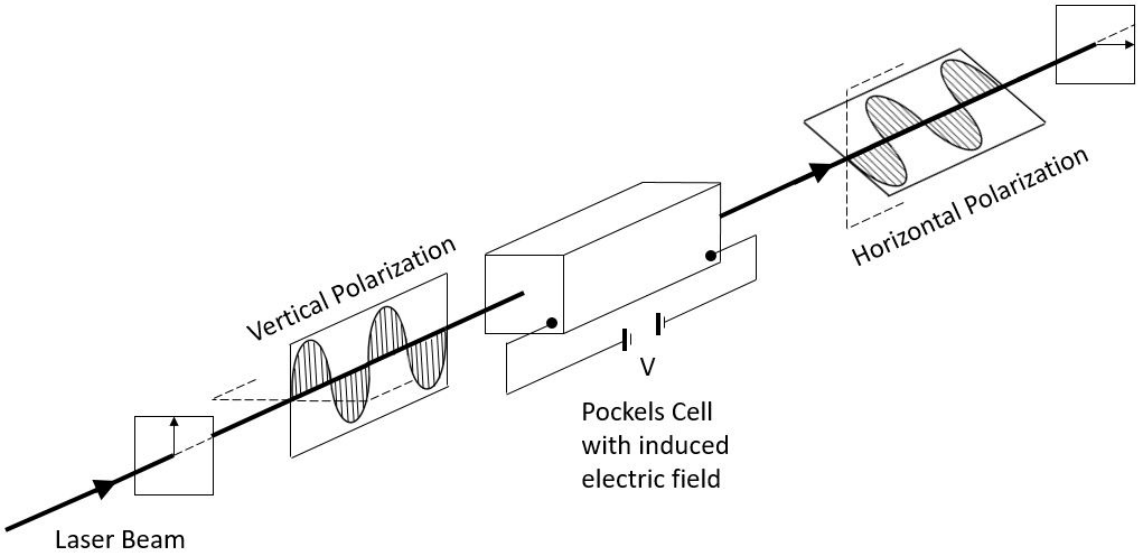

Figure 86. Schematic of a Pockels Cell rotating the polarization of a laser beam from a vertical to horizontal configuration. The exiting polarization can be moved through 180° by variation of the induced electric field.

The emitted fluorescence signal from the sample is typically collected with a PMT or avalanche photodiode (APD) which is mounted onto the top of the microscope. The advantage of using an APD is that they are equipped with a gate circuit which when activated cuts off any detected signal so that the detector is protected from potential damage due to the large influx of photons that are produced during the bleach period. A shutter can also be put in place to protect the detector type during the bleach phase. A data-acquisition card or DAQ is used to interface each piece of hardware to a software platform in order to control the timing of the components during the FPR experiment.

5.2 Experimental

5.2.1 Materials

Sodium 4-vinylbenzesulfonate, 2,2'-bipyridine (bpy) (> 99.0%), copper (I) chloride (CuCl) (>99.995%), sodium chloride (NaCl) (>99.0%), copper (II) chloride ($CuCl_2$) (97.0%), 4-(bromomethyl)benzoic acid (97.0%), sodium hydroxide (NaOH) (>97.0%), fluorescein isothiocyanate isomer 1 (FITC) (>97.5%), and pyridine (>99.0%) were purchased from Sigma Aldrich and used as received. Ethanol (>99.5%, KOPTEC) and methanol (>99.8%, BDH) were purchased from VWR. Sodium nitrate ($NaNO_3$) (>99.0%) was purchased from J. T. Baker. 4-vinylaniline (90%), and sodium phosphate monobasic (NaH_2PO_4) (99.9%) were purchased from Fisher Scientific. Hydrochloric acid standard solution 5 M (HCl) was obtained from Fluka Analytical. Deionized water (18 MΩ·cm) was drawn from a Millipore Milli-Q Type I source.

5.2.2 Synthesis

Non-fluorescently labelled, perfectly sulfonated NaPSS across a range of molar masses was synthesized using an ATRP technique that has been previously described.[217]

Fluorescently labelled NaPSS was synthesized by incorporating a FITC-vinylaniline comonomer adduct at approximately a 1% ratio to the 99% sodium 4-vinylbenzesulfonate monomer before conducting the ATRP reaction.

The fluorescent comonomer was synthesized by dissolving 38 mg of FITC in 8 mL of 200-proof ethanol under stirring in a sealed flask and purged with argon for 30 min. Via syringe, 10 µL of 4-vinylaniline was added and the reaction was heated at 50 °C for 1 h, then removed from the heat and left to stir for 24 h under an argon atmosphere. The comonomer was obtained from rotary evaporation as a bright orange-yellow powder.

5.2.3 Purification of NaPSS

All NaPSS samples were dissolved in water and dialyzed using 3500 MWCO dialysis membrane tubing against pH 7 water with 1000 times the sample volume of dialysis liquid used. Water was evaporated and the NaPSS powder was vacuum dried until no further mass reduction was measured. Fluorescently labelled NaPSS samples were continuously dialyzed until unreacted fluorescent monomer ceased to be observed in the dialysate which was determined by observing no fluorescence when passing a hand held 2 W blue laser through the dialysate.

5.2.4 Molecular Weight Characterization

The SEC-MALS system consisted of an Agilent 1260 infinity II with online degasser, an ISO pump and 1260 vialsampler connected to an Agilent PL aquagel-OH 8 μm guard column prior to two Agilent PL aquagel-OH Mixed-H 8 μm columns connected in series. The MALS system consisted of a Wyatt Dawn Heleos-II with a Wyatt Optilab T-rEX differential refractive index detector operating at 658 nm. Agilent OpenLab software was used to operate the SEC and data acquisition and analysis were done with Wyatt Astra 7.1 software. The mobile phase was a buffer solution of 0.3 M $NaNO_3$ + 0.01 M NaH_2PO_4 + 0.02% NaN_3 at pH 9 under a flow rate of 1.0 mL/min. Polymer samples of concentration ~5 mg/mL were dissolved for 24 h prior to measurements to ensure complete dissolution. Solutions were filtered through Whatman Anotop 0.2 μm filters into Agilent 2 mL SEC vials. All chromatograms shown display the light scattering trace data taken from the 90° detector. Duplicate injections (100 μL) were performed for each sample measured by SEC-MALS and the resulting chromatography was found to be replicable in all cases. The

specific refractive index increment $\delta n/\delta c$ was previously determined to be 0.172 mL/g for NaPSS in buffer solution of 0.3 M $NaNO_3$ + 0.01 M NaH_2PO_4 + 0.02% NaN_3 at λ_0 = 658 nm.

5.2.5 Instrumentation of holographic FPR

The design of the holographic FPR is based on creating two laser beams to converge and focus on a fluorescent sample. We have used a 2 W continuous wave LASER (Model # Genesis SLM CX 488; Make # Coherent) with λ_0 = 488 nm to excite the NaPSS polymers labelled with a fluorescein isothiocyanate fluorophore which has a peak excitation wavelength of 492 nm. This single beam is vertically polarized before passing through a beam splitter, where 50% of the reflected light is directed to the sample, and 50% transmitted to a movable mirror that directs the light to recombine the beams on the sample. The distance at which the mirror is set from the beam splitter controls the beam crossing angle. An AOM placed in the beam path directly after the laser enables switching between bleaching and reading beams. The first-order diffracted beam is used in the holographic FPR instrument. In the off state the majority of laser power is contained in the zero-order beam with only a small amount of light bleeding through the AOM in the first-order beam, which is used as the off-state, while in the on state the AOM switches most of the power from zero to first-order, the bleaching beam. We have used AOM (Model # N23080; Make # Newport) with an RF driver of the same make (Model # N30185-6DS; Make Newport). In place of a reading beam we have used an LED source equipped with a FITC specific filter set (band-pass filter for excitation at 480 nm and barrier filter for fluorescence at 535 nm) to permit blue light to excite the fluorescent sample. The LED source (Model # pE-300lite; Make # CoolLED) is attached to the inverted fluorescence microscope (Model #

AE31E; Make # Motic) and it lightly fluoresces the sample in order to visualize the bleached grating pattern immediately after the crossed bleach beams are attenuated by switching off the AOM. The barrier filter placed in the optical path between objectives and camera to filter out non-fluoresced light. A 20X objective (Model # ULWD CDPlan 20PL 0.4 NA; Make # Olympus) was used to view the sample which was angled to the incoming crossed beam and placed on a mechanical stage to align and focus the sample and fluorescence signal. Sample design and set-up was constructed using a rubber O-ring sandwiched between two microscope cover slips. This design was intended for better optics as the 0.17 mm thick cover slips are specifically designed for these objectives. NaPSS solutions were contained inside the O-ring and between each cover slip. The optical path from the beam to the sample and camera from top-down and side-on viewpoints are shown schematically (Figure 87).

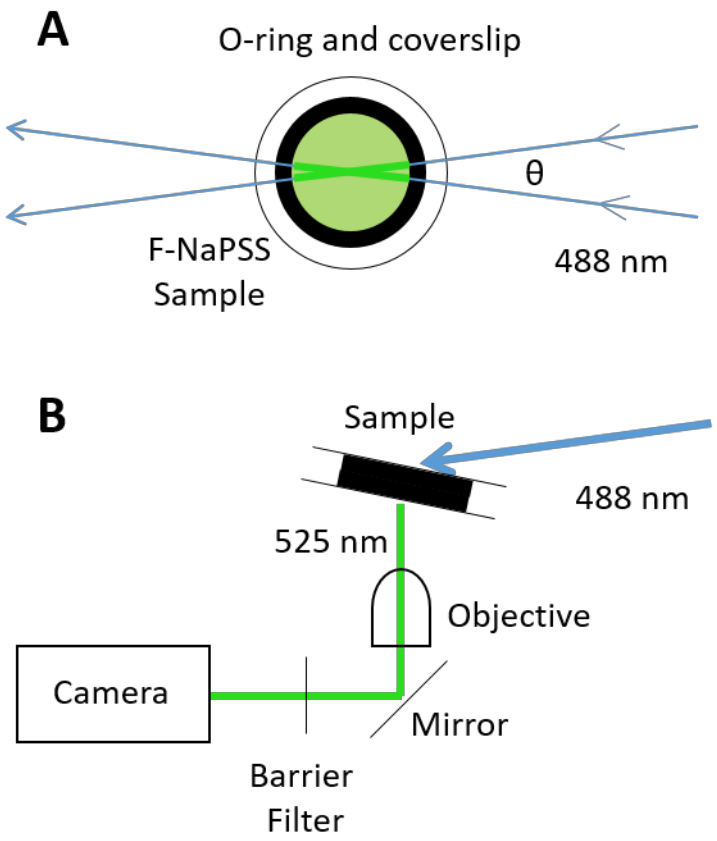

Figure 87. (A) Top-down view of the NaPSS sample contained by an O-ring and sandwiched between two 0.17 mm thick cover slips and the incoming 488 nm crossing beam at angle θ and, (B) side-on view showing sample and beam tilted at an angle to the incoming beams and the fluorescent 525 nm light following the optical path through a barrier filter (535 nm light) to the camera.

Fluorescence images were obtained using a CMOS microscope camera (Model # MU503B; Make # AmScope) mounted to the microscope. This camera had an 8-bit depth and during acquisition operated at 38.3 frames per second producing images of 1280 by 960 pixels. A data acquisition (DAQ) card (Model # USB 6000; Make # National Instruments) provided control of the hardware components of the FPR instrument, such as AOM and shutter. A schematic of the overall set up is provided below (Figure 88).

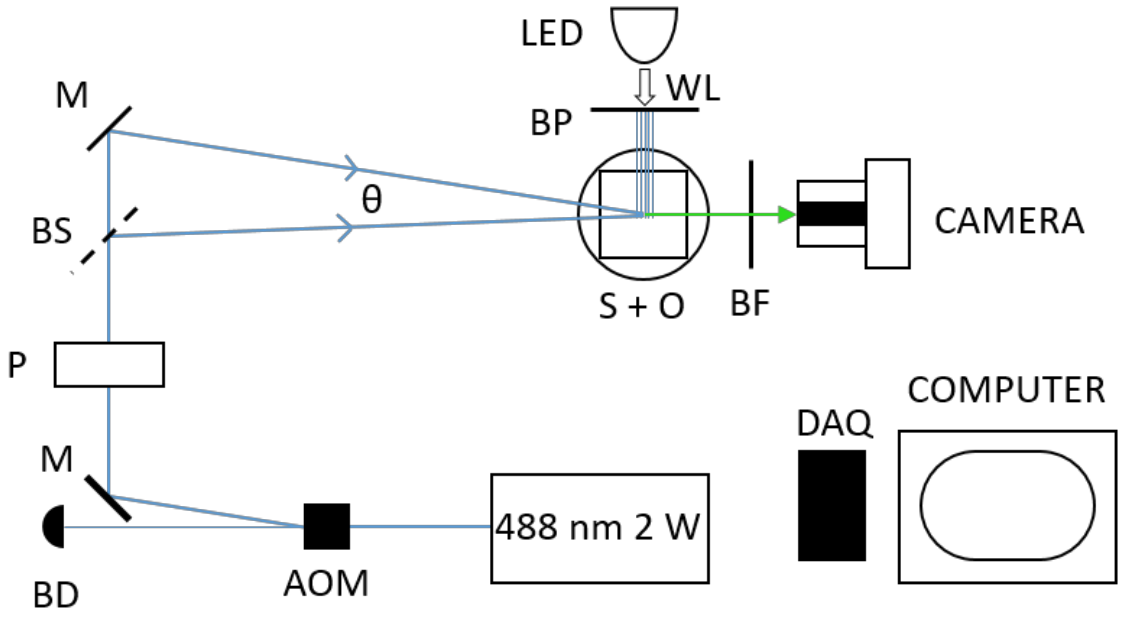

Figure 88. Diagram of the holographic FPR set up showing the AOM, beam dump BD, mirror M, polarizer P, beam splitter BS, beam crossing angle θ, LED white light WL source, band-pass filter BP (480 nm), microscope stage with sample and objective S + O, barrier filter BF (535 nm), camera and the DAQ and computer set up to control the optics. The first-order beam being switched on above signifies bleach mode but when switched off most of the light passes to the zero-order beam and goes to the beam dump. During switching the LED is switched on to fluoresce the sample and observe decay of the bleached pattern.

5.3 Results and Discussion

5.3.1 SEC-MALS Characterization

Molar mass distributions for fluorescent NaPSS samples were obtained with SEC-MALS. All samples displayed monomodal and relatively symmetrical normalized light scattering traces from the 90° detector (Figure 89). Samples are designated by the format: F-NaPSS 31, F is indicating they are fluorescently labeled and the number indicating the samples M_w in kDa.

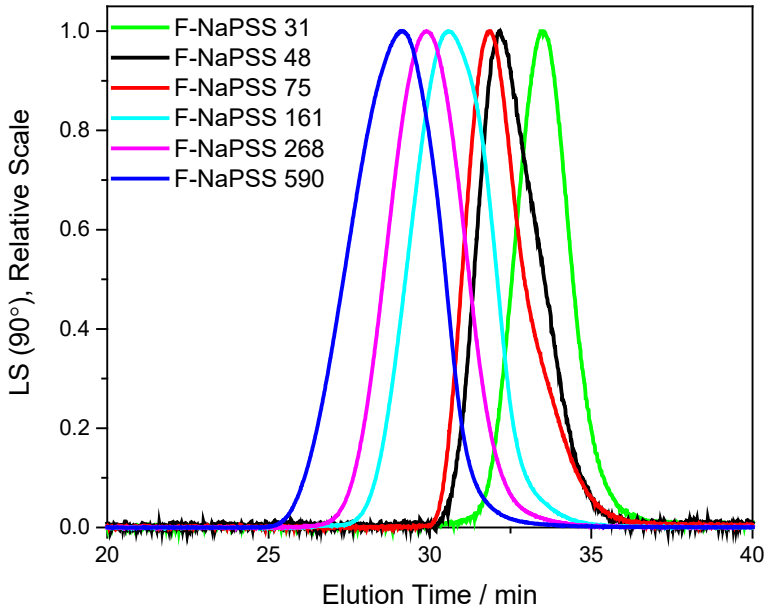

Figure 89. SEC-MALS chromatograms of F-NaPSS dissolved in 0.3 M $NaNO_3$ + 0.01 M NaH_2PO_4 + 0.02% NaN_3 observed at the 90° detector. A $\delta n/\delta c$ value of 0.172 mL/g was used.

F-NaPSS samples used had M_w that ranged from 31 to 590 kDa, $Đ$ values that ranged from 1.06 to 1.25, and for diffusion measurements were dissolved in NaCl solution at semidilute concentrations to produce C_p/C_s values in excess of the critical threshold for ordinary-extraordinary behavior to occur (Table 5).

Table 5. F-NaPSS molecular weight, dispersity and concentration properties.

Sample	M_n (kDa)	M_w (kDa)	$Đ$	C_p/C_s
F-NaPSS 31	29	31	1.06	14
F-NaPSS 48	44	48	1.09	33
F-NaPSS 75	64	75	1.17	32
F-NaPSS 161	129	161	1.25	36
F-NaPSS 268	228	268	1.18	49
F-NaPSS 590	481	590	1.22	38

5.3.2 Theoretical comparison of FPR and DLS spatial frequencies

The comparison of FPR to DLS to probe the ordinary-extraordinary transition is imperfect for two main reasons. The first and more obvious is that DLS senses cooperative motion, producing a mutual diffusion coefficient, whereas FPR senses an optical tracer and produces a self-diffusion coefficient. The second, and key reason, is that FPR typically measures diffusion on long time and distance scales ($L \; or \; d = 2\pi/K$), with FPR distance scales (L ~ 50-100 × 10^3 nm) being orders of magnitude larger than DLS distance scales (d ~ 200-2000 nm). As a result of this discrepancy the temporary aggregates responsible for the slow diffusive mode need only exist for a short time to relax the DLS correlation function but may not maintain integrity for the requisite 1000-10000 times longer in order to be sensed by FPR. Hence, the long time and distance FPR measurement, such as those made by bleaching stripes with a Ronchi ruling, will produce a single diffusion coefficient, representing the average diffusion of both polyelectrolytes moving as single chains and polyelectrolytes moving much slower because they are entrained in temporary aggregates. As the spatial frequency of FPR increases ($K = 2\pi/L$), the characteristic relaxation time for diffusion decreases, and may approach the residence time of a polyelectrolyte chain in

a temporary aggregate. At this point the single diffusion coefficient will split into two when the FPR K values are similar to the q values for DLS. The faster of the two potential FPR modes represents the diffusion of free single chains, but is not at all like the DLS fast mode, and the slower mode will represent dynamics of chains entrained by temporary aggregates, physically similar to the DLS slow mode. Varying the spatial frequency of the FPR instrument to reveal K_s, which is the spatial frequency point where a single diffusion measurement splits into two, enables the estimation of the residence time t_r of a chain in a temporary aggregate. Inserting K_s into the Einstein relation $\langle x^2 \rangle = 2Dt$ and taking x as the diffusion distance $2\pi/K$ then:

$$t_r \approx \frac{2\pi^2}{D_{avg} K_s^2} \tag{90}$$

In theory, the comparison of DLS and FPR instruments and the splitting of the diffusion coefficient as a function of spatial frequency could look like the schematic below (Figure 90).

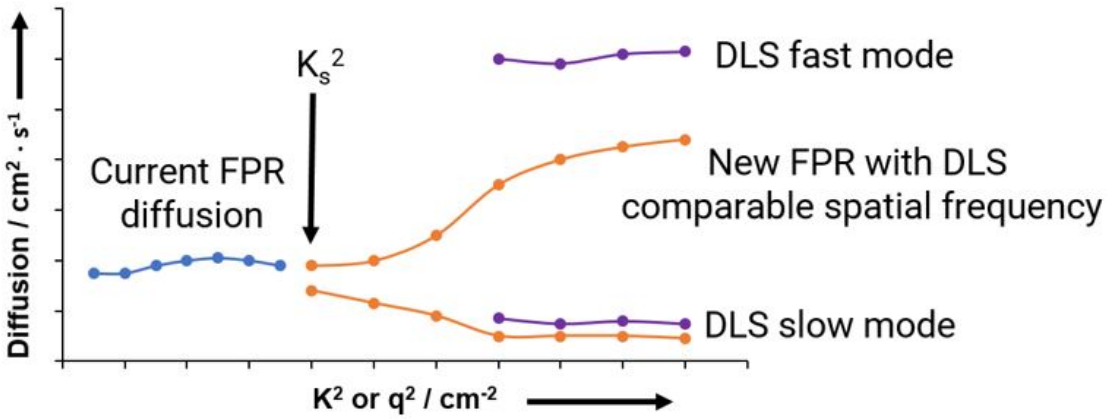

Figure 90. Spatial frequency dependence on the observation of slow mode diffusion in FPR. Current FPR technology only sees one diffusive mode but the development of a new holographic FPR where spatial frequency can be tuned to values similar to what DLS observes may result in the observation of two diffusion coefficients. The point where the coefficients split K_s^2 enables the estimation of chain residence time in temporary aggregates.

Several variables are considerd when designing a holographic FPR instrument with a spatial frequency comparable to DLS. The spatial frequency K for FPR depends primarily on the beam crossing angle whereas for DLS q depends on scattering angle, and in both cases spatial frequency depends on on the laser wavelength. Calculation of $K$and q below for an FPR instrument with a 488 nm laser and a DLS instrument equipped with a 660 nm laser across a variety of beam crossing and scattering angles. The distance scales $d = 2\pi/q$ for DLS and $L = 2\pi/K$ for FPR are also calculated and provided (Table 6).

Table 6. Spatial frequency and distance scale values calculated for DLS and holographic FPR based on scattering angle and beam crossing angle, respectively.

Scatter or Beam Cross θ /°	DLS values with 660 nm laser			FPR values with 488 nm laser		
	q / cm^{-1}	q^2 / cm^{-2}	d / nm	K / cm^{-1}	K^2 / cm^{-2}	L / nm
0.5	1095	1.20E+06	57382	1124	1.26E+06	55921
1	2190	4.80E+06	28691	2247	5.05E+06	27961
2	4380	1.92E+07	14346	4494	2.02E+07	13981
3	6569	4.32E+07	9565	6741	4.54E+07	9321
4	8758	7.67E+07	7174	8987	8.08E+07	6992
5	10946	1.20E+08	5740	11232	1.26E+08	5594
10	**21872**	**4.78E+08**	**2873**	**22443**	**5.04E+08**	**2800**
15	32756	1.07E+09	1918	33611	1.13E+09	1869
20	43577	1.90E+09	1442	44716	2.00E+09	1405
25	54316	2.95E+09	1157	55735	3.11E+09	1127
30	64951	4.22E+09	967	66648	4.44E+09	943

The highlighted row in the above table at a scattering angle and beam crossing angle of 10° shows distance scales of around 2800 nm for both DLS and FPR, respectively. Choosing the angle, and resulting distance scale, depends on a number of criteria that pertain to the experimental set up and limitations of each instrument. For instance, selecting an angle of 1° compared to 30° makes both DLS measurements and the beam splitting set up in FPR more difficult. DLS routinly observes the slow mode at a scattering angle of 30° ($d \sim 1000$ nm), but by moving to scattering angles around 1° the distance scale is now approximately 60 times larger. There is no guarantee of observing the slow mode at these much higher distance scales. The choice of angle directly effects FPR relaxation time of a specific diffuser and hence the bleach and read times of the FPR instrument. Assuming temporary aggregates are diffusers D moving approximately 10^{-8} to 10^{-9} cm^2 · s^{-1} the characteristic FPR relaxation τ_T time can be calculated according to:

$$\tau_T = \frac{1}{K^2 D} \tag{91}$$

From this value the maximum bleach time ($\tau_T \div 10$) and minimum read time ($\tau_T \times 10$) can be calculated. That is because the photobleaching subsystem should meet the rule of 1000, meaning the bleach beam should be at least 1000 times brighter than the read beam used to monitor recovery.[254] This particular number is chosen as the product of three criteria that must be met. One factor of ten arises from the bleach duration having to be less than 10% of the recovery time; another factor of ten is needed because the acquisition time after bleaching needs to be 10 times longer than the recovery time; and the last factor of ten arises from parasitic photobleaching from the read beam during the recovery phase should not exceed 10%.[27] A DLS scattering angle of 30° enables the measurement of the slow mode but for the equivalent distance scale in FPR the bleach and read times translate to 200 μs and 2 s respectively for a diffuser moving around 10^{-9} $cm^2 \cdot s^{-1}$. Since the FPR signal to noise depends on the concentration of fluorescent entities, the shorter the bleach time the less power is delivered by the laser beam to bleach enough entities and provide sufficient signal. FPR bleach times depend on beam power but are typically on the order of milliseconds to seconds. The optical components of the FPR set up take time to switch the beam intensity from read to bleach back to read, and also stop and start fluorescence signal acquisition, so longer bleach times are advantageous from that perspective. With a trade off between comparable DLS distance scales and long enough bleach times we have targeted a hologrpahic FPR beam crossing angle of 10°, as an effective starting point, which results in a bleach time of 2 milliseconds and a distance scale a factor of 3 larger than what is routinly used by DLS to observe the slow mode (Table 7).

Table 7. FPR bleach and read times at different beam crossing angles for diffusers moving at 10^{-8} and 10^{-9} $cm^2 \cdot s^{-1}$.

$D = 1/K^2\tau_T$		D ($cm^2 \cdot s^{-1}$) = 10^{-8}			D ($cm^2 \cdot s^{-1}$) = 10^{-9}		
θ /°	**K^2 / cm^{-2}**	**τ_T / s**	**Bleach / µs**	**Read / s**	**τ_T /s**	**Bleach / µs**	**Read / s**
0.5	1.26E+06	79.211	79211	792.11	792	792114	7921
1	5.05E+06	19.803	19803	198.03	198	198032	1980
2	2.02E+07	4.951	4951	49.51	50	49512	495
3	4.54E+07	2.201	2201	22.01	22	22008	220
4	8.08E+07	1.238	1238	12.38	12	12382	124
5	1.26E+08	0.793	793	7.93	8	7926	79
10	**5.04E+08**	**0.199**	**199**	**1.99**	**2**	**1985**	**20**
15	1.13E+09	0.089	89	0.89	1	885	9
20	2.00E+09	0.050	50	0.50	1	500	5
25	3.11E+09	0.032	32	0.32	0	322	3
30	4.44E+09	0.023	23	0.23	0	225	2

The above values show that a beam crossing angle of 10° provides realistic bounds for minimum and maximum bleaching and reading times to strive for. The diffuser values used are based on approximately equivalent values of the DLS slow mode that account for temporary aggregates. From the above table we see that the photobleaching pulse time should be no longer than 2000 µs, and the corresponding minimum acquisition time post bleach is 2 s.

5.3.3 Calculation and comparison of spatial frequency

In order to directly measure the range of spatial frequencies that can be achieved via the generated holographic patterns, a calibration was first performed using a microscope stage micrometer with 50 µm increment. Images of the micrometer scale enabled the conversion of number of pixels (px) to µm. A comparison of the micrometer image (Figure 91A) to one taken of a 150 lines per inch Ronchi Ruling (Figure 91B) was done to get an idea of the magnitude of spatial frequencies that were achieved with the image-patterned long-distance FPR technique.

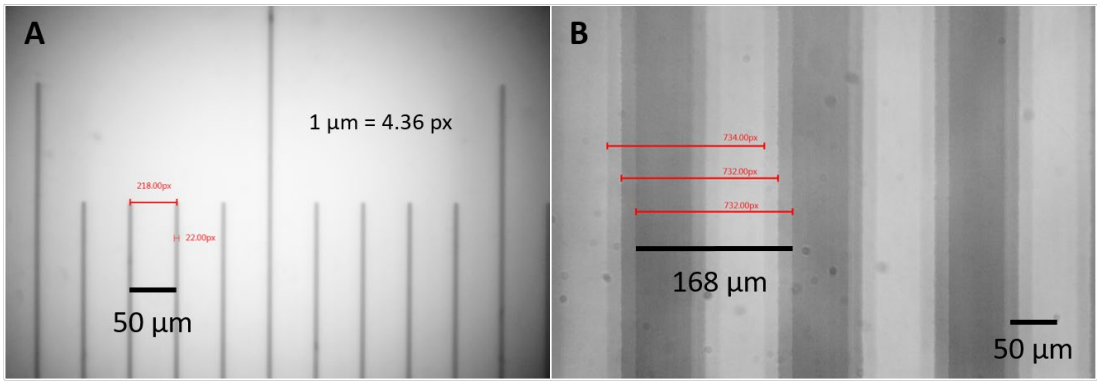

Figure 91. Bright field microscope images of (A) 50 µm scale microscope slide micrometer to be able to convert between pixel distance and real distances, and, (B) a 150 lines per inch Ronchi ruling showing the pattern periodicity L = 168 µm. Conversion of image px to µm is shown along with the width of the micrometer indents being 4 µm and so the error was taken as half that. Scale bars are labeled.

A 50 µm scale bar was drawn between the centers of each indentation mark, hence the associated error was taken to be half the width of each indents, calculated to be approximately 10 px or 2 µm. Unless otherwise stated the error for the 50 µm is 2 µm. The conversion between µm and px was calculated to be 1 µm = 4.36 px. Pattern periodicity of the 150 lines per inch Ronchi Ruling was calculated to be L = 168 µm, with $L = 2\pi/K$ the spatial frequency of the long-distance FPR instrument produced from this Ronchi ruling is $K = 374$ cm^{-1}.

The spatial frequency limit for a holographic FPR using an image analysis technique with a digital camera in conjunction with a conventional microscope depends on two main factors. First is the ability to optically resolve a constructive and destructive interference pattern. This is governed by the Abbe diffraction limit d_A, given by $d_A = \lambda_0/2NA$, which results in a value of 668.75 nm with 535 nm green fluorescent light with a lens of numerical aperture NA of 0.4. In practice this value is higher and these diffraction effects interact with the digital camera's pixel grid resulting in convolution of the point spread functions

of the objective lens and camera. What can be imaged is determined by the spread of the diffraction-limited point spread function which is approximated by:

$$\frac{d_A}{2} = 1.22\lambda_0 N_f \tag{92}$$

where N_f is an objective lens f-number (ratio of focal length to the aperture diameter). For green fluorescent light from FITC and a 20X objective with an f-number of 2 we expect to be able to resolve interference patterns down to approximately 3 μm. These values guided the beam crossing angles which were varied from $\theta \approx 0.5°$ to $\theta \approx 8°$. Resulting grating periods in the range of 21 to 5 μm were achieved, corresponding to spatial frequencies that ranged from 2978 to 12452 cm^{-1}, respectively (Figure 92).

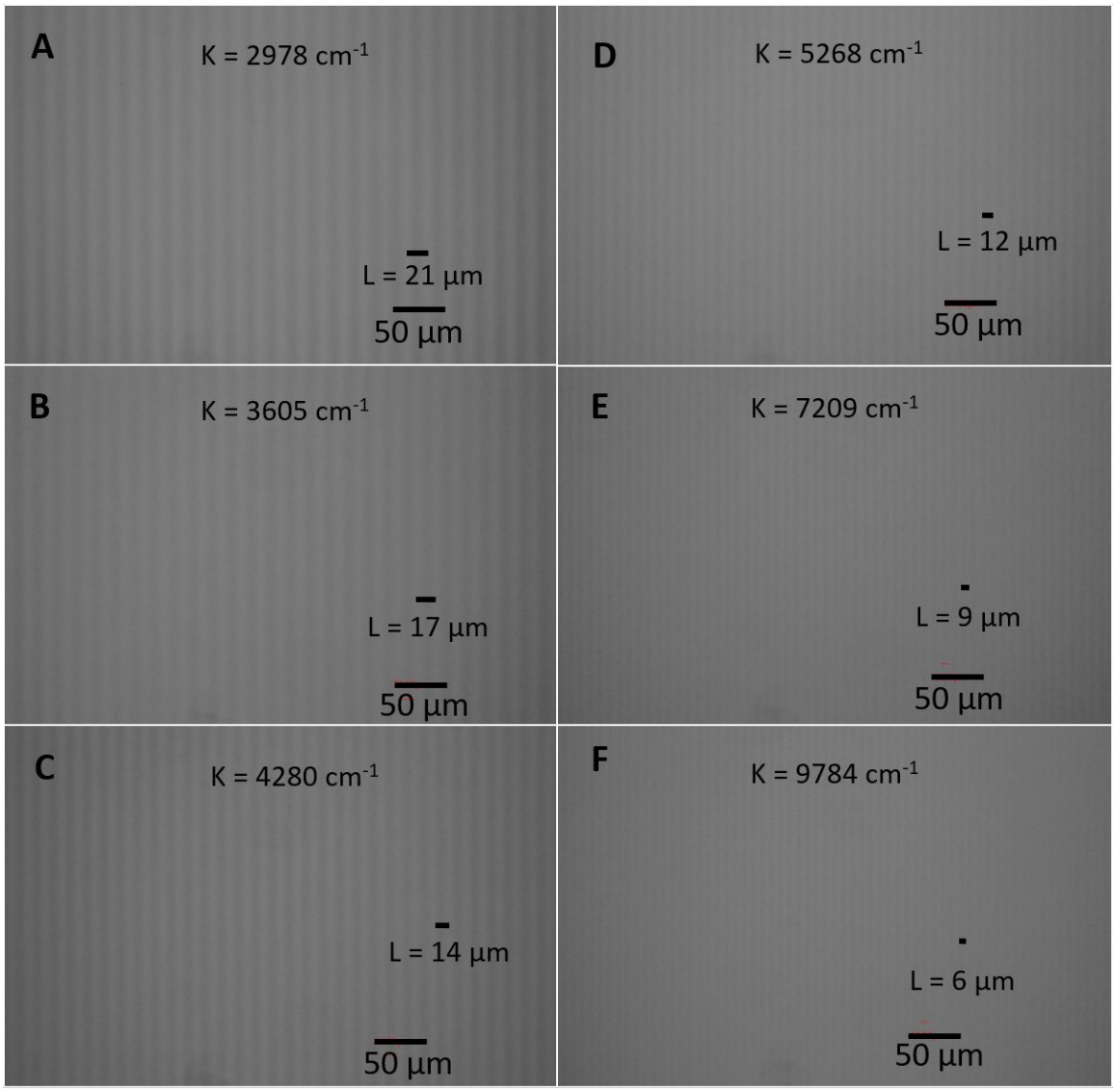

Figure 92. Images of holographic interference pattern of varying periodicity *L* resulting from different beam crossing angles θ. Larger *L* values correspond to smaller θ. *K* values are calculated from the measured *L* and scale bar is shown. (A) *L* = 21 µm, *K* = 2978 cm^{-1}, (B) *L* = 17 µm, *K* = 3605 cm^{-1}, (C) *L* = 14 µm, *K* = 4280 cm^{-1}, (D) *L* = 12 µm, *K* = 5268 cm^{-1}, (E) *L* = 9 µm, *K* = 7209 cm^{-1}, (F) *L* = 6 µm, *K* = 9784 cm^{-1}. Sample is F-NaPSS 75 in NaCl solution at a C_p/C_s ratio of 32.

Spatial frequencies calculated from the above images displayed values an order of magnitude greater than achieved by the long-distance FPR instrument but are a factor of

two-to-ten times smaller than what DLS probes to routinely observe the slow diffusive mode.

5.3.4 Characterization of interference pattern

Images captured during the reading phase of the experiment were analyzed with a custom LabView code we developed. The amplitude of pixel intensity was summed down the rows of each column and was plotted as a function of the number of pixels (columns) horizontally across the image. The resulting intensity vs pixel number plot for crossed beams produces a sinusoidal-like wave with intensity peaks and troughs at the corresponding points of constructive and destructive interference of the laser beam fluorescing the sample. A 1D fast Fourier transform (FFT) of this plot produces a power spectrum of amplitude vs spatial frequency showing fundamental spatial frequency peaks that correspond to the size of the stripes. Screenshots of the LabView software interface are shown below (Figure 93). They show the analysis of the corresponding images from Figure 92 by producing a heat map of fluorescence intensity from the crossed beam on the sample, the sinusoidal pattern from summing pixel intensity down the image as a function of the horizontal axis, and the power spectrum from the 1D FFT.

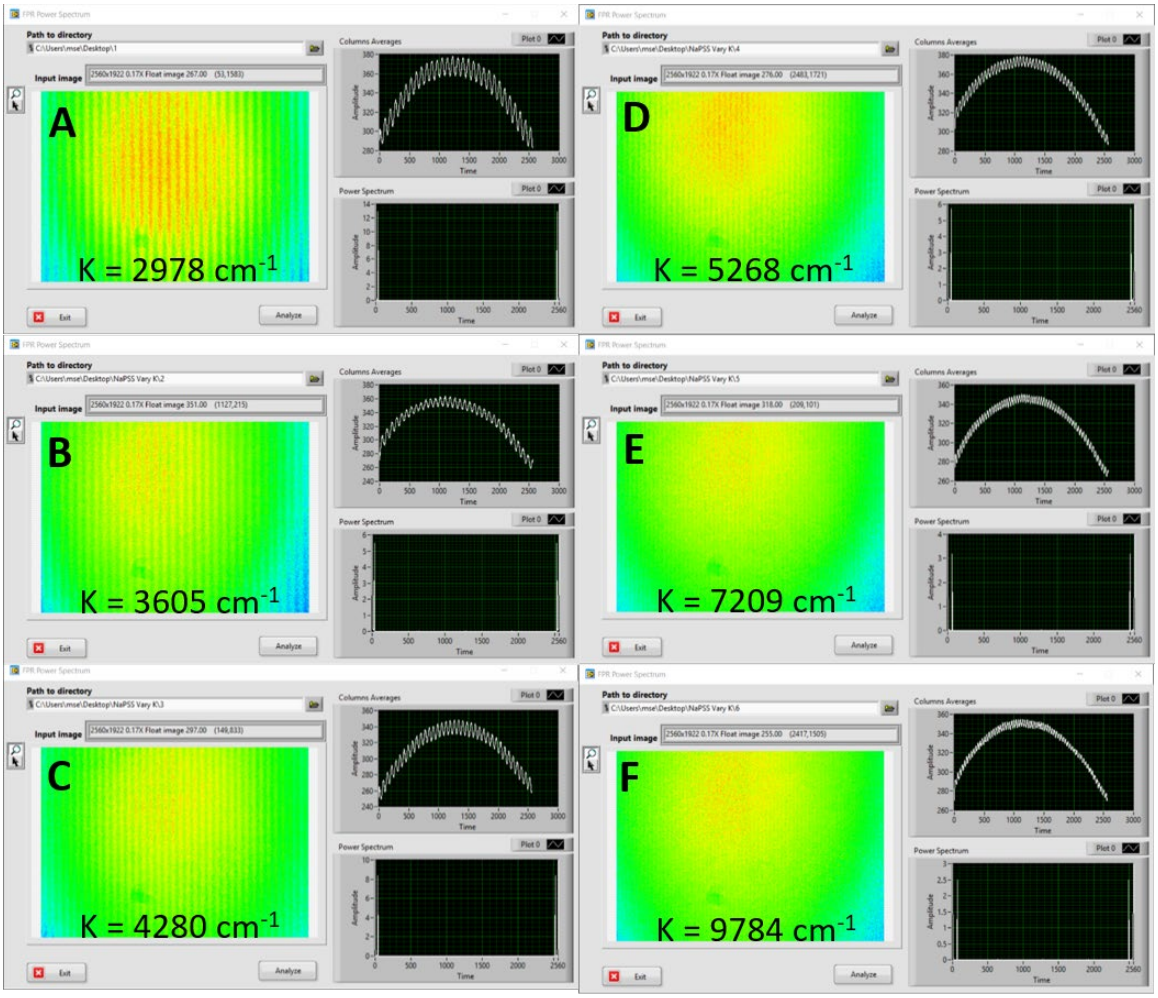

Figure 93. LabView image analysis software interface showing a heat map of pixel intensity for each interference pattern measured at different *K*, which are labeled for (A) through (E), and plots of pixel column average intensity as a function of number of pixels across the row showing the sinusoidal-like shape, and a power spectrum plot which is the 1D FFT of the column summed intensity averages to produce an amplitude vs spatial frequency plot. Sample is F-NaPSS 75 in NaCl solution at a C_p/C_s ratio of 32.

A 1D FFT of images taken at different beam crossing angles, and hence different grating periodicities, display a unique peak in their power spectrum. This spike corresponds to the spatial frequency of the contrast pattern (Figure 94A). Smaller grating periods were produced at larger beam crossing angles and the 1D FFT of images of these smaller periodicities corresponded to peak location at higher spatial frequencies on the power

spectrum. This was observed for gratings with spatial frequencies of K = 4150, 7610 and 12452 cm^{-1}, which produced power spectrum peaks at x-axis values of 36, 62 and 84, respectively (Figure 94B).

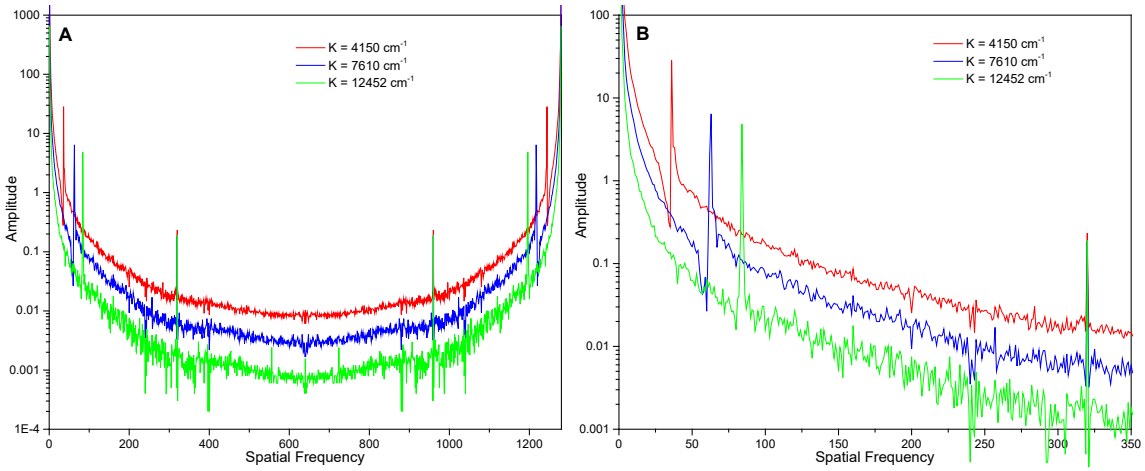

Figure 94. (A) 1D FFT of images taken of samples with gratings of different spatial frequencies and, (B) the power spectrum fundamental peaks that correspond to each specific spatial frequency are shifted to higher x-axis values for higher spatial frequencies. Sample is F-NaPSS 75 in NaCl solution at a C_p/C_s ratio of 32.

Images acquired at a time Δt after photobleaching show the loss of the contrast pattern due to diffusion of fluorescent moieties from the unbleached regions into the bleached regions (Figure 95).

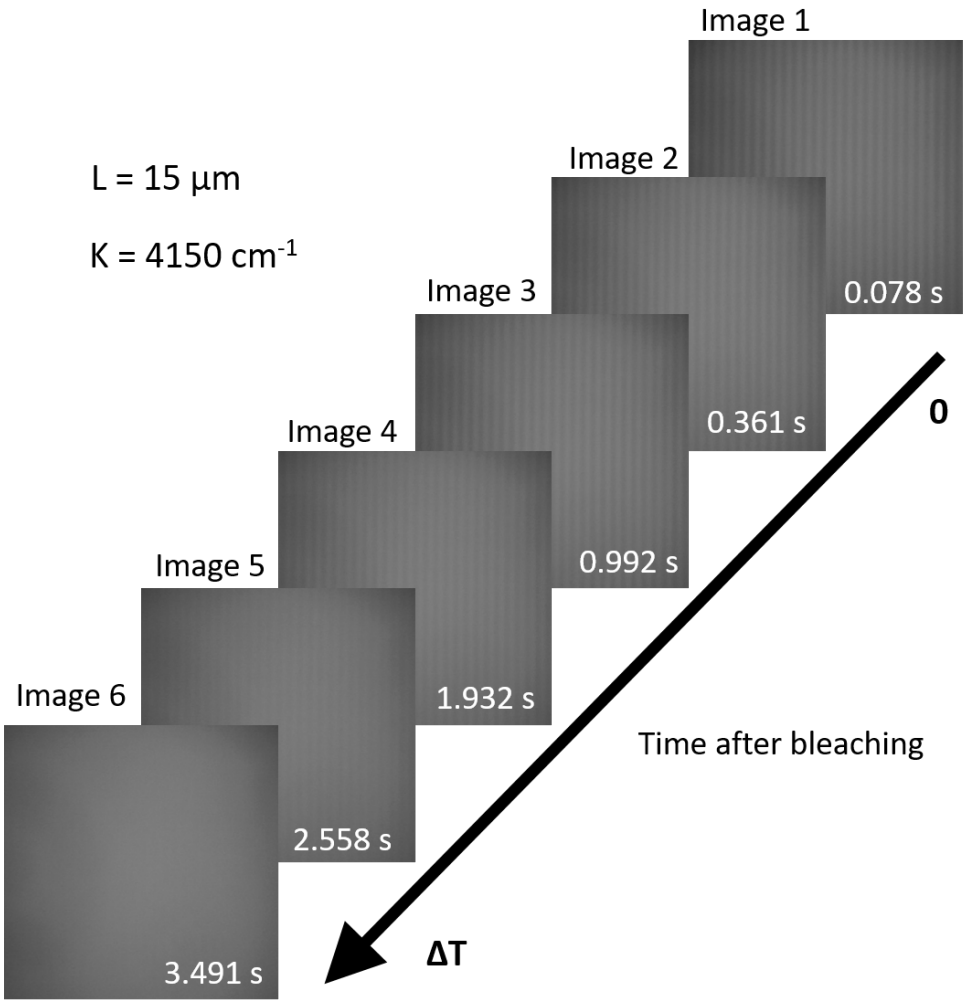

Figure 95. Images acquired at stated time intervals (in seconds) after photobleaching show how the striped pattern decays with time to a point where the stripes are visually indistinct after a long enough time. These images were measured to have a periodicity L = 15 µm and subsequent K = 4150 cm^{-1}. Sample is F-NaPSS 75 in NaCl solution at a C_p/C_s ratio of 32.

Corresponding plots of the summed intensity amplitude down a pixel column vs pixels along the row of the image quantify the decrease in magnitude of the contrast with time (Figure 96).

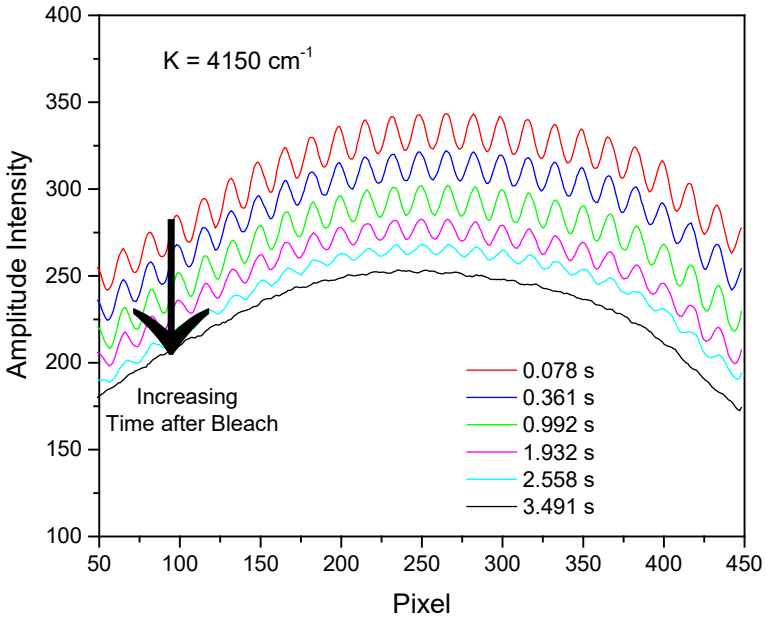

Figure 96. Amplitude of pixel intensity summed down each column vs pixels across an image as a function of time acquired (stated in seconds) after photobleaching. Traces are offset vertically for clarity to observe the sinusoidal-like pattern decay of amplitude. Sample is F-NaPSS 75 in NaCl solution at a C_p/C_s ratio of 32.

Characteristic power spectrum peaks obtained from the 1D FFT of images acquired Δt after photobleaching were tracked as a function of time. The decay of the characteristic peak was clearly observed and quantified, this is shown below for peaks corresponding to images acquired at increasing times after bleaching (Figure 97).

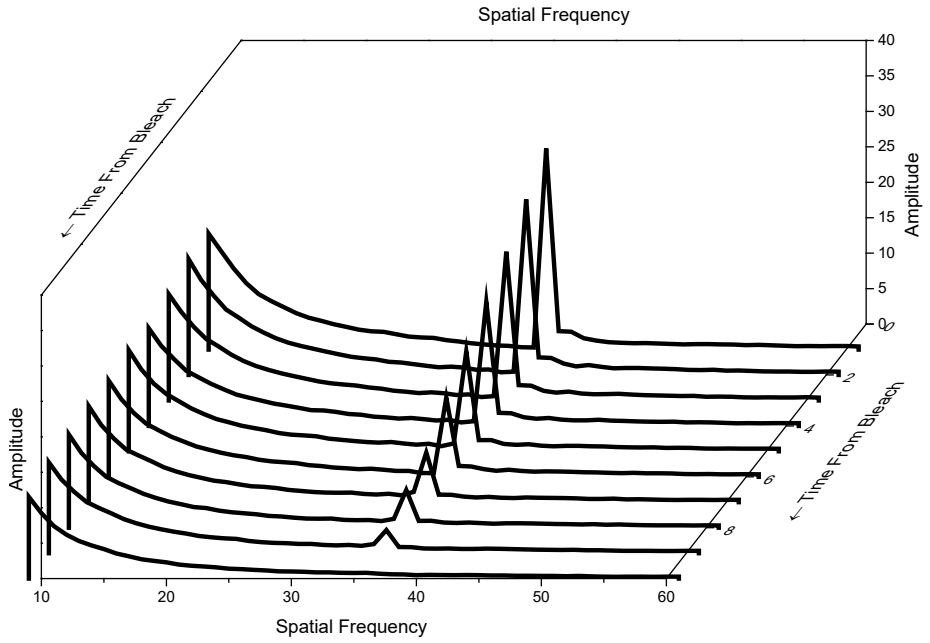

Figure 97. Decay of the magnitude of the characteristic spatial frequency peak as a function of time after photobleaching. Peaks shown are from images at arbitrary times after bleaching to better illustrate the magnitude of the decay. Spatial frequency of the measurement was K = 4150 cm^{-1}. Sample is F-NaPSS 75 in NaCl solution at a C_P/C_S ratio of 32.

The magnitude of the fundamental peak plotted as a function of time after bleaching produces a plot showing the peak decreases in an exponentially decaying fashion that can be described according to $C(t) = C(0)e^{-K^2Dt}$. Images were acquired at a frame rate of 38.3 per second and approximately 200 images were taken after bleaching with each undergoing a 1D FFT to produce a power spectrum peak value. These values were plotted as a function of time after bleaching and the decay of these traces were acquired at three different spatial frequencies, 4150 cm^{-1} (Figure 98A), 7610 cm^{-1} (Figure 98B), and 12452 cm^{-1} (Figure 98C).

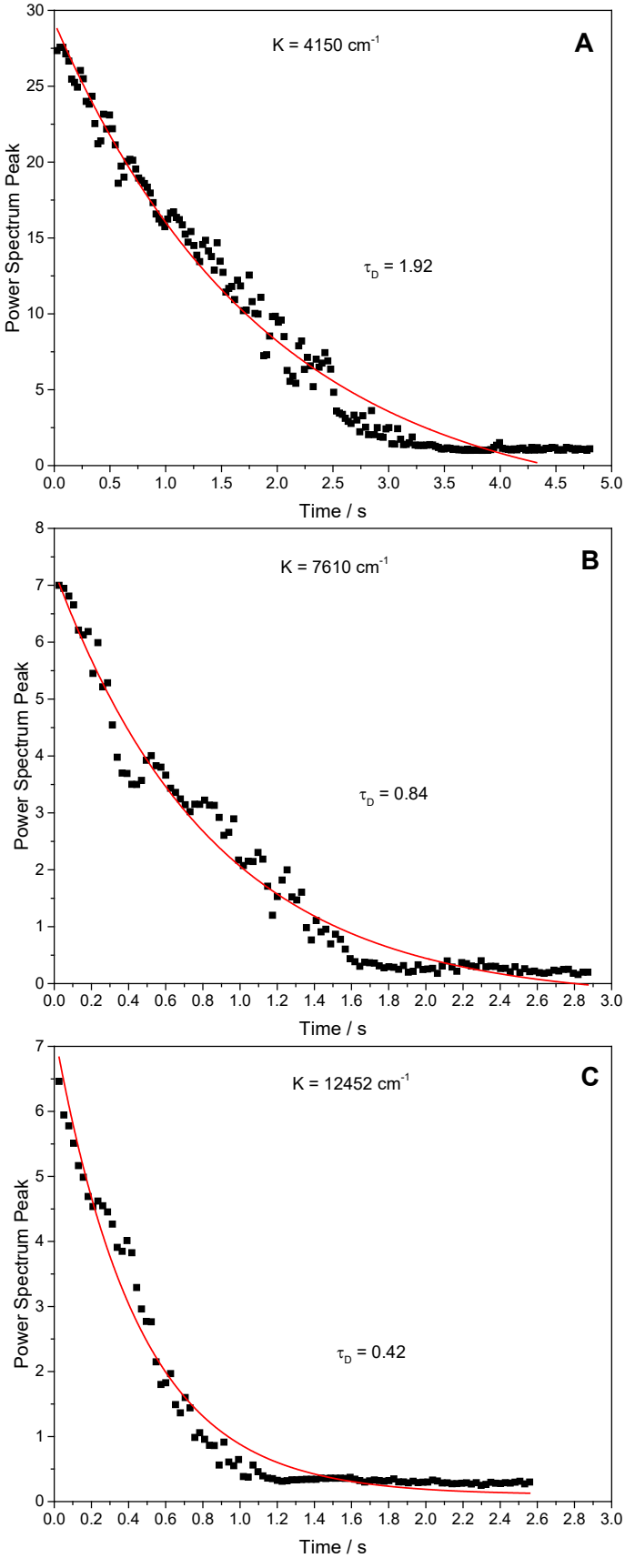
A
K = 4150 cm-1
τD = 1.92
Power Spectrum Peak
Time / s
B
K = 7610 cm-1
τD = 0.84
Power Spectrum Peak
Time / s
C
K = 12452 cm-1
τD = 0.42
Power Spectrum Peak
Time / s

Figure 98. Power spectrum peak decay in magnitude as a function of time after photobleaching measured at (A) K = 4150 cm^{-1}, (B) K = 7610 cm^{-1}, (C) K = 12452 cm^{-1}. FPR relaxation time τ_D values obtained from exponential decay fits to the data. Sample is F-NaPSS 75 in NaCl solution at a C_p/C_s ratio of 32.

The exponential decay fits provided a t value to the above equation which was interpreted as the characteristic FPR relaxation time τ_D. These values obtained from the above fits were plotted against K^2 according to the relation $D = \frac{1}{K^2\tau_D}$ where $\Gamma = 1/\tau_D$ to obtain a self-diffusion coefficient (Figure 99).

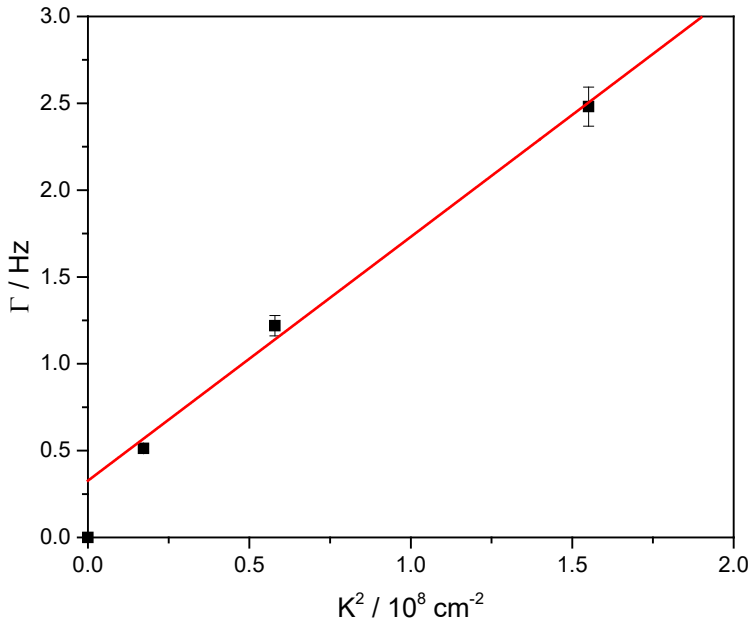

Figure 99. A plot of Γ vs K^2 for F-NaPSS 75 in NaCl solution at a C_p/C_s ratio of 32.

A self-diffusion coefficient of $1.5 \pm 0.1 \times 10^{-8}$ cm$^2 \cdot$ s^{-1} was obtained from the data in Figure 99. An unweighted linear least squares fit to the data should pass through zero but instead produced a y-intercept value of 0.31, which indicates error in the acquisition and/or analysis. Improvements in the technique arise from adhering to the FPR general rule of

thumb of 1000. Firstly, the bleaching times were approximately 50 milliseconds, which according to Table 7 is an order of magnitude longer than what is required for diffusers moving at similar rates. One solution to this would be to perform multiple runs of short bleaches and sum up the signal with each acquisition. It seems that perhaps not enough sample could be bleached with just one short blast. Secondly, a larger power ratio between bleaching and reading beam is required, which assists in reducing bleaching times by increasing the amount of energy that can be delivered in a shorter period of time. This can be achieved with a new and improved AOM device (Model # CQM-110-5-100-488; Make # Brimrose). Finally, a faster camera (100 frames per second) with 16-bit depth (Model # sCMOS edge 5.5 ; Make # PCO), compared to the current 8-bit camera (38.3 frames per second), will enhance the image analysis process and permit for acquiring more data points immediately after photobleaching, which is crucial when fitting an exponential decay curve to obtain Γ values.

5.3.5 Diffusion of NaPSS across a wide range of spatial frequency

The self-diffusion coefficient of $1.5 \pm 0.1 \times 10^{-8}$ $cm^2 \cdot s^{-1}$ for 75 kDa NaPSS measured with the holographic FPR at a C_p/C_s ratio of 32 was significantly smaller than a measured self-diffusion coefficient of $1.8 \pm 0.3 \times 10^{-7}$ $cm^2 \cdot s^{-1}$ for the same molecular weight F-NaPSS at a similar C_p/C_s ratio in Figure 75. Sedlak showed that the slow mode for 47 kDa NaPSS at low salt had a diffusion coefficient of approximately 2-3 $\times 10^{-8}$ $cm^2 \cdot s^{-1}$ as measured by DLS at spatial frequency of q = 172700 cm^{-1}.[109] Similarly, Sedlak and Amis, Jia and Muthukumar, Uppu et al., Reed at al., and Sehgal and Seery, showed slow modes for NaPSS in NaCl solutions measured by DLS at q values that ranged from approximately

50000 to 150000 cm^{-1}.[3, 38, 88, 107, 117, 266] These values along with FPR measurements using a Ronchi ruling from Cong et al., and Tanahatoe and Kuil were compiled, alongside data obtained from this thesis, on a single plot of diffusion coefficient vs spatial frequency (q or K) for NaPSS in aqueous low salt solution (Figure 100).[38, 272]

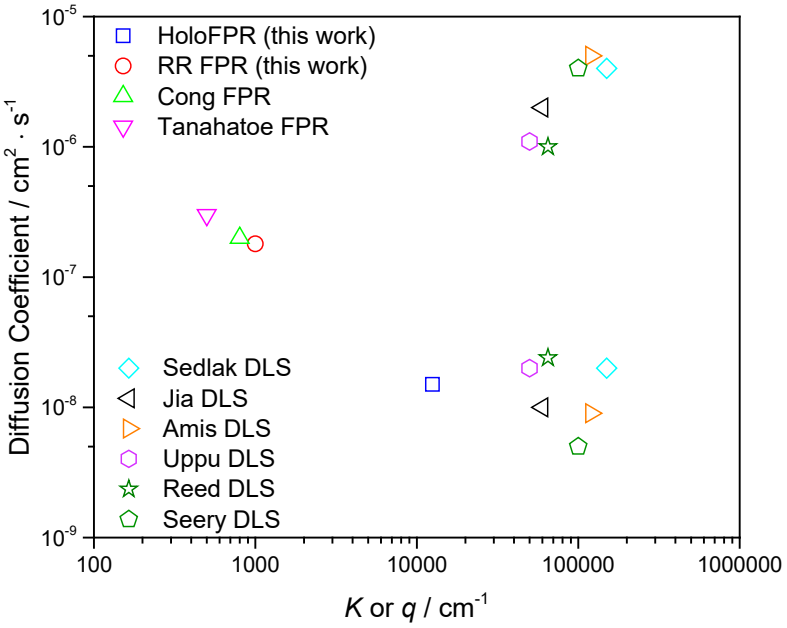

Figure 100. Compilation of diffusion coefficient data for NaPSS in low concentration NaCl solution obtained using FPR or DLS from this work and others as a function of spatial frequency *K* or *q*. RR stands for Ronchi ruling long-distance FPR and holo represents the FPR instrument used in this study. DLS results display both fast and slow diffusive modes.

The plot is labeled according to the data contributed to by each author and shows both the fast and slow modes that are observed in DLS. The above data show how the holographic FPR technique here is reducing the gap in spatial frequency between long-distance Ronchi ruling based FPR instruments and DLS. The diffusion coefficient obtained for NaPSS using

the holographic FPR technique was similar in magnitude to the slow mode values measured by DLS.

5.4 Conclusion

Design and construction of a holographic FPR technique was completed with unique image-based analysis to measure the diffusion coefficient of fluorescent NaPSS in solutions at low salt concentration. Variation of the beam crossing angle produced grating periods in the fluorescent sample that ranged from L = 22 to 5 μm. This enabled an order of magnitude increase in the spatial frequency of the FPR technique, from $K \approx 1000$ cm^{-1} for instruments that utilize a Ronchi ruling to $K \approx 12500$ cm^{-1} for this instrument. Spatial frequencies reached here are comparable to the DLS technique at lower scattering angles ($q \approx 1100$ cm^{-1} at $\theta = 5°$, $\lambda_0 = 660$ nm) but are a factor of 2-5 times smaller than q ranges ($q \approx 60000$ cm^{-1} at $\theta = 30°$) that regularly observe the slow diffusive mode of NaPSS in solutions at low salt concentration. A measured self-diffusion coefficient for NaPSS of M_w 75 kDa was $1.5 \pm 0.1 \times 10^{-8}$ cm$^2 \cdot$ s^{-1} at a C_p/C_s ratio of 32, which was significantly smaller than what previous FPR measurements gave at smaller spatial frequencies. The value was comparable to slow mode values for NaPSS as obtained by DLS but further validation of the diffusion value obtained by this holographic instrument is required. Improvements to the technique to enhance image acquisition and reduce bleach times as well as testing a range of NaPSS molecular weights and concentrations is required to gain further understanding of dynamics probed at these spatial frequencies.

5.5 Acknowledgement

We would like to acknowledge Dr. Jinxin Fu for the insightful discussions and assistance with the optical table set-up. I am grateful to Dr. Alyssa Blake and Dr. Wieslaw Stryjewski for development of the LabView image analysis software. We would like to acknowledge the support of OPALL, STAMI, The Georgia Tech Hightower Family and the support from US Endowment and USDA Forest Service [E17-23].

CHAPTER 6. CONCLUSIONS AND FUTURE WORKS

A focus on developing a convenient way to produce completely sulfonated NaPSS on gram scales over a broad range of molecular weights was the motivation behind the first project in this thesis. Synthesis direct from sodium styrene sulfonate monomer ensured 100 % sulfonation of the final polymer and the use of an aqueous RDRP technique provided reaction control. The adjustment of reaction parameters such as pH, amount of added MeOH cosolvent, incorporation of an added deactivator species in the form of NaCl and variation in initiator to ligand to copper catalyst species suppressed unwanted side reactions common in polar media and reduced the probability for termination events. A range of molecular weights from approximately 1.5–4 × 10^5 g · mol^{-1} were achieved, which are amongst the highest in the field of RDRP conducted under homogenous conditions. In addition, the dispersity values remained low for all syntheses ($Đ$ < 1.3). Parametric optimization, rather than a traditional approach of adjustment of monomer to initiator, enabled successful targeting of such a wide range of molecular weights (Figure 101). Triplicate syntheses highlighted the reproducible nature of the synthetic technique and chain extension reactions showed that chain end fidelity was maintained throughout the reaction.

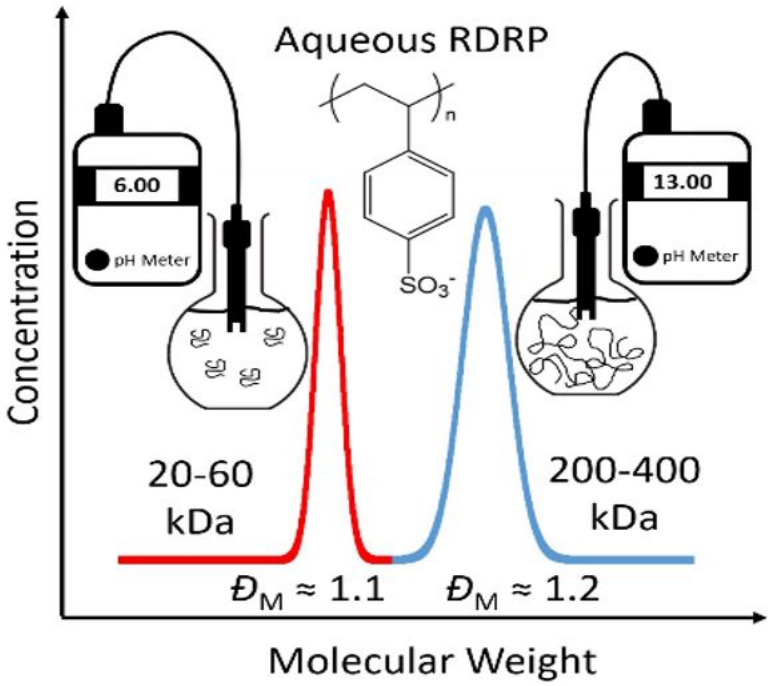

Figure 101. Schematic illustrating the effect of reaction pH on the molecular weight of NaPSS as synthesized by the aqueous RDRP approach.

Evidence for a straightforward method to synthesize completely para-sulfonated NaPSS over a broad molecular weight range is a significant contribution for researchers to investigate fundamental polyelectrolyte and use NaPSS in applications such as in multilayer membrane technologies. This work also contributes to the RDRP community in that it adds to the scope of polymerizable water soluble monomers and ability of the technique to succeed in an environmentally friendly solvent.

The post-treatment of PS is most common method to produce NaPSS, an imperfect approach that results in incomplete sulfonation of the chain, and produces a material inferior to that which we had synthesized. With the majority of research on NaPSS, along with its industrial and commercial applications, being done on an imperfect material sourced from post-treatment techniques, a comparison of fundamental properties of the two

types of NaPSS materials was warranted to justify their differences and the potential effect in their intended application. FTIR, ^{1}H NMR and ^{13}C NMR identified differences between NaP4SS and C-NaPSS, with ^{1}H NMR showing that a degree of sulfonation at the para position for the polymer was able to be quantified. The 100% sulfonated NaP4SS compared to degrees of sulfonation of 88.9 to 94.0% for C-NaPSS translated to measurable differences in the solution and bulk properties of these polymers. In water the $\delta n/\delta c$ values were 0.175 ± 0.001 mL/g compared to 0.172 ± 0.001 mL/g for NaP4SS and C-NaPSS, respectively, which is expected for a higher atomic sulfur content in the NaP4SS material. Flory exponents were 0.6 ± 0.02 for all NaP4SS samples across a broad M range, which by contrast, were 0.5 ± 0.01 for C-NaPSS, also across a broad M range. This difference highlights the adoption of dissimilar solution conformations between the polymers. In addition, T_g values of 210-240 °C were observed for all C-NaPSS samples while no T_g was observed for NaP4SS. A summary of these property differences is shown below (Figure 102).

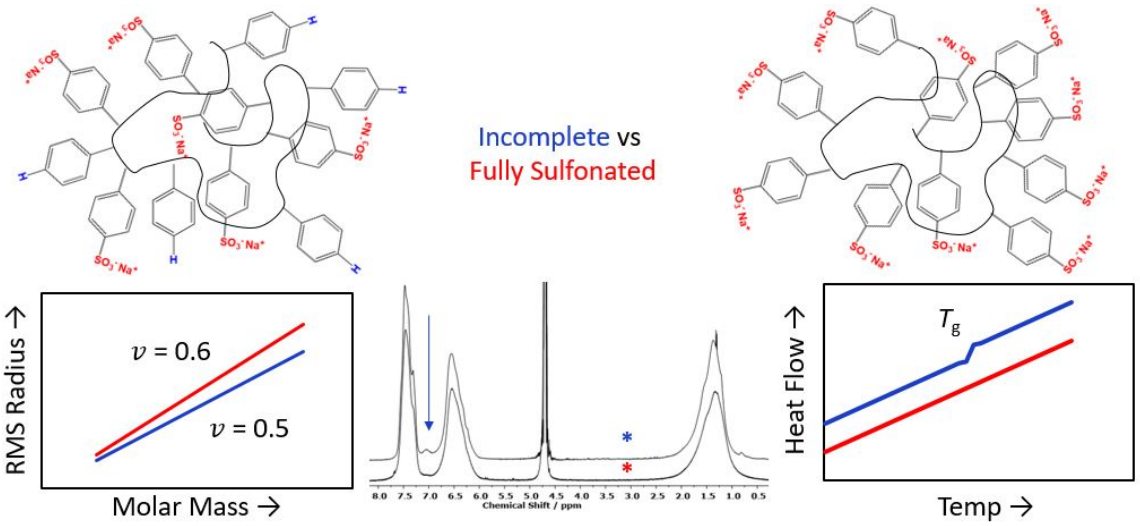

Figure 102. Schematic summarizing solution and bulk differences in the physical properties of NaP4SS (red) and C-NaPSS materials (blue). Conformation plots, DSC traces and ^{1}H NMR reveal these discrepancies.

The knowledge that not all NaPSS materials are created equal with will be beneficial for researchers who investigate topics that vary from charge carrying properties of solid polymer electrolytes to coacervate formation of oppositely charged polyelectrolyte complexes. It has been shown that a higher degree of sulfonation, and site regiospecific sulfonation, for the NaP4SS materials we synthesized, has resulted in substantially different solution and bulk properties. This is of significant interest in applcations where viscosity modification, higher conductivity and ion uptake values, and thermal performance, for example, are important material traits. It also warrants many fundamental polyelectrolyte studies to be re-evaluated with this new NaP4SS material.

Investigation of the dynamics of NaPSS in NaCl solutions at ionic strength, specifically targeted in relation to the critical threshold ratio C_p/C_s where the slow diffusive mode is seen by DLS, was done using FPR. Attachment of a FITC to NaPSS to produce F-NaPSS enabled tracking of this optical probe in single F-NaPSS and mixed F-NaPSS with

unlabeled M-NaPSS matrices. No direct observation of the slow diffusive mode was made in single component F-NaPSS solutions but the FPR measured average diffusion as a function of the C_p/C_s ratio above the critical transition revealed a greater than expected drop in the diffusion coefficients. In mixed F-NaPSS and M-NaPSS solutions at low salt a dependence of probe diffusion on probe M_w as a function of C_{matrix} and matrix M_w was seen. This was contrary to the hypothesis that if probes of all sizes that were entrained in aggregates they would diffuse equally, regardless of matrix conditions. Diffusion of probes in matrices of similar molecular weights were found to scale with concentration according to $D \sim C^{-1/2}$.[106] The C_{matrix} exponent approached -0.5 as the probe and matrix molecular weights became increasingly equivalent from 31 to 161 to 590 kDa for the probes and 450 kDa for the matrix. The diffusion scaling exponent $D_{probe} \sim M_{probe}^{-\beta}$ increased from β to 0.65 ± 0.03 without the presence of matrix to 0.79 ± 0.04 in the presence of added M-NaPSS 450 matrix at 20 mg/mL. Probe diffusion became independent of matrix M_w above at high enough C_{matrix} suggesting deviation from Stokes-Einstein behavior. Regardless of being unable to directly observe the slow mode, substantial information on the diffusion of mixed molecular weight polyelectrolytes at low salt was gained and warrants the development of theory to describe such results. Instead, treatment of the data with scaling theories on neutral polymer systems of probes diffusing through matrices guided our results. A Langevin-Rondelez treatment of the mixed NaPSS results also showed deviation from Stokes-Einstein behavior for smaller probes in smaller matrices, and revealed a dependence of probe diffusion on matrix correlation lengths.

The limitation of Ronchi ruling based FPR technology motivated the need to address the imperfect comparison between dynamic measurements made by FPR and DLS by reducing

the distance scale of the FPR measurement. A crossed-beam holographic FPR instrument was developed to produce grating periods in the fluorescent sample that ranged from L = 22 to 5 μm. This enabled an order of magnitude increase in the spatial frequency of the FPR technique, from K ≈ 1000 cm^{-1} for instruments that utilize a Ronchi ruling to $K \approx$ 12500 cm^{-1} for this instrument. Spatial frequencies of the holographic FPR were comparable to what DLS probes at lower scattering angles ($q \approx 1100$ cm^{-1} at $\theta = 5°$, λ_0 = 660 nm) but are a factor of 2-5 times smaller than q ranges ($q \approx 60000$ cm^{-1} at $\theta = 30°$) that regularly observe the slow diffusive mode of NaPSS in solutions at low salt concentration. In addition, a new image based FPR analysis method was used to track the decay in the fluorescence contrast as a function of time. Custom LabView code analysed images and a self-diffusion coefficient of $1.5 \pm 0.1 \times 10^{-8}$ $cm^2 \cdot s^{-1}$ was obtained for NaPSS of M_w 75 kDa at a C_p/C_s ratio of 32. This value was significantly smaller than what previous FPR measurements gave at smaller spatial frequencies and was comparable to slow mode values for NaPSS in NaCl observed by DLS.

Further validation of the diffusion values measured by the holographic FPR instrument is required, in addition to testing on a wider range of samples that diffuse at different rates. Improvements to the technique include reducing bleach times, a better AOM device and the use of a faster camera with greater bit depth. This will enhance the image acquisition process. Extending the range of NaPSS molecular weights and concentrations is also required to gain further understanding of dynamics probed at these unique spatial frequencies which bridge the gap between long distance FPR and DLS methods.

REFERENCES

1. Lee, W. I.; Schurr, J. M., Laser Light-Scattering Studies of Poly(L-Lysine Hbr) in Aqueous-Solutions. *J Polym Sci Pol Phys* **1975,** *13* (5), 873-888.

2. Schmitz, K. S.; Ramsay, D. J., Qels-Sef Study on Poly(Lysine) in the Extraordinary Phase - Effect of Electric-Field Strength on the Apparent Diffusion-Coefficient. *Biopolymers* **1985,** *24* (7), 1247-1256.

3. Sehgal, A.; Seery, T. A. P., The ordinary-extraordinary transition revisited: A model polyelectrolyte in a highly polar organic solvent. *Macromolecules* **1998,** *31* (21), 7340-7346.

4. Sedlak, M., What can be seen by static and dynamic light scattering in polyelectrolyte solutions and mixtures? *Langmuir* **1999,** *15* (12), 4045-4051.

5. De Gennes, P.-G., *Scaling concepts in polymer physics*. Cornell university press: 1979.

6. Doi, M.; Edwards, S. F., *The theory of polymer dynamics*. Clarendon Press: Oxford, 1986; Vol. 222.

7. Forster, S.; Schmidt, M., Polyelectrolytes in Solution. *Physical Properties of Polymers* **1995,** *120*, 51-133.

8. Muthukumar, M., Theory of counter-ion condensation on flexible polyelectrolytes: Adsorption mechanism. *J Chem Phys* **2004,** *120* (19), 9343-9350.

9. Drifford, M.; Dalbiez, J. P., Light scattering by dilute solutions of salt-free polyelectrolytes. *The Journal of Physical Chemistry* **1984,** *88* (22), 5368-5375.

10. Drifford, M.; Dalbiez, J. P., Effect of Salt on Sodium Polystyrene Sulfonate Measured by Light-Scattering. *Biopolymers* **1985,** *24* (8), 1501-1514.

11. Park, K.; Robinson, J. R., Bioadhesive Polymers as Platforms for Oral-Controlled Drug Delivery - Method to Study Bioadhesion. *International Journal of Pharmaceutics* **1984,** *19* (2), 107-127.

12. Kessler, C.; Ng, J.; Valdez, K.; Xie, H.; Geiger, B., The Use of Sodium Polystyrene Sulfonate in the Inpatient Management of Hyperkalemia. *Journal of Hospital Medicine* **2011,** *6* (3), 136-140.

13. Yeager, H. L.; Steck, A., Ion-Exchange Selectivity and Metal-Ion Separations with a Perfluorinated Cation-Exchange Polymer. *Anal Chem* **1979,** *51* (7), 862-865.

14. Moore, S.; Spackman, D. H.; Stein, W. H., Chromatography of Amino Acids on Sulfonated Polystyrene Resins - an Improved System. *Anal Chem* **1958,** *30* (7), 1185-1190.

15. Rasmusson, M.; Routh, A.; Vincent, B., Flocculation of Microgel Particles with Sodium Chloride and Sodium Polystyrene Sulfonate as a Function of Temperature. *Langmuir* **2004,** *20* (9), 3536-3542.

16. de Assuncao, R. M. N.; Royer, B.; Oliveira, J. S.; Rodrigues, G.; Motta, L. A. D., Synthesis, characterization, and application of the sodium poly(styrenesulfonate) produced from waste polystyrene cups as an admixture in concrete. *J Appl Polym Sci* **2005,** *96* (5), 1534-1538.

17. Lee, S.; Zurcher, S.; Dorcier, A.; Luengo, G. S.; Spencer, N. D., Adsorption and Lubricating Properties of Poly(L-lysine)-graft-poly(ethylene glycol) on Human-Hair Surfaces. *Acs Appl Mater Inter* **2009,** *1* (9), 1938-1945.

18. Chen, S. L.; Krishnan, L.; Srinivasan, S.; Benziger, J.; Bocarsly, A. B., Ion exchange resin/poly styrene sulfonate composite membranes for PEM fuel cells. *J Membrane Sci* **2004,** *243* (1-2), 327-333.

19. Yu, J.; Yi, B.; Xing, D.; Liu, F.; Shao, Z.; Fu, Y.; Zhang, H., Degradation mechanism of polystyrene sulfonic acid membrane and application of its composite membranes in fuel cells. *Phys Chem Chem Phys* **2003,** *5* (3), 611-615.

20. Argun, A. A.; Cirpan, A.; Reynolds, J. R., The first truly all-polymer electrochromic devices. *Adv Mater* **2003,** *15* (16), 1338-+.

21. Lee, B.; Seshadri, V.; Sotzing, G. A., Poly(thieno[3,4-b]thiophene)-poly(styrene sulfonate): A low band gap, water dispersible conjugated polymer. *Langmuir* **2005,** *21* (23), 10797-10802.

22. Chu, P.; Marinsky, J. A., Osmotic Properties of Polystyrenesulfonates .I. Osmotic Coefficients. *J Phys Chem-Us* **1967,** *71* (13), 4352-&.

23. Dobrynin, A. V.; Colby, R. H.; Rubinstein, M., Scaling Theory of Polyelectrolyte Solutions. *Macromolecules* **1995,** *28* (6), 1859-1871.

24. Zan, X. J.; Hoagland, D. A.; Wang, T.; Peng, B.; Su, Z. H., Polyelectrolyte uptake by PEMs: Impacts of molecular weight and counterion. *Polymer* **2012,** *53* (22), 5109-5115.

25. Zero, K.; Cyr, D.; Ware, B. R., Tracer Diffusion of Counterions through a Solution of Poly-Electrolyte. *J Chem Phys* **1983,** *79* (7), 3602-3603.

26. Zero, K.; Ware, B. R., Mobilities of Poly-L-Lysine Molecules in Low-Salt Solutions. *J Chem Phys* **1984,** *80* (4), 1610-1616.

27. Russo, P. S.; Qiu, J.; Edwin, N.; Choi, Y. W.; Doucet, G. J.; Sohn, D., Fluorescence Photobleaching Recovery. In *Soft Matter Characterization*, Borsali, R.; Pecora, R., Eds. Springer Netherlands: Dordrecht, 2008; pp 605-636.

28. Brown, D. W.; Lowry, R. E., Molecular-Weight Standards from Sulfonation of Polystyrene. *J Polym Sci Pol Chem* **1979,** *17* (4), 1039-1046.

29. Coughlin, J. E.; Reisch, A.; Markarian, M. Z.; Schlenoff, J. B., Sulfonation of polystyrene: Toward the "ideal" polyelectrolyte. *J Polym Sci Pol Chem* **2013,** *51* (11), 2416-2424.

30. Tsarevsky, N. V.; Pintauer, T.; Matyjaszewski, K., Deactivation efficiency and degree of control over polymerization in ATRP in protic solvents. *Macromolecules* **2004,** *37* (26), 9768-9778.

31. Tsarevsky, N. V.; Matyjaszewski, K., "Green" atom transfer radical polymerization: From process design to preparation of well-defined environmentally friendly polymeric materials. *Chem Rev* **2007,** *107* (6), 2270-2299.

32. Krope, R., Nielsen, J. Use of sodium polystyrene sulfonate for tightening skin. U.S. Patent 10,478,294. 2002.

33. Batterink, J.; Lin, J.; Au-Yeung, S. H. M.; Cessford, T., Effectiveness of Sodium Polystyrene Sulfonate for Short-Term Treatment of Hyperkalemia. *Can J Hosp Pharm* **2015,** *68* (4), 296-303.

34. Dubas, S. T.; Schlenoff, J. B., Swelling and Smoothing of Polyelectrolyte Multilayers by Salt. *Langmuir* **2001,** *17* (25), 7725-7727.

35. Zhang, Y.; Yildirim, E.; Antila, H. S.; Valenzuela, L. D.; Sammalkorpi, M.; Lutkenhaus, J. L., The influence of ionic strength and mixing ratio on the colloidal stability of PDAC/PSS polyelectrolyte complexes. *Soft Matter* **2015,** *11* (37), 7392-7401.

36. Park, Y.; Berger, J.; Tang, Z.; Müller-Meskamp, L.; Lasagni, A. F.; Vandewal, K.; Leo, K., Flexible, light trapping substrates for organic photovoltaics. *Appl Phys Lett* **2016,** *109* (9), 093301.

37. Kim, Y. H.; Lee, J.; Hofmann, S.; Gather, M. C.; Müller-Meskamp, L.; Leo, K., Achieving High Efficiency and Improved Stability in ITO-Free Transparent Organic Light-Emitting Diodes with Conductive Polymer Electrodes. *Advanced Functional Materials* **2013,** *23* (30), 3763-3769.

38. Cong, R. J.; Temyanko, E.; Russo, P. S.; Edwin, N.; Uppu, R. M., Dynamics of poly (styrenesulfonate) sodium salt in aqueous solution. *Macromolecules* **2006,** *39* (2), 731-739.

39. Muthukumar, M., 50th Anniversary Perspective: A Perspective on Polyelectrolyte Solutions. *Macromolecules* **2017,** *50* (24), 9528-9560.

40. Cicerone, M. T.; Blackburn, F. R.; Ediger, M. D., Anomalous Diffusion of Probe Molecules in Polystyrene - Evidence for Spatially Heterogeneous Segmental Dynamics. *Macromolecules* **1995,** *28* (24), 8224-8232.

41. Hess, M.; Jones, R. G.; Kahovec, J.; Kitayama, T.; Kratochvíl, P.; Kubisa, P.; Mormann, W.; Stepto, R. F. T.; Tabak, D.; Vohlídal, J.; Wilks, E. S., Terminology of polymers containing ionizable or ionic groups and of polymers containing ions (IUPAC Recommendations 2006). In *Pure and Applied Chemistry*, 2006; Vol. 78, p 2067.

42. Radeva, T., *Physical Chemistry of Polyelectrolytes*. Taylor & Francis: 2001.

43. Oosawa, F., A simple theory of thermodynamic properties of polyelectrolyte solutions. *J Polym Sci* **1957,** *23* (103), 421-430.

44. Dobrynin, A. V.; Rubinstein, M., Theory of polyelectrolytes in solutions and at surfaces. *Prog Polym Sci* **2005,** *30* (11), 1049-1118.

45. Guo, L.-C.; Zhang, Y.; Uchida, N.; Uematsu, K., Influence of temperature on stability of aqueous alumina slurry containing polyelectrolyte dispersant. *Journal of the European Ceramic Society* **1997,** *17* (2), 345-350.

46. Sata, T.; Yamaguchi, T.; Matsusaki, K., Interaction between anionic polyelectrolytes and anion exchange membranes and change in membrane properties. *J Membrane Sci* **1995,** *100* (3), 229-238.

47. Bolto, B.; Gregory, J., Organic polyelectrolytes in water treatment. *Water Res* **2007,** *41* (11), 2301-2324.

48. Budhathoki, M.; Barnee, S. H. R.; Shiau, B.-J.; Harwell, J. H., Improved oil recovery by reducing surfactant adsorption with polyelectrolyte in high saline brine. *Colloids and Surfaces A: Physicochemical and Engineering Aspects* **2016,** *498*, 66-73.

49. Llamas, S.; Guzmán, E.; Ortega, F.; Baghdadli, N.; Cazeneuve, C.; Rubio, R. G.; Luengo, G. S., Adsorption of polyelectrolytes and polyelectrolytes-surfactant mixtures at surfaces: a physico-chemical approach to a cosmetic challenge. *Adv Colloid Interfac* **2015,** *222*, 461-487.

50. Hollabaugh, C. B.; Burt, L. H.; Walsh, A. P., Carboxymethylcellulose. Uses and Applications. *Industrial & Engineering Chemistry* **1945,** *37* (10), 943-947.

51. Preska Steinberg, A.; Wang, Z.-G.; Ismagilov, R. F., Food Polyelectrolytes Compress the Colonic Mucus Hydrogel by a Donnan Mechanism. *Biomacromolecules* **2019,** *20* (7), 2675-2683.

52. World Health, O.; Joint, F. A. O. W. H. O. E. C. o. F. A. M., *Safety evaluation of certain food additives / prepared by the Seventy-ninth meeting of the Joint FAO/ WHO Expert Committee on Food Additives (JECFA)*. World Health Organization: Geneva, 2015.

53. Kabiri, K.; Omidian, H.; Hashemi, S. A.; Zohuriaan-Mehr, M. J., Synthesis of fast-swelling superabsorbent hydrogels: effect of crosslinker type and concentration on porosity and absorption rate. *Eur Polym J* **2003,** *39* (7), 1341-1348.

54. Dai, J.; Sullivan, D. M.; Bruening, M. L., Ultrathin, Layered Polyamide and Polyimide Coatings on Aluminum. *Ind Eng Chem Res* **2000,** *39* (10), 3528-3535.

55. Krasemann, L.; Tieke, B., Selective Ion Transport across Self-Assembled Alternating Multilayers of Cationic and Anionic Polyelectrolytes. *Langmuir* **2000,** *16* (2), 287-290.

56. Ai, H.; Jones, S. A.; Lvov, Y. M., Biomedical applications of electrostatic layer-by-layer nano-assembly of polymers, enzymes, and nanoparticles. *Cell Biochemistry and Biophysics* **2003,** *39* (1), 23.

57. Roy, K.; Mao, H.-Q.; Huang, S. K.; Leong, K. W., Oral gene delivery with chitosan–DNA nanoparticles generates immunologic protection in a murine model of peanut allergy. *Nature Medicine* **1999,** *5* (4), 387-391.

58. Macleod, G. S.; Collett, J. H.; Fell, J. T., The potential use of mixed films of pectin, chitosan and HPMC for bimodal drug release. *Journal of Controlled Release* **1999,** *58* (3), 303-310.

59. Lankalapalli, S.; Kolapalli, V. R. M., Polyelectrolyte Complexes: A Review of their Applicability in Drug Delivery Technology. *Indian J Pharm Sci* **2009,** *71* (5), 481-487.

60. Das, S.; Banik, M.; Chen, G.; Sinha, S.; Mukherjee, R., Polyelectrolyte brushes: theory, modelling, synthesis and applications. *Soft Matter* **2015,** *11* (44), 8550-8583.

61. Poncin-Epaillard, F.; Vrlinic, T.; Debarnot, D.; Mozetic, M.; Coudreuse, A.; Legeay, G.; El Moualij, B.; Zorzi, W., Surface treatment of polymeric materials controlling the adhesion of biomolecules. *J Funct Biomater* **2012,** *3* (3), 528-543.

62. Srinivasan, N.; Bhagawati, M.; Ananthanarayanan, B.; Kumar, S., Stimuli-sensitive intrinsically disordered protein brushes. *Nature Communications* **2014,** *5* (1), 5145.

63. Katchalsky, A.; Künzle, O.; Kuhn, W., Behavior of polyvalent polymeric ions in solution. *J Polym Sci* **1950,** *5* (3), 283-300.

64. Flory, P. J., Molecular Configuration of Polyelectrolytes. *The Journal of Chemical Physics* **1953,** *21* (1), 162-163.

65. Alfrey Jr, T.; Berg, P. W.; Morawetz, H., The counterion distribution in solutions of rod-shaped polyelectrolytes. *J Polym Sci* **1951,** *7* (5), 543-547.

66. Fuoss, R. M.; Katchalsky, A.; Lifson, S., The Potential of an Infinite Rod-Like Molecule and the Distribution of the Counter Ions. *Proceedings of the National Academy of Sciences* **1951,** *37* (9), 579.

67. Manning, G. S., Limiting Laws and Counterion Condensation in Polyelectrolyte Solutions .I. Colligative Properties. *J Chem Phys* **1969,** *51* (3), 924-&.

68. De Gennes, P. G.; Pincus, P.; Velasco, R. M.; Brochard, F., Remarks on polyelectrolyte conformation. *J. Phys. France* **1976,** *37* (12), 1461-1473.

69. Lamm, G.; Pack, G. R., Calculation of Dielectric Constants near Polyelectrolytes in Solution. *The Journal of Physical Chemistry B* **1997,** *101* (6), 959-965.

70. Beer, M.; Schmidt, M.; Muthukumar, M., The electrostatic expansion of linear polyelectrolytes: Effects of gegenions, co-ions, and hydrophobicity. *Macromolecules* **1997,** *30* (26), 8375-8385.

71. Loh, P.; Deen, G. R.; Vollmer, D.; Fischer, K.; Schmidt, M.; Kundagrami, A.; Muthukumar, M., Collapse of Linear Polyelectrolyte Chains in a Poor Solvent: When Does a Collapsing Polyelectrolyte Collect its Counterions? *Macromolecules* **2008,** *41* (23), 9352-9358.

72. Dobrynin, A. V.; Rubinstein, M., Counterion Condensation and Phase Separation in Solutions of Hydrophobic Polyelectrolytes. *Macromolecules* **2001,** *34* (6), 1964-1972.

73. Nierlich, M.; Williams, C. E.; Boué, F.; Cotton, J. P.; Daoud, M.; Famoux, B.; Jannink, G.; Picot, C.; Moan, M.; Wolff, C.; Rinaudo, M.; de Gennes, P. G., Small angle neutron scattering by semi-dilute solutions of polyelectrolyte. *J. Phys. France* **1979,** *40* (7), 701-704.

74. Nishida, K.; Kaji, K.; Kanaya, T., Charge Density Dependence of Correlation Length Due to Electrostatic Repulsion in Polyelectrolyte Solutions. *Macromolecules* **1995,** *28* (7), 2472-2475.

75. Muthukumar, M., Double screening in polyelectrolyte solutions: Limiting laws and crossover formulas. *J Chem Phys* **1996,** *105* (12), 5183-5199.

76. Flory, P. J., *Principles of Polymer Chemistry*. Cornell University Press: 1953.

77. Muthukumar, M., Electrostatic correlations in polyelectrolyte solutions. *Polym Sci Ser a+* **2016,** *58* (6), 852-863.

78. Hoagland, D. A.; Arvanitidou, E.; Welch, C., Capillary electrophoresis measurements of the free solution mobility for several model polyelectrolyte systems. *Macromolecules* **1999,** *32* (19), 6180-6190.

79. Stellwagen, E.; Lu; Stellwagen, N. C., Unified Description of Electrophoresis and Diffusion for DNA and Other Polyions. *Biochemistry* **2003,** *42* (40), 11745-11750.

80. Striegel, A. M., Multiple Detection in Size-Exclusion Chromatography of Macromolecules. *Anal Chem* **2005,** *77* (5), 104 A-113 A.

81. Rowland, S. M.; Striegel, A. M., Characterization of Copolymers and Blends by Quintuple-Detector Size-Exclusion Chromatography. *Anal Chem* **2012,** *84* (11), 4812-4820.

82. Burchard, W., Solution properties of branched macromolecules. *Branched Polymers Ii* **1999,** *143*, 113-194.

83. Brewer, A. K.; Striegel, A. M., Characterizing the size, shape, and compactness of a polydisperse prolate ellipsoidal particle via quadruple-detector hydrodynamic chromatography. *Analyst* **2011,** *136* (3), 515-519.

84. Pecora, R., *Dynamic Light Scattering: Applications of Photon Correlation Spectroscopy*. Springer US: 2013.

85. Crank, J.; Crank, E. P. J., *The Mathematics of Diffusion*. Clarendon Press: 1979.

86. Einstein, A., Über die von der molekularkinetischen Theorie der Wärme geforderte Bewegung von in ruhenden Flüssigkeiten suspendierten Teilchen. *Annalen der Physik* **1905,** *322* (8), 549-560.

87. Forster, S.; Schmidt, M.; Antonietti, M., Static and Dynamic Light-Scattering by Aqueous Polyelectrolyte Solutions - Effect of Molecular-Weight, Charge-Density and Added Salt. *Polymer* **1990,** *31* (5), 781-792.

88. Sedlak, M.; Amis, E. J., Dynamics of Moderately Concentrated Salt-Free Polyelectrolyte Solutions - Molecular-Weight Dependence. *J Chem Phys* **1992,** *96* (1), 817-825.

89. Schmitz, K. S., *Macroions in Solution and Colloidal Suspension*. Wiley: 1992.

90. Zhang, Y.; Douglas, J. F.; Ermi, B. D.; Amis, E. J., Influence of counterion valency on the scattering properties of highly charged polyelectrolyte solutions. *The Journal of Chemical Physics* **2001,** *114* (7), 3299-3313.

91. Chremos, A.; Douglas, J. F., Influence of solvation on the structure of highly charged nanoparticles in salt-free solutions. *Polymer* **2019,** *170*, 107-112.

92. Jamieson, A. M.; Presley, C. T., Anisotropic Translational Diffusion in Dilute Aqueous-Solutions of Partially Hydrolyzed Polyacrylamide by Quasi-Elastic Light-Scattering. *Macromolecules* **1973,** *6* (3), 358-360.

93. Lin, S. C.; Lee, W. I.; Schurr, J. M., Brownian-Motion of Highly Charged Poly(L-Lysine) - Effects of Salt and Polyion Concentration. *Biopolymers* **1978,** *17* (4), 1041-1064.

94. Schmitz, K. S., Quasi-Elastic Light-Scattering-Studies on T7 DNA in the Presence of a Sinusoidal Electric-Field. *Chem Phys* **1983,** *79* (2), 297-305.

95. Schmitz, K. S.; Lu, M.; Singh, N.; Ramsay, D. J., Ordinary Extraordinary Phase-Transition of Poly(Lysine) - Comments. *Biopolymers* **1984,** *23* (9), 1637-1646.

96. Schurr, J. M.; Schmitz, K. S., Dynamic Light-Scattering-Studies of Bio-Polymers - Effects of Charge, Shape, and Flexibility. *Annual Review of Physical Chemistry* **1986,** *37*, 271-305.

97. Schmidt, M., Static and dynamic light scattering by an aqueous polyelectrolyte solution without added salt: Quaternized poly(2-vinylpyridine). *Die Makromolekulare Chemie, Rapid Communications* **1989,** *10* (2), 89-96.

98. Sedlák, M.; Koňák, Č.; Štěpánek, P.; Jakeš, J., Semidilute solutions of poly(methacrylic acid) in the absence of salt: Dynamic light-scattering study. *Polymer* **1987,** *28* (6), 873-880.

99. Ghosh, S.; Li, X.; Reed, C. E.; Reed, W. F., Apparent persistence lengths and diffusion behavior of high molecular weight hyaluronate. *Biopolymers* **1990,** *30* (11-12), 1101-1112.

100. Sedlak, M., Domain-Structure of Polyelectrolyte Solutions - Is It Real. *Macromolecules* **1993,** *26* (5), 1158-1162.

101. Liu, S.; Muthukumar, M., Langevin dynamics simulation of counterion distribution around isolated flexible polyelectrolyte chains. *J Chem Phys* **2002,** *116* (22), 9975-9982.

102. Muthukumar, M., Theory of electrophoretic mobility of a polyelectrolyte in semidilute solutions of neutral polymers. *Electrophoresis* **1996,** *17* (6), 1167-1172.

103. Wang, L. X.; Bloomfield, V. A., Cooperative Diffusion of Semidilute Poly-Electrolyte Solutions - Analysis by Renormalization-Group Theory. *Macromolecules* **1989,** *22* (6), 2742-2746.

104. Vilgis, T. A.; Borsali, R., Mean-field theory of concentrated polyelectrolyte solutions: Statics and dynamics. *Physical Review A* **1991,** *43* (12), 6857-6874.

105. Ajdari, A.; Leibler, L.; Joanny, J. F., Cooperative diffusion in weakly charged polyelectrolyte solutions. *The Journal of Chemical Physics* **1991,** *95* (6), 4580-4583.

106. Muthukumar, M., Dynamics of polyelectrolyte solutions. *J Chem Phys* **1997,** *107* (7), 2619-2635.

107. Ghosh, S.; Peitzsch, R. M.; Reed, W. F., Aggregates and Other Particles as the Origin of the Extraordinary Diffusional Phase in Polyelectrolyte Solutions. *Biopolymers* **1992,** *32* (8), 1105-1122.

108. Wissenburg, P.; Odijk, T.; Cirkel, P.; Mandel, M., Multimolecular aggregation of mononucleosomal DNA in concentrated isotropic solutions. *Macromolecules* **1995,** *28* (7), 2315-2328.

109. Sedlak, M., The ionic strength dependence of the structure and dynamics of polyelectrolyte solutions as seen by light scattering: The slow mode dilemma. *J Chem Phys* **1996,** *105* (22), 10123-10133.

110. Muthukumar, M., Ordinary–extraordinary transition in dynamics of solutions of charged macromolecules. *Proceedings of the National Academy of Sciences* **2016,** *113* (45), 12627.

111. Li, J. F.; Li, W.; Huo, H.; Luo, S. Z.; Wu, C., Reexamination of the slow mode in semidilute polymer solutions: The effect of solvent quality. *Macromolecules* **2008,** *41* (3), 901-911.

112. Baigl, D.; Seery, T. A. P.; Williams, C. E., Preparation and characterization of hydrosoluble, partially charged poly(styrenesulfonate)s of various controlled charge fractions and chain lengths. *Macromolecules* **2002,** *35* (6), 2318-2326.

113. Li, J. F.; Ngai, T.; Wu, C., The slow relaxation mode: from solutions to gel networks. *Polym J* **2010,** *42* (8), 609-625.

114. Zhou, K.; Li, J.; Lu, Y.; Zhang, G.; Xie, Z.; Wu, C., Re-examination of Dynamics of Polyeletrolytes in Salt-Free Dilute Solutions by Designing and Using a Novel Neutral−Charged−Neutral Reversible Polymer. *Macromolecules* **2009,** *42* (18), 7146-7154.

115. Sedlak, M., Dynamic light scattering from binary mixtures of polyelectrolytes. I. Influence of mixing on the fast and slow polyelectrolyte mode behavior. *J Chem Phys* **1997,** *107* (24), 10799-10804.

116. Sedlak, M., Dynamic light scattering from binary mixtures of polyelectrolytes. II. Appearance of the medium polyelectrolyte mode upon mixing and comparison with experiments on binary mixtures of neutral polymers. *J Chem Phys* **1997,** *107* (24), 10805-10815.

117. Jia, D.; Muthukumar, M., Effect of Salt on the Ordinary-Extraordinary Transition in Solutions of Charged Macromolecules. *J Am Chem Soc* **2019,** *141* (14), 5886-5896.

118. Berne, B. J.; Pecora, R., *Dynamic light scattering. With applications to chemistry, biology, and physics*. 1976.

119. Jenkins Aubrey, D.; Jones Richard, G.; Moad, G., Terminology for reversible-deactivation radical polymerization previously called "controlled" radical or "living" radical polymerization (IUPAC Recommendations 2010). In *Pure and Applied Chemistry*, 2009; Vol. 82, p 483.

120. Moad, G.; Rizzardo, E., Chapter 1 The History of Nitroxide-mediated Polymerization. In *Nitroxide Mediated Polymerization: From Fundamentals to Applications in Materials Science*, The Royal Society of Chemistry: 2016; pp 1-44.

121. Matyjaszewski, K.; Xia, J., Atom Transfer Radical Polymerization. *Chem Rev* **2001,** *101* (9), 2921-2990.

122. Chiefari, J.; Chong, Y. K.; Ercole, F.; Krstina, J.; Jeffery, J.; Le, T. P. T.; Mayadunne, R. T. A.; Meijs, G. F.; Moad, C. L.; Moad, G.; Rizzardo, E.; Thang, S. H., Living Free-Radical Polymerization by Reversible Addition−Fragmentation Chain Transfer: The RAFT Process. *Macromolecules* **1998,** *31* (16), 5559-5562.

123. Yamago, S.; Iida, K.; Yoshida, J.-i., Organotellurium Compounds as Novel Initiators for Controlled/Living Radical Polymerizations. Synthesis of Functionalized Polystyrenes and End-Group Modifications. *J Am Chem Soc* **2002,** *124* (12), 2874-2875.

124. Hsieh, H.; Quirk, R. P., *Anionic Polymerization: Principles and Practical Applications*. Taylor & Francis: 1996.

125. Matyjaszewski, K., *Cationic Polymerizations: Mechanisms, Synthesis & Applications*. Taylor & Francis: 1996.

126. Bednarek, M.; Biedron, T.; Kubisa, P.; Penczek, S., Activated monomer polymerization of oxiranes. Micro-structure of polymers vs. kinetics and thermodynamics of propagation. *Makromolekulare Chemie. Macromolecular Symposia* **1991,** *42-43* (1), 475-487.

127. Qiu, J.; Charleux, B.; Matyjaszewski, K., Progress in controlled/living polymerization in aqueous media Part I. Principles and methods. *Polimery-W* **2001,** *46* (7-8), 453-460.

128. Coleman, B. D.; Fox, T. G., A Multistate Mechanism for Homogeneous Ionic Polymerization .2. Molecular Weight Distribution. *J Am Chem Soc* **1963,** *85* (9), 1241-&.

129. Matyjaszewski, K., Effect of initiators, Lewis acids, deactivators, additives and medium on controlled/"living" carbocationic systems. *Macromol Symp* **1996,** *107*, 53-63.

130. Wang, J.-S.; Matyjaszewski, K., Controlled/"living" radical polymerization. atom transfer radical polymerization in the presence of transition-metal complexes. *J Am Chem Soc* **1995,** *117* (20), 5614-5615.

131. Matyjaszewski, K., Transformation of "living" carbocationic and other polymerizations to controlled "living" radical polymerization. *Macromol Symp* **1998,** *132*, 85-101.

132. Tang, W.; Kwak, Y.; Braunecker, W.; Tsarevsky, N. V.; Coote, M. L.; Matyjaszewski, K., Understanding atom transfer radical polymerization: Effect of ligand and initiator structures on the equilibrium constants. *J Am Chem Soc* **2008,** *130* (32), 10702-10713.

133. Tang, W.; Matyjaszewski, K., Effects of Initiator Structure on Activation Rate Constants in ATRP. *Macromolecules* **2007,** *40* (6), 1858-1863.

134. Tang, W.; Matyjaszewski, K., Macromol. Theory Simul. 7–8/2008. *Macromolecular Theory and Simulations* **2008,** *17* (7-8).

135. Matyjaszewski, K., The importance of exchange reactions in controlled/living radical polymerization in the presence of alkoxyamines and transition metals. *Macromol Symp* **1996,** *111*, 47-61.

136. Tsarevsky, N. V.; Braunecker, W. A.; Matyjaszewski, K., Electron transfer reactions relevant to atom transfer radical polymerization. *J Organomet Chem* **2007,** *692* (15), 3212-3222.

137. Tang, W.; Tsarevsky, N. V.; Matyjaszewski, K., Determination of equilibrium constants for atom transfer radical polymerization. *J Am Chem Soc* **2006,** *128* (5), 1598-1604.

138. Percec, V.; Guliashvili, T.; Ladislaw, J. S.; Wistrand, A.; Stjerndahl, A.; Sienkowska, M. J.; Monteiro, M. J.; Sahoo, S., Ultrafast synthesis of ultrahigh molar mass polymers by metal-catalyzed living radical polymerization of acrylates, methacrylates, and vinyl chloride mediated by SET at 25 degrees C. *J Am Chem Soc* **2006,** *128* (43), 14156-14165.

139. Matyjaszewski, K.; Tsarevsky, N. V.; Braunecker, W. A.; Dong, H.; Huang, J.; Jakubowski, W.; Kwak, Y.; Nicolay, R.; Tang, W.; Yoon, J. A., Role of Cu-0 in controlled/"living" radical polymerization. *Macromolecules* **2007,** *40* (22), 7795-7806.

140. Zhang, Y.; Wang, Y.; Peng, C.-h.; Zhong, M.; Zhu, W.; Konkolewicz, D.; Matyjaszewski, K., Copper-Mediated CRP of Methyl Acrylate in the Presence of Metallic Copper: Effect of Ligand Structure on Reaction Kinetics. *Macromolecules* **2012,** *45* (1), 78-86.

141. Perrier, S.; Armes, S. P.; Wang, X. S.; Malet, F.; Haddleton, D. M., Copper(I)-mediated radical polymerization of methacrylates in aqueous solution. *Journal of Polymer Science Part A: Polymer Chemistry* **2001,** *39* (10), 1696-1707.

142. Matyjaszewski, K.; Wei, M.; Xia, J.; Gaynor, S. G., Atom transfer radical polymerization of styrene catalyzed by copper carboxylate complexes. *Macromol Chem Phys* **1998,** *199* (10), 2289-2292.

143. Iddon, P. D.; Robinson, K. L.; Armes, S. P., Polymerization of sodium 4-styrenesulfonate via atom transfer radical polymerization in protic media. *Polymer* **2004,** *45* (3), 759-768.

144. Paneva, D.; Mespouille, L.; Manolova, N.; Degee, P.; Rashkov, I.; Dubois, P., Comprehensive study on the formation of polyelectrolyte complexes from (quaternized) poly[2-(dimethylamino)ethyl methacrylate] and poly(2-acrylamido-2-methylpropane sodium sulfonate). *J Polym Sci Pol Chem* **2006,** *44* (19), 5468-5479.

145. Sedlak, M., Generation of multimacroion domains in polyelectrolyte solutions by change of ionic strength or pH (macroion charge). *J Chem Phys* **2002,** *116* (12), 5256-5262.

146. Cong, R.; Temyanko, E.; Russo, P. S., Diffusion of labeled polyelectrolyte probes in unlabeled polyelectrolyte matrix solutions. *Macromolecules* **2005,** *38* (26), 10627-10630.

147. Sutherland, J. E., Synthesis and Characterization of Sodium(Polystyrene Sulfonate) for Calibration of Aqueous Exclusion Chromatography. *Abstr Pap Am Chem S* **1976,** *172* (Sep3), 90-90.

148. Shibuya, N.; Porter, R. S., Kinetics of Peek Sulfonation in Concentrated Sulfuric-Acid. *Macromolecules* **1992,** *25* (24), 6495-6499.

149. Kucera, F.; Jancar, J., Homogeneous and heterogeneous sulfonation of polymers: A review. *Polym Eng Sci* **1998,** *38* (5), 783-792.

150. Theodoropoulos, A. G.; Tsakalos, V. T.; Valkanas, G. N., Sulfone-Type Cross-Links in Sulfonation of Macronet Polystyrene Backbone. *Polymer* **1993,** *34* (18), 3905-3910.

151. Holboke, A. E.; Pinnell, R. P., Sulfonation of Polystyrene - Preparation and Characterization of an Ion-Exchange Resin in the Organic Laboratory. *J Chem Educ* **1989,** *66* (7), 613-614.

152. Roth, H. H., Sulfonation of Poly(Vinyl Aromatics). *Industrial and Engineering Chemistry* **1957,** *49* (11), 1820-1822.

153. Michel, R. C.; Reed, W. F., New evidence of the nonequilibrium nature of the "slow modes" of diffusion in polyelectrolyte solutions. *Biopolymers* **2000,** *53* (1), 19-39.

154. Mitsukami, Y.; Donovan, M. S.; Lowe, A. B.; McCormick, C. L., Water-soluble polymers. 81. Direct synthesis of hydrophilic styrenic-based homopolymers and block copolymers in aqueous solution via RAFT. *Macromolecules* **2001,** *34* (7), 2248-2256.

155. Phan, T. N. T.; Bertin, D., Synthesis of water-soluble homopolymers and block copolymers in homogeneous aqueous solution via nitroxide-mediated polymerization. *Macromolecules* **2008,** *41* (5), 1886-1895.

156. Keoshkerian, B.; Georges, M. K.; Boilsboissier, D., Living Free-Radical Aqueous Polymerization. *Macromolecules* **1995,** *28* (18), 6381-6382.

157. Choi, C. K.; Kim, Y. B., Atom transfer radical polymerization of styrenesulfonic acid sodium salts (SSNa) in aqueous phase. *Polym Bull* **2003,** *49* (6), 433-439.

158. Tsarevsky, N. V.; Pintauer, T.; Matyjaszewski, K., Atom transfer radical polymerization of ionic monomers in aqueous solution: Mechanistic studies and synthesis. *Abstr Pap Am Chem S* **2002,** *224*, U440-U440.

159. Huberty, W.; Tong, X. W.; Balamurugan, S.; Deville, K.; Russo, P. S.; Zhang, D. H., Colorful Polyelectrolytes: An Atom Transfer Radical Polymerization Route to Fluorescent Polystyrene Sulfonate. *Journal of Fluorescence* **2016,** *26* (2), 609-615.

160. Li, Y. T.; Armes, S. P.; Jin, X. P.; Zhu, S. P., Direct synthesis of well-defined quaternized homopolymers and diblock copolymers via ATRP in protic media. *Macromolecules* **2003,** *36* (22), 8268-8275.

161. Rosen, B. M.; Percec, V., Single-Electron Transfer and Single-Electron Transfer Degenerative Chain Transfer Living Radical Polymerization. *Chem Rev* **2009,** *109* (11), 5069-5119.

162. Rosen, B. M.; Jiang, X.; Wilson, C. J.; Nguyen, N. H.; Monteiro, M. J.; Percec, V., The Disproportionation of Cu(I)X Mediated by Ligand and Solvent into Cu(0) and Cu(II)X-2 and Its Implications for SET-LRP. *J Polym Sci Pol Chem* **2009,** *47* (21), 5606-5628.

163. Levere, M. E.; Nguyen, N. H.; Leng, X. F.; Percec, V., Visualization of the crucial step in SET-LRP. *Polym Chem-Uk* **2013,** *4* (5), 1635-1647.

164. Percec, V.; Popov, A. V.; Ramirez-Castillo, E.; Monteiro, M.; Barboiu, B.; Weichold, O.; Asandei, A. D.; Mitchell, C. M., Aqueous room temperature metal-catalyzed living radical polymerization of vinyl chloride. *J Am Chem Soc* **2002,** *124* (18), 4940-4941.

165. Zhang, Q.; Wilson, P.; Li, Z. D.; McHale, R.; Godfrey, J.; Anastasaki, A.; Waldron, C.; Haddleton, D. M., Aqueous Copper-Mediated Living Polymerization: Exploiting Rapid Disproportionation of CuBr with Me6TREN. *J Am Chem Soc* **2013,** *135* (19), 7355-7363.

166. Jones, G. R.; Li, Z. D.; Anastasaki, A.; Lloyd, D. J.; Wilson, P.; Zhang, Q.; Haddleton, D. M., Rapid Synthesis of Well-Defined Polyacrylamide by Aqueous Cu(0)-Mediated Reversible-Deactivation Radical Polymerization. *Macromolecules* **2016,** *49* (2), 483-489.

167. Nikolaou, V.; Simula, A.; Droesbeke, M.; Risangud, N.; Anastasaki, A.; Kempe, K.; Wilson, P.; Haddleton, D. M., Polymerisation of 2-acrylamido-2-methylpropane sulfonic acid sodium salt (NaAMPS) and acryloyl phosphatidylcholine (APC) via aqueous Cu(0)-mediated radical polymerisation. *Polym Chem-Uk* **2016,** *7* (14), 2452-2456.

168. Konkolewicz, D.; Krys, P.; Gois, J. R.; Mendonca, P. V.; Zhong, M. J.; Wang, Y.; Gennaro, A.; Isse, A. A.; Fantin, M.; Matyjaszewski, K., Aqueous RDRP in the Presence of Cu-0: The Exceptional Activity of Cu-I Confirms the SARA ATRP Mechanism. *Macromolecules* **2014,** *47* (2), 560-570.

169. Anastasaki, A.; Nikolaou, V.; Nurumbetov, G.; Wilson, P.; Kempe, K.; Quinn, J. F.; Davis, T. P.; Whittaker, M. R.; Haddleton, D. M., Cu(0)-Mediated Living Radical Polymerization: A Versatile Tool for Materials Synthesis. *Chem Rev* **2016,** *116* (3), 835-877.

170. Matyjaszewski, K.; Coca, S.; Gaynor, S. G.; Wei, M. L.; Woodworth, B. E., Zerovalent metals in controlled "living" radical polymerization. *Macromolecules* **1997,** *30* (23), 7348-7350.

171. Konkolewicz, D.; Wang, Y.; Krys, P.; Zhong, M. J.; Isse, A. A.; Gennaro, A.; Matyjaszewski, K., SARA ATRP or SET-LRP. End of controversy? *Polym Chem-Uk* **2014,** *5* (15), 4396-4417.

172. Krys, P.; Konkolewicz, D.; Wang, Y.; Zhong, M. J.; Peng, C. H.; Zhang, Y. Z.; Matyjaszewski, K., RDRP in the presence of Cu-0: SARA ATRP vs. SET-LRP. *Abstr Pap Am Chem S* **2014,** *248*.

173. Lorandi, F.; Fantin, M.; Isse, A. A.; Gennaro, A., RDRP in the presence of Cu-0: The fate of Cu(I) proves the inconsistency of SET-LRP mechanism. *Polymer* **2015,** *72*, 238-245.

174. Konkolewicz, D.; Krys, P.; Matyjaszewski, K., Explaining Unexpected Data via Competitive Equilibria and Processes in Radical Reactions with Reversible Deactivation. *Accounts Chem Res* **2014,** *47* (10), 3028-3036.

175. Fantin, M.; Isse, A. A.; Gennaro, A.; Matyjaszewski, K., Understanding the Fundamentals of Aqueous ATRP and Defining Conditions for Better Control. *Macromolecules* **2015,** *48* (19), 6862-6875.

176. Averick, S.; Simakova, A.; Park, S.; Konkolewicz, D.; Magenau, A. J. D.; Mehl, R. A.; Matyjaszewski, K., ATRP under Biologically Relevant Conditions: Grafting from a Protein. *Acs Macro Lett* **2012,** *1* (1), 6-10.

177. Leng, X. F.; Nguyen, N. H.; van Beusekom, B.; Wilson, D. A.; Percec, V., SET-LRP of 2-hydroxyethyl acrylate in protic and dipolar aprotic solvents. *Polym Chem-Uk* **2013,** *4* (10), 2995-3004.

178. Bortolamei, N.; Isse, A. A.; Magenau, A. J. D.; Gennaro, A.; Matyjaszewski, K., Controlled Aqueous Atom Transfer Radical Polymerization with Electrochemical Generation of the Active Catalyst. *Angew Chem Int Edit* **2011,** *50* (48), 11391-11394.

179. Konkolewicz, D.; Magenau, A. J. D.; Averick, S. E.; Simakova, A.; He, H. K.; Matyjaszewski, K., ICAR ATRP with ppm Cu Catalyst in Water. *Macromolecules* **2012,** *45* (11), 4461-4468.

180. Simakova, A.; Averick, S. E.; Konkolewicz, D.; Matyjaszewski, K., Aqueous ARGET ATRP. *Macromolecules* **2012,** *45* (16), 6371-6379.

181. Nguyen, N. H.; Jiang, X.; Fleischmann, S.; Rosen, B. M.; Percec, V., The Effect of Ligand on the Rate of Propagation of Cu(0) Wire Catalyzed SET-LRP of MA in DMSO at 25 degrees C. *J Polym Sci Pol Chem* **2009,** *47* (21), 5629-5638.

182. Yu, H. L.; Wu, Y.; Gao, J. L.; Wang, W. X.; Zhang, Z. B.; Zhu, X. L., Copper(0)-Mediated Radical Copolymerization of Vinyl Acetate and Acrylonitrile in DMSO at Ambient Temperature. *J Polym Sci Pol Chem* **2012,** *50* (23), 4983-4989.

183. Iddon, P. D.; Robinson, K. L.; Armes, S. P., Polymerization of sodium 4-styrenesulfonate via atom transfer radical polymerization. *Abstr Pap Am Chem S* **2004,** *228*, U352-U352.

184. Smolne, S.; Buback, M., Kinetic Investigations of Cu-Mediated ATRP in Aqueous Solution. *Macromol Chem Phys* **2015,** *216* (8), 894-902.

185. Robinson, K. L.; Khan, M. A.; Banez, M. V. D.; Wang, X. S.; Armes, S. P., Controlled polymerization of 2-hydroxyethyl methacrylate by ATRP at ambient temperature. *Abstr Pap Am Chem S* **2001,** *221*, U362-U363.

186. Perrier, S.; Haddleton, D. M., Effect of water on copper mediated living radical polymerization. *Macromol Symp* **2002,** *182*, 261-272.

187. Mincheva, R.; Paneva, D.; Mespouille, L.; Manolova, N.; Rashkov, I.; Dubois, P., Optimized Water-Based ATRP of an Anionic Monomer: Comprehension and Properties Characterization. *J Polym Sci Pol Chem* **2009,** *47* (4), 1108-1119.

188. Wang, Y.; Zhong, M. J.; Zhu, W. P.; Peng, C. H.; Zhang, Y. Z.; Konkolewicz, D.; Bortolamei, N.; Isse, A. A.; Gennaro, A.; Matyjaszewski, K., Reversible-Deactivation Radical Polymerization in the Presence of Metallic Copper. Comproportionation-Disproportionation Equilibria and Kinetics. *Macromolecules* **2013,** *46* (10), 3793-3802.

189. Simms, R. W.; Cunningham, M. F., High molecular weight poly(butyl methacrylate) by reverse atom transfer radical polymerization in miniemulsion initiated by a redox system. *Macromolecules* **2007,** *40* (4), 860-866.

190. Mueller, L.; Jakubowski, W.; Matyjaszewski, K.; Pietrasik, J.; Kwiatkowski, P.; Chaladaj, W.; Jurczak, J., Synthesis of high molecular weight polystyrene using AGET ATRP under high pressure. *Eur Polym J* **2011,** *47* (4), 730-734.

191. Simula, A.; Anastasaki, A.; Haddleton, D. M., Methacrylic Zwitterionic, Thermoresponsive, and Hydrophilic (Co)Polymers via Cu(0)-Polymerization: The Importance of Halide Salt Additives. *Macromol Rapid Comm* **2016,** *37* (4), 356-361.

192. Peng, C. H.; Kong, J.; Seeliger, F.; Matyjaszewski, K., Mechanism of Halogen Exchange in ATRP. *Macromolecules* **2011,** *44* (19), 7546-7557.

193. Adams, M. E.; Russell, G. T.; Casey, B. S.; Gilbert, R. G.; Napper, D. H.; Sangster, D. F., Bimolecular Termination Events in the Seeded Emulsion Polymerization of Styrene. *Macromolecules* **1990,** *23* (21), 4624-4634.

194. Johnston-Hall, G.; Monteiro, M. J., Bimolecular radical termination: New perspectives and insights. *J Polym Sci Pol Chem* **2008,** *46* (10), 3155-3173.

195. Carmean, R. N.; Becker, T. E.; Sims, M. B.; Sumerlin, B. S., Ultra-High Molecular Weights via Aqueous Reversible-Deactivation Radical Polymerization. *Chem-Us* **2017,** *2* (1), 93-101.

196. Mahabadi, H. K.; Odriscoll, K. F., Absolute Rate Constants in Free-Radical Polymerization .2. Termination Rate Constant in Free-Radical Polymerization. *J Polym Sci Pol Chem* **1977,** *15* (2), 283-300.

197. Graessley, W. W., Polymer-Chain Dimensions and the Dependence of Viscoelastic Properties on Concentration, Molecular-Weight and Solvent Power. *Polymer* **1980,** *21* (3), 258-262.

198. Dubin, P. L.; Tecklenburg, M. M., Size-Exclusion Chromatography of Strong Poly-Electrolytes on Porous-Glass Columns. *Anal Chem* **1985,** *57* (1), 275-279.

199. Bose, A.; Rollings, J. E.; Caruthers, J. M.; Okos, M. R.; Tsao, G. T., Poly-Electrolytes as Secondary Calibration Standards for Aqueous Size-Exclusion Chromatography. *J Appl Polym Sci* **1982,** *27* (3), 795-810.

200. Knaul, J. Z.; Bui, V. T.; Creber, K. A. M., Viscometric constants for sodium polystyrene sulfonate standards in solvents of 0.1 M CH3COOH/0.2 M NaCl and 0.2 M CH3COOH/0.1 M CH3COONa at 25.0 degrees C. *J Chem Eng Data* **2000,** *45* (3), 508-511.

201. Cohen, J.; Priel, Z., Viscosity of dilute polyelectrolyte solutions: concentration dependence on sodium chloride, magnesium sulfate and lanthanum nitrate. *Macromolecules* **1989,** *22* (5), 2356-2358.

202. Cohen, J.; Priel, Z., Viscosity of dilute polyelectrolyte solutions: Temperature dependence. *The Journal of Chemical Physics* **1990,** *93* (12), 9062-9068.

203. Shimizu, K.; Sakai, N.; Takahashi, A., Agarose Gel Electrophoresis of Polyelectrolytes. *Polym J* **1990,** *22* (10), 901-907.

204. Colby, R. H.; Boris, D. C.; Krause, W. E.; Tan, J. S., Polyelectrolyte conductivity. *Journal of Polymer Science Part B: Polymer Physics* **1997,** *35* (17), 2951-2960.

205. Takahashi, A.; Kato, T.; Nagasawa, M., The Second Virial Coefficient of Polyelectrolytes. *The Journal of Physical Chemistry* **1967,** *71* (7), 2001-2010.

206. Hirose, E.; Iwamoto, Y.; Norisuye, T., Chain Stiffness and Excluded-Volume Effects in Sodium Poly(styrenesulfonate) Solutions at High Ionic Strength. *Macromolecules* **1999,** *32* (25), 8629-8634.

207. Cong, R. J.; Turksen, S.; Russo, P., A new synthesis of fluorescein isothiocyanate labeled poly(styrenesulfonate sodium salt). *Macromolecules* **2004,** *37* (12), 4731-4735.

208. Hirao, A.; Goseki, R.; Ishizone, T., Advances in Living Anionic Polymerization: From Functional Monomers, Polymerization Systems, to Macromolecular Architectures. *Macromolecules* **2014,** *47* (6), 1883-1905.

209. Frey, H.; Ishizone, T., Living Anionic Polymerization Celebrates 60 Years: Unique Features and Polymer Architectures. *Macromol Chem Phys* **2017,** *218* (12), 1700217.

210. Kim, G. Y.; Salovey, R.; Aklonis, J. J., Model Filled Polymers .4. Preparation of Conducting Composite Polymers Beads. *Polym Bull* **1990,** *23* (5), 543-547.

211. Turbak, A. F., Polymer Sulfonation without Cross Linking. The Sulfur Trioxide-Phosphate System. *I&EC Product Research and Development* **1962,** *1* (4), 275-278.

212. Peppas, N. A.; Bussing, W. R.; Slight, K. A., Structure of Friedel-Crafts Crosslinked Polystyrene and Sulfonated Resins Thereof. *Polym Bull* **1981,** *4* (3), 193-198.

213. Sollner, K.; Neihof, R., Strong-Acid Type of Permselective Membrane. *Arch Biochem Biophys* **1951,** *33* (1), 166-168.

214. Vink, H., A New Convenient Method for the Synthesis of Poly(Styrenesulfonic Acid). *Macromolecular Chemistry and Physics-Makromolekulare Chemie* **1981,** *182* (1), 279-281.

215. Regas, F. P., Physical Characterization of Suspension-Crosslinked Polystyrene Particles and Their Sulfonated Products .2. Ionic Networks. *Polymer* **1984,** *25* (2), 249-253.

216. Kim, M. W.; Peiffer, D. G., Poly-Electrolyte Properties of Ionomeric Polymers. *Europhys Lett* **1988,** *5* (4), 321-326.

217. Balding, P.; Cueto, R.; Russo, P. S.; Gutekunst, W. R., Synthesis of perfectly sulfonated sodium polystyrene sulfonate over a wide molar mass range via reversible-deactivation radical polymerization. *J Polym Sci Pol Chem* **2019,** *57* (14), 1527-1537.

218. Zoghlami, O.; Guettari, M.; Tajouri, T., Effect of Temperature and a Non-Solvent Addition on the Specific Volume of Poly (Sodium-4-Styrene Sulfonate) in Water. *Journal of Macromolecular Science, Part B* **2016,** *55* (12), 1173-1188.

219. Sen, A. K.; Roy, S.; Juvekar, V. A., - On the Importance of Purification of Sodium Polystyrene Sulfonate. **2012,** - *2012*.

220. Zundel, G., Hydration Structure and Intermolecular Interaction in Polyelectrolytes. *Angew Chem Int Edit* **1969,** *8* (7), 499-&.

221. Yang, J. C.; Jablonsky, M. J.; Mays, J. W., NMR and FT-IR studies of sulfonated styrene-based homopolymers and copolymers. *Polymer* **2002,** *43* (19), 5125-5132.

222. Orler, E. B.; Yontz, D. J.; Moore, R. B., Sulfonation of Syndiotactic Polystyrene for Model Semicrystalline Ionomer Investigations. *Macromolecules* **1993,** *26* (19), 5157-5160.

223. Komber, H.; Chakraborty, S.; Voit, B.; Banerjee, S., Degree of sulfonation and microstructure of post-sulfonated polyethersulfone studied by NMR spectroscopy. *Polymer* **2012,** *53* (8), 1624-1631.

224. Weill, G.; Vogl, O., Head-to-Head Polymers .10. High-Resolution Nmr-Spectroscopy of Polystyrene and Polyvinyl Cyclohexane). *Polym Bull* **1978,** *1* (3), 181-189.

225. Wackerly, J. W.; Dunne, J. F., Synthesis of Polystyrene and Molecular Weight Determination by H-1 NMR End-Group Analysis. *J Chem Educ* **2017,** *94* (11), 1790-1793.

226. Smith, R. N.; McCormick, M.; Barrett, C. J.; Reven, L.; Spiess, H. W., NMR studies of PAH/PSS polyelectrolyte multilayers adsorbed onto silica. *Macromolecules* **2004,** *37* (13), 4830-4838.

227. Kwei, T. K.; Dai, Y. K.; Lu, X.; Weiss, R. A., Solid-state NMR analysis of blends of nylon 6 and zinc salts of sulfonated polystyrene ionomers. *Macromolecules* **1993,** *26* (24), 6583-6588.

228. Adriaensens, P.; Carleer, R.; Storme, L.; Vanderzande, D.; Gelan, J., Morphological study of a poly(3,4-ethylenedioxythiophene)/polystyrenesulfonic acid mixture by solid state 13C-CP/MAS NMR relaxometry. *Polymer* **2002,** *43* (25), 7003-7006.

229. Striegel, A. M., Specific refractive index increment ($\partial n/\partial c$) of polymers at 660 nm and 690 nm. *Chromatographia* **2017,** *80* (6), 989-996.

230. Blakey, I.; Conley, W.; George, G. A.; Hill, D. J. T.; Liu, H.; Rasoul, F.; Whittaker, A. K., *Synthesis of high refractive index sulfur containing polymers for 193 nm immersion lithography: a progress report*. SPIE: 2006; Vol. 6153.

231. Matsumoto, K.; Costner, E. A.; Nishimura, I.; Ueda, M.; Willson, C. G., High Index Resist for 193 nm Immersion Lithography. *Macromolecules* **2008,** *41* (15), 5674-5680.

232. Weiner, B. B.; D, B. B. W. P., *Let There Be Light: Characterizing Physical Properties of Colloids, Nanoparticles, Polymers & Proteins Using Light Scattering*. Amazon Digital Services LLC - Kdp Print Us: 2019.

233. Striegel, A., *Modern Size-Exclusion Liquid Chromatography: Practice of Gel Permeation and Gel Filtration Chromatography*. 2009.

234. Wandrey, C.; Bartkowiak, A.; Hunkeler, D., Partial Molar and Specific Volumes of Polyelectrolytes: Comparison of Experimental and Predicted Values in Salt-free Solutions. *Langmuir* **1999,** *15* (12), 4062-4068.

235. Linow, K. J.; Okatova, O.; Philipp, B., Determination of the Partial Specific Volume of Dissolved Polymers by Continuous Density-Measurement. *Acta Polym* **1983,** *34* (6), 376-377.

236. DeVoe, H., *Thermodynamics and Chemistry*. Prentice Hall: 2001.

237. Salamanca, C.; Contreras, M.; Gamboa, C., Partial molar volume of anionic polyelectrolytes in aqueous solution. *J Colloid Interf Sci* **2007,** *309* (2), 435-439.

238. Tondre, C.; Zana, R., Apparent Molal Volumes of Polyelectrolytes in Aqueous-Solutions. *J Phys Chem-Us* **1972,** *76* (23), 3451-&.

239. Wandrey, C., Molecular mass and ionic strength dependence of electrochemical properties of flexible polyelectrolytes. *Ber Bunsen Phys Chem* **1996,** *100* (6), 869-875.

240. Rubinstein, M.; Colby, R. H.; Dobrynin, A. V., Dynamics of Semidilute Polyelectrolyte Solutions. *Physical Review Letters* **1994,** *73* (20), 2776-2779.

241. Wandrey, C., Concentration Regimes in Polyelectrolyte Solutions. *Langmuir* **1999,** *15* (12), 4069-4075.

242. Jiang, D. D.; Yao, Q.; McKinney, M. A.; Wilkie, C. A., TGA/FTIR studies on the thermal degradation of some polymeric sulfonic and phosphonic acids and their sodium salts. *Polym Degrad Stabil* **1999,** *63* (3), 423-434.

243. Yao, Q.; Wilkie, C. A., Thermal degradation of blends of polystyrene and poly(sodium 4-styrenesulfonate) and the copolymer, poly(styrene-co-sodium 4-styrenesulfonate). *Polym Degrad Stabil* **1999,** *66* (3), 379-384.

244. Wallace, R. A., Glass Transition in Partially Sulfonated Polystyrene. *J Polym Sci A2* **1971,** *9* (7), 1325-&.

245. Inc., P. S. Sample P4083-USSO3H. https://www.polymersource.ca/.

246. Su, Z. H.; Li, X.; Hsu, S. L., Spectroscopic and Thermal Studies of Sulfonated Syndiotactic Polystyrene. *Macromolecules* **1994,** *27* (1), 287-291.

247. Axelrod, D.; Koppel, D. E.; Schlessinger, J.; Elson, E.; Webb, W. W., Mobility Measurement by Analysis of Fluorescence Photobleaching Recovery Kinetics. *Biophysical Journal* **1976,** *16* (9), 1055-1069.

248. Peters, R.; Peters, J.; Tews, K. H.; Bähr, W., A microfluorimetric study of translational diffusion in erythrocyte membranes. *Biochimica et Biophysica Acta (BBA) - Biomembranes* **1974,** *367* (3), 282-294.

249. Smith, B. A.; Mcconnell, H. M., Determination of Molecular-Motion in Membranes Using Periodic Pattern Photobleaching. *P Natl Acad Sci USA* **1978,** *75* (6), 2759-2763.

250. Jacobson, K.; Wu, E.; Poste, G., Measurement of the translation mobility of concanavalin a in glycerol-saline solutions and on the cell surface by fluorescence recovery after photobleaching. *Biochimica et Biophysica Acta (BBA) - Biomembranes* **1976,** *433* (1), 215-222.

251. Poo, M.-m.; Cone, R. A., Lateral diffusion of rhodopsin in the photoreceptor membrane. *Nature* **1974,** *247* (5441), 438-441.

252. Smith, B. A., Measurement of Diffusion in Polymer-Films by Fluorescence Redistribution after Pattern Photobleaching. *Macromolecules* **1982,** *15* (2), 469-472.

253. Kovaleski, J. M.; Wirth, M. J., Applications of fluorescence recovery after photobleaching. *Anal Chem* **1997,** *69* (19), A600-A605.

254. Axelrod, D.; Elson, E. L.; Schlessinger, J.; Koppel, D. E., Reminiscences on the "Classic" 1976 FRAP Article in Biophysical Journal. *Biophysical Journal* **2018,** *115* (7), 1156-1159.

255. Lanni, F.; Ware, B. R., INTENSITY DEPENDENCE OF FLUOROPHORE PHOTOBLEACHING BY A STEPPED-INTENSITY SLOW-BLEACH EXPERIMENT. *Photochemistry and Photobiology* **1981,** *34* (2), 279-281.

256. Stout, A. L.; Axelrod, D., SPONTANEOUS RECOVERY OF FLUORESCENCE BY PHOTOBLEACHED SURFACE-ADSORBED PROTEINS. *Photochemistry and Photobiology* **1995,** *62* (2), 239-244.

257. Soumpasis, D., Theoretical analysis of fluorescence photobleaching recovery experiments. *Biophysical journal* **1983,** *41* (1), 95-97.

258. Starr, T. E.; Thompson, N. L., Fluorescence pattern photobleaching recovery for samples with multi-component diffusion. *Biophysical Chemistry* **2002,** *97* (1), 29-44.

259. Lanni, F.; Ware, B. R., Modulation detection of fluorescence photobleaching recovery. *Review of Scientific Instruments* **1982,** *53* (6), 905-908.

260. Koppel, D. E., Analysis of Macromolecular Polydispersity in Intensity Correlation Spectroscopy: The Method of Cumulants. *The Journal of Chemical Physics* **1972,** *57* (11), 4814-4820.

261. Brown, W., *Dynamic light scattering: the method and some applications*. Clarendon Press: 1993.

262. Chen, P. Y.; Huang, Z. H.; Liang, J. S.; Cui, T. Q.; Zhang, X. H.; Miao, B.; Yan, L. T., Diffusion and Directionality of Charged Nanoparticles on Lipid Bilayer Membrane. *Acs Nano* **2016,** *10* (12), 11541-11547.

263. Pulko, I.; Kolar, M.; Krajnc, P., Atrazine removal by covalent bonding to piperazine functionalized PolyHIPEs. *Sci Total Environ* **2007,** *386* (1-3), 114-123.

264. Mathieu, K.; Jerome, C.; Debuigne, A., Influence of the Macromolecular Surfactant Features and Reactivity on Morphology and Surface Properties of Emulsion-Templated Porous Polymers. *Macromolecules* **2015,** *48* (18), 6489-6498.

265. Ermi, B. D.; Amis, E. J., Domain structures in low ionic strength polyelectrolyte solutions. *Macromolecules* **1998,** *31* (21), 7378-7384.

266. Muthukumar, M., Ordinary-extraordinary transition in dynamics of solutions of charged macromolecules. *P Natl Acad Sci USA* **2016,** *113* (45), 12627-12632.

267. Oostwal, M.; Odijk, T., Novel Dynamic Scaling Hypothesis for Semidilute and Concentrated-Solutions of Polymers and Polyelectrolytes. *Macromolecules* **1993,** *26* (24), 6489-6497.

268. Sehgal, A.; Seery, T. A. P., Polyelectrolyte self-diffusion: Fluorescence recovery after photobleaching of sodium poly(styrenesulfonate) in N-methylformamide. *Macromolecules* **2003,** *36* (26), 10056-10062.

269. Lodge, T. P.; Muthukumar, M., Physical chemistry of polymers: Entropy, interactions, and dynamics. *J Phys Chem-Us* **1996,** *100* (31), 13275-13292.

270. Tirrell, M., Polymer Self-Diffusion in Entangled Systems. *Rubber Chem Technol* **1984,** *57* (3), 523-556.

271. Fong, B.; Stryjewski, W.; Russo, P. S., On the use of pattern fluorescence photobleaching recovery with modulation detection to obtain colloidal size distributions. *J Colloid Interf Sci* **2001,** *239* (2), 374-379.

272. Tanahatoe, J. J.; Kuil, M. E., Dynamic light scattering of a flexible highly charged polyelectrolyte in the dilute concentration regime. *Macromolecules* **1997,** *30* (20), 6102-6106.

273. Bu, Z.; Russo, P. S., Diffusion of Dextran in Aqueous (Hydroxypropyl)Cellulose. *Macromolecules* **1994,** *27* (5), 1187-1194.

274. Furukawa, R.; Arauzlara, J. L.; Ware, B. R., Self-Diffusion and Probe Diffusion in Dilute and Semidilute Aqueous-Solutions of Dextran. *Macromolecules* **1991,** *24* (2), 599-605.

275. Doucet, G. J.; Dorman, D.; Cueto, R.; Neau, D.; Russo, P. S., Matrix fluorescence photobleaching recovery for polymer molecular weight distributions and other applications. *Macromolecules* **2006,** *39* (26), 9446-9455.

276. Matsuoka, H.; Schwahn, D.; Ise, N., Observation of Cluster Formation in Polyelectrolyte Solutions by Small-Angle Neutron-Scattering .1. A Steep Upturn of the Scattering Curves from Solutions of Sodium Poly(Styrenesulfonate) at Scattering Vectors Below 0.01(a)-1. *Macromolecules* **1991,** *24* (14), 4227-4228.

277. Jia, D.; Muthukumar, M., Effect of Salt on the Ordinary–Extraordinary Transition in Solutions of Charged Macromolecules. *J Am Chem Soc* **2019,** *141* (14), 5886-5896.

278. Sohn, D. W.; Russo, P. S.; Davila, A.; Poche, D. S.; McLaughlin, M. L., Light scattering study of magnetic latex particles and their interaction with polyelectrolytes. *J Colloid Interf Sci* **1996,** *177* (1), 31-44.

279. Yamakawa, H., *Modern Theory of Polymer Solutions*. Harper & Row: 1971.

280. Kirkwood, J. G.; Riseman, J., The Intrinsic Viscosities and Diffusion Constants of Flexible Macromolecules in Solution. *J Chem Phys* **1948,** *16* (6), 565-573.

281. Oono, Y.; Baldwin, P., Cooperative Diffusion of a Semidilute Polymer-Solution - a Preliminary-Study. *Physical Review A* **1986,** *33* (5), 3391-3398.

282. Phillies, G. D. J., Universal Scaling Equation for Self-Diffusion by Macromolecules in Solution. *Macromolecules* **1986,** *19* (9), 2367-2376.

283. Phillies, G. D. J., Derivation of the universal scaling equation of the hydrodynamic scaling model via renormalization group analysis. *Macromolecules* **1998,** *31* (7), 2317-2327.

284. Langevin, D.; Rondelez, F., Sedimentation of Large Colloidal Particles through Semidilute Polymer-Solutions. *Polymer* **1978,** *19* (8), 875-882.

285. Park, I. H.; Johnson, C. S.; Gabriel, D. A., Probe diffusion in polyacrylamide gels as observed by means of holographic relaxation methods: search for a universal equation. *Macromolecules* **1990,** *23* (5), 1548-1553.

286. Cukier, R. I., Diffusion of Brownian Spheres in Semidilute Polymer-Solutions. *Macromolecules* **1984,** *17* (2), 252-255.

287. Altenberger, A. R.; Tirrell, M., On the Theory of Self-Diffusion in a Polymer Gel. *J Chem Phys* **1984,** *80* (5), 2208-2213.

288. Ogston, A. G.; Preston, B. N.; Wells, J. D.; Ogston, A. G.; Preston, B. N.; Snowden, J. M.; Wells, J. D., Transport of Compact Particles through Solutions of Chain-Polymers. *P Roy Soc Lond a Mat* **1973,** *333* (1594), 297-316.

289. Phillies, G. D. J., The Hydrodynamic Scaling Model for Polymer Self-Diffusion. *J Phys Chem-Us* **1989,** *93* (13), 5029-5039.

290. Delong, L. M.; Russo, P. S., Thermodynamic and Dynamic Behavior of Semiflexible Polymers in the Isotropic-Phase. *Macromolecules* **1991,** *24* (23), 6139-6155.

291. Stockley, P. G.; Twarock, R.; Bakker, S. E.; Barker, A. M.; Borodavka, A.; Dykeman, E.; Ford, R. J.; Pearson, A. R.; Phillips, S. E. V.; Ranson, N. A.; Tuma, R., Packaging signals in single-stranded RNA viruses: nature's alternative to a purely electrostatic assembly mechanism. *J Biol Phys* **2013,** *39* (2), 277-287.

292. Wanunu, M., Nanopores: A journey towards DNA sequencing. *Physics of life reviews* **2012,** *9* (2), 125-58.

293. Singh, S. P.; Muthukumar, M., Electrophoretic mobilities of counterions and a polymer in cylindrical pores. *J Chem Phys* **2014,** *141* (11).

294. Ware, B. R., Laser Techniques for the Study of Counterion Condensation. In *Advances in Laser Spectroscopy*, Garetz, B. A., Lombardi,J.R., Ed. John Wiley and Sons: New York, 1986; Vol. 3, pp 171-188.

295. Prabhu, V. M.; Amis, E. J.; Bossev, D. P.; Rosov, N., Counterion associative behavior with flexible polyelectrolytes. *J Chem Phys* **2004,** *121* (9), 4424-4429.

296. Imhof, A.; Vanblaaderen, A.; Maret, G.; Mellema, J.; Dhont, J. K. G., A Comparison between the Ion-Time Self-Diffusion and Low Shear Viscosity of Concentrated Dispersions of Charged Colloidal Silica Spheres. *J Chem Phys* **1994,** *100* (3), 2170-2181.

297. Davoust, J.; Devaux, P. F.; Leger, L., Fringe Pattern Photobleaching, a New Method for the Measurement of Transport-Coefficients of Biological Macromolecules. *Embo Journal* **1982,** *1* (10), 1233-1238.